NASA/TM—2002-211366

Measurements of Turbulent Flow Field in Separate Flow Nozzles With Enhanced Mixing Devices—Test Report

James Bridges
Glenn Research Center, Cleveland, Ohio

February 2002

The NASA STI Program Office . . . in Profile

Since its founding, NASA has been dedicated to the advancement of aeronautics and space science. The NASA Scientific and Technical Information (STI) Program Office plays a key part in helping NASA maintain this important role.

The NASA STI Program Office is operated by Langley Research Center, the Lead Center for NASA's scientific and technical information. The NASA STI Program Office provides access to the NASA STI Database, the largest collection of aeronautical and space science STI in the world. The Program Office is also NASA's institutional mechanism for disseminating the results of its research and development activities. These results are published by NASA in the NASA STI Report Series, which includes the following report types:

- TECHNICAL PUBLICATION. Reports of completed research or a major significant phase of research that present the results of NASA programs and include extensive data or theoretical analysis. Includes compilations of significant scientific and technical data and information deemed to be of continuing reference value. NASA's counterpart of peer-reviewed formal professional papers but has less stringent limitations on manuscript length and extent of graphic presentations.

- TECHNICAL MEMORANDUM. Scientific and technical findings that are preliminary or of specialized interest, e.g., quick release reports, working papers, and bibliographies that contain minimal annotation. Does not contain extensive analysis.

- CONTRACTOR REPORT. Scientific and technical findings by NASA-sponsored contractors and grantees.

- CONFERENCE PUBLICATION. Collected papers from scientific and technical conferences, symposia, seminars, or other meetings sponsored or cosponsored by NASA.

- SPECIAL PUBLICATION. Scientific, technical, or historical information from NASA programs, projects, and missions, often concerned with subjects having substantial public interest.

- TECHNICAL TRANSLATION. English-language translations of foreign scientific and technical material pertinent to NASA's mission.

Specialized services that complement the STI Program Office's diverse offerings include creating custom thesauri, building customized data bases, organizing and publishing research results . . . even providing videos.

For more information about the NASA STI Program Office, see the following:

- Access the NASA STI Program Home Page at ***http://www.sti.nasa.gov***

- E-mail your question via the Internet to help@sti.nasa.gov

- Fax your question to the NASA Access Help Desk at 301–621–0134

- Telephone the NASA Access Help Desk at 301–621–0390

- Write to:
  NASA Access Help Desk
  NASA Center for AeroSpace Information
  7121 Standard Drive
  Hanover, MD 21076

NASA/TM—2002-211366

Measurements of Turbulent Flow Field in Separate Flow Nozzles With Enhanced Mixing Devices—Test Report

James Bridges
Glenn Research Center, Cleveland, Ohio

National Aeronautics and
Space Administration

Glenn Research Center

February 2002

Acknowledgments

The PIV instrumentation used in this work was developed by Dr. Mark P. Wernet of NASA Glenn Research Center's Instrumentation Branch. Dr. Wernet also processed the PIV images to velocity maps. The jet noise suppression nozzles used were designed by engineers at General Electric Aircraft Engines and at Pratt & Whitney. The jet rig was assembled and operated in the AeroAcoustic Propulsion Laboratory under the guidance of Mr. Thomas Griffin of the Aeropropulsion Test Engineering Branch.

This report is a formal draft or working paper, intended to solicit comments and ideas from a technical peer group.

This report contains preliminary findings, subject to revision as analysis proceeds.

Available from

NASA Center for Aerospace Information
7121 Standard Drive
Hanover, MD 21076

National Technical Information Service
5285 Port Royal Road
Springfield, VA 22100

Available electronically at http://gltrs.grc.nasa.gov/GLTRS

Measurements of Turbulent Flow Field in Separate Flow Nozzles with Enhanced Mixing Devices—Test Report

James Bridges
National Aeronautics and Space Administration
Glenn Research Center
Cleveland, Ohio 44135

1 Abstract

As part of the Advanced Subsonic Technology Program, a series of experiments was conducted at NASA Glenn Research Center on the effect of mixing enhancement devices on the aeroacoustic performance of separate flow nozzles. Initial acoustic evaluations of the devices showed that they reduced jet noise significantly, while creating very little thrust loss. The explanation for the improvement required that turbulence measurements, namely single point mean and RMS statistics and two-point spatial correlations, be made to determine the change in the turbulence caused by the mixing enhancement devices that lead to the noise reduction. These measurements were made in the summer of 2000 in a test program called Separate Nozzle Flow Test 2000 (SFNT2K) supported by the Aeropropulsion Research Program at NASA Glenn Research Center.

Given the hot high-speed flows representative of a contemporary bypass ratio 5 turbofan engine, unsteady flow field measurements required the use of an optical measurement method. To achieve the spatial correlations, the Particle Image Velocimetry technique was employed, acquiring high-density velocity maps of the flows from which the required statistics could be derived. This was the first successful use of this technique for such flows, and shows the utility of this technique for future experimental programs. The extensive statistics obtained were likewise unique and give great insight into the turbulence which produces noise and how the turbulence can be modified to reduce jet noise.

This report documents the test facilities and procedures used to obtain the turbulence data. It also contains an indexed overview of the results, both in graphical and numerical formats.

2 Table of Contents

3 Introduction

NASA's recent Advanced Subsonic Technology (AST) program had as its goal the reduction of aircraft noise in the current and near-term fleet. Hence, it focussed on technologies that were compatible with current engine configurations. One of these engine configurations deemed vulnerable to jet noise reduction was the separate flow exhaust nozzle. It was believed that nozzle modifications that decreased the core flow velocity in the plume by enhancing mixing would cause overall noise reduction. Such modifications would be required to have minimal thrust loss to be acceptable as a noise reduction technique.

In 1997, a series of separate flow nozzle concepts were tested, concepts which were submitted by General Electric Aircraft Engines, Pratt & Whitney, Rolls-Royce Allison, and NASA Glenn Research Center. This test was dubbed the Separate Flow Nozzle Test 1997 (SFNT97). Several of these nozzle concepts provided significant noise reduction benefits with negligible thrust penalty. During the SFNT97, many measurements were made on the jet flows: far-field acoustics, total and static pressure and total temperature surveys of the plume, infrared imagery of the plume, acoustic source distribution estimation by phased arrays, and Schlieren images. These combined to describe the mean flow field and acoustic fields for the jet flows, leading to some understanding of how changes in the flow field caused beneficial changes in the acoustic sources. Results of this test are documented in references **1**, **2**, **3**, and **4**.

As successful as the SFNT97 was, one key class of information was not acquired: unsteady fluid dynamics measurements. Turbulence statistics are the main information that aeroacoustic theory requires to relate flow to sound. Specifically, leading theories require two-point space-time correlations of the velocity field as input to predict acoustic output of the jet flow. Although such measurements were attempted at NASA Langley in 1997, researchers were ultimately unsuccessful in obtaining this information. So important were these measurements that a second series of tests were performed in 2000 on the original AAPL test rig in a test called SFNT2K, and this time the efforts were successful. The datasets for the separate flow nozzle tests now have turbulence measurements, including two-point space correlations, for the three most important nozzle configurations.

Beyond the immediate need for understanding of the results of a particular test is the more general need to explore and capture the relationship between turbulence and aeroacoustic noise. Given the difficulty in measuring turbulence in hot, high-speed jets, this work was ground-breaking in that it demonstrated the potential of Particle Image Velocimetry (PIV) in making the high-order turbulence measurements that are apparently required to establish this relationship. This report documents these initial experiments using PIV at the NASA Glenn AeroAcoustic Propulsion Laboratory.

4 Facilities

The AST Separate Flow Nozzle Tests were conducted at the AeroAcoustic Propulsion Laboratory (AAPL) at NASA Glenn Research Center in Cleveland, Ohio. The exhaust nozzle models were mounted on a hydrogen fired jet engine exhaust simulator rig inside a freejet, providing a scaled model of engine nozzles at appropriate hot flow conditions in simulated flight. These facilities are described below.

4.1 AAPL

The Aeroacoustic Propulsion Laboratory (AAPL) at NASA Glenn Research Center is a 65ft (20m) radius, anechoic, geodesic-dome. The walls of the dome and approximately half of the floor area are treated with acoustic wedges made from fiberglass wool to render the facility anechoic above 220 Hz. A 60 inch (1.5m) exhaust fan in the top of the dome provides air circulation. Flows from all rigs are directed out the 55ft (16.8m) wide by 35 ft (10.7) high doorway onto an open field bordering on the 9x15 Low Speed Wind Tunnel.

4.2 NATR

Within the confines of the AAPL dome is the Nozzle Acoustic Test Rig (NATR), a free-jet, forward-flight-simulation test rig, shown in Figure 4.1. The NATR consists of a 10 ft (3m) diameter acoustically lined duct functioning as an ejector for an annular air injector system. The ejector system provides a free-jet Mach number up number up to 0.3 at 300 lbm/s (135kg/s), approximately 100lbm/s (19.5kg/s) of which is supplied

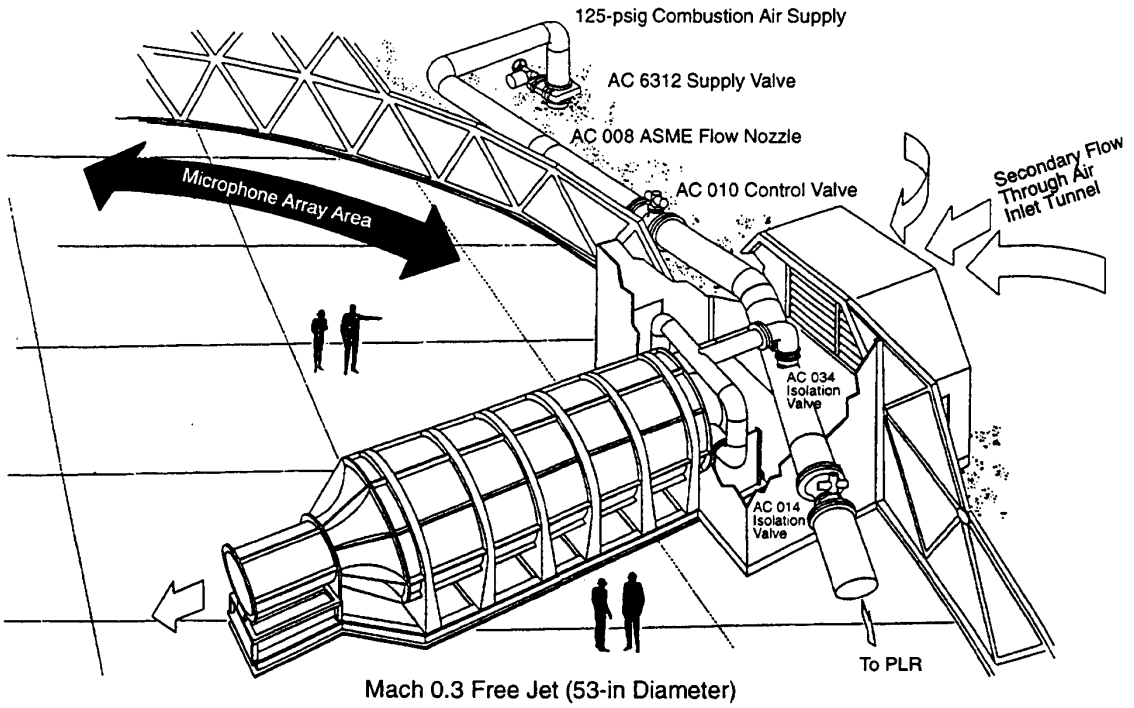

Figure 4.1 NATR positioned in AAPL

through the ejector driver nozzles by the Laboratory's central air supply system at 150psia (1.0MPa). The remaining 200 lbm/s (39kg/s) is pulled into the duct through louvered walls in an inlet tunnel. Thirty foot (9m) into the AAPL dome the 10 foot (3m) duct contracts to an inner diameter of 53 inches (1.35m); the contraction is an ASME long-radius, low-β-ratio nozzle. The 53 inch diameter duct extends for 11.1 feet (3.4m) with a centerline 10 ft (3m) above the concrete floor. By careful design of acoustic lining and flow conditioning screens in the tunnel the background sound inside the dome facility is extremely low and the freestream turbulence is less than 1 percent [**5**]. A 16 ft (5m) high wall, constructed of aluminum box beam covered with plywood and fiberglass wedges, separates the anechoic test area with NATR from the acoustically untreated part of the dome.

4.3 JER

The last 12 ft (3.7m) of the NATR is a constant diameter, unlined, duct. Nozzle models to be tested are installed on the aft end of the hydrogen-fired jet exit rig (JER) that is located in this duct. The JER is the structure through which hot airflow is delivered to the test article via connections to facility compressed air supplies. A detailed description of the JER (along with more information about the NATR) is given in Castner[**6**]. For this program, the JER became a tandem-strut arrangement (NASA drawing 28529M42AOOO) consisting of the hydrogen fueled dual stream rig (JER) augmented by a dual flow 'pod' attached just aft of the combustor. Only the core stream of the dual stream rig was used to provide the hot core flow while the fan flow came from a secondary strut into the dual flow pod. This rig setup and arrangement relative to the NATR are shown in Figure 4.2. Locations on the rig are given in inches as JER stations relative to the leading point of the rig.

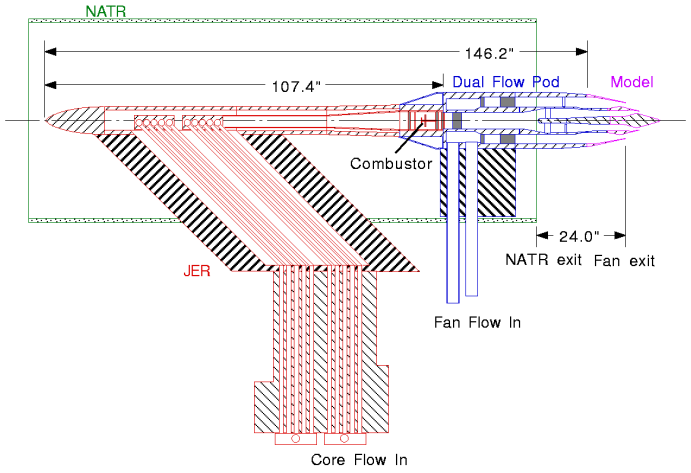

Figure 4.2 Hydrogen fueled jet exit rig (JER) with Dual Flow Pod in NATR.

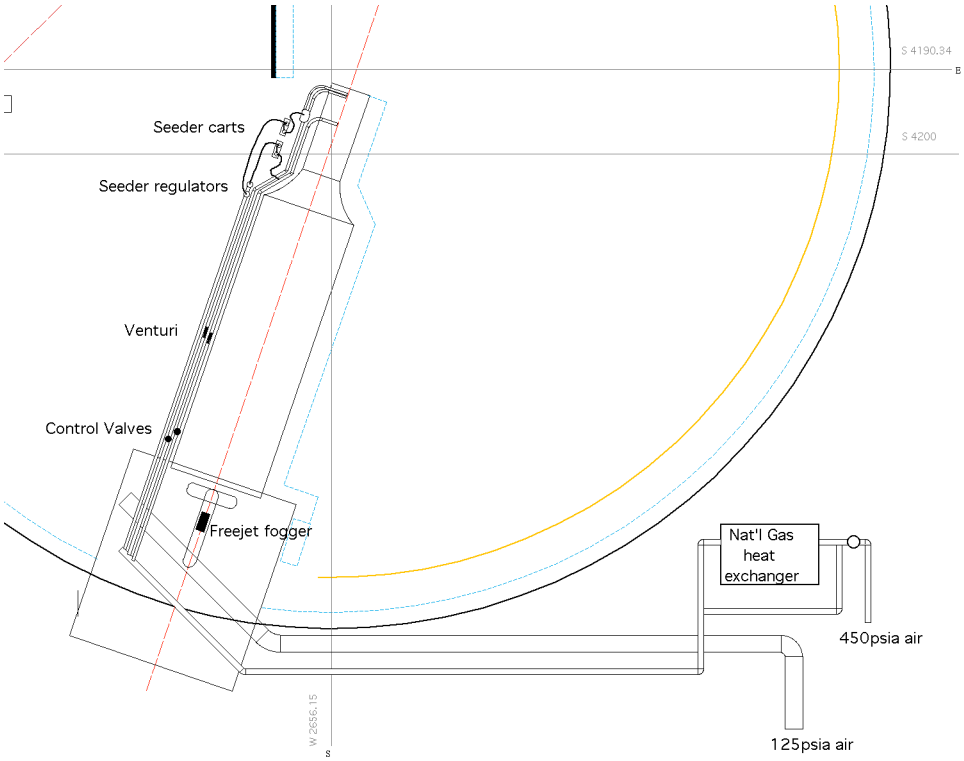

Figure 4.3 Supply piping to jet exit rig and NATR in AAPL.

Figure 4.3 illustrates the supply piping routing for the 450psig (3.1MPa) and 150 psig (1.0MPa) lines which feed the model and the freejet. Supply air at 450psi (3.1MPa) is preheated to roughly fan flow temperature of 600°R (330°K) by a natural gas fired heat exchanger outside the dome. The flow is split into core and fan flows, which are independently metered and throttled down by a control valve in 4 inch (10cm) flow lines.

The core air is brought to the base of the JER strut where it is split into 10 flow tubes to pass through the main strut of the JER and into the plenum at the upstream end of the rig. For this test, only the five flow tubes connected to the primary stream pipe were used. The air is passed through the hydrogen injector plate where the combustion of the hydrogen increases its temperature to that of the core flow of an aircraft engine. After passing over flow mixing devices to hasten the temperature uniformity, the flow is passed through two choke plates, reticulated metal foam and screens. The reticulated foam metal was removed during this test as seed would clog and break the foam metal. A charging station constisting of three azimuthally distributed rakes of alternating total pressure and total

temperature sensors is located just upstream of the beginning of the centerbody section, which is held in the middle of the core stream by three thin airfoil struts. The centerbody section holds the nozzle plug.

The fan air is split into two 3inch (7.6cm) tubes in a manifold by which it is guided through a 16inch (41cm) airfoil section that penetrates the NATR in the last 18inches (46cm) of the freejet. The air in the two tubes is rejoined in an annular plenum before passing through a series of choke plates, reticulated foam metal and screens. For the PIV measurements, a small-hole choke plate replaced the reticulated foam metal to keep seed from clogging and destroying the foam metal. In addition, problems developed with the screen downstream of the choke plate and it had to be removed. This modification was checked for impact on freestream turbulence levels and found to be minimal. A charging station consisting of total pressure and total temperature rakes measures the flow conditions immediately before the upstream end of the fan nozzle.

The JER main bore has axial locations given as stations in inches from the highlight of the upstream tip of the rig. Separate-flow exhaust system model fan nozzle hardware was designed to attach to the dual flow pod at cold JER station 146.12. Model core cowl/nozzle hardware was designed to attach to the facility core duct at cold JER station 146.12. Model centerbody/plug hardware was designed to attach to the facility core/tailcone extension weldment at cold JER station 142.19. When assembled and positioned, the separate-flow exhaust system fan nozzle exit plane was positioned at cold JER station 156.49, and the NATR exit plane was to be located at cold JER station 132.10, putting the fan nozzle exit 24inches (51cm) downstream of the freejet exit. The nozzle model centerline was elevated about 10 feet (3.05m) above the facility floor.

Nozzle airflows, pressures, and temperatures are monitored using JER/NATR instrumentation. Mass flow was measured using choked-flow venturi located in the 4inch (10cm) supply lines downstream of the fan/core flow split, in the long horizontal pipe runs alongside NATR. Two total pressure and two temperature rakes (with five elements each) were installed at the charging station of the fan and of the core ducts of the dual flow pod. The fan rakes are installed at circumferential angle positions of 0°, 90°, 180°, and 270° (aft looking forward). Core nozzle rakes are located at circumferential angles of 60°, 150°, 240°, and 330° (aft looking forward). The PT/TT measurement plane for the fan flow is JER station 140.025. The PT/TT measurement plane for the core flow is JER station 140.741.

4.4 Flow Seeding

For PIV, the flow motion being measured is marked by use of particles. These particles must be very small so they will have no slip relative to the fluid and so that the motion is the same as the fluid motion. This is an ideal case, but the smaller the particle, the greater the fidelity. As the particle size increases, high velocity gradients, associated with high frequency or small scale motions, are not recorded properly, effectively adding a lowpass filter to the measurements. In addition, all fluid must be laden with particles at a density high enough that sufficient particles (5-10) are found in an interrogation region of the PIV image. This is made difficult when one has several flow streams that are mixing together in the measurement region. In these tests three fluids are mixed, the core stream, the fan stream, and the ambient. It is also crucial that the seed be fully mixed with its flow long before the measurement region, something that can be tricky in high speed rigs. Finally, the seed must not be affected by the high temperatures of the gas; this is especially true of the seed in the core stream at 1500°R (833°K).

In these tests, the core and bypass streams were seeded with aluminum oxide (Al_2O_3) powder using two identical, specially built seeders. The specific gravity of the alumina powder is 3.96 and the particle size distribution has a mean of 2.75×10^{-5} inch (0.7 μm) and a standard deviation of 7.8×10^{-6} inch (0.2 μm). Alumina is listed on its Material Safety Data Sheet (MSDS) as a desiccant with a low health risk by inhalation; it should be treated as a nuisance dust. It is non-flammable. The ambient flow was seeded with oil droplets of roughly 0.2-0.3 micron diameter produced by a commercial fogger. The manufacturers' proprietary formulation of fogger oil (a variant of mineral oil) has been certified to be non-toxic by the FDA and OSHA.

4.4.1 Core & Bypass Seed Injection

4.4.1.1 System description

The core and fan flows were seeded with aluminum oxide powder, a dry particulate with roughly the consistency of corn starch. This material was introduced into the feedstreams well upstream of the rig. Air was tapped from the 450psia supply line upstream of the control valves through a 1inch (2.5cm) tube, split into core and fan flow streams to feed the two seeders for the two streams. This air was brought through remote control valves, regulators, filters, and one-way valves and into the seeders. Figure 4.4 is a picture of the seeder carts and regulator/valve equipment used to inject the seed into the rig.

Figure 4.4 Seeder system layout. Circle A denotes the regulator/valve strings, B is the bypass seeder cart, C is the core seeder cart, and D is the injection boss for the core flow seed into the core flow piping.

The heavily seeded air destined to be mixed with the fan flow was directed into the fan flow line through a 1 inch (2.5cm) flexible hose. A 1inch (2.5cm) boss welded onto the manifold simply dumped this seeded air into the feedpipe, giving it 20 diameters or more to mix before the flow dumped into the plenum of the dual flow pod, passed through a choke plate and exited the fan nozzle.

On the core flow side, hoses from the seeder injected the seed into the 4inch (10cm) feedpipe through a 1 inch (2.5cm) boss welded onto the pipe roughly at the bellmouth of the NATR. The seed mixed thoroughly with the main core flow over the 50 pipe diameters, through the JER strut, plenum, and combustor before exiting the core nozzle.

4.4.1.2 Dry seeder design

The fluidized bed seeder system is comprised of two chambers, a fluidized-bed chamber and a swirl chamber (see Figure 4.5). The fluidized bed chamber has a felt metal plate near its bottom which holds the seed material and allows air to flow through it, levitating the seed. Air is introduced into this chamber from the bottom. The seed is levitated and carried off with the air through a 1 inch (2.5cm) port in the chamber side. This seeded air is brought into the swirl chamber below a pair of small tangential jets that set up a swirling flow in the chamber. This swirl causes larger particles, or more likely aggregates of particles, to be thrown to the side of the chamber where they will drop to the bottom of the chamber. The small particles and air are carried up through a port in the top of the chamber and are piped into the supply pipe of the jet rig with a 1 inch (2.5cm) rubber hose. Figure 4.6 is a picture of the seeder cart.

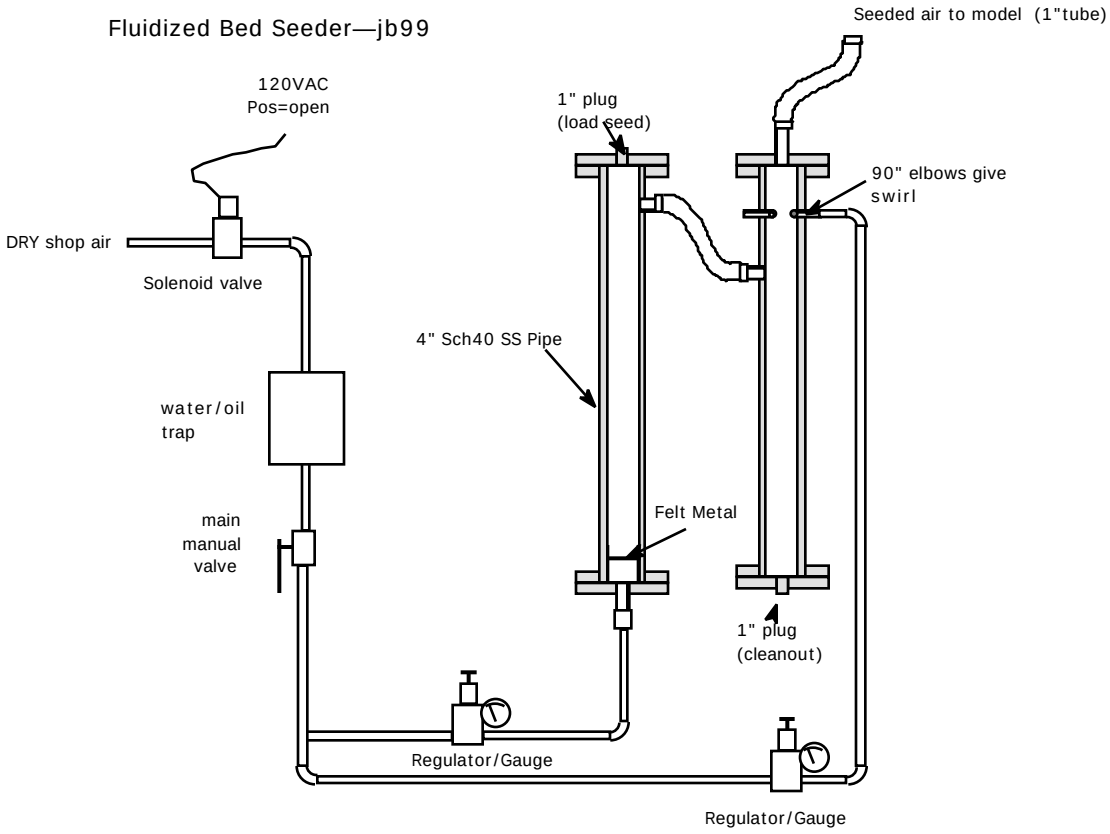

Figure 4.5. Schematic of fluidized bed seeder design.

Figure 4.6. Seeder cart.

4.4.1.3 Operation, estimate of seed density

Inlet pressure to the seeders was controlled remotely to appropriately match the back pressure of the rig, as judged by the seed density obtained in the PIV images. A remote control video camera aimed at the gauges in the regulator-control valve string monitored the pressures of the seeders. For the setpoint used in this test, the core flow required roughly 120psia (830kPa) and the fan flow required 160psia (1.1MPa) supply pressure. The one-way valve kept seed from being blown backwards through the supply string before the seeder main valve was opened.

Judging by the images, seeding density was very good most of the time. The seeders were not entirely steady, occasionally puffing a large slug of seed. No doubt deposits of seed within the rig helped to smooth out the unevenness in the seeder operation. This became apparent by the large amount of seed that was observed to come from the rig at startup before the seeders were turned on. Changes in internal flow separations must have loosened deposits of seed within the piping and rig during these changes in flow. Monitoring the rate at which seed was used, it is estimated that the seeders provided roughly 0.5liters/hour each, seeding the flow at a rate of 20 particles/mm. Given the light sheet thickness of 0.2mm, this produces on the order of 10 particles in a 2mm by 2mm interrogation region.

The core and fan stream seeders were usually left running during the run once PIV image acquisition had begun, even during traverse movement and image storage periods.

4.4.2 Freejet fogger

4.4.2.1 System description

If ambient air around the jet is not seeded, the measured velocity statistics will be biased because the low speed ambient fluid, entrained by the seeded jet fluid, will not be recorded. Ideally, the jet fluid and ambient fluid will be seeded at equal density. Having a freejet flow surrounding the model jet is actually an aid in doing this as the surrounding fluid can be seeded evenly by introducing seed sufficiently far upstream that it can be thoroughly mixed before the measurement region.

4.4.2.2 Fogger design

In the current test the freejet flow was seeded with oil droplets generated by a light oil fog generator manufactured by Corona Technologies, Ltd of Canada, specifically model Vicount 5000. This seeder produces droplets in the 0.2-0.3 micron diameter range at a rate of 5 liters/hour. The seeder functions by forcing the oil through a heated nozzle along with nitrogen, evaporating the oil in the heated nozzle and condensing it into the small droplets which quickly form spheres that are essentially ‘dry’, leaving a minimal oil film on surfaces.

4.4.2.3 Operation in NATR, estimate of seed density

The fogger was placed in the NATR inlet house, four feet upstream of the NATR freejet ejector plane on the centerline of the NATR. The fogger was supplied by facility nitrogen, regulated to 60 psig (410kPa). The remote control feature of the fogger was replaced by a directly wired switch line to the laser trailer control panel because the metal enclosure of the inlet house shielded the radio frequency remote control. The fogger was activated shortly before data acquisition was to commence, and was typically left on during the entire 45 minute run period.

It is important to note that although the droplets were 0.2 – 0.3 micron in diameter, the image formed on the imaging plane of the camera was larger, being the diffraction limited size produced by the long focal length lens. This is satisfactory, providing the fluid marker functionality while having less mass and hence higher frequency response.

Based upon PIV images and on estimates of delivery rates of the fogger and the freejet mass flow at M=0.28 (300 lbm/s or 135kg/s), the particle density was estimated to be 1000 particles/mm^3 in the measurement region near the nozzle exit. Given the light sheet thickness of 0.2mm, this produces on the order of 100 particles in a 2mm by 2mm interrogation region.

Figure 4.7 is a typical image taken at the core nozzle exit illustrating seeding density. Note the relative uniformity of the seed in the core and fan streams; this was not always the case, but did not seem to adversely affect the data within the range of variation we observed. Also note the discernable difference between the fan and ambient seeding, manifest of the difference in seed size and density.

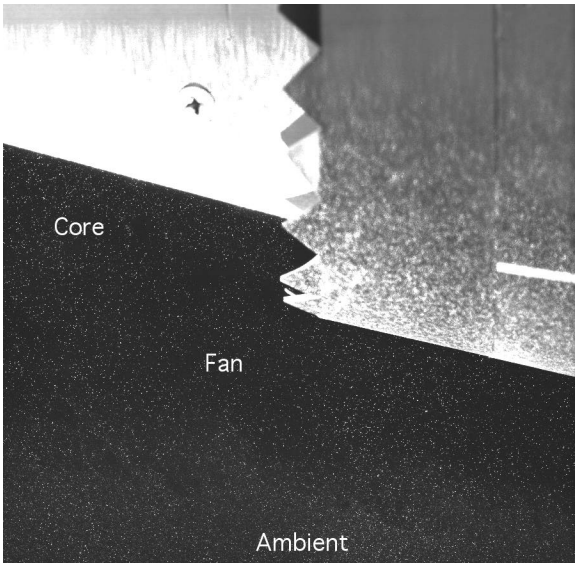

Figure 4.7. Example of PIV image showing seed density.

4.4.2.4 Prelim tests, lessons learned

Some ad hoc trials on placement of the fogger in the inlet area were run using a laser sheet normal to the jet axis to determine the fog effectiveness at the downstream end of NATR. Although the data was acquired on a vertical plane below the model, placing the fogger two feet below centerline at the inlet did not improve seed density significantly in the measurement region and risked missing some fluid entrained from above the jet. In the end it was found that putting the fogger on the centerline of the NATR gave adequate seed density for all regions of the jet being measured, roughly 12 inches (30cm) below centerline and up to 120 inches (3m) downstream of the NATR exit.

Although one Vicount 5000 fogger usually seemed sufficient, a second fogger was added just below the first when it appeared that the first fogger was not as effective as needed. Eventually it was found that the nitrogen pressure was insufficient on the original fogger and the second fogger was no longer used after this was corrected. It was also found to be necessary to clean the fogger nozzle occasionally by reaming it with the manufacturer-provided drill bit.

Placing the fogger only four feet upstream of the centerbody of the NATR ejector resulted in the centerbody becoming coated with oil. Before it was discovered that the fogger nozzle required periodic cleaning, large oil droplets were observed in a few of the PIV images. This was due to sputtering of the fogger, collecting oil on the NATR that then shed off in large drops. When the test was finished, the NATR screens were cleaned of oil and other debris; it is not clear how much of this oil loading occurred while the fogger was operating properly and how much occurred during the time the fogger was sputtering.

5 Models & flow conditions

This chapter describes the three models that were extensively studied, and gives full description of the nozzle geometries and flow conditions measured. It also includes a quick test narrative that indicates some of the difficulties experienced during the test.

5.1 Test plan

5.1.1 Models tested

In the PIV portion of the SFNT2K covered in this report, three nozzles were measured in detail. These were the baseline (3BB), alternating 12 count chevron ($3A_{12}B$), and 24 count alternating tabbed nozzle ($3T_{24}B$). These were chosen because they had the most dramatic (and beneficial!) acoustic and mean flow changes as measured during the 1997 SFNT. The SFNT series models were named by a convention comprised of a number followed by two letters. The number signified bypass ratio and whether the model had an internal or external plug. The two single-letter designations denoting the type of mixing enhancement device on the core and on the fan, the first letter referring to the core nozzle and the second to the fan nozzle. Subscripts on the letters gave the count of the tabs or chevrons on each nozzle. For this test all models were of the 3xx series, being of bypass ratio 5 and having an external plug.

5.1.2 Simulated Engine Power Conditions

For the PIV test only one flow condition was used, that being the power code 21 as defined in the SFNT97 test plan. This condition is a simulation of a take-off power setting of a contemporary subsonic medium to large commercial transport craft and is given in the table below. The facility controllers were set to maintain 0.5% tolerance of all four parameters.

The freejet was run at M=0.28, again to simulate flight effects during takeoff. This value was maintained during the runs to within 1.5%.

Table 5.1. Flow conditions tested.

Stream	NPR	Ttotal (°R)
Fan	1.830	600
Core	1.680	1500

5.1.3 Data acquired

In the test results being reported herein, a two-component PIV system employing two cameras was used to measure axial and radial velocity components in a single plane. The two cameras were used in tandem, one above the other, with slightly overlapping fields of view to decrease test time. The field of view was traversed axially to cover the first 95 inches (2.4m) of the jet flow field with 400 image pairs being collected from each camera at each location. From these images instantaneous velocity maps were created, and standard single-point and two-point turbulent velocity statistics were computed.

In a follow-on test that has not yet been fully analyzed, three-component stereo images were acquired for the same nozzles; however, due to problems with vibration of camera mounts it is doubtful that any but a handful of this data will be satisfactory.

5.1.4 Spatial regions measured

The test plan for the PIV portion of SFNT2K was to thoroughly measure as much of the jet plume as possible within the axial limitations of the traverse, assuming symmetry. For the baseline 3BB nozzle this required only one radial plane. Because $3A_{12}B$ and $3T_{24}B$ models had a 30° symmetry, this entailed acquiring seven planes of data. By virtue of the adaptor spool piece just upstream of the final core nozzle having 9 holes on its upstream flange and 8 on its downstream, a 5 degree angular increment in nozzle orientation was possible. Hence the angular increments were accomplished by rotation of the model while the PIV optical system was kept fixed in a vertical orientation. Data was acquired on the lower half of the jet with the field of view allowing data to be processed starting roughly 0.5 inch (0.012m) above the centerline. Each radial plane was acquired in a separate test run, often run on different test days. This decreased the quality of the match when the planes were assembled in post processing, especially since the rig is known to thermally grow in an inconsistent manner.

An additional complication comes from the fact that the light sheet must be slightly moved off the plane of symmetry so that the flare from the model does not burn the camera sensor. By moving the light sheet approximately 2mm away from the camera, the light reflected from the model is directed away from the camera; or put another way, the camera cannot see the place on the model where the light sheet makes impact. This slight modification should be kept in mind when comparing data close to the model. It should also be noted that the model has been known to move about by 1-2mm over a period of several minutes due to thermal loading, making precise location of the sheet relative to the model rather difficult.

Figure 5.1 graphically indicates the axial and angular grid used.

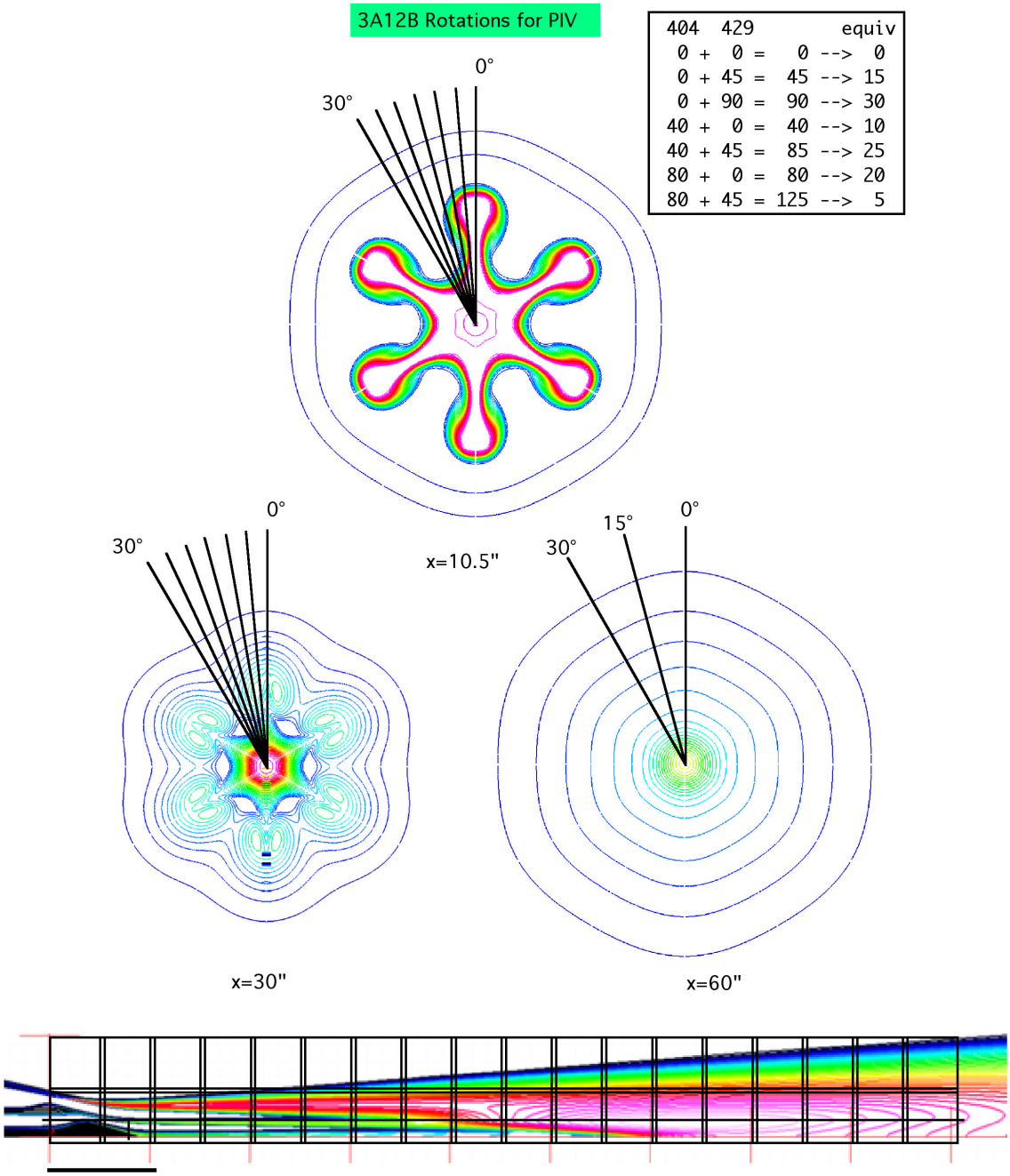

Figure 5.1. Orientations of measurement planes.

5.1.5 Spatial limitations

The axial traverse was limited to 96 inches (2.4m) of travel. Further, due to optical restrictions and image resolution issues, the widest field of view that could be accommodated was 5.5 inches (14cm) square. By dividing up the axial traverse into 5 inch (12.7cm) increments with 0.5 inch (1.3cm) overlap between frames, the total plane of data could be acquired in 19 segments. By using two cameras mounted one atop to the other a total field of view 5.5inches (14cm) wide by 10.5inches (26.7cm) tall could be acquired. The lower part of Figure 5.1 shows how the longitudinal measurement plane was segmented into the 2 by 19 overlapping fields.

5.1.6 Other limitations

Due to limitations in the amount of image data that could be stored on the PIV acquisition computer (roughly 60GB uncompressed), only two complete data planes could be acquired on a given day. This filled two of the three disk drives, leaving the third to store the compressed images that were sent over the local ethernet to other computers for processing. Due to these limitations, of the seven planes per nozzle desired, only three, the 0°, 15°, and 30° angles, were full length. The other four planes were only measured for half the axial length as it was determined that the angular variations were minimal downstream of that point. Thus it should have taken roughly two and one-half test days to acquire the data for one nozzle. Of course, rarely did a test day go perfectly (see Test Narrative).

5.2 Models tested

5.2.1 3BB—Axisymmetric baseline nozzle

Model 3BB was the baseline nozzle, being axisymmetric on both core and fan nozzles. This model represented a generic separate flow nozzle such as are flying on medium twin engine commercial transports today.

The plug angle is approximately 16°. The core cowl exit diameter is 5.156 inches (13.09cm) measured cold and the core cowl external boattail angle is approximately 14°. Also, at cold conditions, the core cowl exit plane is 4.267 inches (10.84cm) downstream of the fan nozzle exit plane.

An assembly drawing of this model and a photo are given in Figure 5.2.

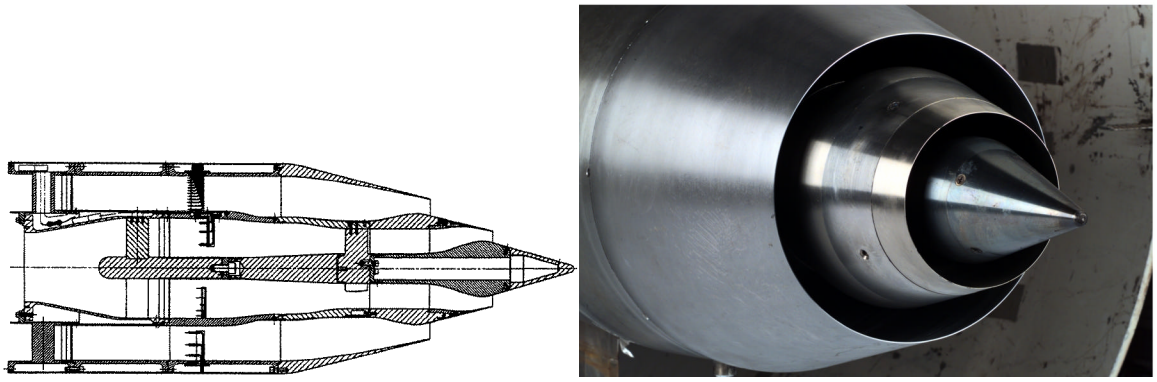

Figure 5.2. Nozzle 3BB. (a) Cross section of model nozzle system. (b) photo of assembled nozzle in NATR.

One important note on a significant imperfection in the model system is in order. It was determined after the test that the models had a significant droop, creating a slightly nonsymmetric flow field. Figure 5.3 and

Table 5.2 documents this asymmetry. This is important to keep in mind when comparing centerline data from these measurements with other data or simulations. Differences between the models is relatively unaffected by this droop.

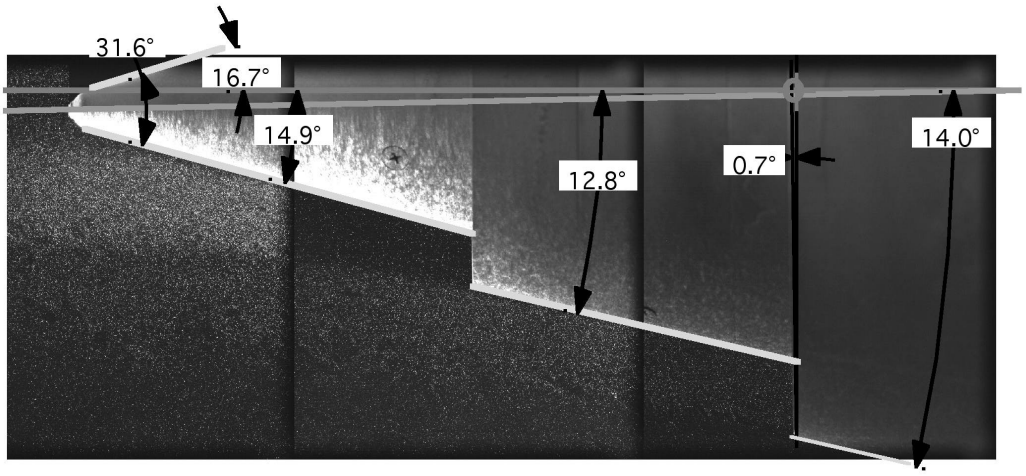

Figure 5.3. Measured deflections in model parts, measured after PIV runs.

Table 5.2. Measured angles of model and traverse.

Part	*top*	*bottom*	*average*	*design*	*droop*
Plug:	17.5°	14.9°	16.2°	16°	1.3°
Core:	15.0°	13.0°	14.0°	14°	1.0°
Fan:	14.7°	13.3°	14.0°	14°	0.7°
Freejet:	---	0.1°	---	0°	0°
Traverse:	---	-0.3°	-0.3°	0°	-0.3°

5.2.2 $3A_{12}B$—Alternating 12-count chevron core nozzle with axisymmetric fan nozzle

Model $3A_{12}B$ substituted an alternating chevron trailing edge on the core nozzle for the axisymmetric one of 3BB. Chevrons can be thought of as being cut into the otherwise axisymmetric nozzle to have the baseline throat at the half height of the chevrons. Basic chevrons follow flow lines of baseline nozzle past throat. The alternating chevron core nozzle can be thought of as starting from a flow–aligned chevron design with half of the chevrons being bent into the core stream approximately 4.5° with a small additional cusp to the chevron. The other half of the chevrons are bent into the fan stream by roughly 8°. Penetrations were intended to extend 2 boundary layer heights into the flow. More details about the original design philosophy and acoustic performance are given in reference 4, the report on the 1997 SFNT generated by GEAE, the designers of this nozzle. The result is a mean core flow with a six-sided star-shaped cross-section shortly downstream of the plug.

Although its thrust coefficient was reduced by roughly 0.5% by the addition of the chevrons (reference 1), this nozzle produced roughly 3dB suppression at the takeoff power condition. Because of the extreme change in both mean flow profile and far-field noise produced by the alternating chevron design, this model was chosen for detailed PIV measurements.

An assembly drawing of the model and a photo are given in Figure 5.4.

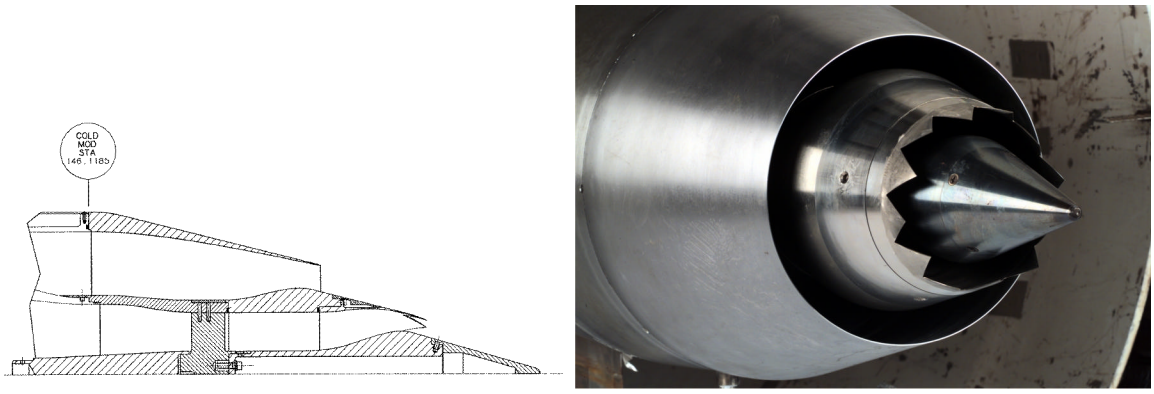

Figure 5.4. Nozzle $3A_{12}B$. (a) Cross section of model nozzle. (b) photo of assembled nozzle in NATR.

5.2.3 $3T_{24}B$—24 count alternating tabbed core nozzle with axisymmetric fan nozzle

Model $3T_{24}B$ substituted an alternating tab trailing edge on the core nozzle for the axisymmetric one of 3BB. Two aspects of the tab design distinguish it from the chevron design. First, the tabs protrude into the flow from the nominal flow alignment starting with a hard break, not a gradual bend. The tabs make an angle of approximately 45° with the flow, making a significant blockage of the flow. Second, in alternating the tab bending pattern, six of the tabs were bent inward, 6 were bend outward, and 12 were left aligned with the flow. This six-count pattern then again resulted in a mean core flow with a six-sided star-shaped cross-section shortly downstream of the plug.

Although its thrust coefficient was reduced by roughly 1.0% by the addition of the tabs, the $3T_{24}B$ nozzle produced roughly 3dB suppression at the takeoff power condition. However, it produced much greater mixing than the $3A_{12}B$ model, suppressing low frequency more, but producing more high frequency noise in balance. Because of the extreme change in both mean flow profile and far-field noise produced by the alternating tab design, this model was chosen for detailed PIV measurements.

An assembly drawing of the model and a photo are given in Figure 5.5.

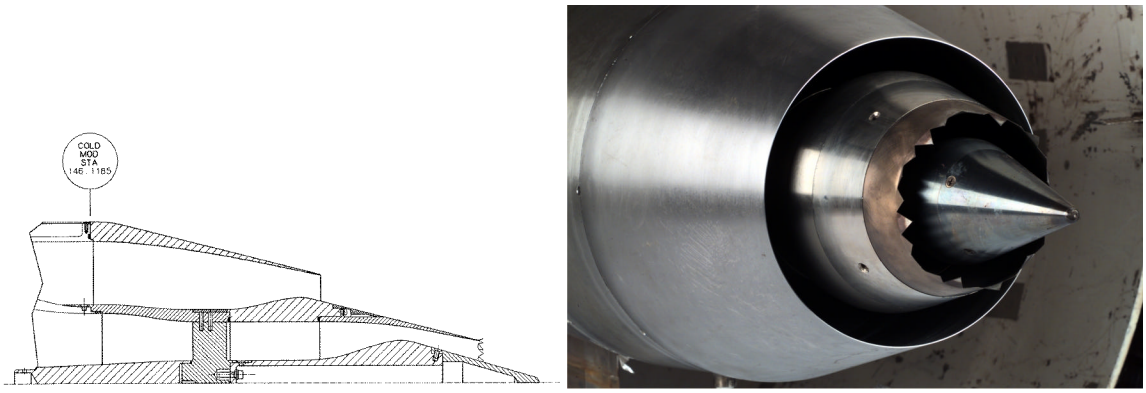

Figure 5.5. Nozzle $3T_{24}B$. (a) Cross section of model nozzle. (b) photo of assembled nozzle in NATR.

6 PIV Instrumentation

6.1.1 Big Blue traverse

For this test the PIV system was totally carried on the large AAPL traverse. This traverse, known as BigBlue (Figure 6.1), has had two tables added to its original frame, one on each side of the flow. The

traverse can actuate a set of vertical rakes across the flow while the entire frame rolls along a track in the axial direction. For this test, the PIV equipment was simply translated axially by the leadscrew attached to the floor. By using anti-backlash actuation the axial traverse maintains a position accuracy of ±0.04 inches (±0.001m) over a traverse distance of 96 inches (2.4m). The traverse was controlled by the Precision Actuation Control System (PACS) software created at Glenn for this purpose. Two additional tables were built onto BigBlue to carry the laser and the cameras together. Newport X95 rails and clamps were used, along with MicroBench optical mounts to position laser optics and cameras.

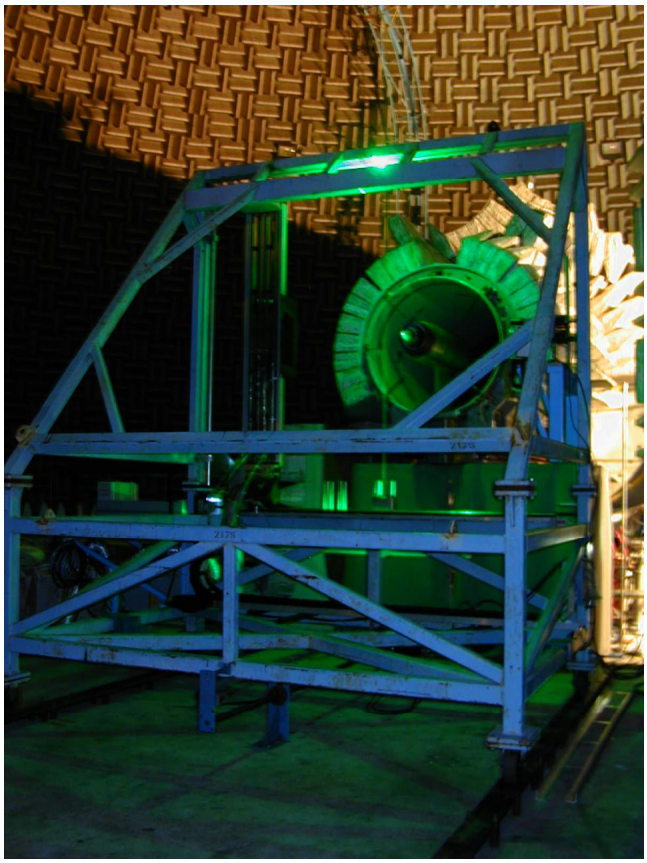

Figure 6.1. Big Blue. Traverse for moving PIV system to different measurement locations.

6.1.2 Optical layout

A series of mirrors and lenses directed the laser beam from the double-headed pulsed Nd:Yag laser into a vertical light sheet aligned with the flow axis. The laser was mounted transverse to the rig at the front of BigBlue, outboard of the main frame, at a level well below the freejet. This same table carried the power supplies, data acquisition computer, and syncronizer hardware. A small roof was built over this table to protect from rain coming in through the AAPL vent fan located directly overhead. Figure 6.2 shows how the optical components were laid out on the traverse.

From the laser head the beam was directed along the lower frame rail of BigBlue to the centerline of the rig where it was directed upward by a 45° mirror. A 2m focal length uncoated spherical lens was placed just before this mirror, 60 inches (1.52m) before the beam crossed the rig centerline. A -40mm focal length cylindrical lens was placed 4 inches (10cm) above the mirror, to create the light sheet. The light sheet was flared to a 13.5 inch (340mm) by 0.025 inch (0.6mm) cross-section at its waist, located nominally at the jet centerline. By the time the light sheet impacted the dome ceiling its cross-section was approximately 8 feet (2.4m) wide, making the energy load on the fiberglass wedges and vent fan structure entirely safe.

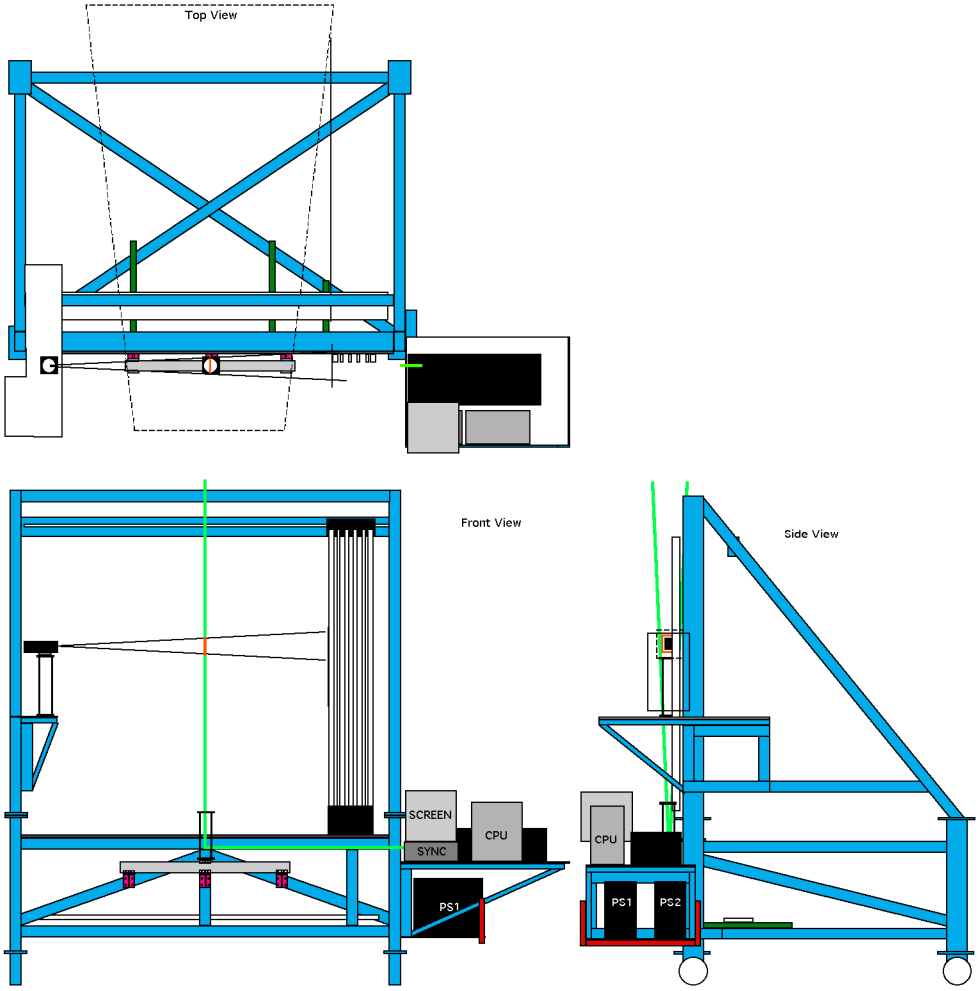

Figure 6.2. Optical layout on BigBlue.

6.2 Laser, cameras, frame grabber

6.2.1 Laser specs

A dual head Nd:YAG laser operating at 532 nm was used to generate the 400 mJ/pulse light sheet. The laser pulses were synchronized with the cameras and frame-grabbers using TSI's Insight (Version 3.2) software and Synchronizer. The Synchronizer controlled the timing of the pulsed light source relative to the CCD camera frame transfer period. Image frame pairs are obtained by straddling adjacent frame boundaries. A PCI frame digitizer was used to acquire image data directly to disk in 400 image sequences.

6.2.2 Camera specs

Two cameras were used together in this setup, being treated by the controlling software as if they were being used for stereo PIV even though they had independent fields of view. The cameras were mounted one atop the other 52 inches (1.32m) away from the light sheet. Each camera was a 1000x1000 pixel Kodak ES 10 camera equipped with an f/5.6, 85 mm Nikkor lens and an 8mm extension ring. This combination produced a 5.5 inch (0.127m) square field of view. The two cameras were positioned to overlap their fields of view by 0.5 inches, yielding a composite field of view 10.5 inches high by 5 inches wide (0.267m x 0.127m).

6.3 Acquisition parameters

PIV image frame pairs, required to produce an instantaneous velocity map, were acquired primarily at a time separation of 2.2 microseconds. This was done to accommodate the expected out of plane motion, instantaneously as high as 150m/s, with a light sheet 0.6mm thick. Previous experience with PIV in jets showed that out of plane motion was a limiting factor in obtaining accurate results. To test this understanding, limited data points were acquired with 4 and 6 microsecond pulse delays (presented in section 5.3). 400 image pairs were recorded by each camera at each location.

7 PIV Analysis

7.1 Image Processing

Measuring a single plane of data 95 inches (2.4m) by 10.5 inches (0.27m) required 30,400 images, each 8bit monochrome image of 1024 by 1024 pixels taking 1MB. Storing, transporting, and processing of this volume of data is an enormous task with current computer resources.

7.1.1 PIVPROC

The collected PIV image data were processed using an in-house developed code. An in-house image processing package, PIVPROC, uses fuzzy logic data validation to ensure that high quality velocity vector maps are obtained [**7**]. The correlation based processing allows subregion image shifting, asymmetric subregion sizes and multi-pass correlation processing.

7.1.2 Grid determination, scaling

A grid was constructed, registered on the nozzle lip from the first frame image, so that velocities computed from each image would create a uniform map. Five velocity grid cells overlapped in the radial direction and three in the axial direction. A multipass scheme was employed, using first a 64 by 64 pixel region to determine mean shift of images, followed by a 32 by 32 pixel pass with 50% overlap between grid cells. The 32 by 32 pixel grid corresponded to a 0.088 inch (2.24mm) grid size in physical space.

7.1.3 Acceptance criteria for vectors

The procedure for computing statistics from a series of processed PIV image velocity vector maps utilizes several acceptance criteria to qualify vectors and identify and remove incorrect vectors: signal to noise ratios for the image correlation, hard velocity cutoff limits and an automated procedure for identifying outliers. In the data processing done here, the peak signal to noise criteria for the correlation/peak detection was set to 1.5. The high and low velocity cutoff limits were set to -150m/s and 600 m/s for the axial component, and ±150m/s for the radial. Next, the mean and standard deviation are computed at each grid point in the velocity vector map. The automated procedure for removing outliers is based on Chauvenet's criterion (Taylor 1982), in which the probability of occurrence of a given point deviating from the mean is computed. The main assumption here is that the parent velocity distribution is Gaussian. The number of standard deviations that a given point lies from the mean is first computed. Then the probability that a given point could deviate from the mean by this many standard deviations is computed from the normal error integral and multiplied by the number of points in the distribution. If the computed probability is less than a preset level (in this case 3%) then the point is removed.

In all data presented from this test, a relative data 'quality' metric is the number of accepted velocity vectors at a point. If no vectors are rejected, this number would be 400, the same as the number of image pairs acquired. Typically, this value is between 380 and 400.

7.2 Definition of turbulence statistics

7.2.1 One-point statistics

Following standard turbulence practice [**8**], subdivide the instantaneous velocity vector $\vec{u}$ into time mean and instantaneous parts:

$$\vec{u}(\vec{x},t) = \bar{U}(\vec{x}) + \tilde{\vec{u}}(\vec{x},t)$$

where

$$\bar{U}(\vec{x}) = \frac{1}{T}\int_0^T \tilde{\vec{u}}(\vec{x})dt = \left\langle \vec{u}(\vec{x}) \right\rangle$$

is the time average velocity, denoted by the $\langle\ \rangle$ brackets. Then the mean square of the fluctuating part, e.g. the variance of velocity, can be defined

$$\left\langle \vec{u}^{\,2}(\vec{x}) \right\rangle = \frac{1}{T}\int_0^T (\bar{U}(\vec{x}) - \tilde{\vec{u}}(\vec{x}))^2\, dt\ .$$

Taking the square root of the variance gives the root mean square (rms) of the fluctuating part of the velocity.

Because of the way data was acquired in radial planes, we should choose a cylindrical polar coordinate system with axial, radial, and polar coordinates in that order:

$\vec{x}$ = (x,y,θ); $\vec{u}$ = (u,v,w).

In this system, measurements were taken in the axial (x) and radial (y) planes and only the axial and radial components of velocity (u, v) were measured. However, because of the way data three-dimensional visualization packages work, many of the graphs show a Cartesian coordinate system. Just remember that data is actually taken in polar coordinates and that the y-coordinate and v-component of velocity refer to a radial plane.

Likewise, for notational convenience in the graphs, the following notation was adopted:

mean values $\left\langle \vec{u}(\vec{x}) \right\rangle$ are denoted by <U>, <V>,

variances $\left\langle \vec{u}^{\,2}(\vec{x}) \right\rangle$ are denoted by <u^2>, <v^2>.

7.2.2 Two-point statistics

Our interest in two-point statistics is driven by aeroacoustic theory. Specifically, aeroacoustic theory requires knowledge of spatial correlations of the velocity field:

$$\mathbf{R}(\vec{\xi},\vec{x}) = \left\langle \vec{u}(\vec{x} + \vec{\xi}/2)\vec{u}'(\vec{x} - \vec{\xi}/2) \right\rangle$$

where $\vec{\xi}$ is a small displacement about the spatial point $\vec{x}$. This quantity has five terms (assuming symmetry) in three spatial dimensions for every point in physical space. Since we only have two components of velocity in a plane, we only can compute three of the five components in two dimensions in a plane. Notationally, we compute

<uu'>(ξ_1, ξ_2; x,y),

<uv'>(ξ_1, ξ_2; x,y),

<vv'>(ξ_1, ξ_2; x,y),

for displacements $\vec{\xi}$ =(ξ_1, ξ_2, ξ_3), where ξ_3 is dropped, data being only in the radial plane.

The correlation is normalized in our data by the root mean squares at the reference point,

$$\tilde{\mathbf{R}}(\vec{\xi},\vec{x}) = \frac{\left\langle \vec{u}(\vec{x}+\vec{\xi}/2)\vec{u}'(\vec{x}-\vec{\xi}/2)\right\rangle}{\sqrt{\left\langle \vec{u}^{\,2}(\vec{x})\right\rangle}\sqrt{\left\langle \vec{u}'^{2}(\vec{x})\right\rangle}}$$

which is different from the oft-used normalization

$$\frac{\left\langle \vec{u}(\vec{x}+\vec{\xi}/2)\vec{u}'(\vec{x}-\vec{\xi}/2)\right\rangle}{\left\langle \vec{u}(\vec{x})\right\rangle\left\langle \vec{u}'(\vec{x})\right\rangle}.$$

The latter expression is not useful in flows where U_2 is near zero, as it is on the jet centerline.

In contour plots of the two-point correlation, the correlation of the field with a given reference point is shown by

$$\tilde{\mathbf{R}}'(\vec{\xi},\vec{x})\frac{\left\langle \vec{u}(\vec{x})\vec{u}'(\vec{x}+\vec{\xi})\right\rangle}{\sqrt{\left\langle \vec{u}^{\,2}(\vec{x})\right\rangle}\sqrt{\left\langle \vec{u}'^{2}(\vec{x}+\vec{\xi})\right\rangle}}.$$

In these cases, symmetry may not be assumed and both permutations <uv'> and <vu'> are shown.

Models for two-point correlations have traditionally been developed by assuming a functional form separable in space and time. From the equations of motion certain constraints apply (Batchelor)

$$\frac{\left\langle u_i u_j'\right\rangle}{\left\langle u_1^{\,2}\right\rangle} = R_{ij}(\vec{\xi})g(\tau)$$

$$R_{ij}(\vec{\xi}) = \left[\left(f + \frac{|\xi| f'}{2}\right)\delta_{ij} - \frac{f'\xi_i\xi_j}{2|\xi|}\right], f' = \frac{\partial f}{\partial|\xi|}$$

A popular analytic model for the two-point spatial correlation is the Gaussian form

$$f(|\xi|) = e^{\left(\frac{-\pi|\xi|^2}{L^2}\right)}$$

yielding the forms

$$R_{11}(\vec{\xi}) = \left(1 - \frac{\pi\xi_2^{\,2} + \pi\xi_3^{\,2}}{L^2}\right)e^{\left(\frac{-\pi|\xi|^2}{L^2}\right)}$$

$$R_{22}(\vec{\xi}) = \left(1 - \frac{\pi\xi_1^{\,2} + \pi\xi_3^{\,2}}{L^2}\right)e^{\left(\frac{-\pi|\xi|^2}{L^2}\right)}$$

When compared against current data, the Gaussian form seems a poor fit—the correlation does not seem to have a zero derivative at $\xi = 0$, instead dropping much faster. Theoretically, the correlation must have a zero derivative at $\xi = 0$ [**9**], in fact the second derivative (curvature of the correlation at the origin) here is the Taylor microscale, associated with the finest scales of motion. Contrast this with the largest lengthscales of motion, defined by the integral of the correlation curve, and we see why, for this large Reynolds number, the Taylor microscale is so much smaller than the integral lengthscale—the curvature at the origin cannot be seen in the experimental data. Modifying the model above by changing the power of the exponent, setting

$$f(\xi) = e^{\sqrt{\left(\frac{-\pi\xi^2}{L^2}\right)}}$$

produces a more satisfying fit to the data, as was found by Frenkel[**10**] and Laurence [**11**].

Another part of the popular model that does not agree with data is the assumption of isotropy. Indeed, it has been found that the the two cross-stream turbulence intensities are nearly equal, but are less than the axial turbulence intensity. For this reason an axisymmetric turbulence model is examined. Referencing Khavaran [**12**], the axisymmetric model with Gaussian decay is given by

$$\langle u_1 u'_1 \rangle(\vec{\xi}) = -2Q_1\left(1 - \mathrm{X}_2 - \mathrm{X}_3\right)$$

$$\langle u_2 u'_2 \rangle(\vec{\xi}) = \left(-1 + 2\mathrm{X}_3{}^2\right)Q_2$$

$$+ 2\left(-1 - \left(-2 + \Delta^2\right)\mathrm{X}_3{}^2 + \left(-1 + 2\Delta^2\right)\mathrm{X}_1{}^2 + 2\left(-1 + \Delta^2\right)^2 \mathrm{X}_1{}^2\mathrm{X}_3{}^2\right)Q_1$$

$$Q_1 = -\frac{\langle u_1{}^2 \rangle}{2} e^{-\pi\left(\frac{\xi_1{}^2}{L_1{}^2} + \frac{\xi_2{}^2 + \xi_3{}^2}{L_2{}^2}\right)}; \quad Q_2 = \left(\langle u_2{}^2 \rangle - \langle u_1{}^2 \rangle\right) e^{-\pi\left(\frac{\xi_1{}^2}{L_1{}^2} + \frac{\xi_2{}^2 + \xi_3{}^2}{L_2{}^2}\right)}$$

$$\mathrm{X}_i = \frac{\sqrt{\pi}}{L_2}\xi_i; \qquad \Delta = \frac{L_2}{L_1}$$

An axisymmetric model with single-power exponential decay is given by

$$\langle u_1 u'_1 \rangle(\vec{\xi}) = -2Q_1\left(1 - \mathrm{X}_2 - \mathrm{X}_3\right)$$

$$\langle u_2 u'_2 \rangle(\vec{\xi}) = \left(2 + \pi^2\mathrm{X}_3{}^2\right)\frac{Q_2}{2}$$

$$+ \left(8\gamma + \pi^2\left(\mathrm{X}_1{}^2\left(2\gamma - 4\gamma\Delta^2 + \pi\left(\pi\gamma\left(-1 + \Delta^2\right)^2 + (-1 + \Delta^2)L_2\right)\right)\mathrm{X}_3{}^2\right)\right.$$

$$\left. + \mathrm{X}_3{}^2\left(-4\gamma + \pi\Delta^2 L_2\left(\mathrm{X}_2{}^2 + \mathrm{X}_3{}^2\right)\right)\right)\right)\frac{Q_1}{4\gamma}$$

$$Q_1 = -\frac{\langle u_1{}^2 \rangle}{2} e^{-\pi\sqrt{\left(\frac{\xi_1{}^2}{L_1{}^2} + \frac{\xi_2{}^2 + \xi_3{}^2}{L_2{}^2}\right)}}; \quad Q_2 = \left(\langle u_2{}^2 \rangle - \langle u_1{}^2 \rangle\right) e^{-\pi\sqrt{\left(\frac{\xi_1{}^2}{L_1{}^2} + \frac{\xi_2{}^2 + \xi_3{}^2}{L_2{}^2}\right)}}$$

$$\mathrm{X}_i = \frac{\sqrt{\pi}}{L_2\gamma}\xi_i; \qquad \Delta = \frac{L_2}{L_1}; \qquad \gamma^2 = \Delta^2\xi_1{}^2 + \xi_2{}^2 + \xi_3{}^2$$

7.2.3 Integral Lengthscales

In modeling the two-point spatial velocity correlation, it is often assumed that there is some displacement over which the velocities become uncorrelated. One definition of this is the integral lengthscale **L**

$$\mathbf{L}(\vec{x}) = \int_0^\infty \mathbf{R}(\vec{\xi}, \vec{x})d\xi,$$

which happens to nicely match the scaling exponent L of the Gaussian form. One can still apply the same definition for **L** to cases where the flow is not isotropic. However, computing this integral with discrete data over a finite range, such as is obtained in experiments, does introduce a significant uncertainty in the measure of **L**. Fitting a reasonable functional form to the data and integrating it yields a cleaner statistic. After looking at all the correlation data, the Gaussian model does not seem to be the best fit to the data; instead, the data was fitted to the single-power exponent expressions that do fit the data much better. Figure 7.1 illustrates the relative fits between single exponential and Gaussian expressions. Also given in the figure, but only showing up in the Rvvx component, are curve fits for both isotropic and axisymmetric models of the single and double exponential forms.

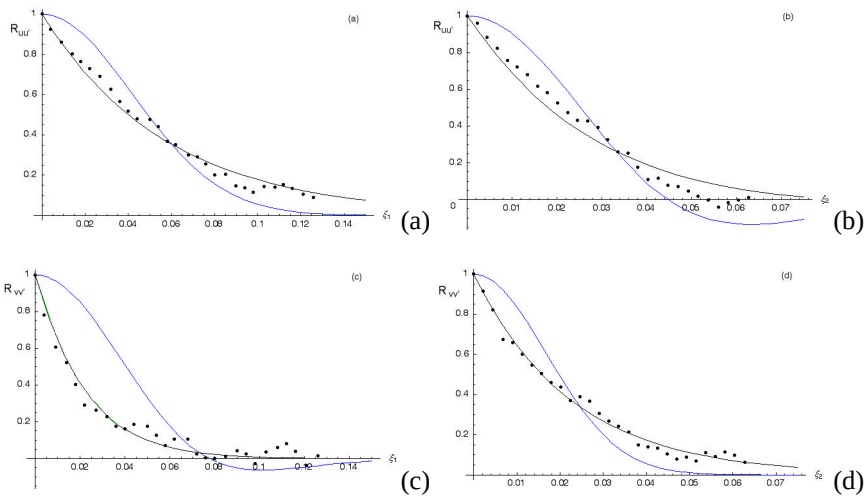

Figure 7.1 Two-point spatial correlations with single and double exponential forms fitted to the data.

Operationally, four fits to the axisymmetric single-power exponential form were performed at every evaluation point with the u(x,y), v(x,y) data, and four lengthscales determined:

- two estimates for L_1, Iuux from <uu'>(ξ_1) and Ivvx from <vv'>(ξ_1).

- two estimates for L_2, Iuuy from <uu'>(ξ_2) and Ivvy from <vv'>(ξ_2).

7.3 Analysis of error

7.3.1 First principle estimate of PIV accuracy

The accuracy of the velocity estimates is inversely proportional to the particle displacement between exposures. The maximum displacement is restricted to 1/4 of the correlation subregion size, hence using a correlation subregion size of 32x32 pixels yields a maximum measurable displacement of 8 pixels. The correlation peak location in the PIV algorithm can nominally be estimated to within 0.1 pixels, yielding measurement errors on the order of 1% of full scale for 32x32 pixel subregion processing. This translates to an instantaneous, single frame uncertainty of 12m/s. Errors in first order statistics, such as mean velocity, computed from N samples, scale as N^{-1}, yielding an uncertainty of 0.04m/s in the mean velocity from PIV processing itself. Second order statistics scale as $N^{-1/2}$ giving an uncertainty in turbulence intensity of 0.6m/s. Again, note that this is the uncertainty due to the PIV processing itself; there are many other factors, such as variation in seed densities, non-stationarity in the operation of the facility, etc. that will increase this uncertainty.

7.3.2 Particle lag

One measure of the error introduced by the particle velocity not equaling the fluid velocity is the particle's frequency response which quantifies how fast the particle moves in response to a change in the fluid velocity. The frequency response and particle lag distance behind an oblique shock for various seed materials has been reported by Melling [**13**]. Simple application of Melling's results show that the frequency response of a particle of diameter d_p and density ρ_p in a fluid with viscosity μ_f would be

$$\frac{18\mu_f}{10\rho_p d_p^2}$$

Using these results, the seed particles used here would have a frequency response of 35kHz. This can be interpreted as a low-pass filter on the velocity data and was most noticeable as a loss of particles in the cores of vortices just downstream of the chevrons in some planes.

7.3.3 Loss of data

Another major factor leading to loss of accuracy in PIV turbulence measurements is the loss of some velocity vectors due to image errors, manifest in signal to noise ratio. This can result from error in camera focus, from having too few or too many particles in a correlation region, from particles moving into or out of the light sheet between light pulses, from particle images too fine to be resolved in the digitized image, from stray light from model glare, and from large velocity gradients across the interrogation region. This error is generally caught in the acceptance stage of processing and results in lower data quality statistic, the number of accepted vectors out of all images acquired. However, in regions where the data quality is relatively low, there is reason to suspect that the acceptance schemes did not remove all spurious data. For instance, one of the acceptance schemes, Chauvenet's criteria, uses the variance of the data itself as a measure of how much variance to allow in the distribution of values. Bottom line: if turbulence statistics seem out of line in regions where the data quality is poor it probably should not be trusted. Not many regions of the current test dataset have this problem. The main problem area is in the vectors right next to the model where reflection was a problem, and near the edges of the images where diffraction of the image mask in the camera may have removed some particle images from the interrogated region, leaving too few particles. In this test there was no correlation of poor data quality with regions of high out of plane velocity. This indicates that the two components of velocity vectors measured are not biased by removal of data with high out of plane component.

7.3.4 Direct test of Δt error

One direct test of the out of plane error and of the accuracy limits imposed by the choice of maximum displacement is to increase this maximum displacement by increasing the time delay between laser pulses and observing how the flow statistics change. To this end, data was acquired in the 3BB nozzle at the exit plane of the core nozzle at three different time delays—2.2μs (standard), 4μs, and 6μs. Figure 7.2 shows the location of the line where the data being examined was acquired. The changes in the data quality, the mean velocity profiles, and the variance in axial and radial velocities are plotted in Figure 7.3 for the three different time delays.

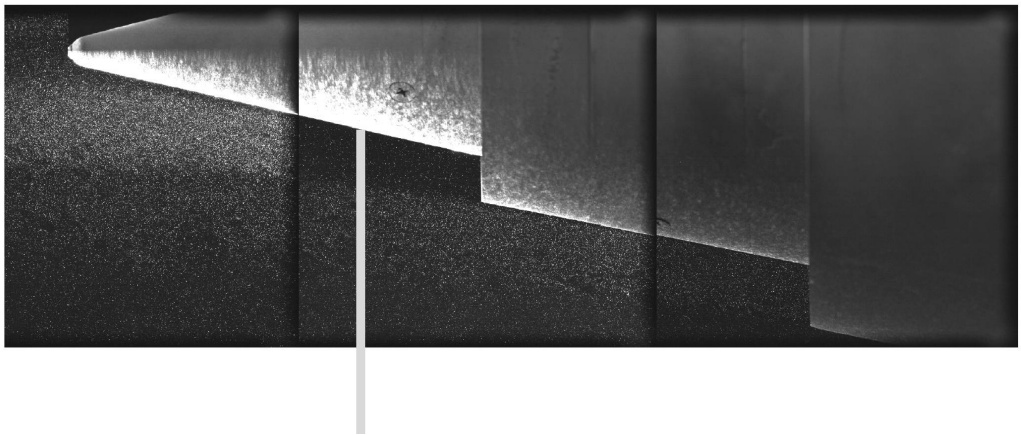

Figure 7.2. Location of radial line for Δt example.

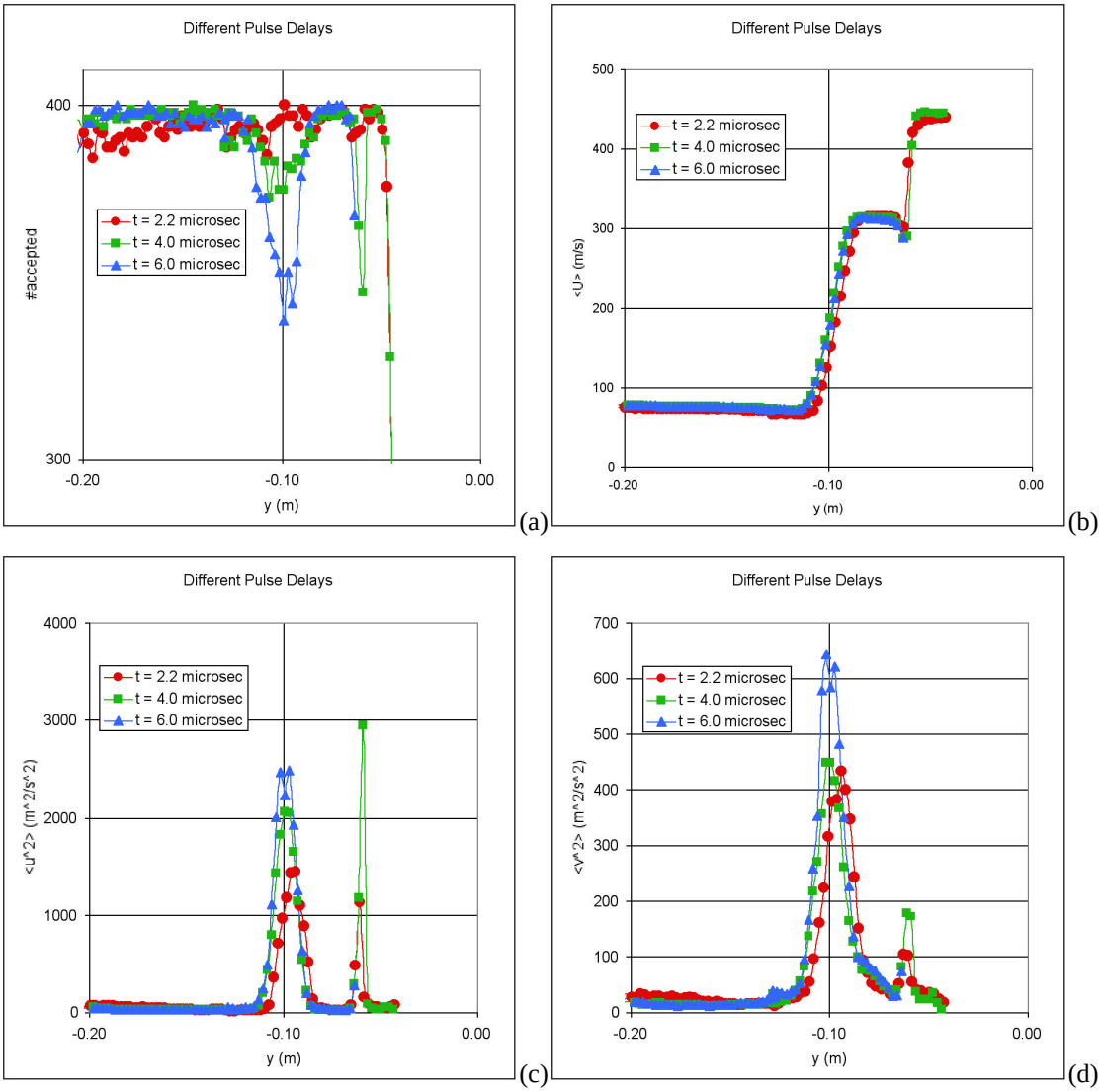

Figure 7.3. Measurements taken with three different Δt between laser pulses. (a) Data quality, (b) mean axial velocity, (c) variance of axial velocity, (d) variance of radial velocity.

In Figure 7.3a, the data quality in the core/fan shear layer ($y \approx -0.1$m) drops with increased time delay, probably due to an increased occurrence of out of plane motion. However, the data quality is near perfect in other regions, except for $y > -0.05$m, where the mean displacement is simply too great at $\Delta t = 6\mu s$ for the interrogation region. Differences in mean axial velocity in Figure 7.3b are less than 1% in the fan flow and less than 0.1% between the 2.2μs and 4μs data. The differences between the curves in the shear layers is probably due to known problems with the model moving slightly during operation, shifting the location of the shear layer over times of the order of minutes.

Differences in the variances of the velocity (Figure 7.3c,d), especially in the core/fan shear layer at ($y \approx -0.1$m) lead to a question of which is the worse source of error: increased uncertainty in each velocity measurement with small Δt, or increased possibility of false acceptance of bad data with larger Δt and out of plane motions. Combined with the data quality plot in Figure 7.3a, it would seem that the latter is clearly a problem for the $\Delta t=6\mu s$ data, while its effect on the 4μs data is unclear. The difference in uncertainty between the 2.2μs and 4μs data are large, but given the data quality plots, the 2.2μs data seems most reliable. Thankfully, most of the measurement region has data quality well in excess of that found in this portion of the core/fan shear layer.

8 Presentation of Data

This chapter is mostly an orientation to the graphical presentation of the data, and it also describes the file format of the numerical datafiles to aid users who are wanting to extract the data for their own purposes. Appendix A contains the graphical presentation of the data.

8.1 Organization of figures

The figures are organized first by nozzle geometry (baseline, $3A_{12}B$, $3T_{24}B$). Then the data is shown in two separate groups of figures, the first presenting the data from oblique view to aid in orientation and perception, the second presented as planar cuts for more quantitative comparisons. Inside the oblique view section all the statistical properties are shown, first the one-point statistics and then the two-point statistics. Inside the planar cut section, all the statistics are presented together for each cut. The integral lengthscale statistics are only shown in these planar cuts.

8.2 Data format of digital data

The raw velocity maps, comprising 400 vector fields per location, are stored as tab-delimited files and are not available due to logistical constraints. The statistics computed from these maps, presented graphically in Appendix A, are available as plot3D files [**14**]. They are in formatted, 3D, scalar files along with the corresponding grid file. There are typically 1080 axial by 115 radial grid points for the 0°, 15°, and 30° planes. There are 513 axial by 115 radial grid points for the 5°, 10°, 20°, and 25° planes. The following files are available for the 3BB, $3A_{12}B$, $3T_{24}B$ nozzles:

One-point statistics, filenames			
Model	**3BB**	**$3A_{12}B$**	**$3T_{24}B$**
Grid	3bbx.x	3abP.x	3tbP.x
<u>(x,y,q)	3bbx.U	3abP.U	3tbP.U
<v>(x,y,q)	3bbx.V	3abP.V	3tbP.V
<u><v>(x,y,q)	3bbx.UV	3abP.UV	3tbP.UV
<u^2>(x,y,q)	3bbx.u	3abP.u	3tbP.u
<v^2>(x,y,q)	3bbx.v	3abP.v	3tbP.v
<uv>(x,y,q)	3bbx.uv	3abP.uv	3tbP.uv
number good points out of 400	3bbx.N	3abP.N	3tbP.N
Note: 'P' is replaced by letter to designate plane:	'a' -- 30° 'b' -- 25° 'c' -- 20°	'd' -- 15° 'e' -- 10° 'f' -- 5°	'g' -- 0°

Two-point statistics, filenames			
Model	**3BB**	**$3A_{12}B$**	**$3T_{24}B$**
Grid	3bbx.x	3abP.x	3tbP.x
<uu'>(x,y,q)	3bbx.uu	3abPrR.uu	3tbPrR.uu
<uv'>(x,y,q)	3bbx.uv	3abPrR.uv	3tbPrR.uv
<vu'>(x,y,q)	3bbx.vu	3abPrR.vu	3tbPrR.vu

<vv'>(x,y,q)	3bbx.vv	3abPrR.vv	3tbPrR.vv
Note: 'P' is replaced by letter to designate plane:	'a' -- 30° 'b' -- 25° 'c' -- 20°	'd' -- 15° 'e' -- 10° 'f' -- 5°	'g' -- 0°
Note: 'R' is replaced by letter to designate reference point:	'0' -- y = 0.00" '1' -- y = 0.03" '2' -- y = 0.06	'3' -- y = 0.09 '4' -- y = 0.12 '5' -- y = 0.15	'6' -- y = 0.18 '7' -- y = 0.21 '8' -- y = 0.24

Lengthscale statistics, filenames			
Model	**3BB**	**$3A_{12}B$**	**$3T_{24}B$**
Grid	3bbxls.x	3abPls.x	3tbPls.x
$L_1(x,y,q)$	3bbxls.luux	3abPls.luux	3tbPls.luux
$L_2(x,y,q)$	3bbxls.luuy	3abPls.luuy	3tbPls.luuy
$L_1(x,y,q)$	3bbxls.lvvx	3abPls.lvvx	3tbPls.lvvx
$L_2(x,y,q)$	3bbxls.lvvy	3abPls.lvvy	3tbPls.lvvy
Note: 'P' is replaced by letter to designate plane:	'a' -- 30° 'b' -- 25° 'c' -- 20°	'd' -- 15° 'e' -- 10° 'f' -- 5°	'g' -- 0°

9 Summary of Results

This is a minimal "what do we see in the data" chapter. More analysis of the results will be done in follow-on papers; this paper is supposed to be a documentation of the experiments and of the data.

9.1 Comparisons with Plume Survey Measurements

There are few if any previous measurements of the velocity field of a separate flow nozzle operating with hot core in a simulated flight environment—that was the point in taking these measurements! However, we can compare the mean velocity fields measured with the PIV system with those found using standard pressure and temperature rake technology. Total pressure and total temperature measurements were made of these nozzles in the 1997 test, and are brought out to compare with current PIV data. It is known that the 1997 plume rake data is somewhat flawed because it assumes that static pressure is constant. This was shown to give velocities that were low by up to 10% near the nozzle, and even being 5% low by 0.3m downstream. Although the plot at this scale does not show it, detailed examination of the two data sets bears out this difference with the two agreeing to within 10%. The majority of the discrepancy is due to the nozzle droop in the PIV data, a feature introduced into the model during reassembly of the model in 2000.

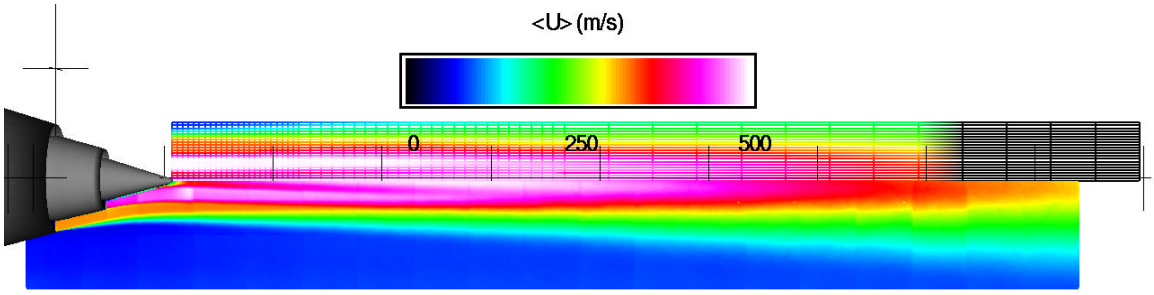

Figure 9.1. Comparison of mean axial velocity as calculated from Pt, Tt (1997; top), and as measured using PIV (2000; bottom).

9.2 Comparisons with Computational Results

As part of the Advanced Subsonic Technology program in 1997, a contract was let by NASA to compute Reynolds averaged Navier-Stokes (RANS) solutions for the flows from selected SFNT nozzles. Under this contract, Combustion Research and Flow Technology, Inc. (CRAFT, Inc), computed the flow field of the three nozzles studied in this report. Details of this computation are found in [**15**].

In the following three figures the predicted flow fields for the 3BB nozzle are shown in the upper half of the plume while the data are shown in the lower half. It must be noted that the experimental data overlays the centerline by 0.01m and slightly biases the eye on the centerline. Figure 9.2 gives the comparison for the mean velocity fields, where the main difference seen is that the actual nozzle had a droop and the wake of the centerbody drops downward. Decay of the high speed core flow is properly predicted and the spread is also well matched. Figure 9.3, the comparison of radial mean velocity, is included for completeness, although it could be argued that the flow at the nozzle is very easy to predict and that the differences downstream are not visible at this contour scale. In actuality, the experimental error in finding zero radial velocity is as great as the differences between the two radial velocity fields.

Figure 9.4 compares turbulence kinetic energy as predicted by the CRAFT RANS code and as measured by the PIV system. There are two aspects of this figure which require discussion. First, turbulence kinetic energy, strictly speaking, is defined as

$$k = \frac{1}{2}\left(\left\langle u_1{}^2\right\rangle + \left\langle u_2{}^2\right\rangle + \left\langle u_3{}^2\right\rangle\right).$$

Because the CRAFT RANS code, like most other compressible RANS codes, are formulated in Favre-averaged variables, e.g., with density-weighted primitive variables $\rho\bar{u}$, the turbulent kinetic energy from the prediction is actually

$$k = \frac{1}{2\langle\rho\rangle}\left(\left\langle \rho u_1{}^2\right\rangle + \left\langle \rho u_2{}^2\right\rangle + \left\langle \rho u_3{}^2\right\rangle\right).$$

The slight difference, that the prediction values include the correlation of density fluctuations, will create a slight difference in the value of k, especially given the temperature variations that exist instantaneously.

Another approximation made in constructing the figure, this time from the experimental data side, is the assumption of axisymmetry in the turbulence. It has been noted in earlier LDV measurements that the <v^2> and <w^2> terms are nearly identical in an axisymmetric jet [**16**]. This assumption is used here to provide the missing <w^2> term in κ for the experimental data shown in the lower half of Figure 9.4.

With those two caveats in mind, the prediction of κ can be said to have its region of peak intensity within 10% of the right magnitude, but this region is too far downstream and is too small. The data shows a region of $\kappa > 2500 m^2/s^2$ spanning from 1 to 2.25 m downstream, while the comparable region in the prediction spans only from 1.75 to 2.5m. So while the CRAFT solution is a good prediction of mean velocities and jet spread, it seems to underpredict the region of maximum turbulent kinetic energy, the caveats regarding the quantities being compared notwithstanding.

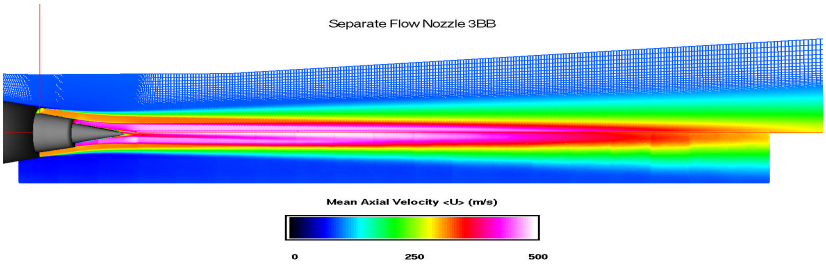

Figure 9.2. Comparison of axial mean velocity, CFD Reynolds averaged Navier Stokes solution of [15] on top, PIV data on bottom.

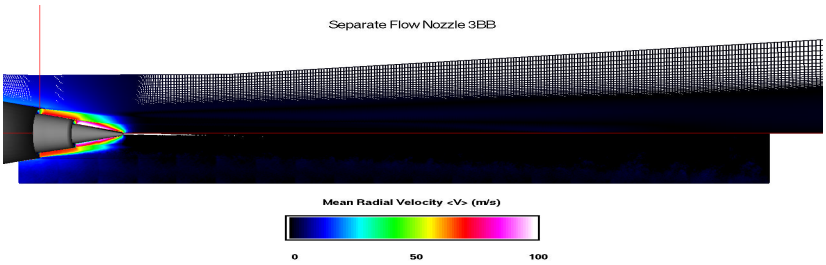

Figure 9.3. Comparison of radial mean velocity, CFD Reynolds averaged Navier Stokes solution of [15] on top, PIV data on bottom.

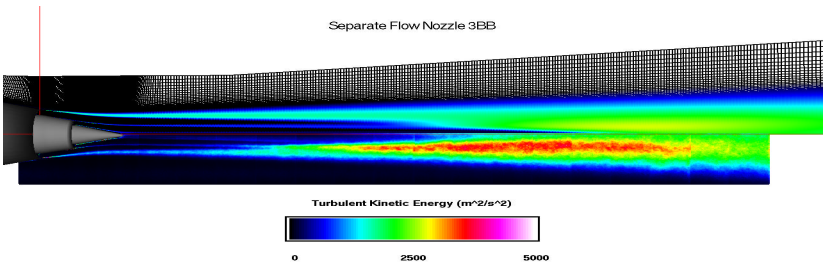

Figure 9.4. Comparison of turbulent kinetic energy, CFD Reynolds averaged Navier Stokes solution of [15] on top, PIV data on bottom. See note in text regarding definitions.

10 Summary

Detailed turbulence statistics were measured in three external plug, bypass ratio 5, separate flow nozzles operating at a typical take-off condition with simulated flight of 0.3 Mach. The nozzles in the study were ones whose acoustic fields had been extensively studied previously and had shown significant noise reduction. The three nozzles were an axisymmetric baseline, an alternating 12 chevron design on the core nozzle, and an alternating 24 tab design on the core nozzle. Instantaneous velocity maps were acquired using PIV and statistics, including mean, variance, two-point correlation, and integral lengthscale, were computed from these velocity maps. The turbulence statistics will be used to better understand what aspects of the unsteady flow field give rise to noise and what measures are useful in reducing this noise.

The main point should be taken from this work: particle image velocimetry works well in acquiring turbulence data in hot, high speed jets.

11 References

1 Saiyed, N., Mikkelsen, K.L., and Bridges, J., 2000, "Acoustics and Thrust of Separate-Flow Exhaust Nozzles With Mixing Devices for High-Bypass-Ratio Engines," *NASA TM 2000-209948*.

2 Saiyed, N., ed., 2000, "Separate Flow Nozzle Test Status Meeting," *NASA CP 2000-210524*.

3 Low, J.K.C., Schweiger, J.C., Premo, J.W., and Barber, T.J., 2000, "Advanced Subsonic Technology (AST) Separate-Flow High-Bypass Ratio Nozzle Noise Reduction Program Test Report," *NASA CR 2000-210040*.

4 Janardan, B.A., Hoff, G.E., Barter, J.W., Martens, S., Gliebe, P.R., Mengle, V., and Dalton, W.N., 2000, "AST Critical Propulsion and Noise Reduction Technologies for Future Commercial Subsonic Engines Separate-Flow Exhaust System Noise Reduction Concept Evaluation," *NASA CR 2000-210039*.

5 Long, M.J., 1992, "Experimental Investigation of an Ejector-Powered Free-Jet Facility," *NASA TM-105868*.

6 Castner, R.S., 1994, "The Nozzle Acoustic Test Rig: An Acoustic and Aerodynamic Free-Jet Facility," *NASA TM 106495*.

7 Wernet, M.P., 1999, "Fuzzy Logic Enhanced Digital PIV Processing Software," *NASA TM 1999-209274.*

8 Bradshaw, P, ed., 1978, *Topics in Applied Physics: Turbulence*, Springer-Verlag.

9 Hinze, J.O., 1951, *Turbulence: An Introduction to its Mechanism and Theory*, McGraw-Hill, p. 54.

10 Frenkiel, F.N. 1948, *J. Aeronautical Science* **15**, 57.

11 Laurence, J.C. 1956, "Intensity, Scale and Spectra of Turbulence in Mixing Region of Free Subsonic Jet," *NACA report 1292*.

12 Khavaran, A 1999, "Role of Anisotropy in Turbulent Mixing Noise," *AIAAJ* **37**, 832.

13 Melling, A 1997, "Tracer Particles and Seeding for Particle Image Velocimetry," *Measurement Science and Technology* **8**, 1406.

14 Walatka, B. & Buning, P., 1989, "Plot3D User's Manual," *NASA TM 101067*.

15 Kenzakowski, D.C., Shipman, J., & Dash, S.M., 2001, "Task 2-Flow Solution for Advanced Separate Flow Nozzles Response A: Structured Grid Navier-Stokes Approach," *NASA CR 2001-210611*.

16 Podboy, G.G., Bridges, J., Saiyed, N., & Krupar, M.J. 1995, "Laser Doppler Velocimeter System for Subsonic Jet Mixer Nozzle Testing at the NASA Lewis Aeroacoustic Propulsion Lab," *NASA TM 106984*.

12 Appendix A: Test narrative

02.08.2000

Configuration: Jet Exit Rig has been reassembled and configured for laser testing. Aluminum oxide seed will be injected into the core and bypass flows. The RFM in the core and bypass lines has been replaced with choke plates. Charging station instrumentation has been replaced with older rakes from past programs. The traversing rake is installed behind the JER.

Objectives: Check out the operation of the rig with the reticulated foam metal (RFM) removed and replaced by choke plates. Compare data with previous runs to insure that the rig is performing as expected. Check out new charging station rake instrumentation. Also, check out the operation of the traversing rake and the effect of the freejet airflow on laser components mounted on the traverse rake shelves.

Results: Completed all objectives. The rig is performing the same as it did before the rebuild. traversing rake was moved axially and the automated traverse system (PACS) profile was checked out. Facility data acquisition system (Escort) acquired data automatically at each stopping point. The flow of the freejet impinged on the camera and backplate mounted on the traversing rake. There was only slight movement noticed of the camera's. A stiffening bracket will be added.

11.08.2000

Configuration: Same as previous.

Objectives: Check out the operation of the seeder carts for the core and bypass system. Measure the seed flow with PIV laser to see if they are producing the right amount of seed.

Results: Run cancelled. Unable to align laser due to procedure specified in safety permit did not allow for alignment of the laser with protective eyewear removed which is standard. Issue will be worked with the laser safety office.

14.08.2000

Configuration: Same as previous.

Objectives: Check out the operation of the seeder carts for the core and bypass system. Measure the seed flow with PIV laser to see if they are producing the right amount of seed.

Results: Complete checkout of the freejet smoke generator and bypass seeder cart. Both worked well and produced enough seed for the laser to measure the flow field.

Problems: The core seeder cart did not produce seed consistently. After the solenoid valve is opened there is a short duration of seed, then the supply pressure drops off and the seed stops. Will investigate further on the next run.

15.08.2000

Configuration: Same as previous.

Objectives: Check out the operation of the seeder carts for the core and bypass system. Measure the seed flow with PIV laser to see if they are producing the right amount of seed.

Results: Continued with troubleshooting the core seeder cart operation. As the pressure of the cart is increased above the core line pressure that we are injecting seed into, the supply pressure of the cart decreases until it matches core line pressure. No seed is produced.

Problems: The core seeder regulator works statically without any flow but drops off when connected to the core air line. We suspect the supply solenoid valve is not opening completely.

16.08.2000

Configuration: Same as previous.

Objectives: Check out the operation of the seeder carts for the core and bypass system. Measure the seed flow with PIV laser to see if they are producing the right amount of seed.

Results: Still having difficulties getting the core seeder system to work properly we replaced the solenoid valve which supplies air to the cart but had the same results. We also plumbed the system so that bypass solenoid valve supplied both carts but again the core seeder would not supply seed.

17.08.2000

Configuration: Same as previous. Gate valves added to core and bypass seeder carts for back pressure the regulators.

Objectives: Check out the operation of the seeder carts for the core and bypass system. Measure the seed flow with PIV laser to see if they are producing the right amount of seed.

Results: fWe added regulators to the core and seeder carts which improved the range of control for the bypass seeder; however, the core seeder still is not producing seed. For tomorrow's run we are swapping pressure regulators between to the core and the seeder carts to see if that is the problem.

18.08.2000

Configuration: Same as previous.

Objectives: Check out the operation of the seeder carts for the core and bypass system. Measure the seed flow with PIV laser to see if they are producing the right amount of seed.

Results: We finally had successful checkout of the core seeder. The problem was the solenoid valve that supplied the cart was not opening fully and supply pressure was dropping off once flow started. The solenoid valve was replaced earlier in the week so this was unexpected. We are replacing the solenoid valve with an air operated ball valve which will serve the same purpose. PIV data acquired for nozzle 3BB from the nozzle exit plane back to 90 inches in 5 inch increments. The data looked good and we are proceeding with our test plan. However, fan stream screen just downstream of choke plates let go during run. Tore down the rig and tried to repair screens by tacking back on (see Figure 13.1).

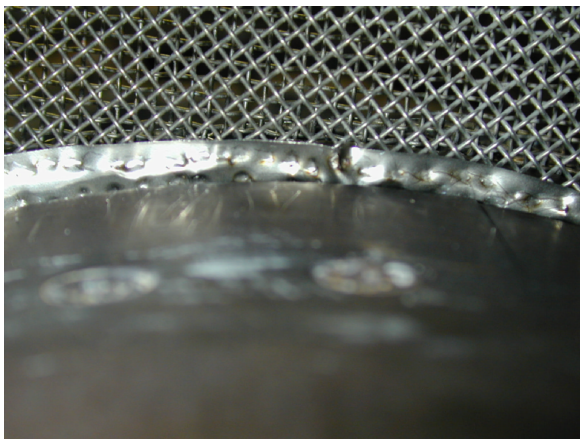

Figure 13.1. Repaired fan screen, with excess nichrome strips to strengthen screen near welds.

23.08.2000

Configuration: Same as previous. Fan flow straightening screens have been field repaired.

Objectives: Acquire PIV laser data at power cycle 21 conditions for nozzle 3BB. Move the traversing rake axially from 0" to 90", stopping every 5 " to acquire laser data.

Results: Completed research objectives for nozzle 3BB. Time: 17:53-19:40

Problems: Had to shut down at 18:54 for more fogger oil. Back up at 19:30.

24.08.2000

Configuration: Same as previous.

Objectives: Acquire PIV laser data at power cycle 21 conditions. Move the traversing rake axially from 0" to 90", stopping every 5" to acquire laser data.

Results: Started the run at 15:35. Seeders caked up at 14:01. Had to break the seed up with stick. In future, only use dry seed, and clean out daily. Came up again, but fogger not turned on. Finished 3AB at 0° clocking at 18:40. Came up on 3AB at 30° at 19:16 and finished at 20:48.

Completed the research objectives for nozzle 3A12B at 0 degree and 30 degree clocking.

25.08.2000

Configuration: Same as previous.

Objectives: Acquire PIV laser data at power cycle 21 conditions. Move the traversing rake axially from 0" to 40", stopping every 5" to acquire laser data.

Results: Started at 14:04. Finished by 15:47. Completed research objectives for nozzle 3A12B at 15° clocking. Fan flow screens had ripped out again.

29.08.2000

Configuration: Same as previous. JER fan flow straightening screens removed. See Figure 13.2

Objectives: Verify the flow characteristics of the JER fan section with the flow straightening screens removed. The screens have failed twice since we began laser testing and are removed. We need to compare the flow of the fan section with the screens removed versus data we took with the screens in place.

Results: We acquired acoustics data with the fan screens removed for nozzle 3BB and 3A12B. Acoustic data showed that chevrons were still providing 2+ EPNdB suppression, so it was deemed acceptable to continue testing without fan screens downstream of choke plate.

PIV laser overtemp switch tripped out which prevented us from acquiring laser data.

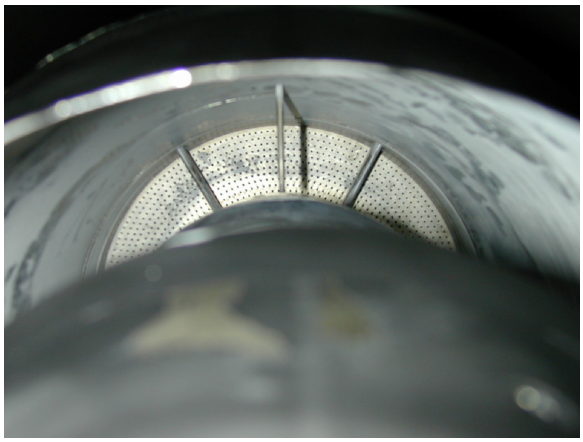

Figure 13.2. Fan flow passage as seen from the nozzle exit with screen removed.

30.08.2000

Configuration:

Same as previous. Air conditioner added to direct chilled air onto laser power supplies.

Objectives: Verify the flow characteristics of the JER fan section with the flow straightening screens removed. The screens have failed twice since we began laser testing and are removed. We need to compare the flow of the fan section with the screens removed versus data we took with the screens in place.

Results: Acquired PIV laser data for nozzles 3BB and 3A12B. Data showed minimal impact from screens being removed. See Figure 13.3.

Had poor freejet seeding on the first run. Saw sparkles in the seeding indicating large droplets of oil. Cleaned Vicount seeder nozzle between runs. Fogger worked better, no droplets. Put lots of oil on NATR centerbody and framework in doghouse.

Took minimal data to look for problems with screen. First run from 17:32 to 18:00; second run 19:08 to19:55.

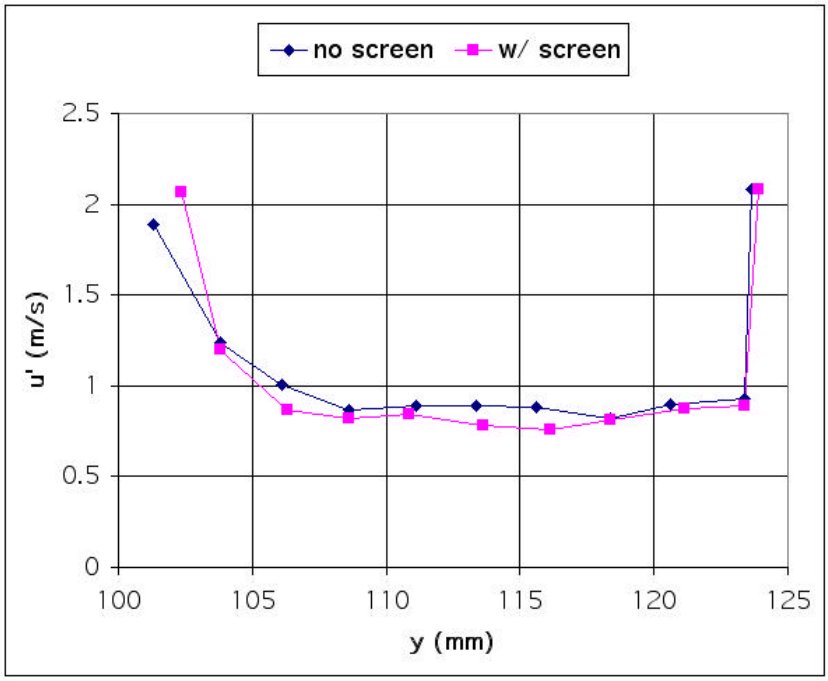

Figure 13.3. Comparison of fan stream freestream turbulence with and without screen in rig. Removal of screen did not increase turbulence levels.

06.09.2000

Configuration: Same as previous.

Objectives: Acquire PIV laser data at power cycle 21 conditions. Move the traversing rake axially from 0" to 40", stopping every 5" to acquire laser data. Test the 3A12B nozzle at 5°, 20°, and 15° clockings.

Results: Acquired desired data. Long run of 3A12B @ 15° orientation took from 15:41 to 17:26. Short run of 3A12B @ 5° orientation 18:15 to 19:00. Short run of 3A12B @ 20° orientation 20:04 to 21:42. Later found that 5° data was not at 5°.

07.09.2000

Configuration: Same as previous.

Objectives: Acquire PIV laser data at power cycle 21 conditions. Move the traversing rake axially from 0" to 40", stopping every 5" to acquire laser data. Test nozzle 3A12B at 20°, and 30° clockings.

Results: Acquired desired data. Short runs:16:10 to 16:44 for 5° orientation, 17:07 to 18:25 for 20° orientation, 20:25 to 22:29 for 30° orientation.

08.09.2000

Configuration: Same as previous.

Objectives: Acquire PIV laser data at power cycle 21 conditions. Move the traversing rake axially from 0" to 90", stopping every 5" to acquire laser data. Run nozzle 3A12B at 30° clocking and 3T24C at 0° clocking.

Results: Acquired desired data. Long runs at 30° from 16:20 to 18:00 and at 0° from 18:25 to 20:29.

11.09.2000

Configuration: Same as previous.

Objectives: Acquire PIV laser data at power cycle 21 conditions. Move the traversing rake axially from 0" to 90", stopping every 5" to acquire laser data. Test nozzle 3T24C at 30° clocking.

Results: Laser beams went out of alignment during the run. There was not enough time to realign and complete another data set so we will repeat the configuration tomorrow. Light sheets were found not to overlap. Must confirm overlap every day!

12.09.2000

Configuration: Same as previous.

Objectives: Acquire PIV laser data at power cycle 21 conditions. Move the traversing rake axially from 0" to 90", stopping every 5" to acquire laser data. Test nozzle 3T24C at 15° clocking.

Results: Acquired desired data. We had to shut down during the run due to an oil leak on the output valve of the Central Air C16 compressor. The leak was repaired by the valve shop and the run resumed.

13.09.2000

Configuration: Same as previous.

Objectives: Acquire PIV laser data at power cycle 21 conditions. Move the traversing rake axially from 0" to 40", stopping every 5" to acquire laser data. Test nozzle 3T24C at 10°, 25°, and 30° clocking.

Results: Acquired desired data. Things are starting to get productive and boring.

14.09.2000

Configuration: Same as previous.

Objectives: Acquire PIV laser data at power cycle 21 conditions. Move the traversing rake axially from 0" to 40", stopping every 5" to acquire laser data. Test nozzle 3T24C at 5°, 10°, 25°, 3A12B at 25°, and nozzle 3BB.

Results: Acquired desired data.

19.09.2000

Configuration: Same as previous. Setup PIV cameras in stereo mode.

Objectives: Acquire PIV laser data at power cycle 21 conditions. Move the traversing rake axially from 0" to 90", stopping every 5" to acquire laser data. Test nozzle 3BB.

Results: Tried to do Stereo (3C) PIV. No good data was taken this day. Setups were a problem.

20.09.2000

Configuration Same as previous.

Objectives: Acquire PIV laser data at power cycle 21 conditions. Move the traversing rake axially from 0" to 90", stopping every 5" to acquire laser data. Test nozzle 3BB and 3A12B at 0° clocking.

Results: Set up cameras in Scheimplug configuration. Light sheet began to move and the left side of the images was bad. Found that one camera had moved ALOT! Tightened it up and had it move again after the second run. Again, no good data.

21.09.2000

Configuration: Same as previous.

Objectives: Acquire PIV laser data at power cycle 21 conditions. Move the traversing rake axially from 0" to 90", stopping every 5" to acquire laser data. Test nozzle 3A12B at 30 degree clocking. Spot check acoustic properties of new inward chevron fan nozzle. Run a matrix of 3 NPR's for nozzles 3BB, 3I12B, 3I12I24, and 3A12I24.

Results: Cameras continue to move despite torqueing down on mounts. No good data.

25.09.2000

Configuration: Same as previous.

Objectives: Acquire PIV laser data at power cycle 21 conditions. Move the traversing rake axially from 0" to 90", stopping every 5" to acquire laser data. Test nozzle 3BO with max area at the top of the nozzle and 3BB.

Results: Really clamped down on cameras using second beam and C-clamps. Camera didn't move noticeably.

26.09.2000

Configuration: Same as previous.

Objectives: Acquire PIV laser data at power cycle 21 conditions. Move the traversing rake axially from 0" to 90", stopping every 5" to acquire laser data. Test nozzle 3BO with max area at the bottom.

Results: Acquired desired data. Camera didn't move. Data may be good. This completes the PIV laser phase of the Separate Flow Nozzle program.

13 Appendix B: Data plots

Appendix B contains 384 plots of turbulence statistics rendered from the data.

1. Model 3bb
    1. Oblique Views
        1. One-Point Statistics
        2. Two-Point Statistics
    2. Single Plane Views
        1. Theta = 0°
            1. One-Point Statistics
            2. Two-Point Statistics
            3. Lengthscale Statistics
2. Model 3ab
    1. Oblique Views
        1. One-Point Statistics
        2. Two-Point Statistics
    2. Single Plane Views
        1. Theta = 0°
            1. One-Point Statistics
            2. Two-Point Statistics
            3. Lengthscale Statistics
        2. Theta = 5°
            1. One-Point Statistics
            2. Two-Point Statistics
            3. Lengthscale Statistics
        3. Theta = 10°
            1. One-Point Statistics
            2. Two-Point Statistics
            3. Lengthscale Statistics
        4. Theta = 15°
            1. One-Point Statistics
            2. Two-Point Statistics
            3. Lengthscale Statistics
        5. Theta = 20°
            1. One-Point Statistics
            2. Two-Point Statistics

2. Two-Point Statistics
3. Lengthscale Statistics

6. Theta = 25°
    1. One-Point Statistics
    2. Two-Point Statistics
    3. Lengthscale Statistics
7. Theta = 30°
    1. One-Point Statistics
    2. Two-Point Statistics
    3. Lengthscale Statistics

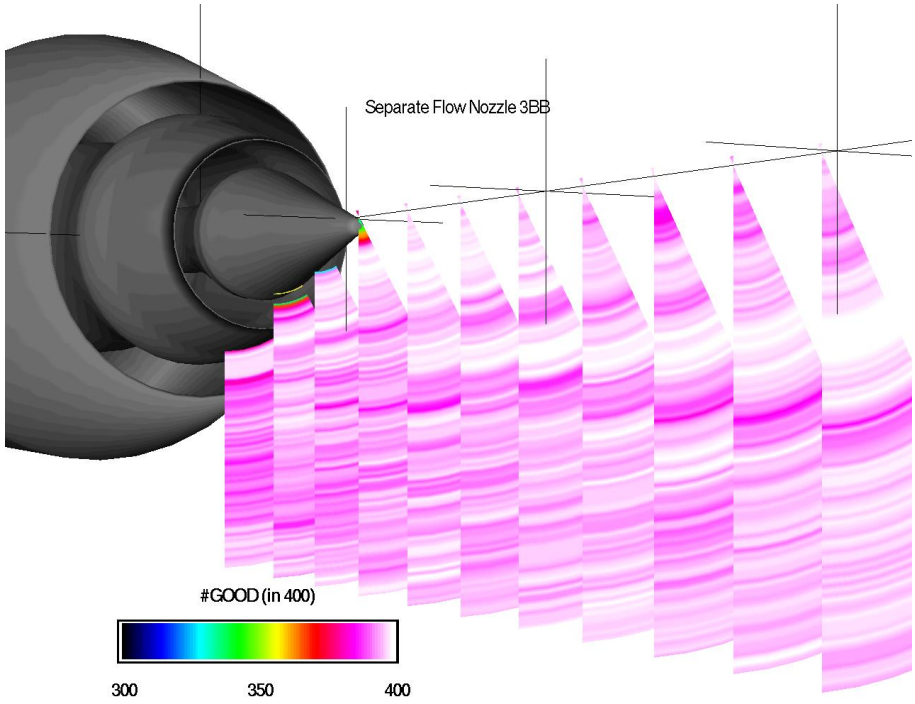

Figure 1.0.1.1 Model 3bb. Contour plots of data quality (#good out of 400). Slices taken at x = {0.047 0.132 0.199 0.267 0.334 0.401 0.468 0.535 0.603 0.670 0.737} meters.

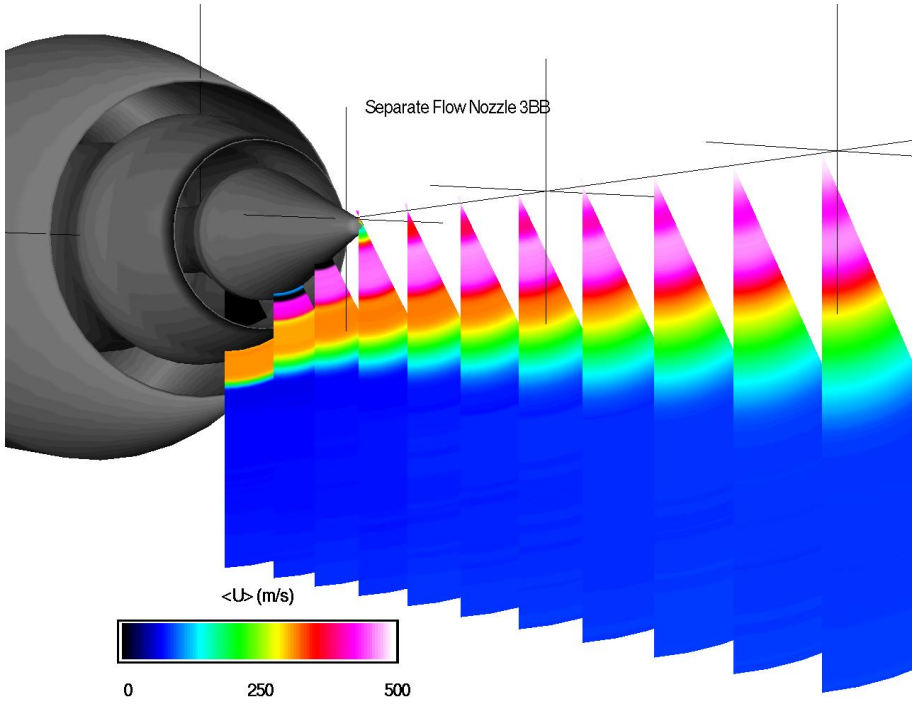

Figure 1.0.1.2 Model 3bb. Contour plots of time average axial velocity (m/s). Slices taken at x = {0.047 0.132 0.199 0.267 0.334 0.401 0.468 0.535 0.603 0.670 0.737} meters.

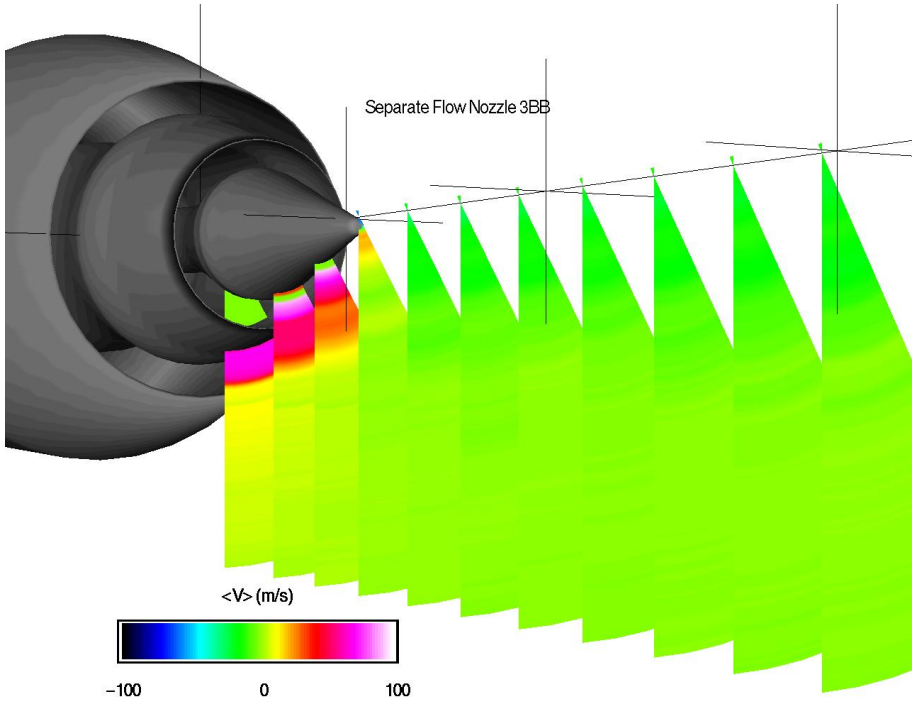

Figure 1.0.1.3 Model 3bb. Contour plots of time average radial velocity (m/s). Slices taken at x = {0.047 0.132 0.199 0.267 0.334 0.401 0.468 0.535 0.603 0.670 0.737} meters.

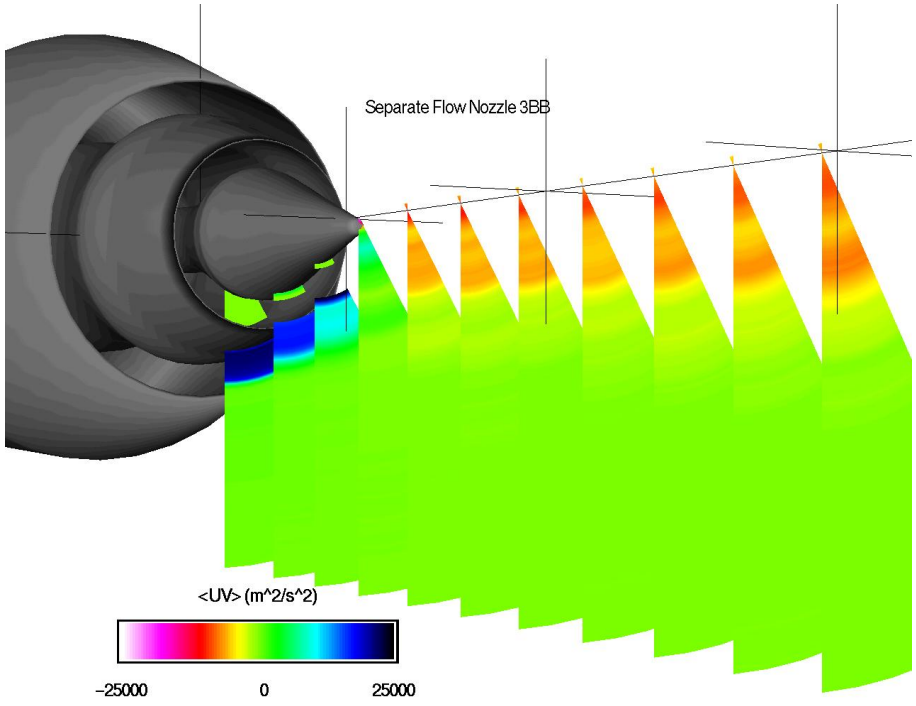

Figure 1.0.1.4 Model 3bb. Contour plots of time average Reynolds stress (m^2/s^2). Slices taken at x = {0.047 0.132 0.199 0.267 0.334 0.401 0.468 0.535 0.603 0.670 0.737} meters.

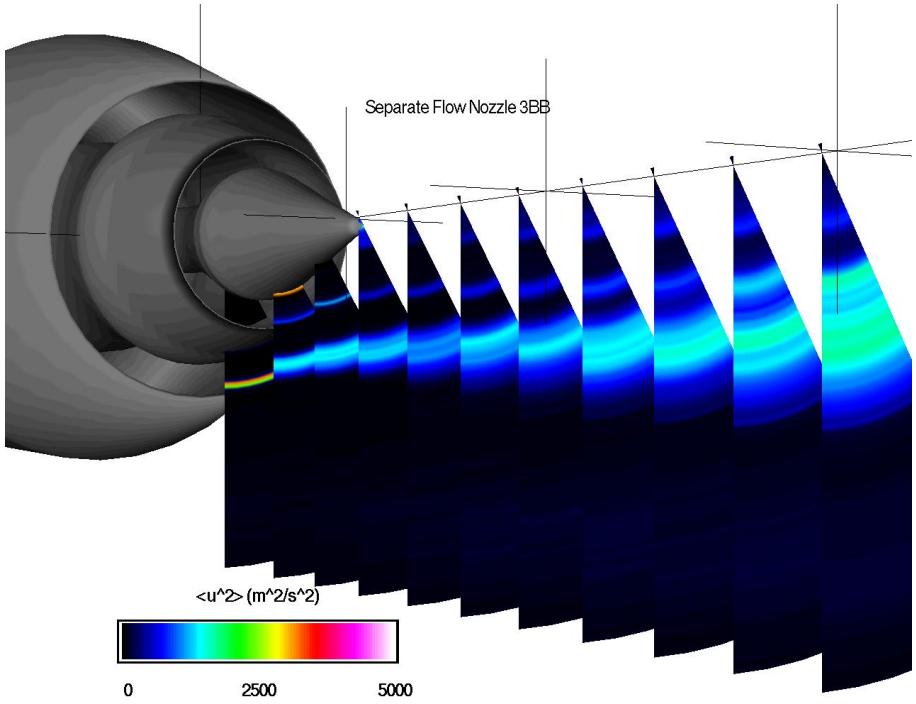

Figure 1.0.1.5 Model 3bb. Contour plots of variance of axial velocity (m^2/s^2). Slices taken at x = {0.047 0.132 0.199 0.267 0.334 0.401 0.468 0.535 0.603 0.670 0.737} meters.

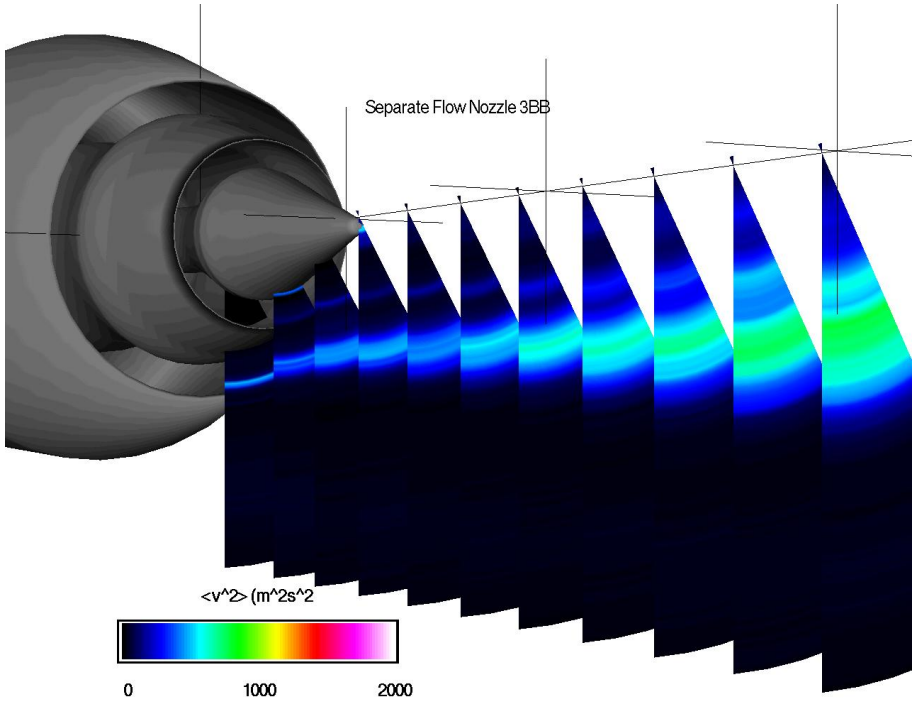

Figure 1.0.1.6 Model 3bb. Contour plots of variance in radial velocity (m^2/s^2). Slices taken at x = {0.047 0.132 0.199 0.267 0.334 0.401 0.468 0.535 0.603 0.670 0.737} meters.

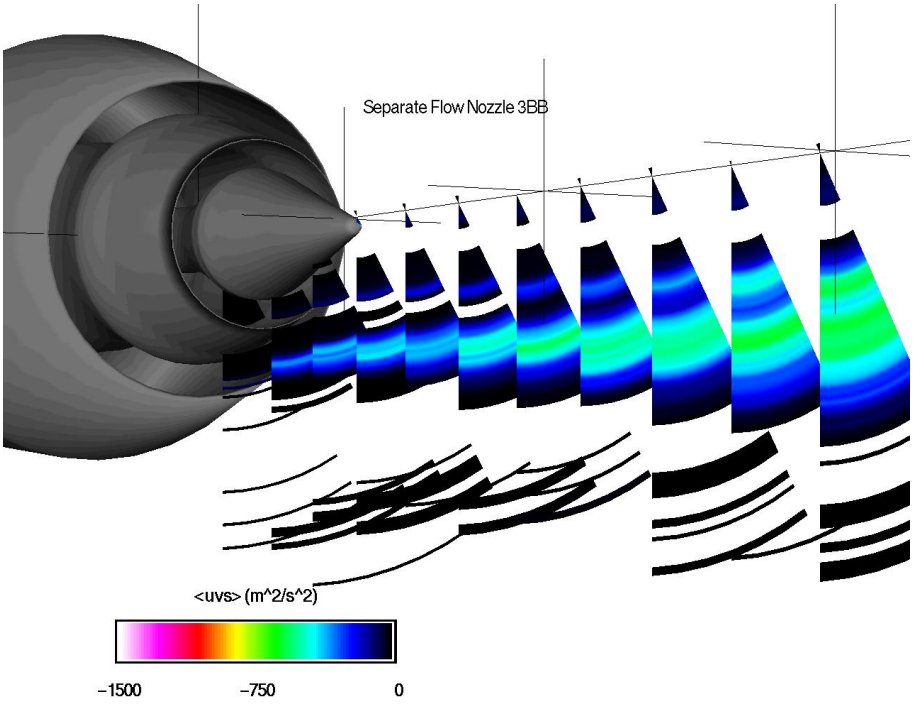

Figure 1.0.1.7 Model 3bb. Contour plots of unsteady Reynolds stress (m^2/s^2). Slices taken at x = {0.047 0.132 0.199 0.267 0.334 0.401 0.468 0.535 0.603 0.670 0.737} meters.

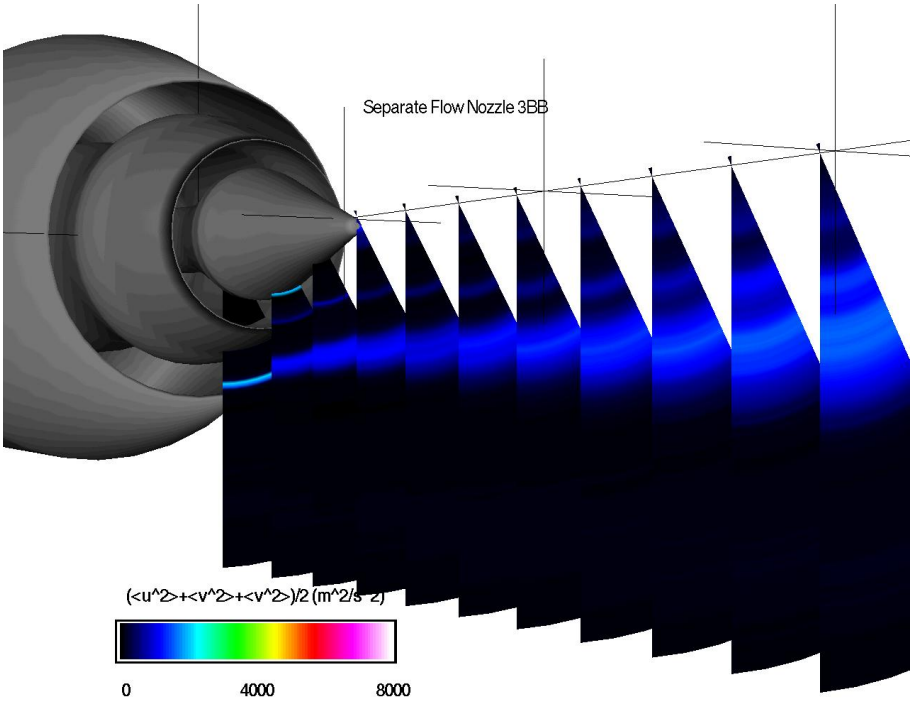

Figure 1.0.1.8 Model 3bb. Contour plots of turbulent kinetic energy (m^2/s^2). Slices taken at x = {0.047 0.132 0.199 0.267 0.334 0.401 0.468 0.535 0.603 0.670 0.737} meters.

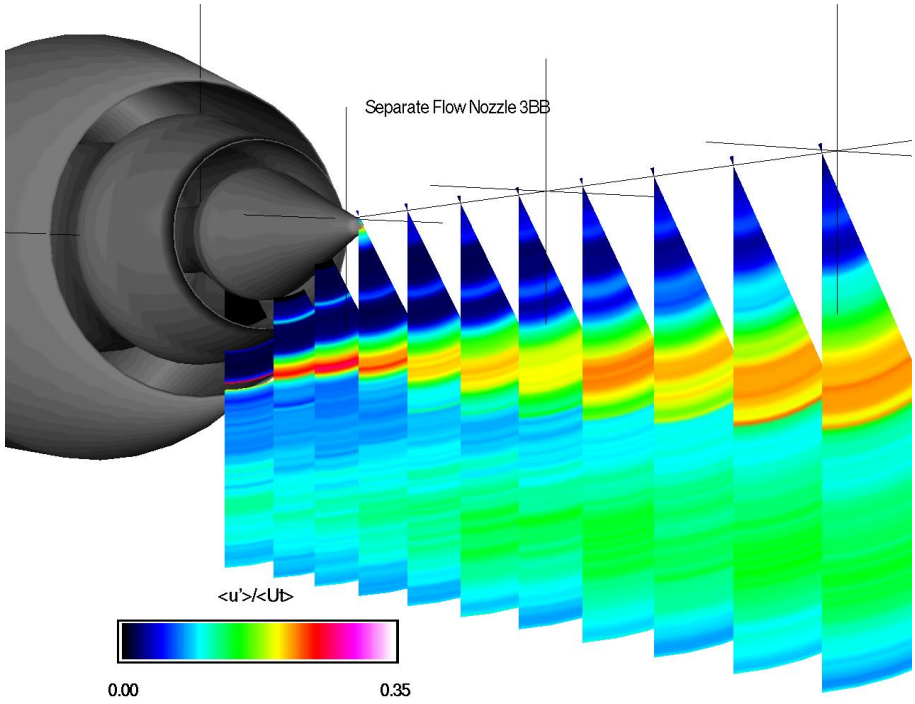

Figure 1.0.1.9 Model 3bb. Contour plots of axial turbulence intensity. Slices taken at x = {0.047 0.132 0.199 0.267 0.334 0.401 0.468 0.535 0.603 0.670 0.737} meters.

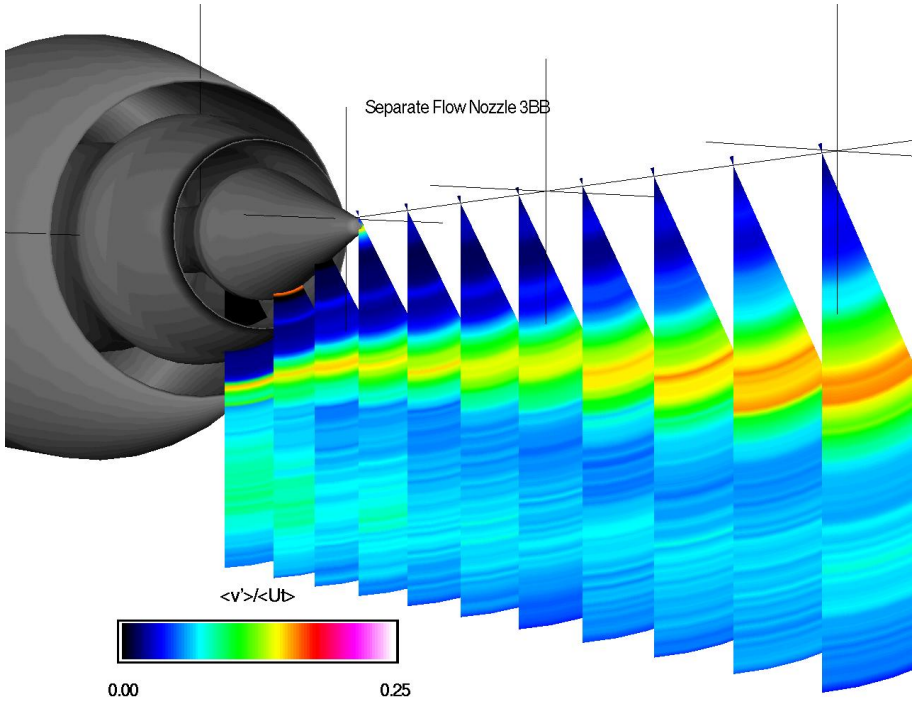

Figure 1.0.1.10 Model 3bb. Contour plots of radial turbulence intensity. Slices taken at x = {0.047 0.132 0.199 0.267 0.334 0.401 0.468 0.535 0.603 0.670 0.737} meters.

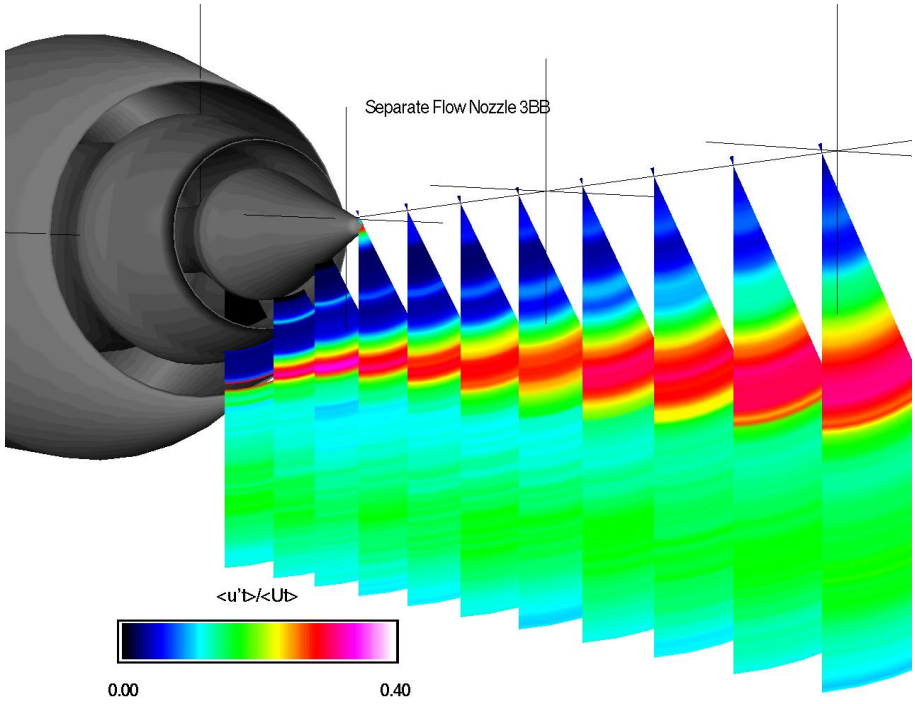

Figure 1.0.1.11 Model 3bb. Contour plots of turbulence intensity. Slices taken at x = {0.047 0.132 0.199 0.267 0.334 0.401 0.468 0.535 0.603 0.670 0.737} meters.

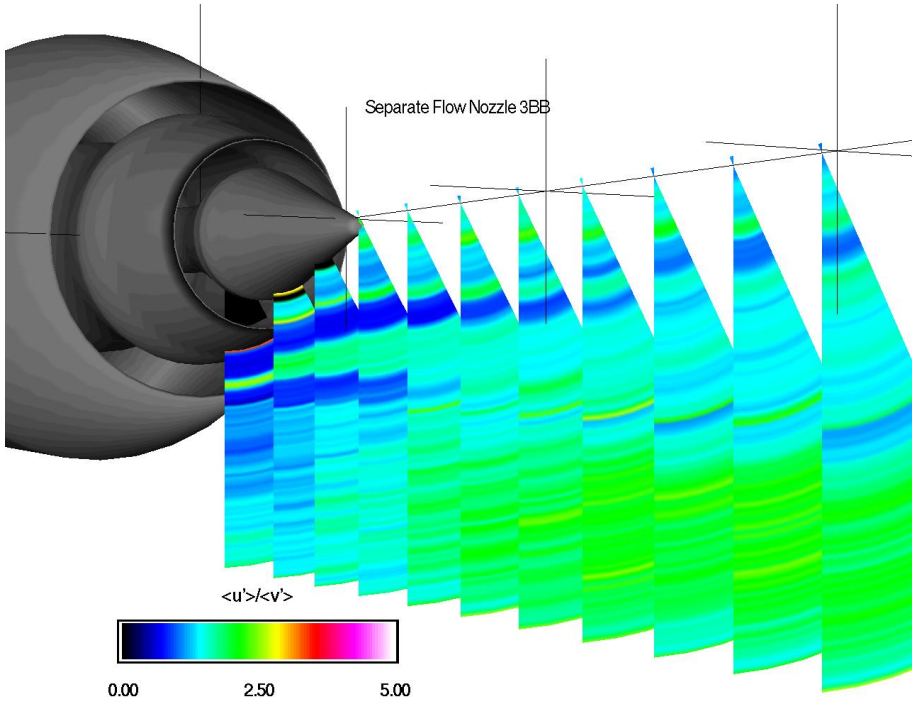

Figure 1.0.1.12 Model 3bb. Contour plots of ratio of axial to radial turbulence. Slices taken at x = {0.047 0.132 0.199 0.267 0.334 0.401 0.468 0.535 0.603 0.670 0.737} meters.

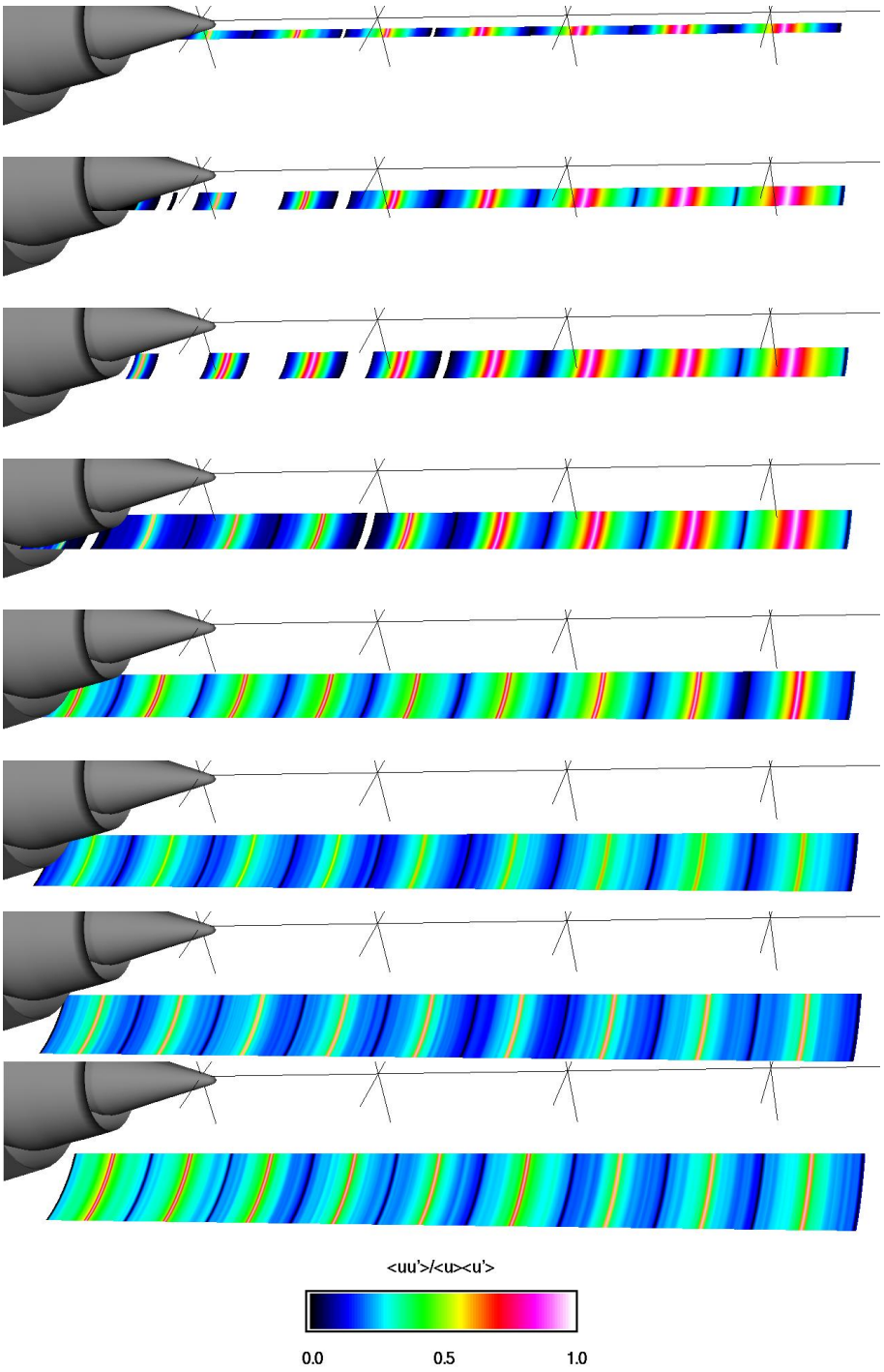

Figure 1.0.2.1 Model 3bb. Contour plots of u(xref)u(x). Slices taken at radius = {0.00 0.03 0.06 0.09 0.12 0.15 0.18 0.21 0.24} meters.

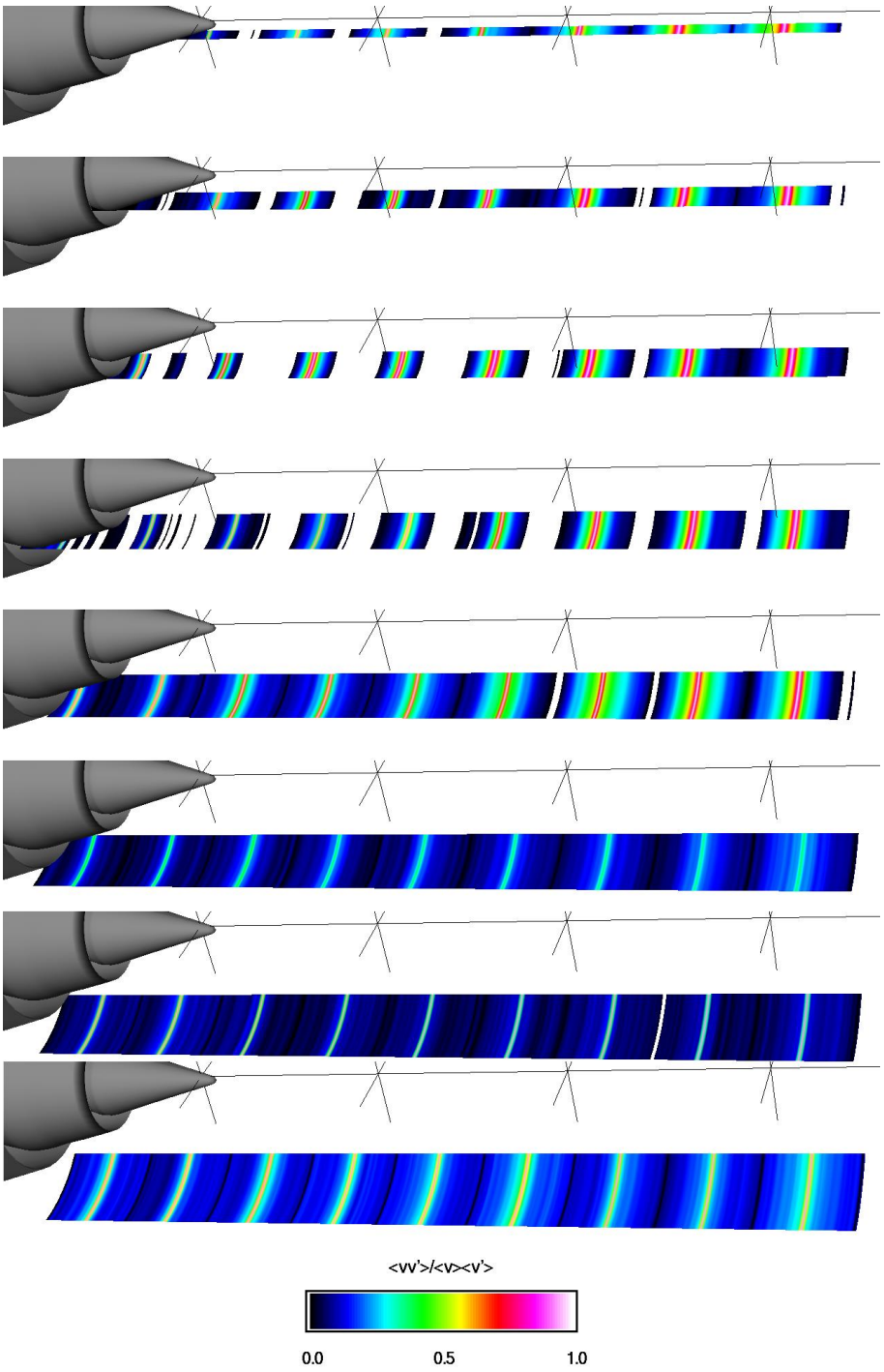

Figure 1.0.2.2 Model 3bb. Contour plots of v(xref)v(x). Slices taken at radius = {0.00 0.03 0.06 0.09 0.12 0.15 0.18 0.21 0.24} meters.

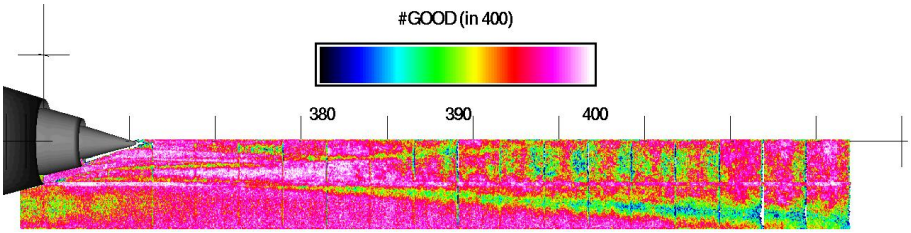

Figure 1.1.1.1 Model 3bb. Contour plots of data quality (#good out of 400). Slice taken at circumferential angle = 0°.

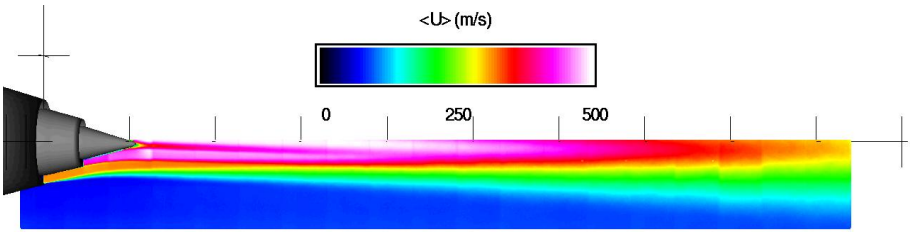

Figure 1.1.1.2 Model 3bb. Contour plots of time average axial velocity (m/s). Slice taken at circumferential angle = 0°.

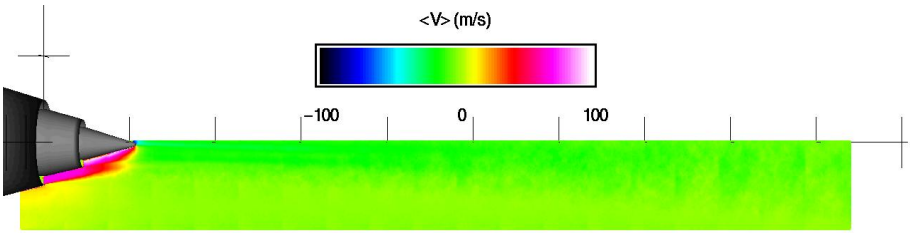

Figure 1.1.1.3 Model 3bb. Contour plots of time average radial velocity (m/s). Slice taken at circumferential angle = 0°.

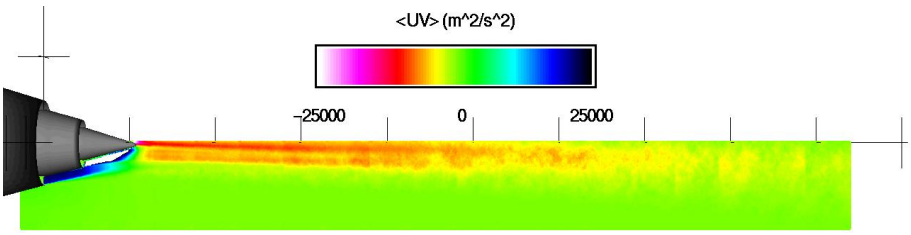

Figure 1.1.1.4 Model 3bb. Contour plots of time average Reynolds stress (m^2/s^2). Slice taken at circumferential angle = 0°.

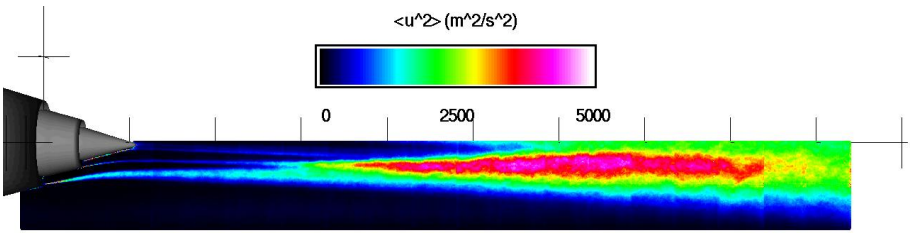

Figure 1.1.1.5 Model 3bb. Contour plots of variance of axial velocity (m^2/s^2). Slice taken at circumferential angle = 0°.

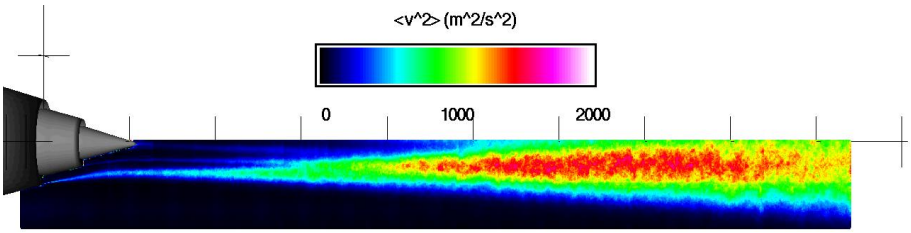

Figure 1.1.1.6 Model 3bb. Contour plots of variance in radial velocity (m^2/s^2). Slice taken at circumferential angle = 0°.

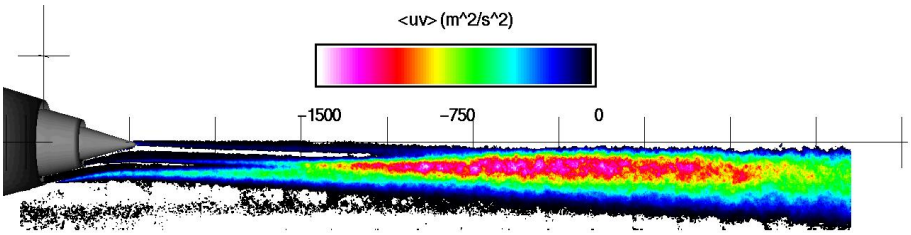

Figure 1.1.1.7 Model 3bb. Contour plots of unsteady Reynolds stress (m^2/s^2). Slice taken at circumferential angle = 0°.

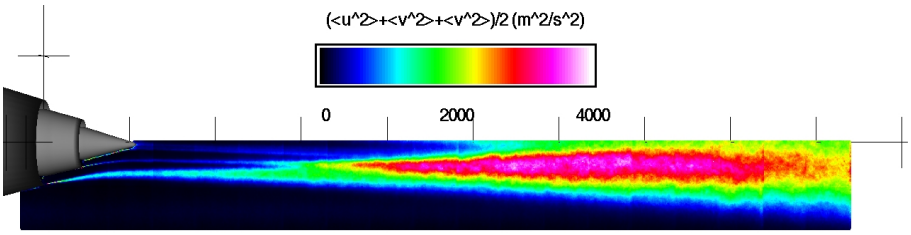

Figure 1.1.1.8 Model 3bb. Contour plots of turbulent kinetic energy (m^2/s^2). Slice taken at circumferential angle = 0°.

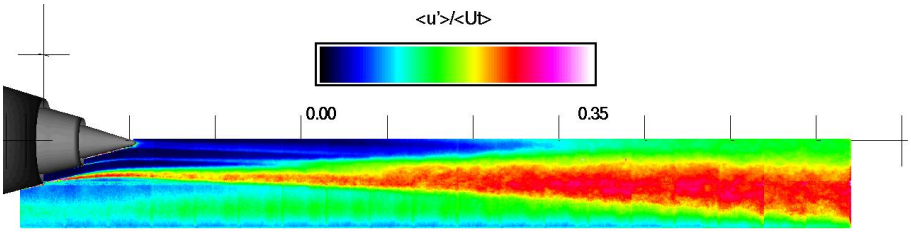

Figure 1.1.1.9 Model 3bb. Contour plots of axial turbulence intensity. Slice taken at circumferential angle = 0°.

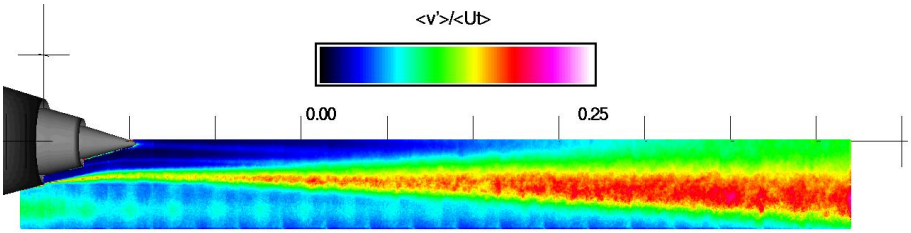

Figure 1.1.1.10 Model 3bb. Contour plots of radial turbulence intensity. Slice taken at circumferential angle = 0°.

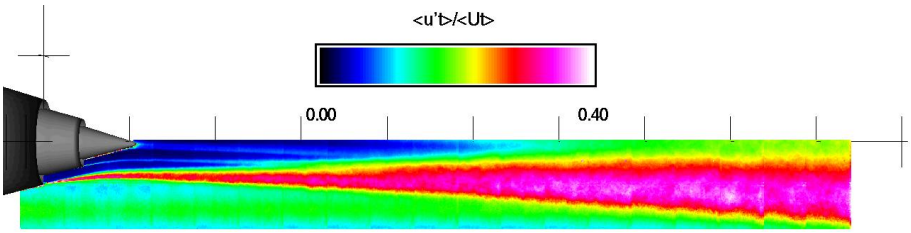

Figure 1.1.1.11 Model 3bb. Contour plots of turbulence intensity. Slice taken at circumferential angle = 0°.

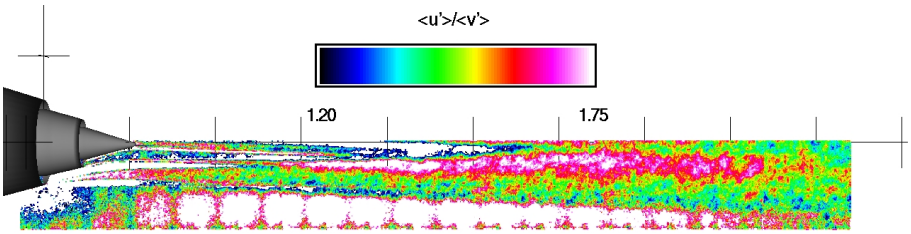

Figure 1.1.1.12 Model 3bb. Contour plots of ratio of axial to radial turbulence. Slice taken at circumferential angle = 0°.

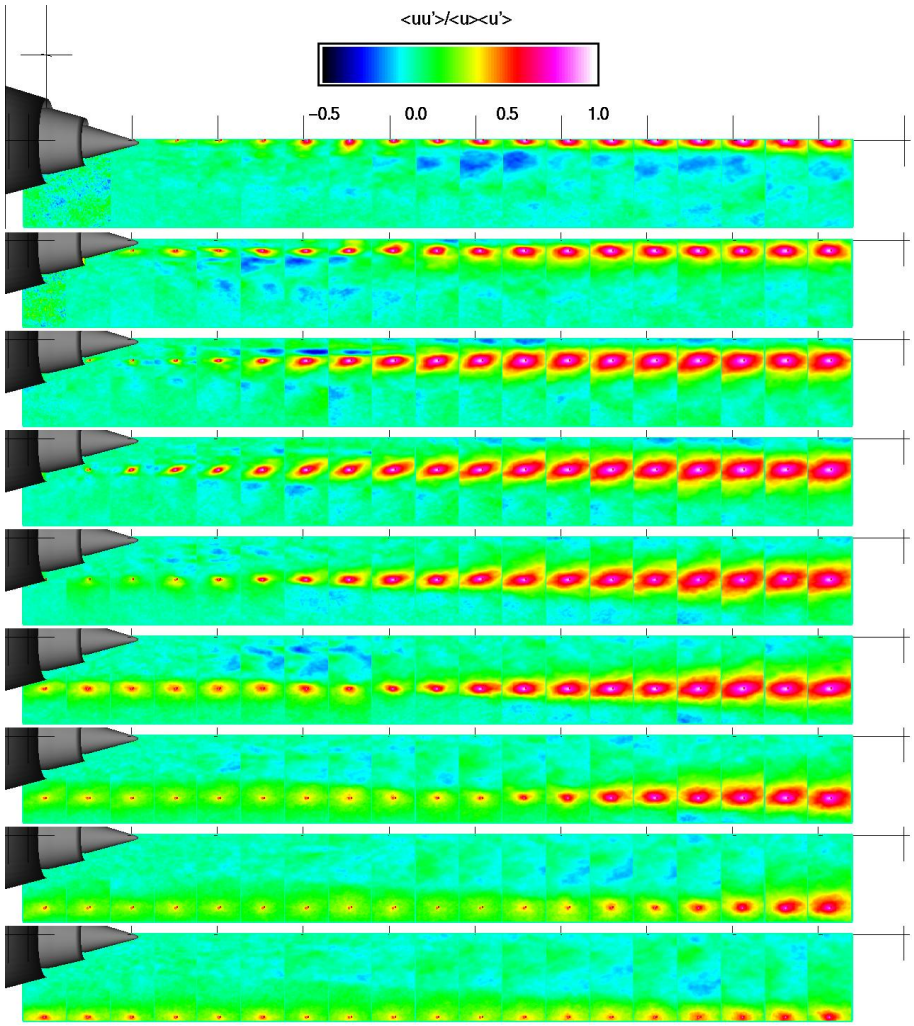

Figure 1.1.2.1 Model 3bb. Contour plots of u(xref)u(x). Slice taken at circumferential angle = 0°.

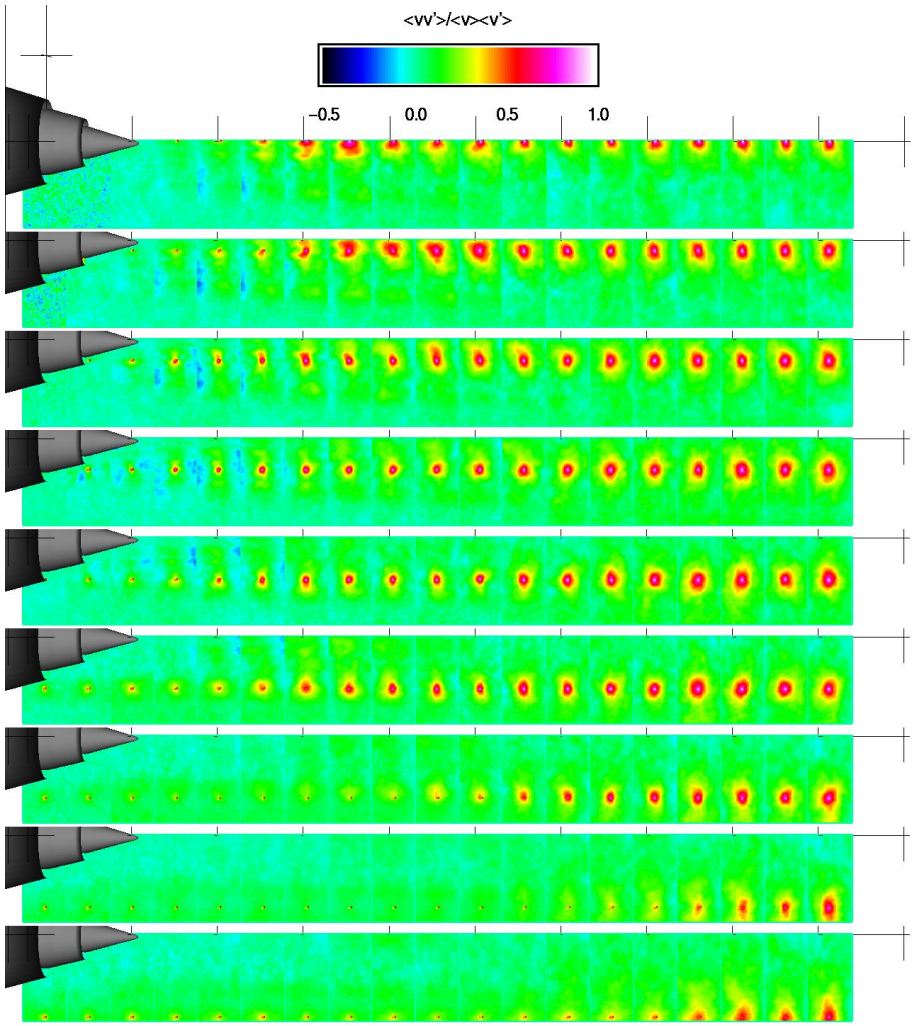

Figure 1.1.2.2 Model 3bb. Contour plots of v(xref)v(x). Slice taken at circumferential angle = 0°.

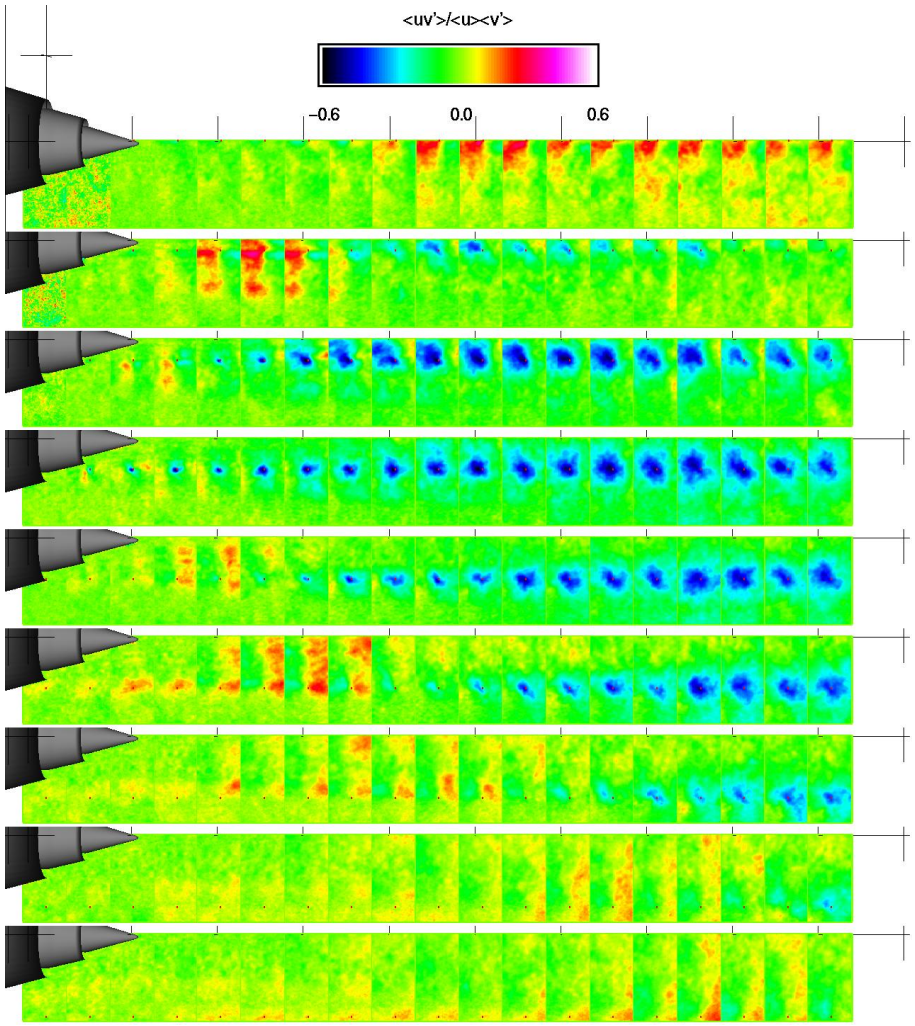

Figure 1.1.2.3 Model 3bb. Contour plots of u(xref)v(x). Slice taken at circumferential angle = 0°.

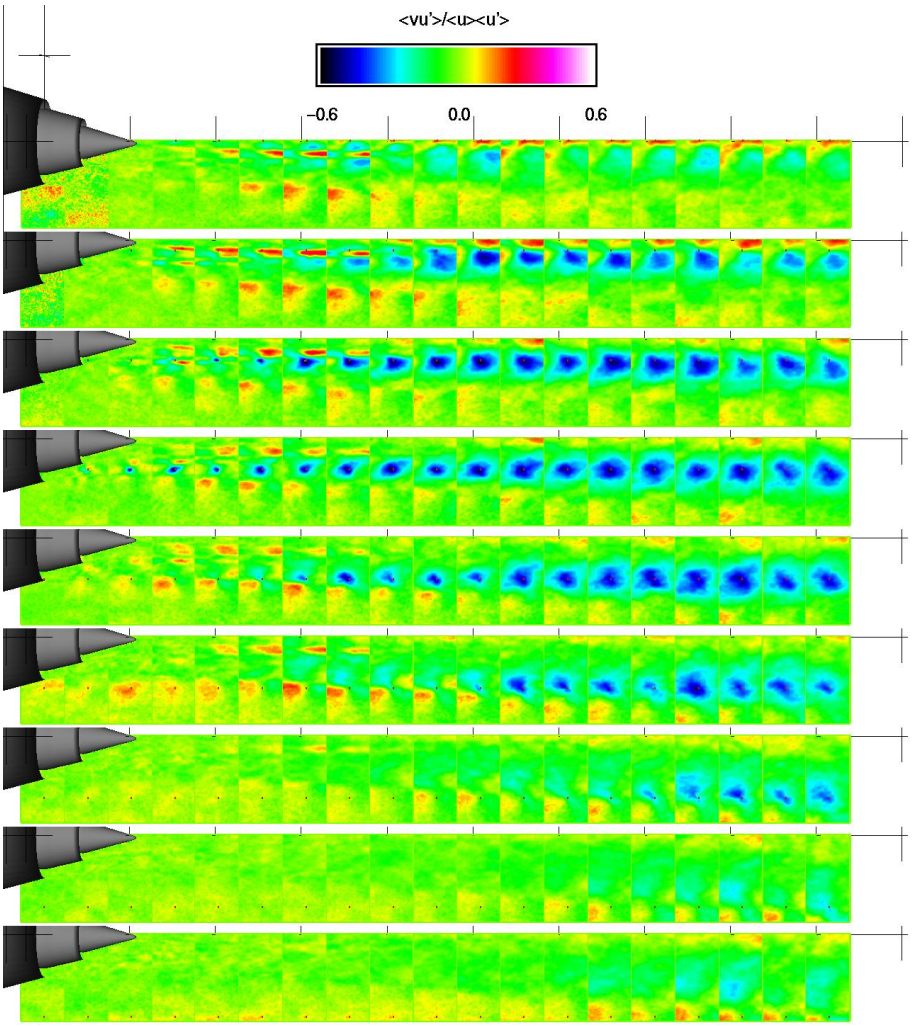

Figure 1.1.2.4 Model 3bb. Contour plots of v(xref)u(x). Slice taken at circumferential angle = 0°.

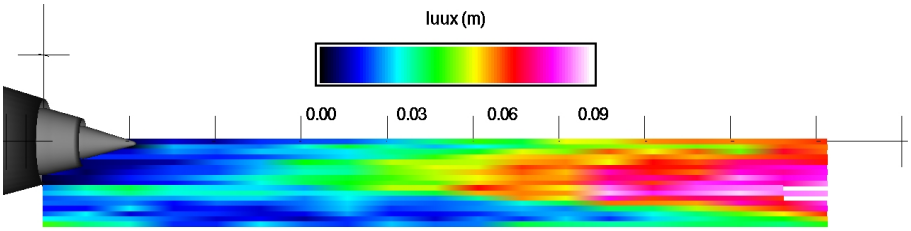

Figure 1.1.3.1 Model 3bb. Contour plots of Luu(x). Slice taken at circumferential angle = 0°.

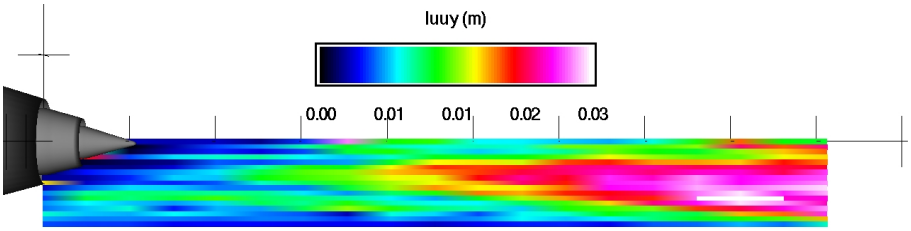

Figure 1.1.3.2 Model 3bb. Contour plots of Luu(y). Slice taken at circumferential angle = 0°.

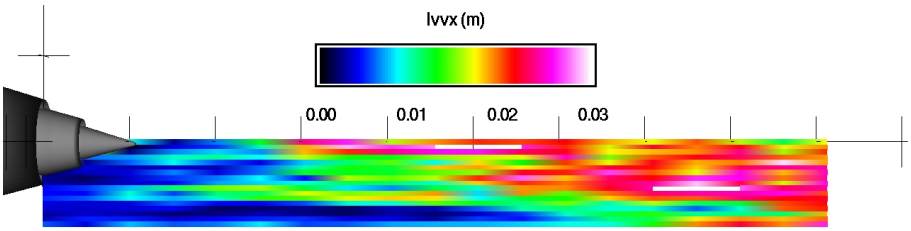

Figure 1.1.3.3 Model 3bb. Contour plots of Lvv(x). Slice taken at circumferential angle = 0°.

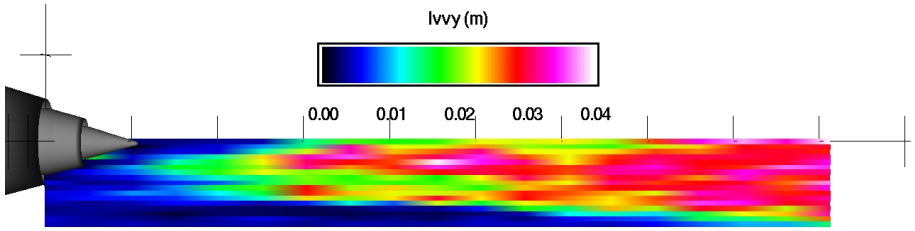

Figure 1.1.3.4 Model 3bb. Contour plots of Lvv(y). Slice taken at circumferential angle = 0°.

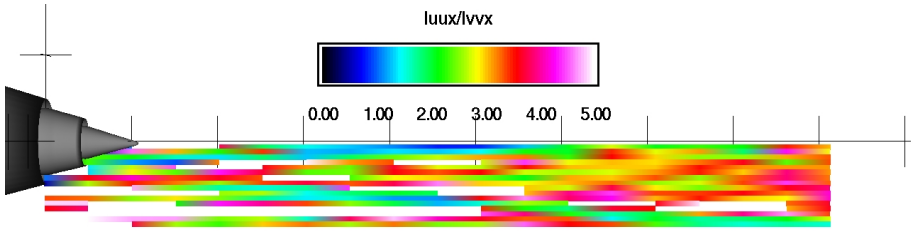

Figure 1.1.3.5 Model 3bb. Contour plots of Luu(x)/Lvv(x). Slice taken at circumferential angle = 0°.

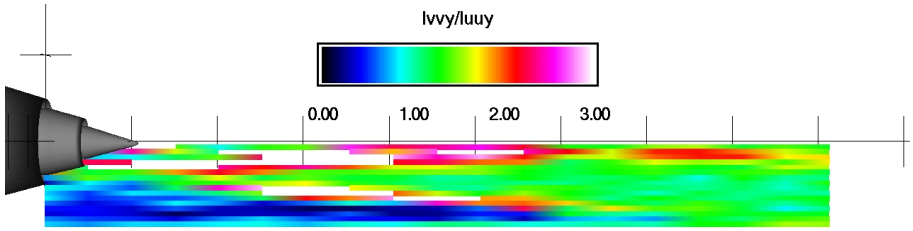

Figure 1.1.3.6 Model 3bb. Contour plots of Lvv(y)/Luu(y). Slice taken at circumferential angle = 0°.

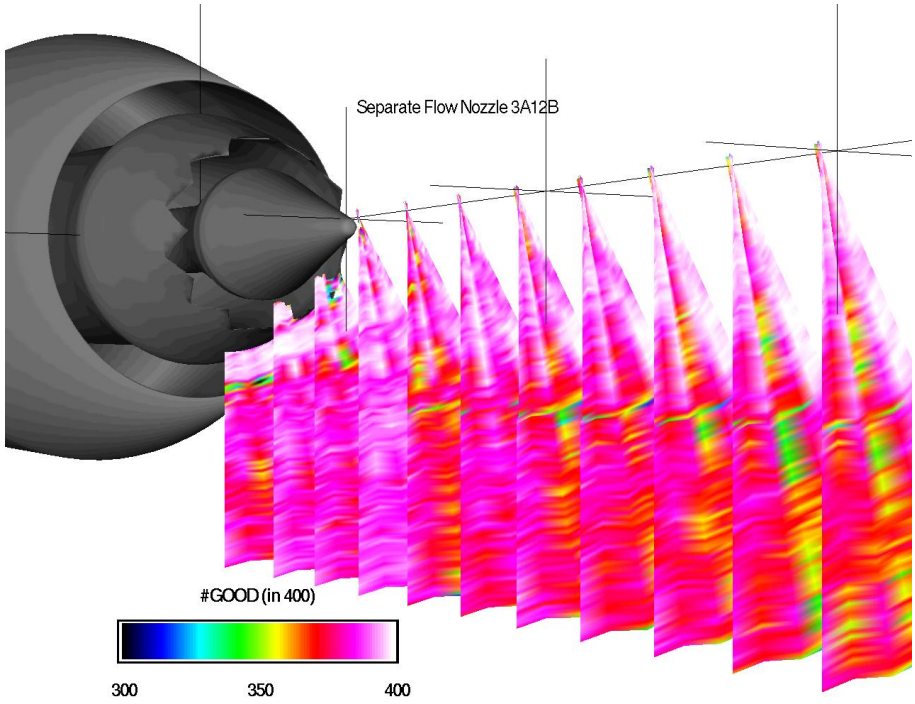

Figure 2.0.1.1 Model 3ab. Contour plots of data quality (#good out of 400). Slices taken at x = {0.047 0.132 0.199 0.267 0.334 0.401 0.468 0.535 0.603 0.670 0.737} meters.

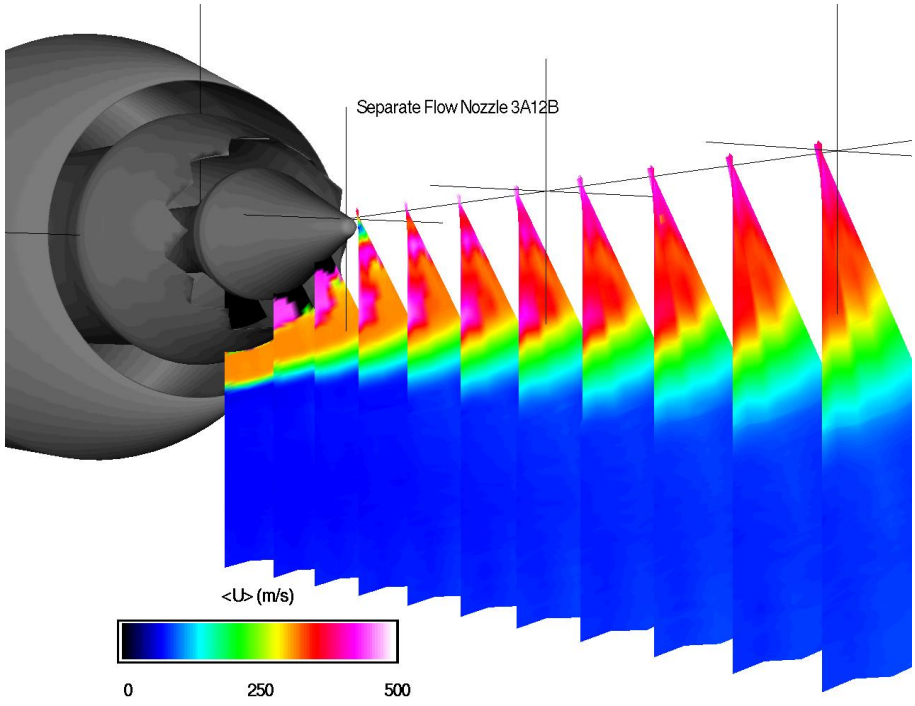

Figure 2.0.1.2 Model 3ab. Contour plots of time average axial velocity (m/s). Slices taken at x = {0.047 0.132 0.199 0.267 0.334 0.401 0.468 0.535 0.603 0.670 0.737} meters.

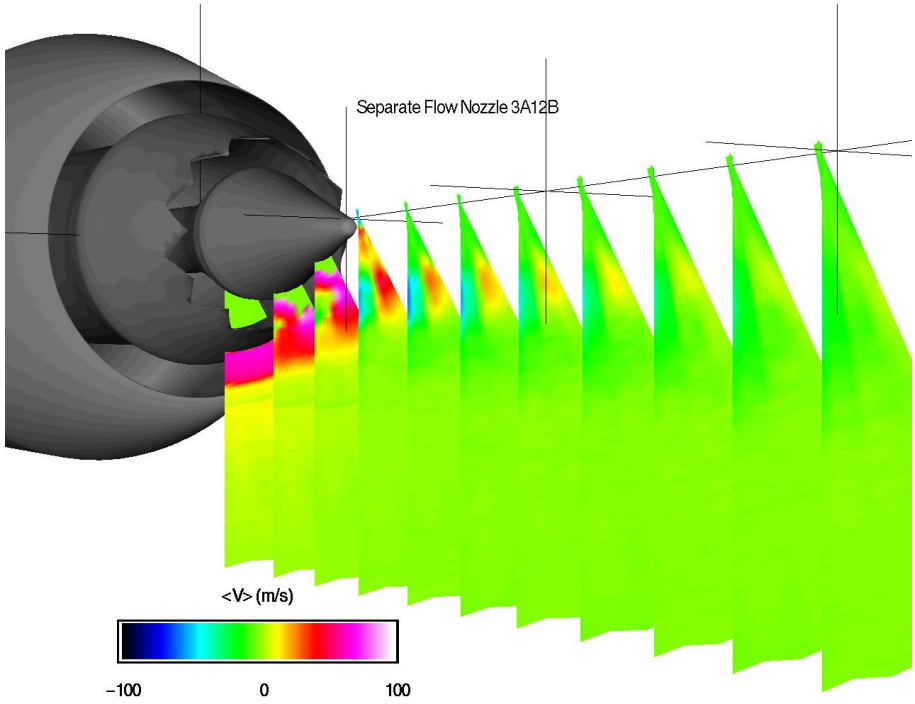

Figure 2.0.1.3 Model 3ab. Contour plots of time average radial velocity (m/s). Slices taken at x = {0.047 0.132 0.199 0.267 0.334 0.401 0.468 0.535 0.603 0.670 0.737} meters.

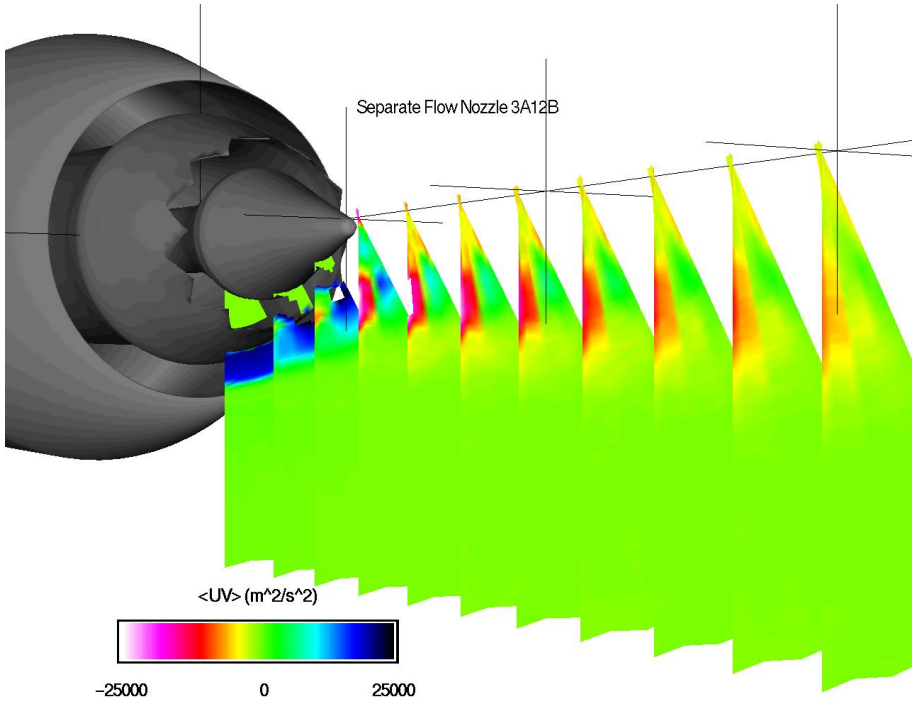

Figure 2.0.1.4 Model 3ab. Contour plots of time average Reynolds stress (m^2/s^2). Slices taken at x = {0.047 0.132 0.199 0.267 0.334 0.401 0.468 0.535 0.603 0.670 0.737} meters.

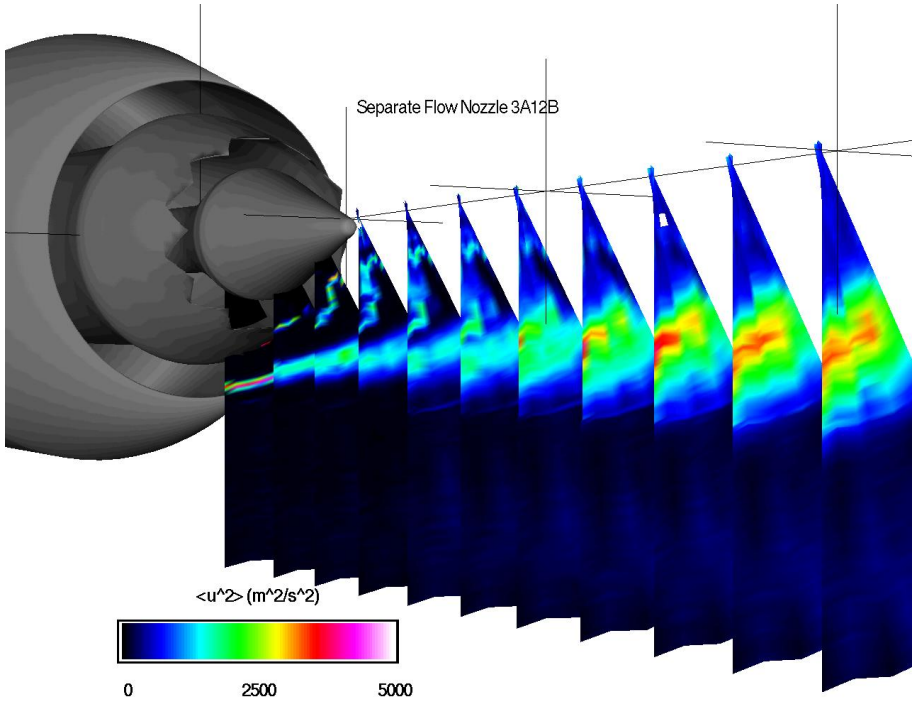

Figure 2.0.1.5 Model 3ab. Contour plots of variance of axial velocity (m^2/s^2). Slices taken at x = {0.047 0.132 0.199 0.267 0.334 0.401 0.468 0.535 0.603 0.670 0.737} meters.

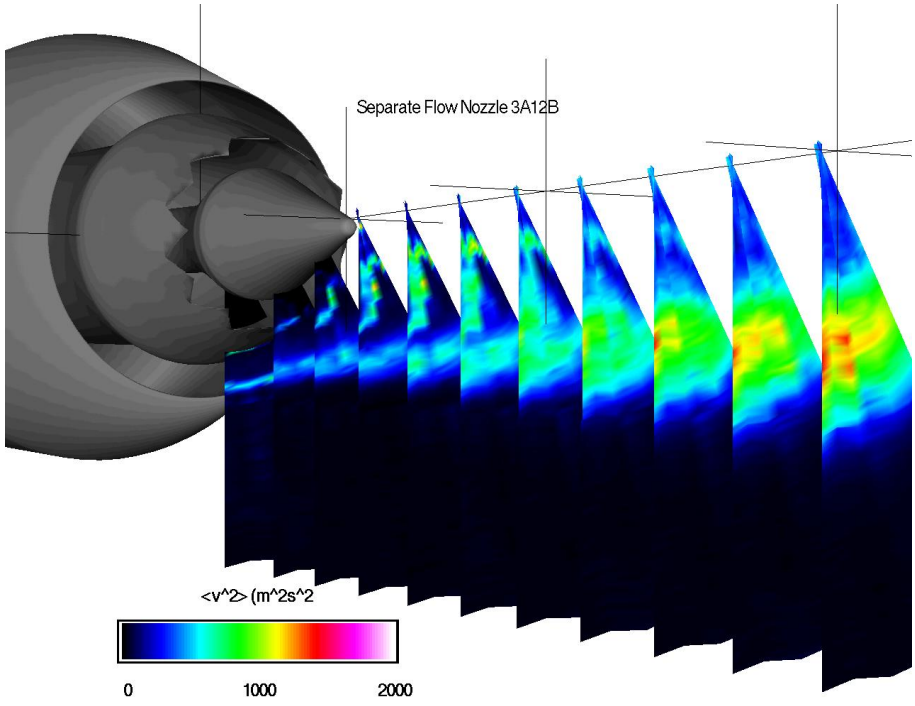

Figure 2.0.1.6 Model 3ab. Contour plots of variance in radial velocity (m^2/s^2). Slices taken at x = {0.047 0.132 0.199 0.267 0.334 0.401 0.468 0.535 0.603 0.670 0.737} meters.

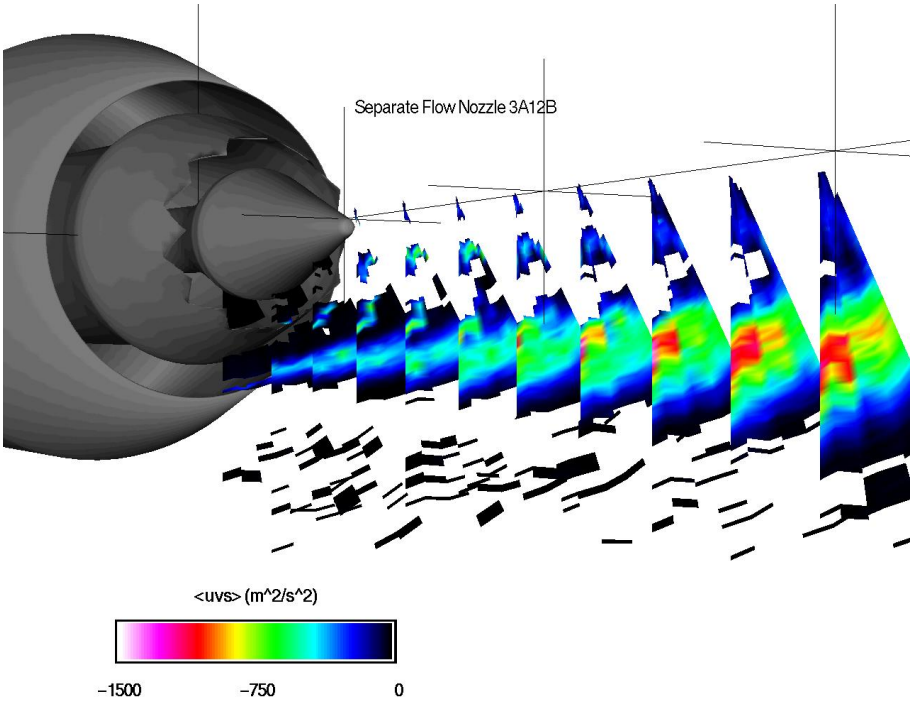

Figure 2.0.1.7 Model 3ab. Contour plots of unsteady Reynolds stress (m^2/s^2). Slices taken at x = {0.047 0.132 0.199 0.267 0.334 0.401 0.468 0.535 0.603 0.670 0.737} meters.

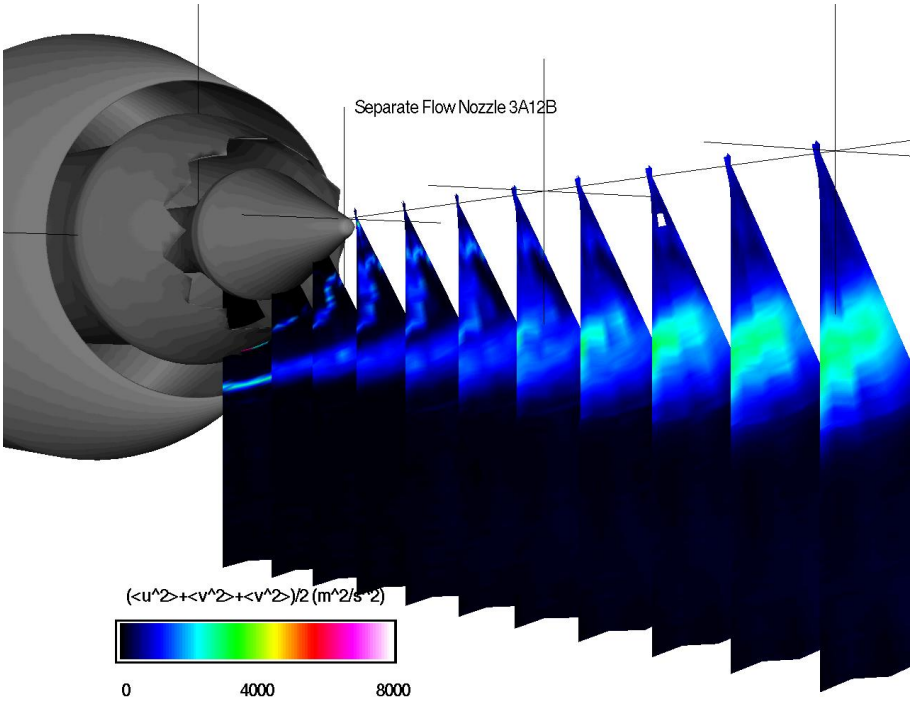

Figure 2.0.1.8 Model 3ab. Contour plots of turbulent kinetic energy (m^2/s^2). Slices taken at x = {0.047 0.132 0.199 0.267 0.334 0.401 0.468 0.535 0.603 0.670 0.737} meters.

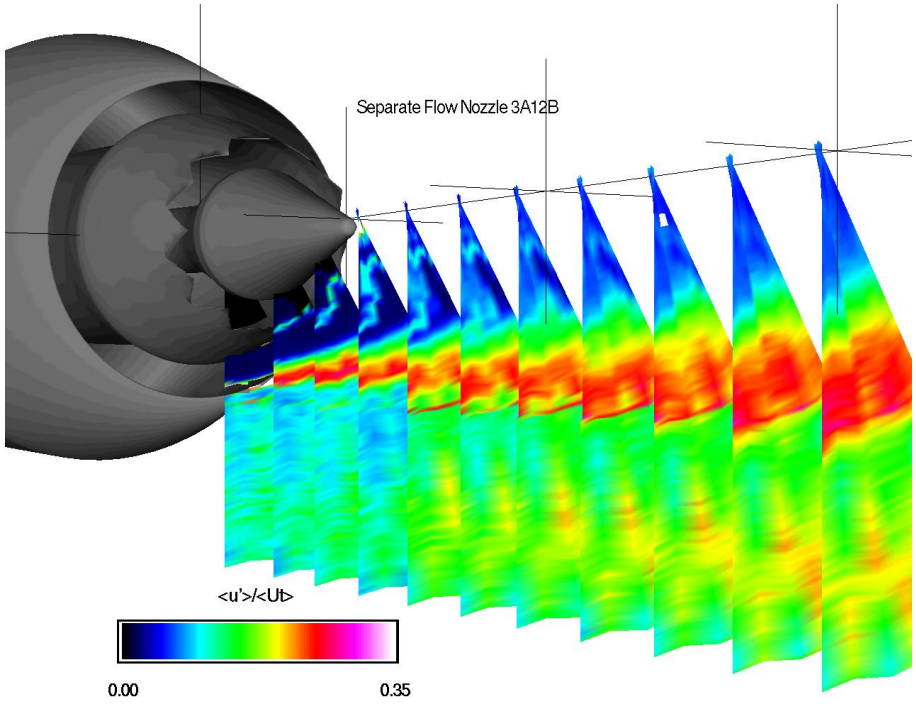

Figure 2.0.1.9 Model 3ab. Contour plots of axial turbulence intensity. Slices taken at x = {0.047 0.132 0.199 0.267 0.334 0.401 0.468 0.535 0.603 0.670 0.737} meters.

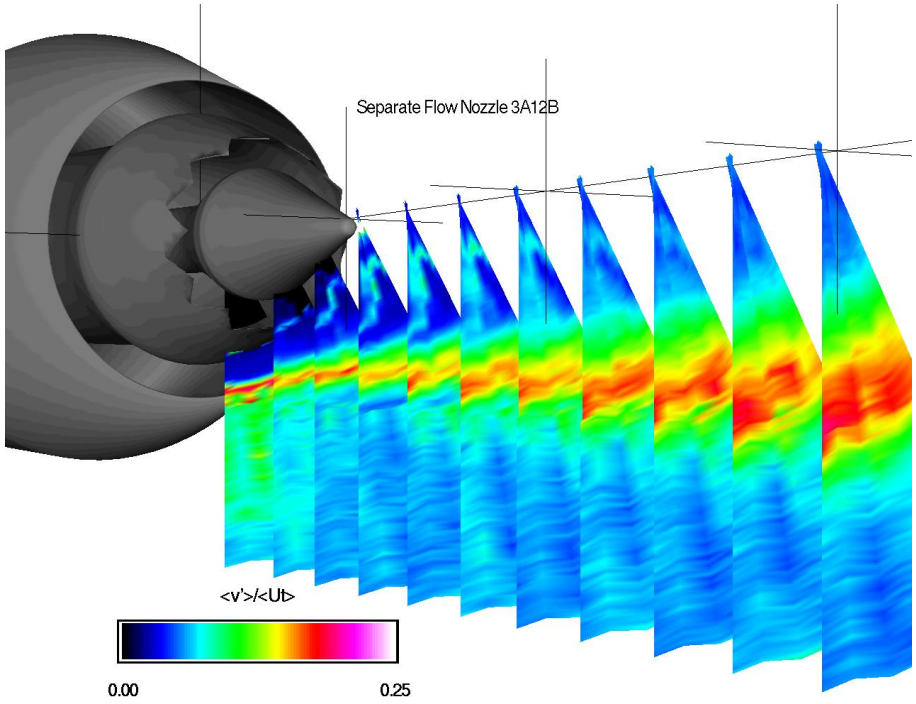

Figure 2.0.1.10 Model 3ab. Contour plots of radial turbulence intensity. Slices taken at x = {0.047 0.132 0.199 0.267 0.334 0.401 0.468 0.535 0.603 0.670 0.737} meters.

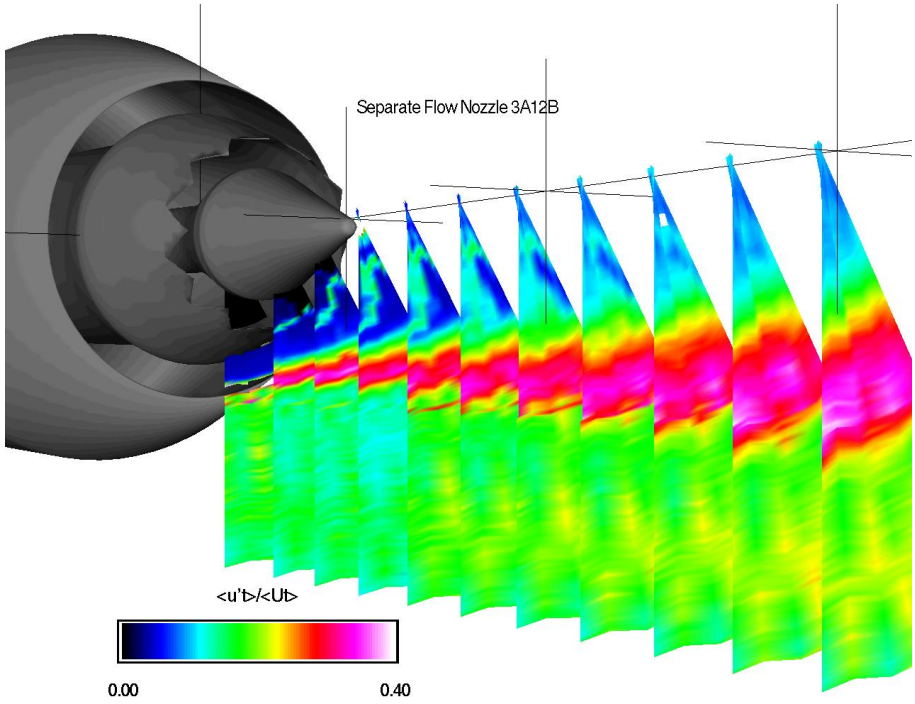

Figure 2.0.1.11 Model 3ab. Contour plots of turbulence intensity. Slices taken at x = {0.047 0.132 0.199 0.267 0.334 0.401 0.468 0.535 0.603 0.670 0.737} meters.

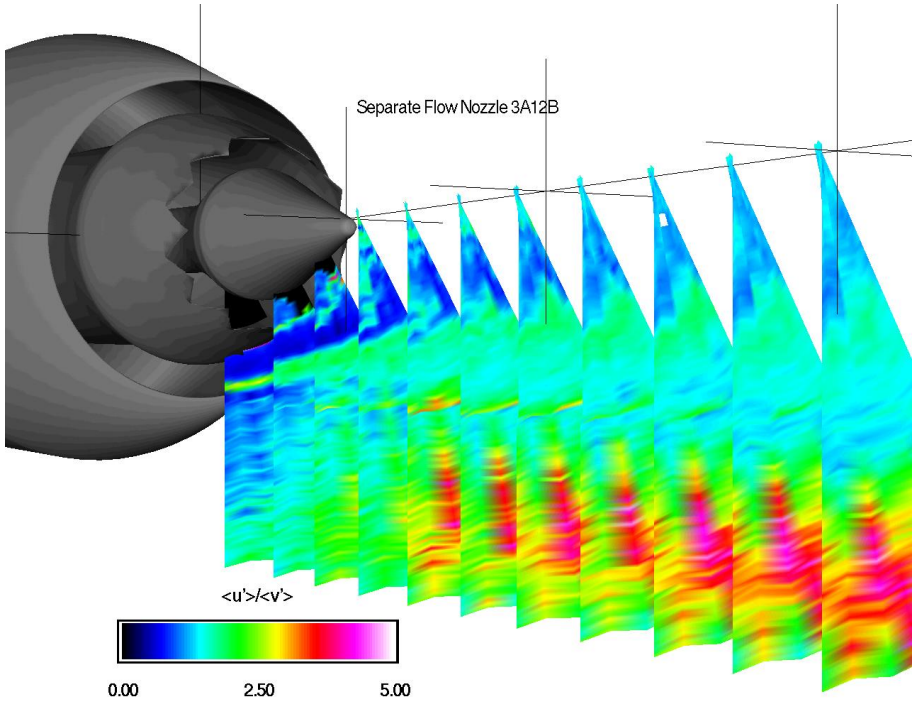

Figure 2.0.1.12 Model 3ab. Contour plots of ratio of axial to radial turbulence. Slices taken at x = {0.047 0.132 0.199 0.267 0.334 0.401 0.468 0.535 0.603 0.670 0.737} meters.

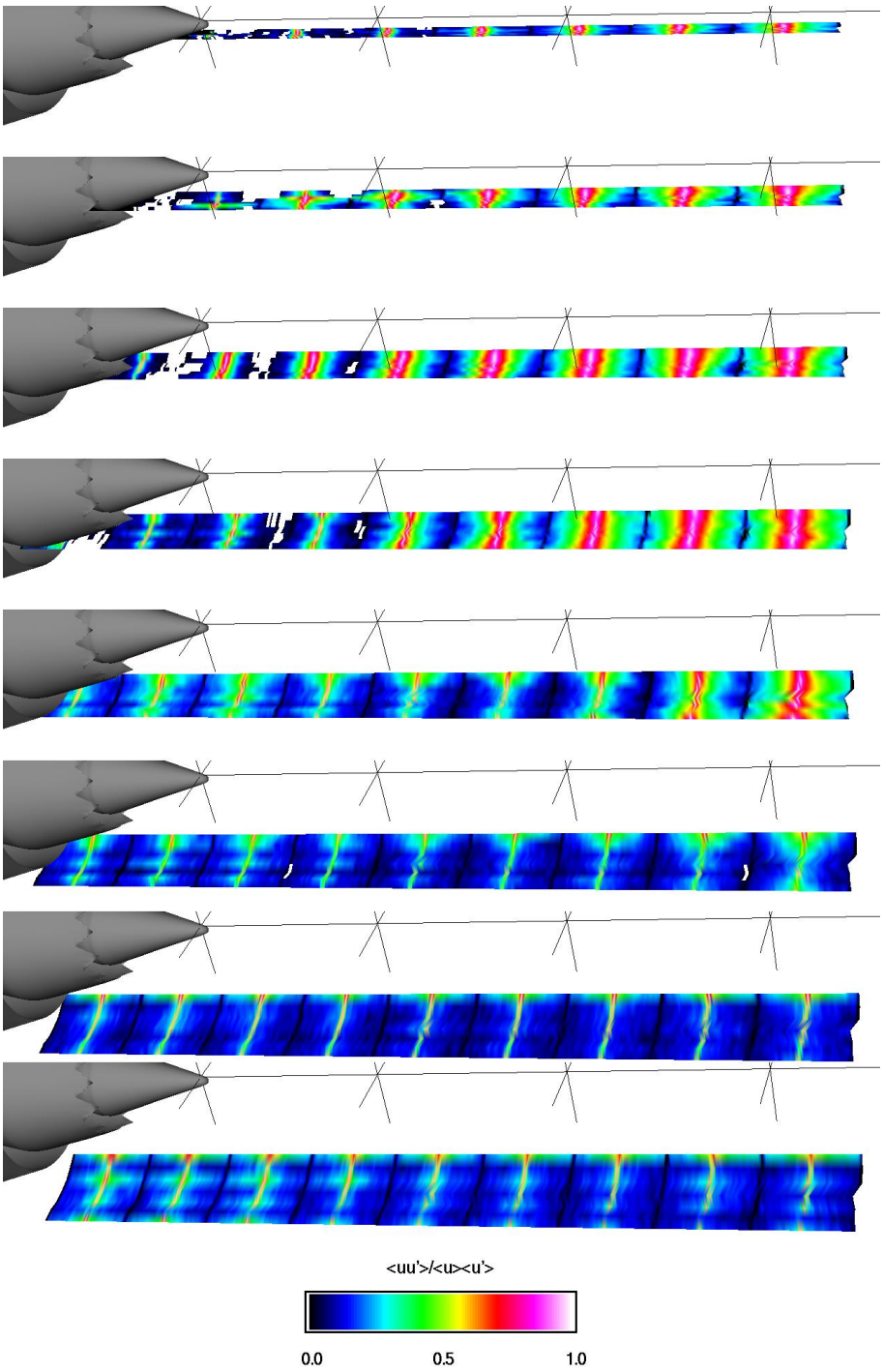

Figure 2.0.2.1 Model 3ab. Contour plots of u(xref)u(x). Slices taken at radius = {0.00 0.03 0.06 0.09 0.12 0.15 0.18 0.21 0.24} meters.

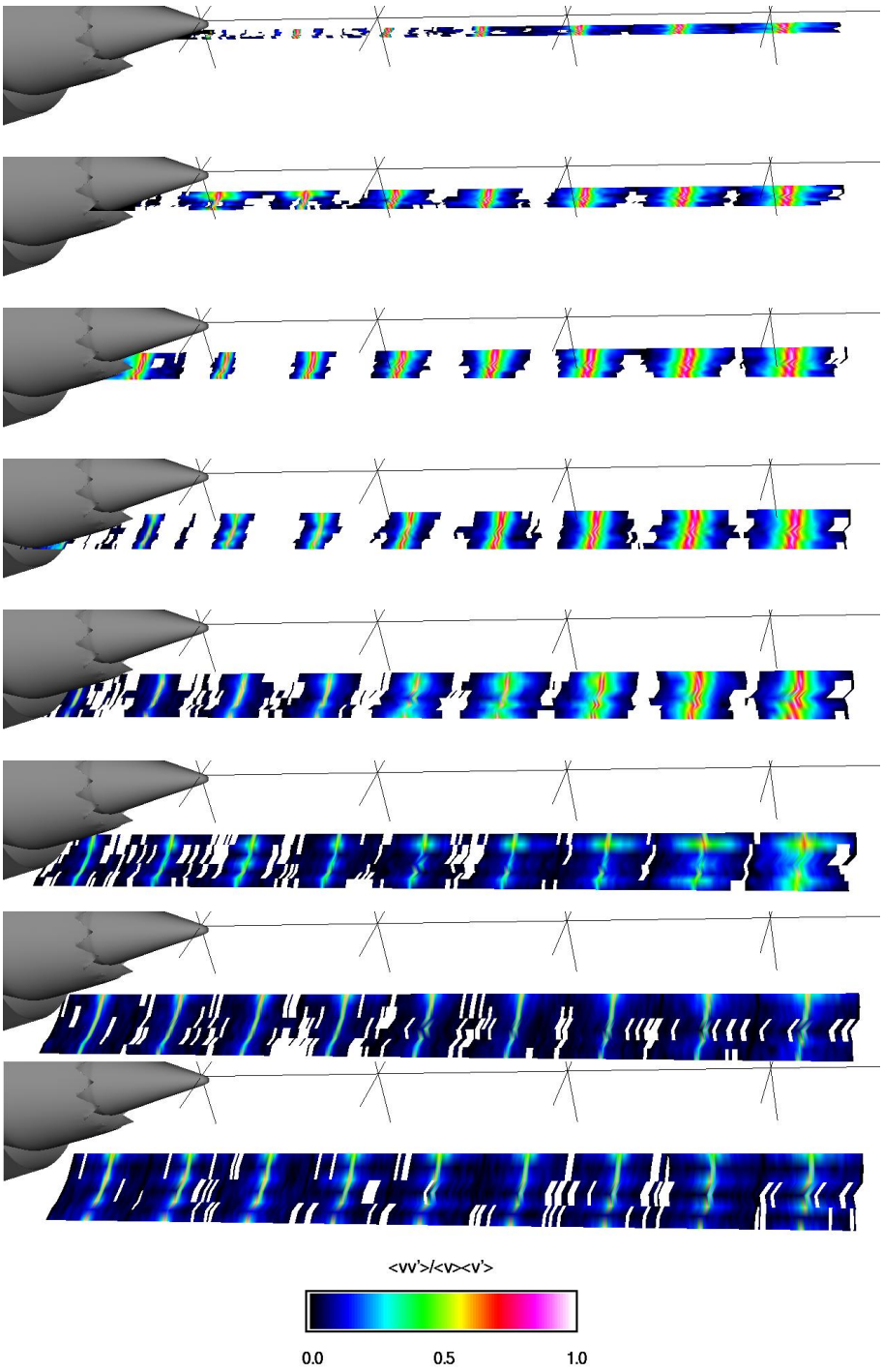

Figure 2.0.2.2 Model 3ab. Contour plots of v(xref)v(x). Slices taken at radius = {0.00 0.03 0.06 0.09 0.12 0.15 0.18 0.21 0.24} meters.

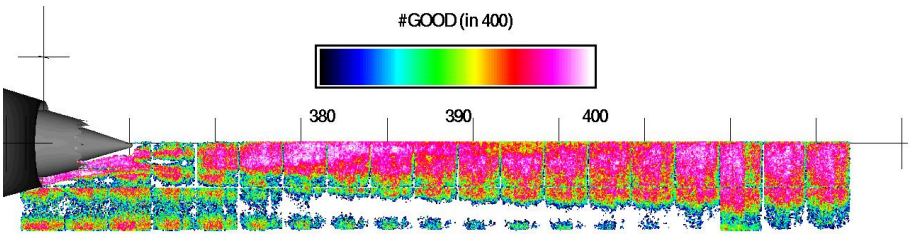

Figure 2.1.1.1 Model 3ab. Contour plots of data quality (#good out of 400). Slice taken at circumferential angle = 0°.

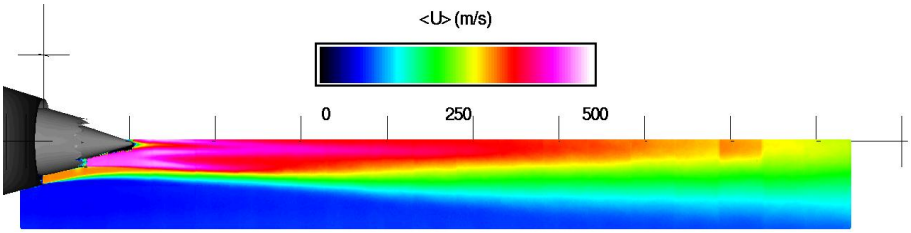

Figure 2.1.1.2 Model 3ab. Contour plots of time average axial velocity (m/s). Slice taken at circumferential angle = 0°.

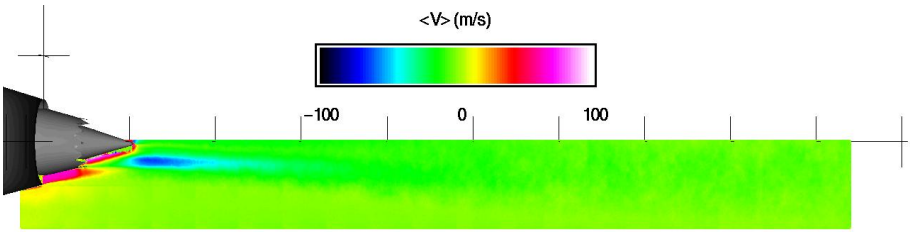

Figure 2.1.1.3 Model 3ab. Contour plots of time average radial velocity (m/s). Slice taken at circumferential angle = 0°.

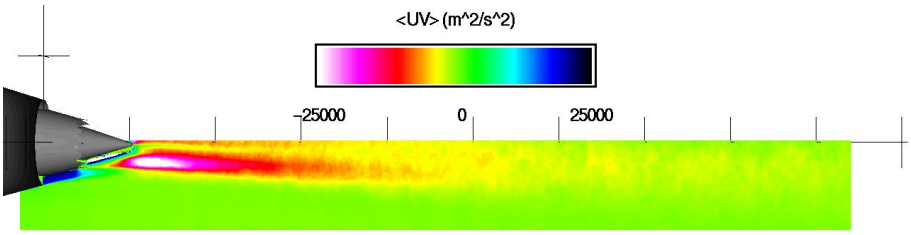

Figure 2.1.1.4 Model 3ab. Contour plots of time average Reynolds stress (m^2/s^2). Slice taken at circumferential angle = 0°.

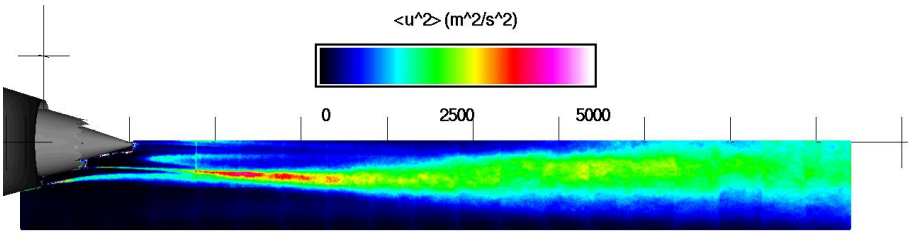

Figure 2.1.1.5 Model 3ab. Contour plots of variance of axial velocity (m^2/s^2). Slice taken at circumferential angle = 0°.

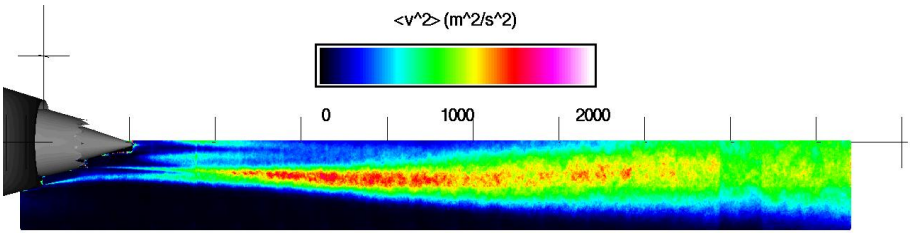

Figure 2.1.1.6 Model 3ab. Contour plots of variance in radial velocity (m^2/s^2). Slice taken at circumferential angle = 0°.

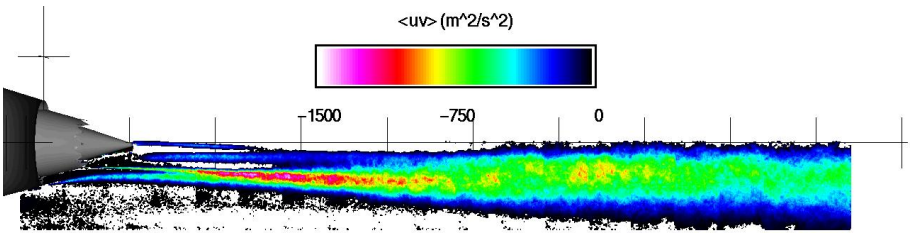

Figure 2.1.1.7 Model 3ab. Contour plots of unsteady Reynolds stress (m^2/s^2). Slice taken at circumferential angle = 0°.

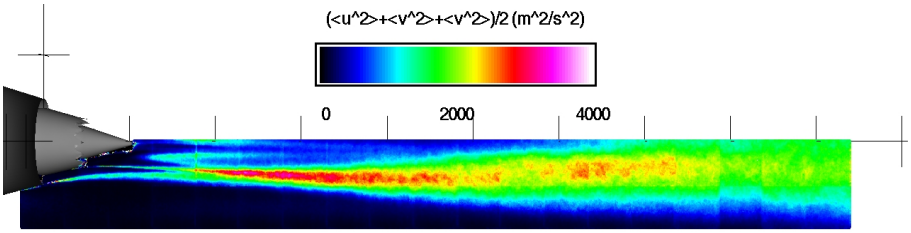

Figure 2.1.1.8 Model 3ab. Contour plots of turbulent kinetic energy (m^2/s^2). Slice taken at circumferential angle = 0°.

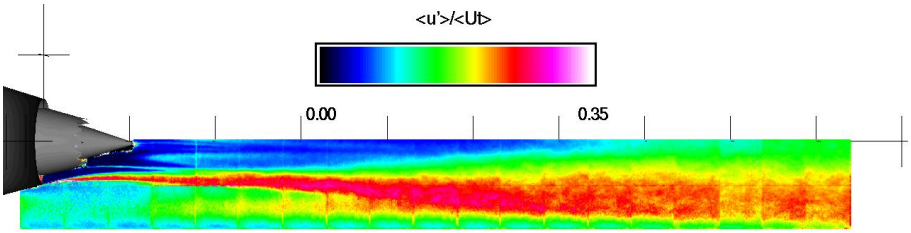

Figure 2.1.1.9 Model 3ab. Contour plots of axial turbulence intensity. Slice taken at circumferential angle = 0°.

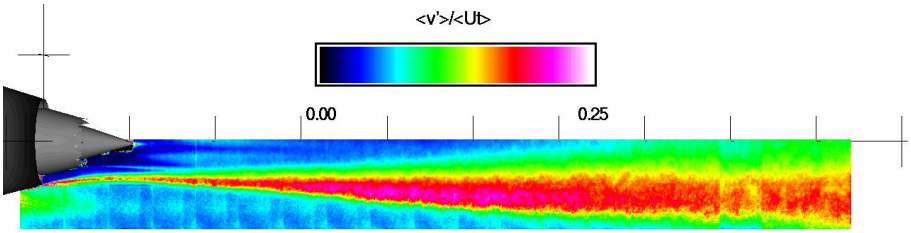

Figure 2.1.1.10 Model 3ab. Contour plots of radial turbulence intensity. Slice taken at circumferential angle = 0°.

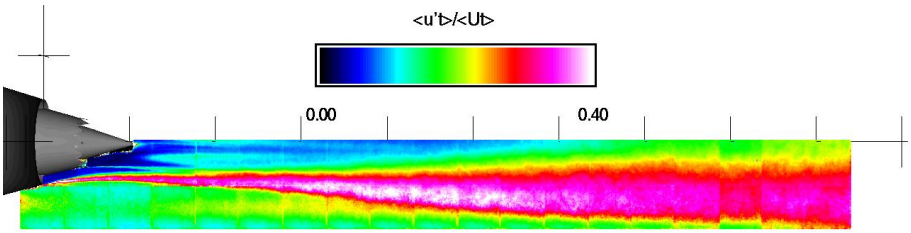

Figure 2.1.1.11 Model 3ab. Contour plots of turbulence intensity. Slice taken at circumferential angle = 0°.

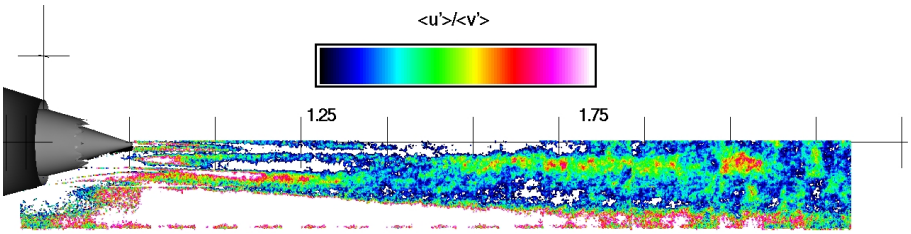

Figure 2.1.1.12 Model 3ab. Contour plots of ratio of axial to radial turbulence. Slice taken at circumferential angle = 0°.

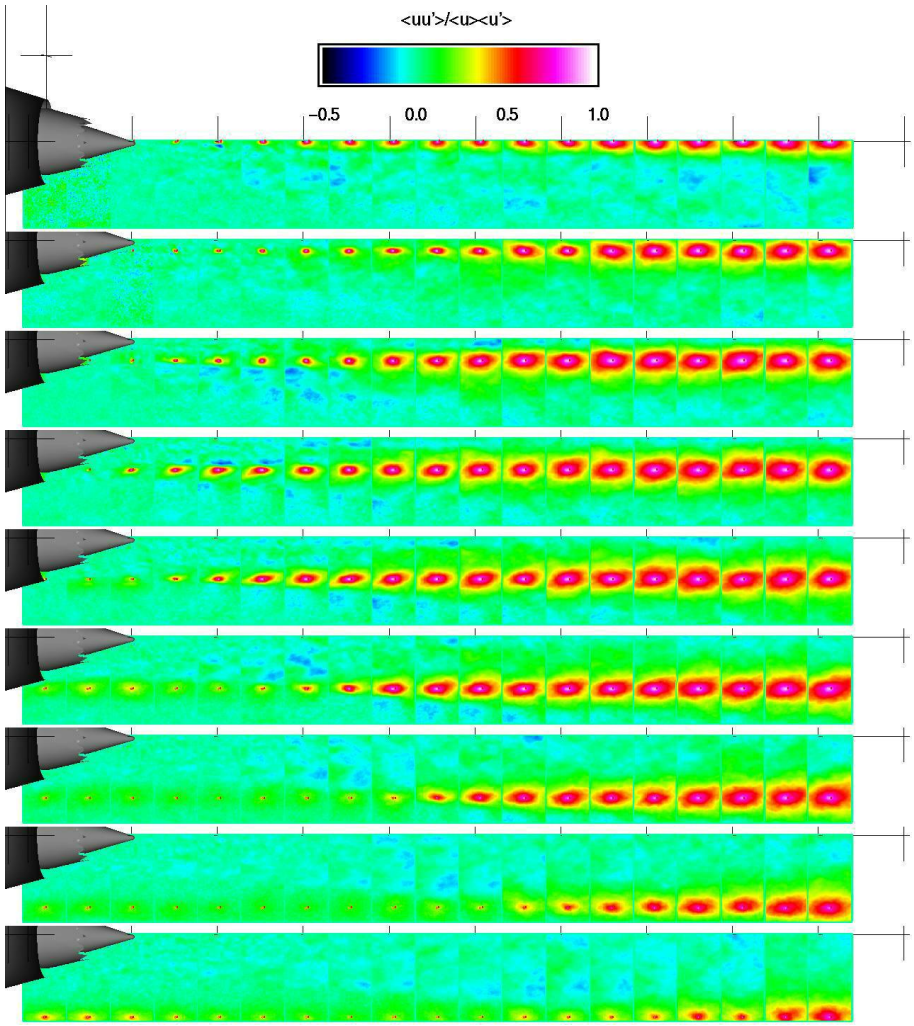

Figure 2.1.2.1 Model 3ab. Contour plots of u(xref)u(x). Slice taken at circumferential angle = 0°.

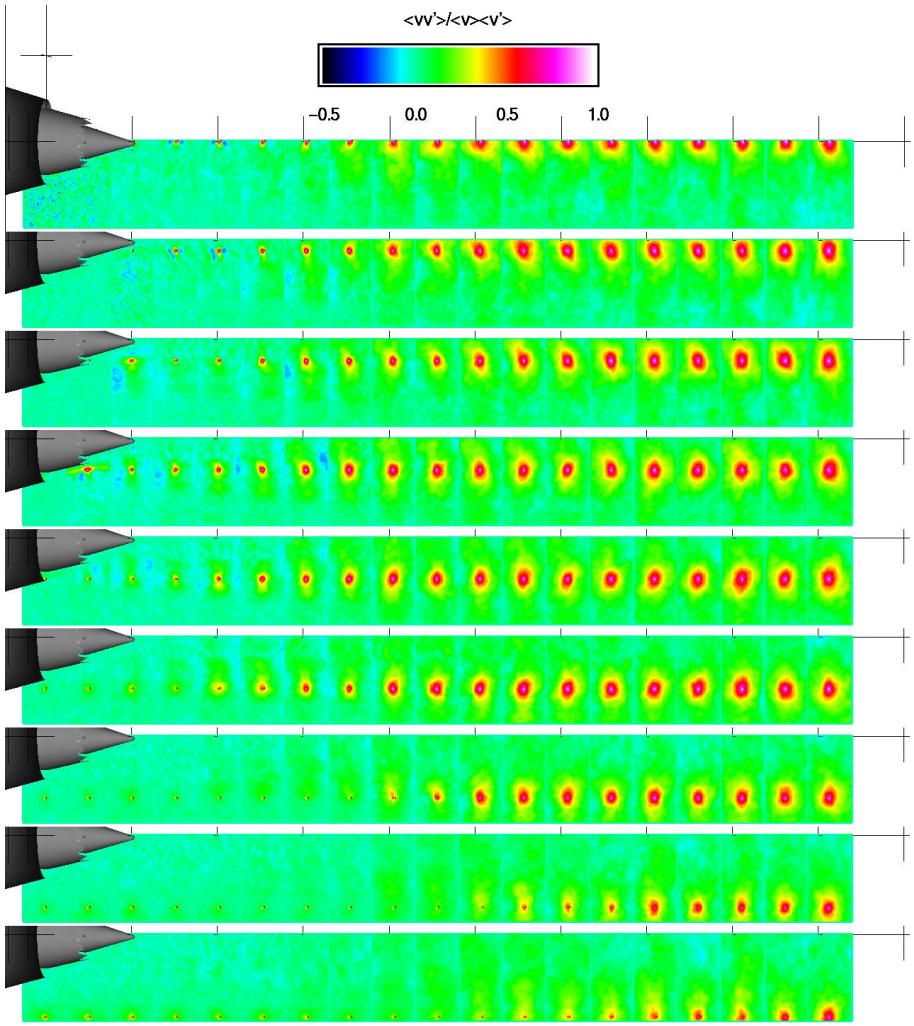

Figure 2.1.2.2 Model 3ab. Contour plots of v(xref)v(x). Slice taken at circumferential angle = 0°.

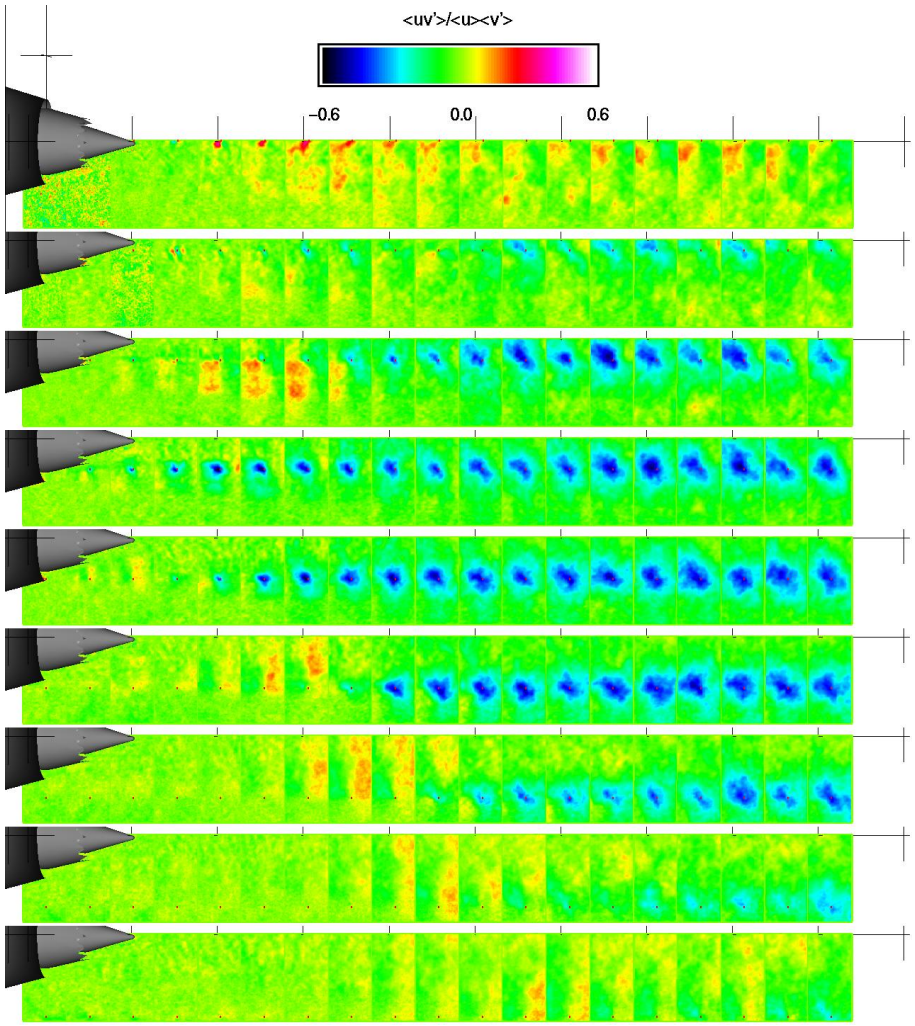

Figure 2.1.2.3 Model 3ab. Contour plots of u(xref)v(x). Slice taken at circumferential angle = 0°.

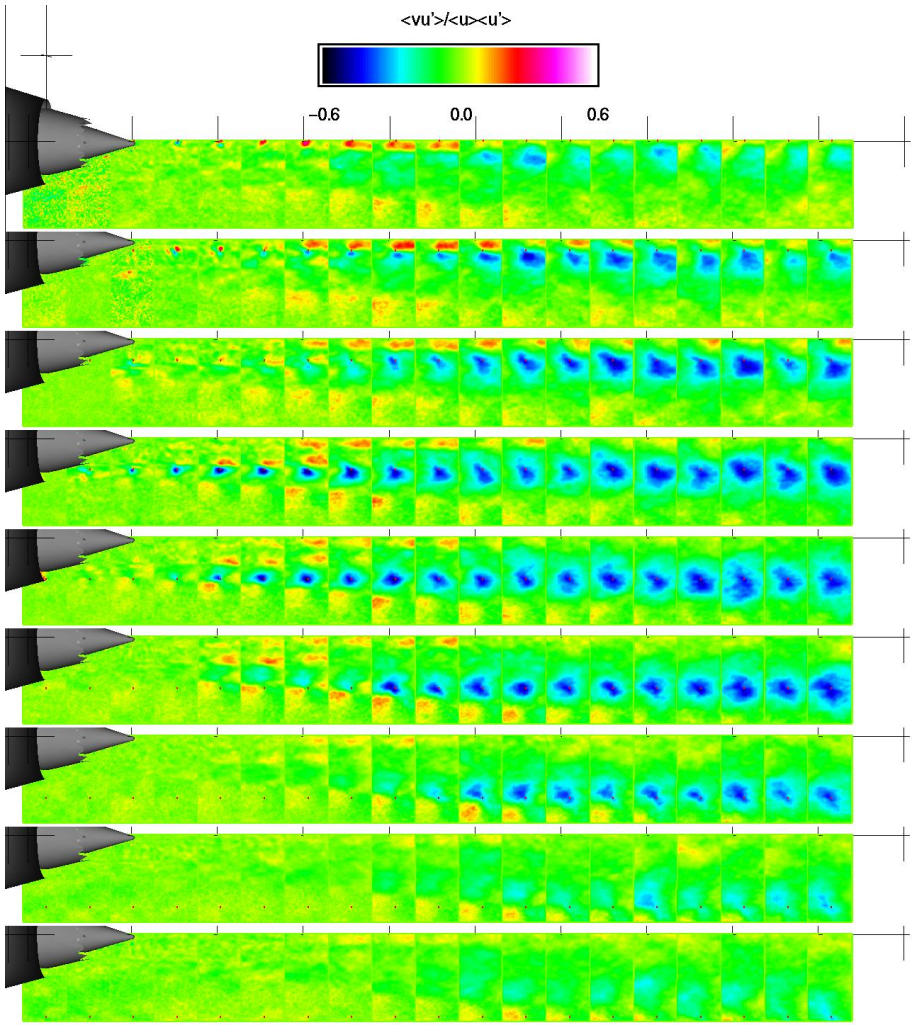

Figure 2.1.2.4 Model 3ab. Contour plots of v(xref)u(x). Slice taken at circumferential angle = 0°.

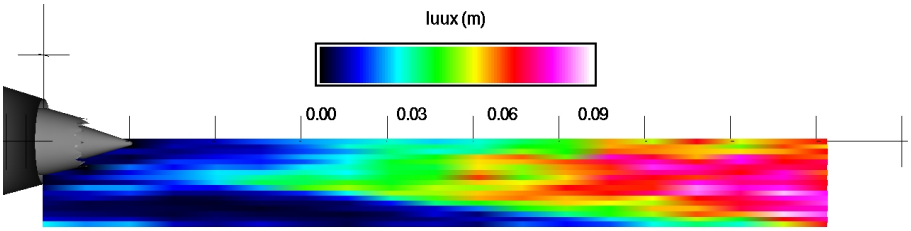

Figure 2.1.3.1 Model 3ab. Contour plots of Luu(x). Slice taken at circumferential angle = 0°.

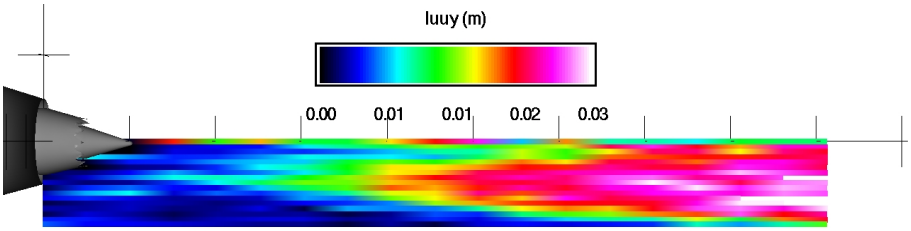

Figure 2.1.3.2 Model 3ab. Contour plots of Luu(y). Slice taken at circumferential angle = 0°.

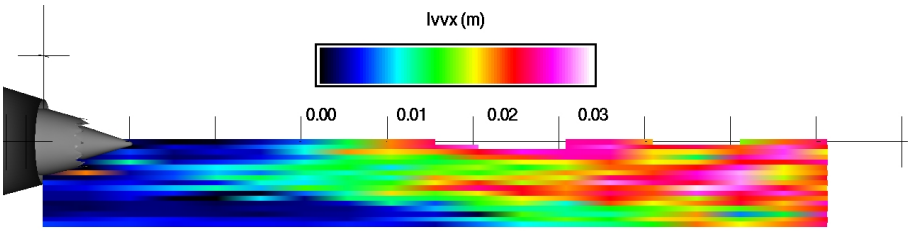

Figure 2.1.3.3 Model 3ab. Contour plots of Lvv(x). Slice taken at circumferential angle = 0°.

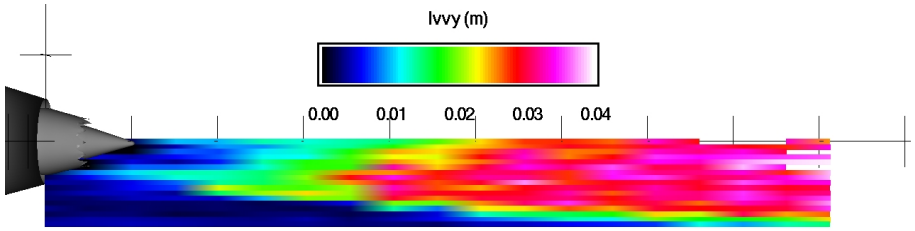

Figure 2.1.3.4 Model 3ab. Contour plots of Lvv(y). Slice taken at circumferential angle = 0°.

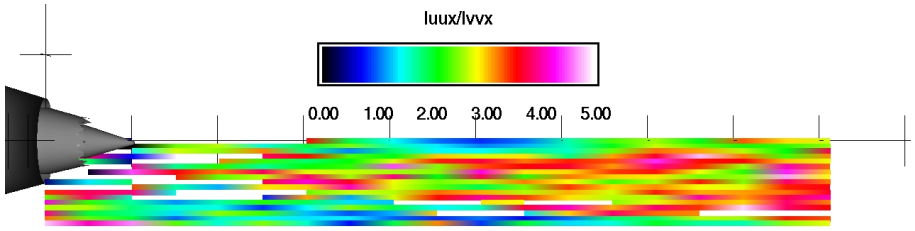

Figure 2.1.3.5 Model 3ab. Contour plots of Luu(x)/Lvv(x). Slice taken at circumferential angle = 0°.

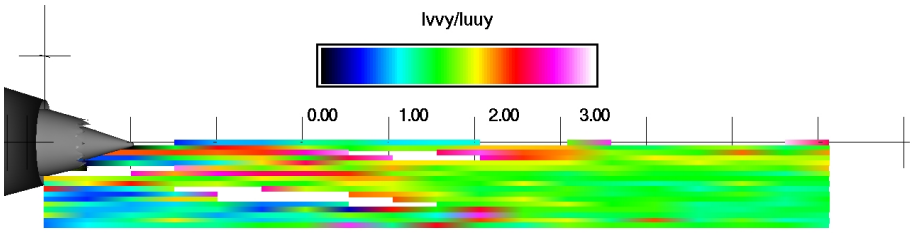

Figure 2.1.3.6 Model 3ab. Contour plots of Lvv(y)/Luu(y). Slice taken at circumferential angle = 0°.

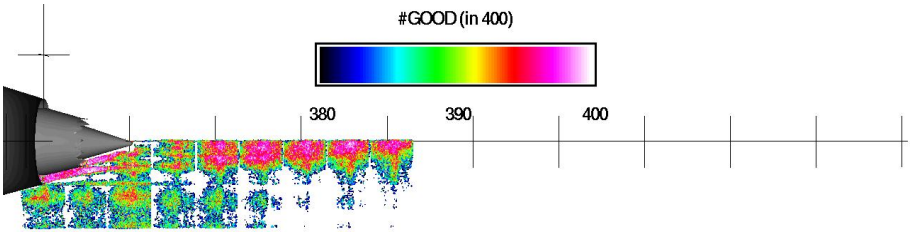

Figure 2.2.1.1 Model 3ab. Contour plots of data quality (#good out of 400). Slice taken at circumferential angle = 5°.

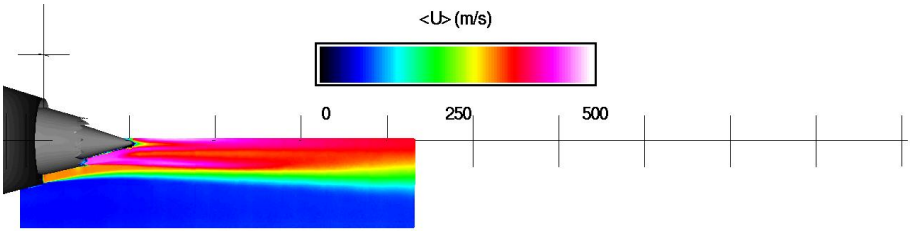

Figure 2.2.1.2 Model 3ab. Contour plots of time average axial velocity (m/s). Slice taken at circumferential angle = 5°.

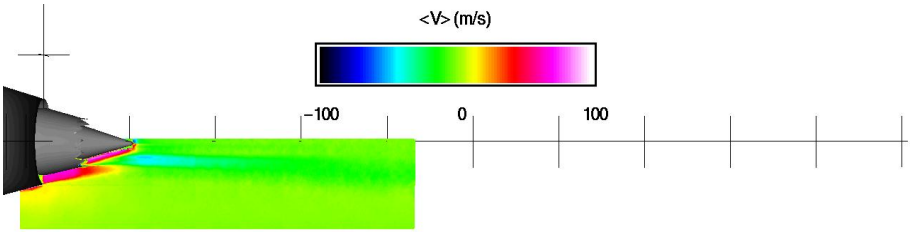

Figure 2.2.1.3 Model 3ab. Contour plots of time average radial velocity (m/s). Slice taken at circumferential angle = 5°.

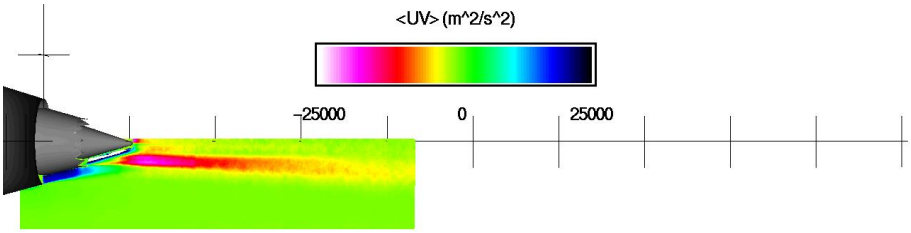

Figure 2.2.1.4 Model 3ab. Contour plots of time average Reynolds stress (m^2/s^2). Slice taken at circumferential angle = 5°.

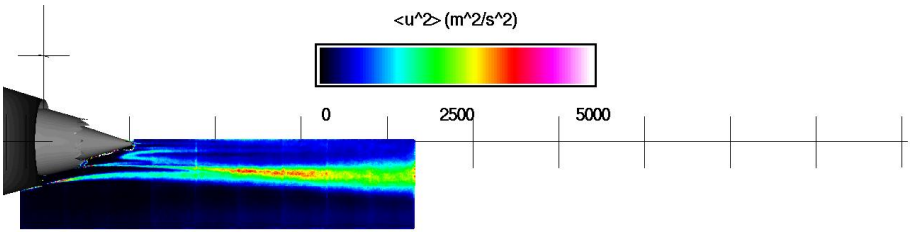

Figure 2.2.1.5 Model 3ab. Contour plots of variance of axial velocity (m^2/s^2). Slice taken at circumferential angle = 5°.

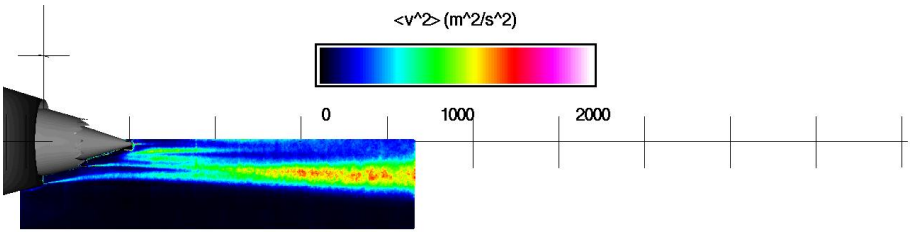

Figure 2.2.1.6 Model 3ab. Contour plots of variance in radial velocity (m^2/s^2). Slice taken at circumferential angle = 5°.

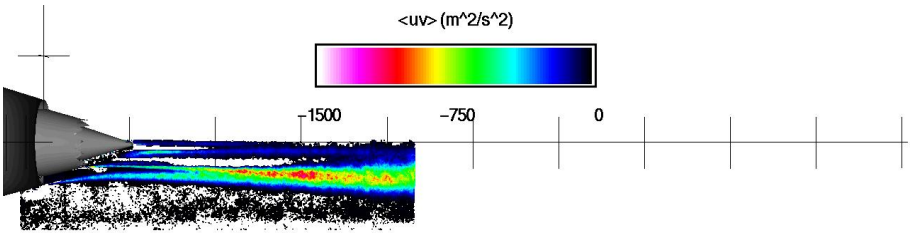

Figure 2.2.1.7 Model 3ab. Contour plots of unsteady Reynolds stress (m^2/s^2). Slice taken at circumferential angle = 5°.

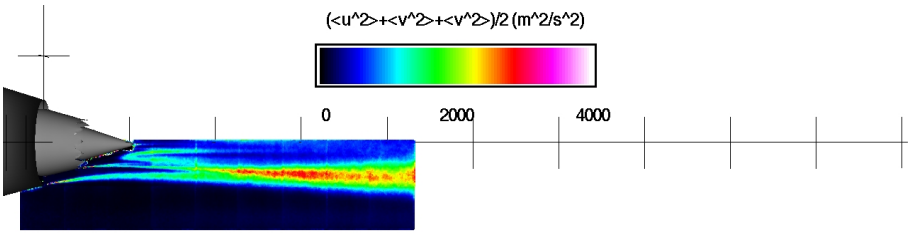

Figure 2.2.1.8 Model 3ab. Contour plots of turbulent kinetic energy (m^2/s^2). Slice taken at circumferential angle = 5°.

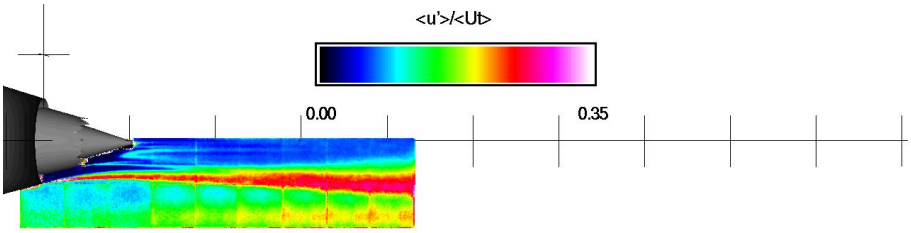

Figure 2.2.1.9 Model 3ab. Contour plots of axial turbulence intensity. Slice taken at circumferential angle = 5°.

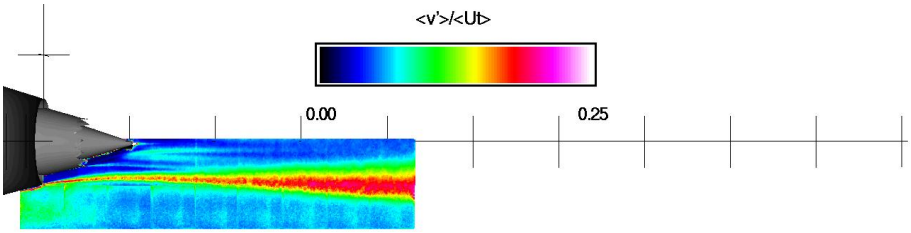

Figure 2.2.1.10 Model 3ab. Contour plots of radial turbulence intensity. Slice taken at circumferential angle = 5°.

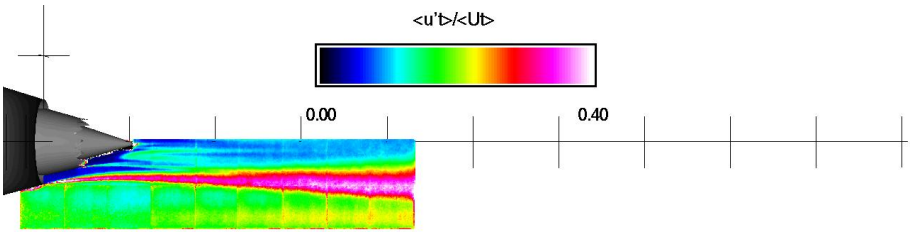

Figure 2.2.1.11 Model 3ab. Contour plots of turbulence intensity. Slice taken at circumferential angle = 5°.

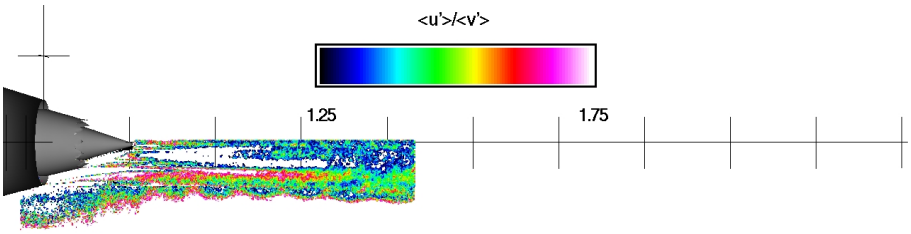

Figure 2.2.1.12 Model 3ab. Contour plots of ratio of axial to radial turbulence. Slice taken at circumferential angle = 5°.

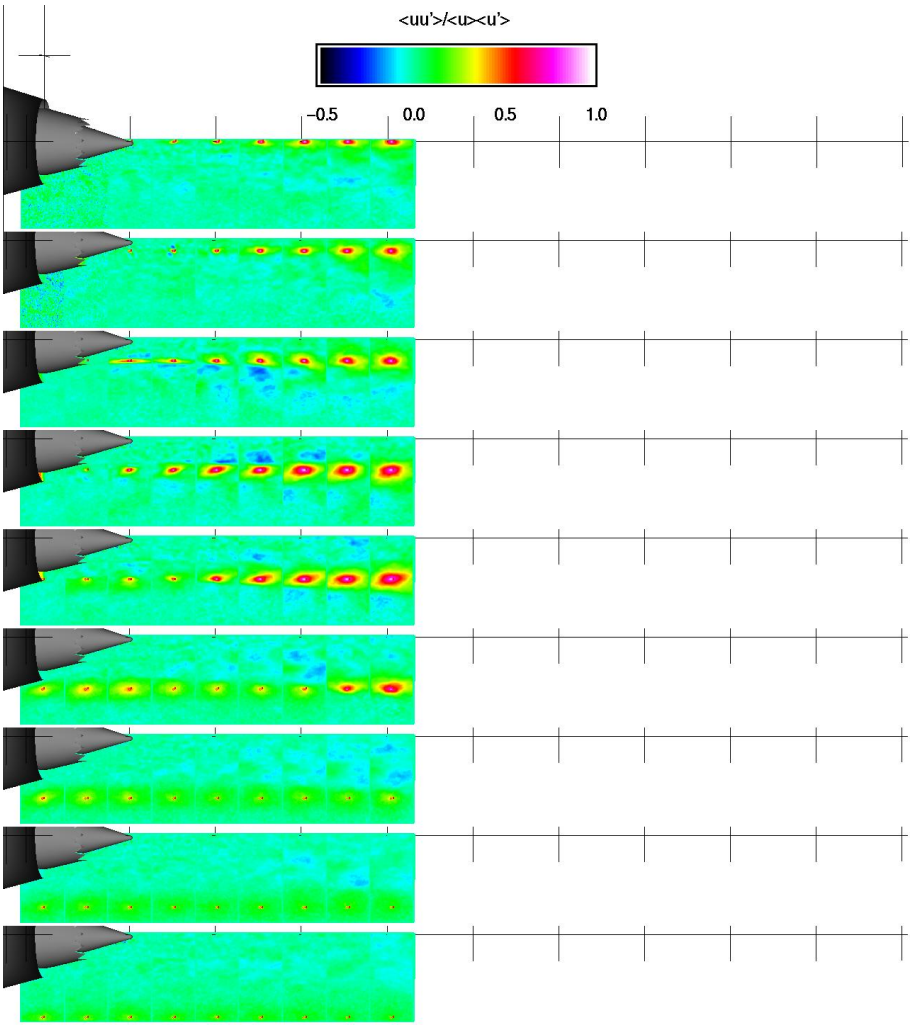

Figure 2.2.2.1 Model 3ab. Contour plots of u(xref)u(x). Slice taken at circumferential angle = 5°.

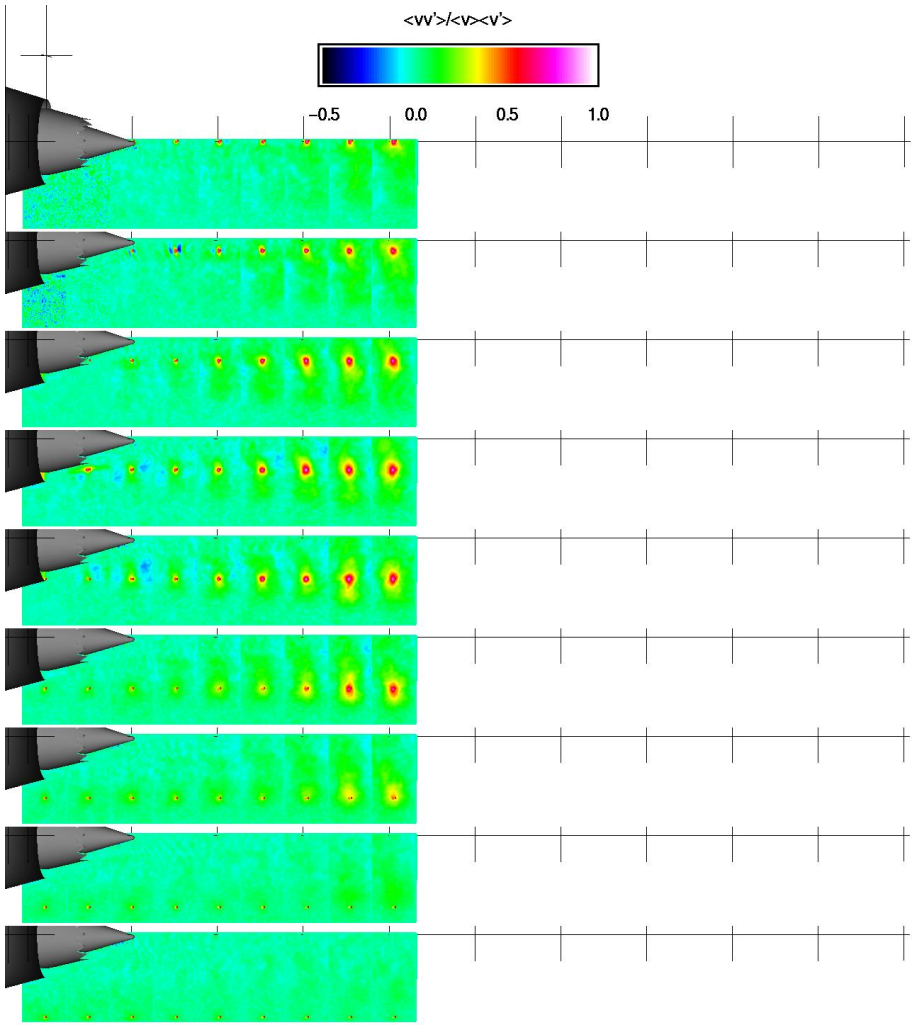

Figure 2.2.2.2 Model 3ab. Contour plots of v(xref)v(x). Slice taken at circumferential angle = 5°.

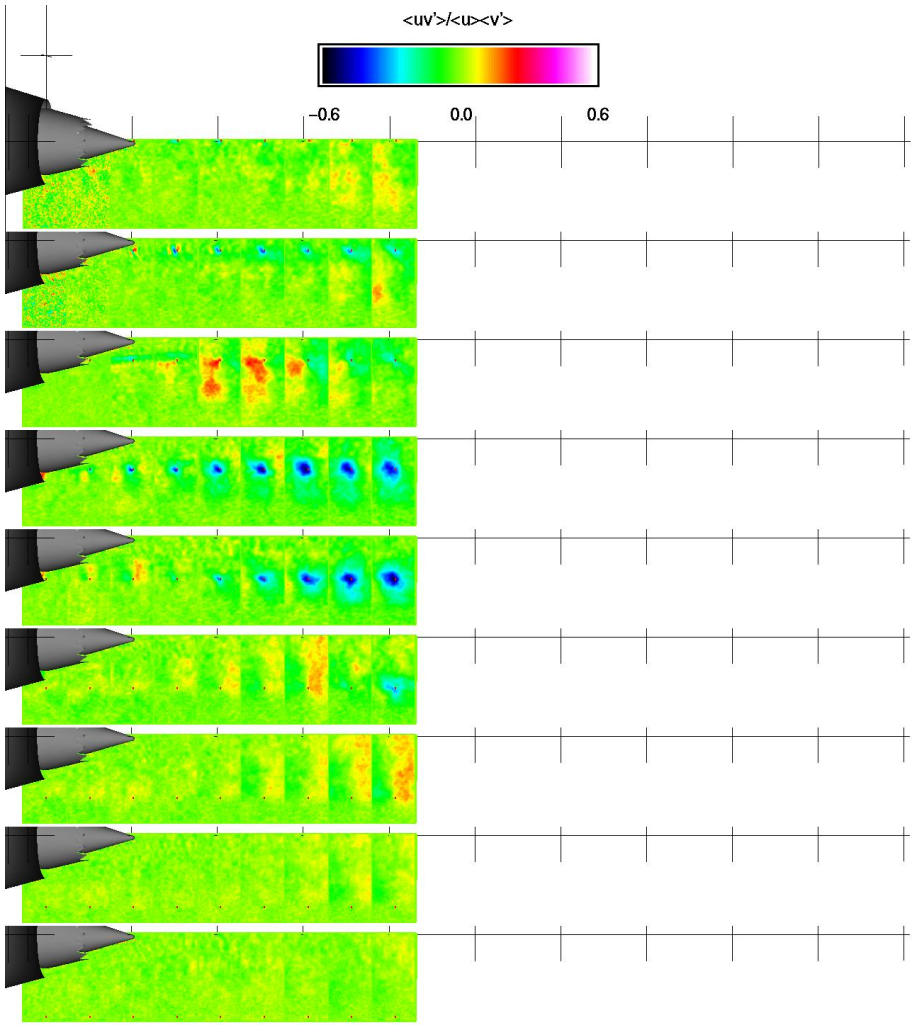

Figure 2.2.2.3 Model 3ab. Contour plots of u(xref)v(x). Slice taken at circumferential angle = 5°.

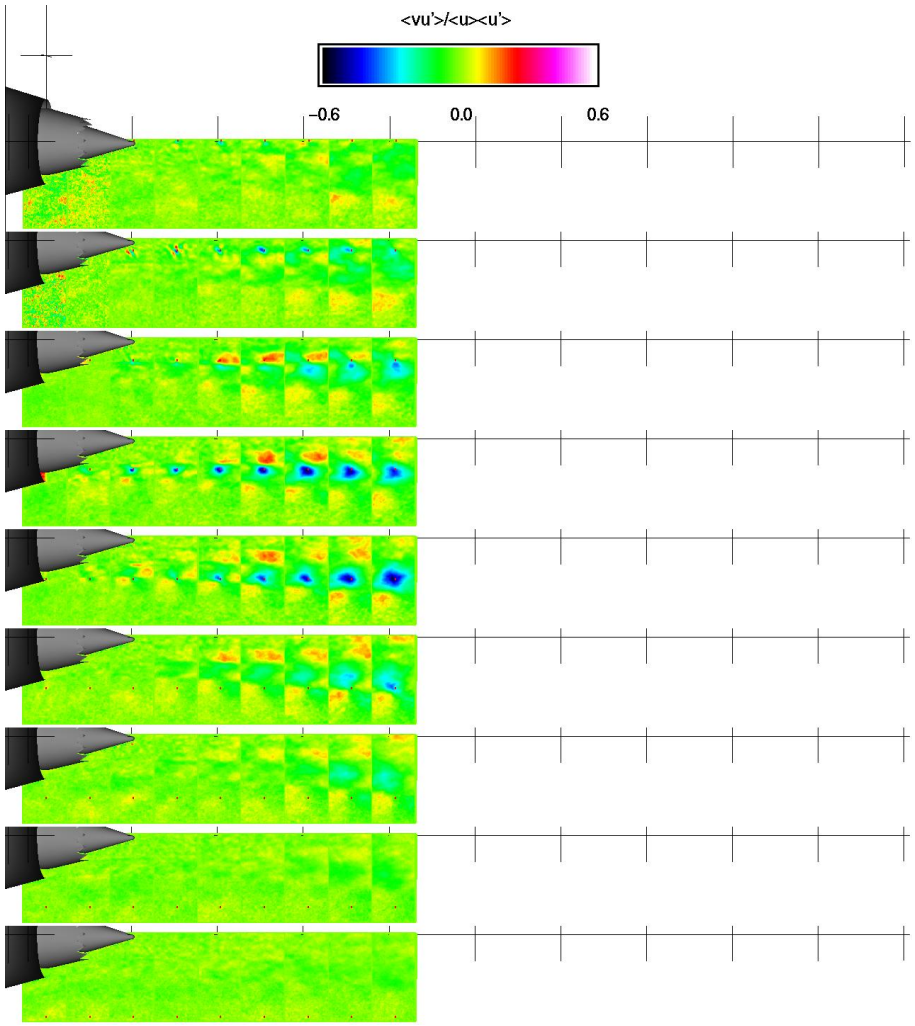

Figure 2.2.2.4 Model 3ab. Contour plots of v(xref)u(x). Slice taken at circumferential angle = 5°.

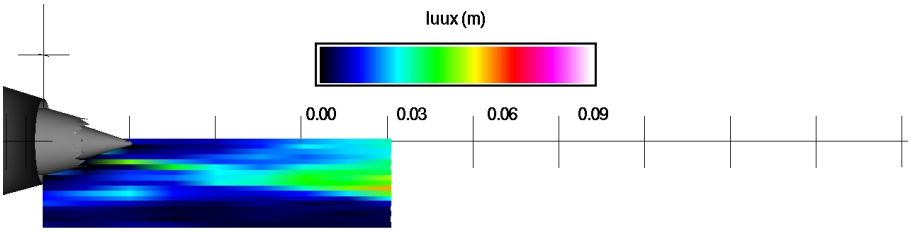

Figure 2.2.3.1 Model 3ab. Contour plots of Luu(x). Slice taken at circumferential angle = 5°.

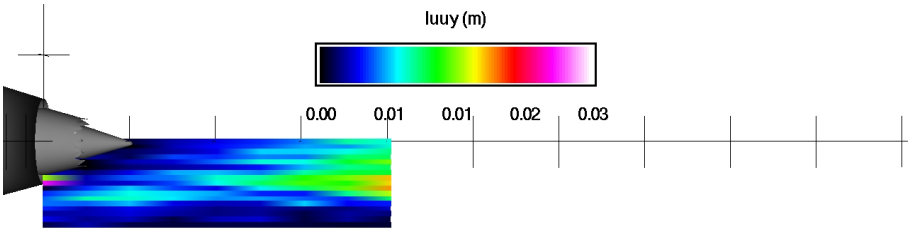

Figure 2.2.3.2 Model 3ab. Contour plots of Luu(y). Slice taken at circumferential angle = 5°.

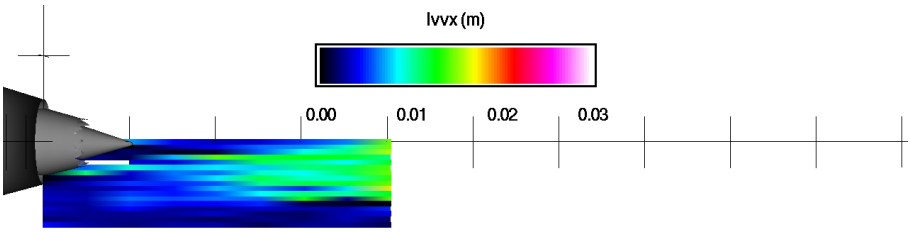

Figure 2.2.3.3 Model 3ab. Contour plots of Lvv(x). Slice taken at circumferential angle = 5°.

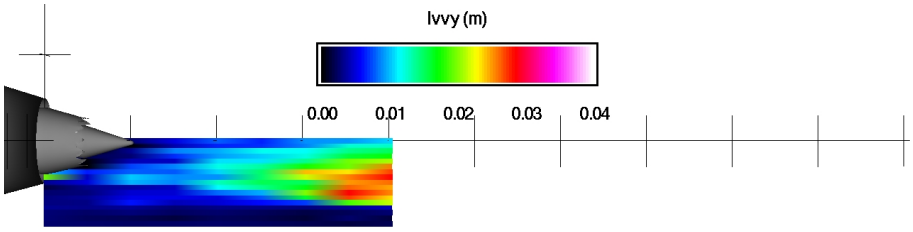

Figure 2.2.3.4 Model 3ab. Contour plots of Lvv(y). Slice taken at circumferential angle = 5°.

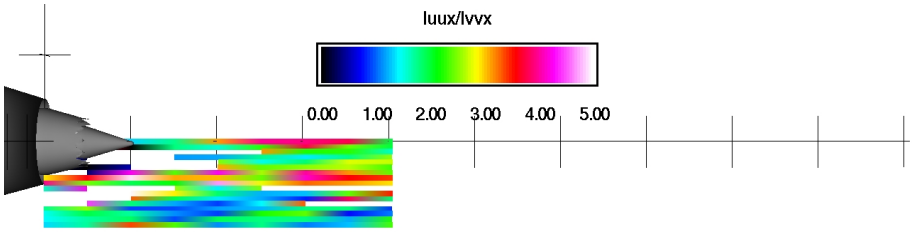

Figure 2.2.3.5 Model 3ab. Contour plots of Luu(x)/Lvv(x). Slice taken at circumferential angle = 5°.

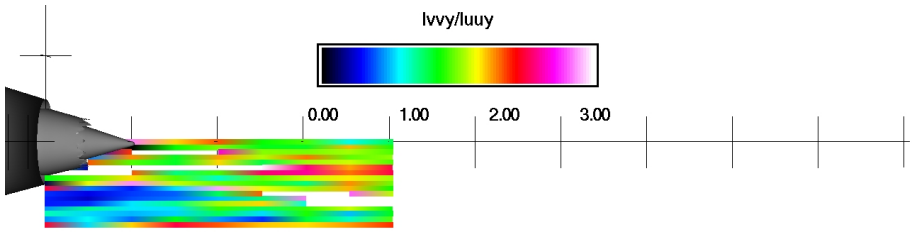

Figure 2.2.3.6 Model 3ab. Contour plots of Lvv(y)/Luu(y). Slice taken at circumferential angle = 5°.

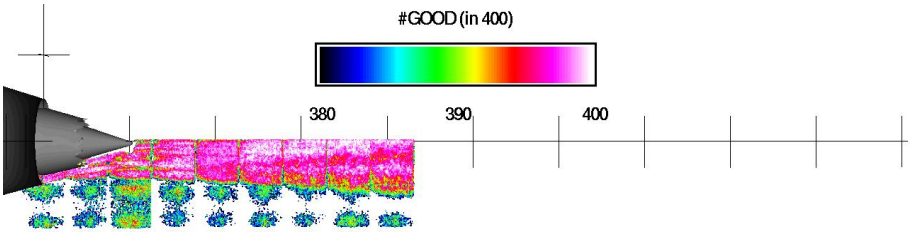

Figure 2.3.1.1 Model 3ab. Contour plots of data quality (#good out of 400). Slice taken at circumferential angle = 10°.

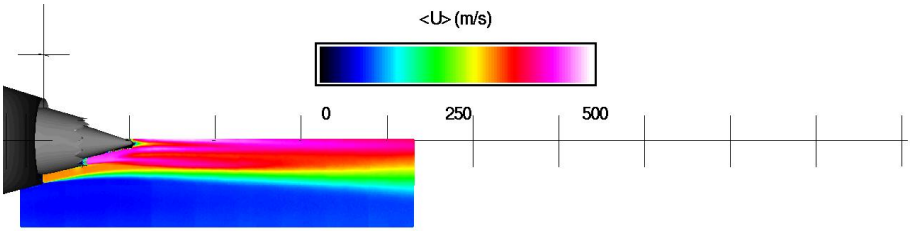

Figure 2.3.1.2 Model 3ab. Contour plots of time average axial velocity (m/s). Slice taken at circumferential angle = 10°.

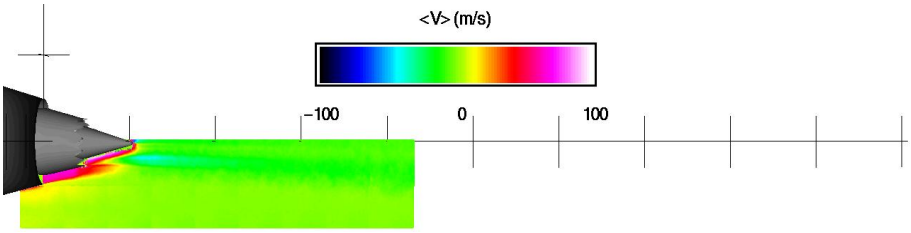

Figure 2.3.1.3 Model 3ab. Contour plots of time average radial velocity (m/s). Slice taken at circumferential angle = 10°.

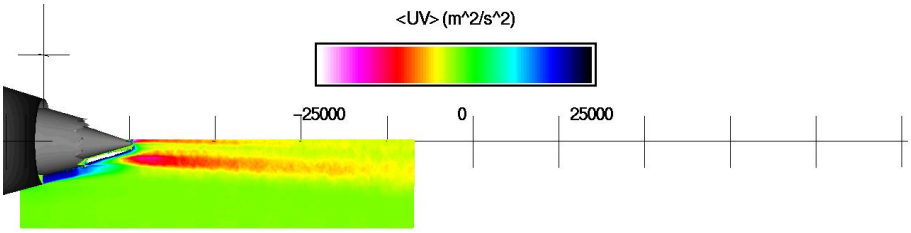

Figure 2.3.1.4 Model 3ab. Contour plots of time average Reynolds stress (m^2/s^2). Slice taken at circumferential angle = 10°.

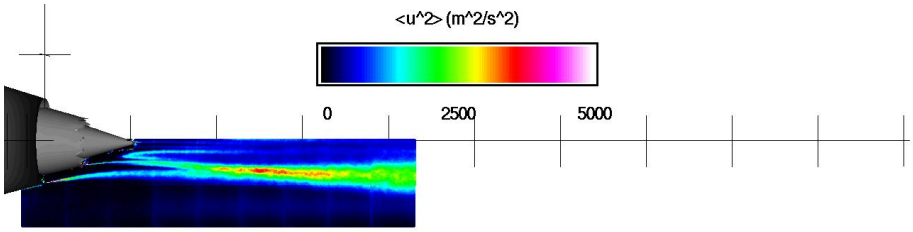

Figure 2.3.1.5 Model 3ab. Contour plots of variance of axial velocity (m^2/s^2). Slice taken at circumferential angle = 10°.

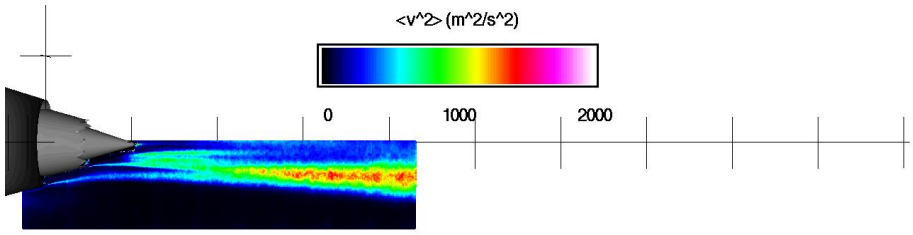

Figure 2.3.1.6 Model 3ab. Contour plots of variance in radial velocity (m^2/s^2). Slice taken at circumferential angle = 10°.

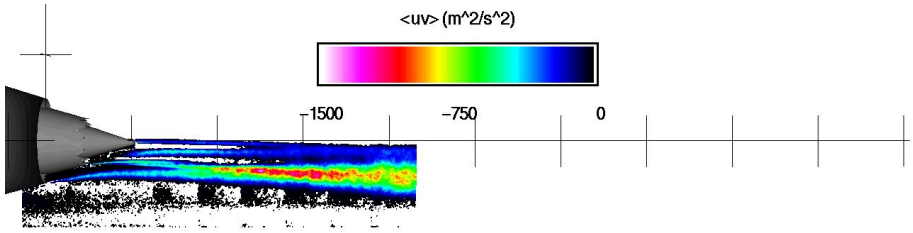

Figure 2.3.1.7 Model 3ab. Contour plots of unsteady Reynolds stress (m^2/s^2). Slice taken at circumferential angle = 10°.

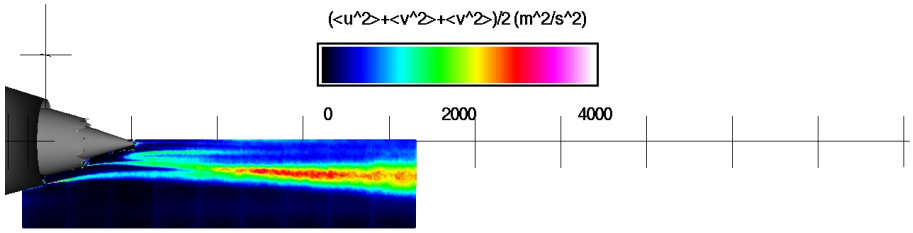

Figure 2.3.1.8 Model 3ab. Contour plots of turbulent kinetic energy (m^2/s^2). Slice taken at circumferential angle = 10°.

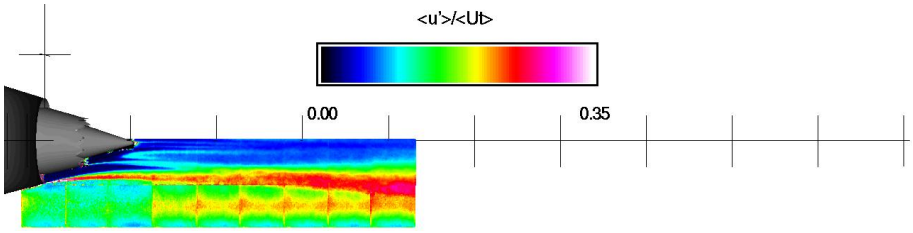

Figure 2.3.1.9 Model 3ab. Contour plots of axial turbulence intensity. Slice taken at circumferential angle = 10°.

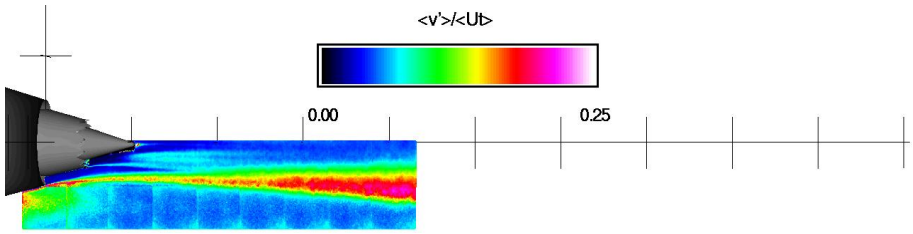

Figure 2.3.1.10 Model 3ab. Contour plots of radial turbulence intensity. Slice taken at circumferential angle = 10°.

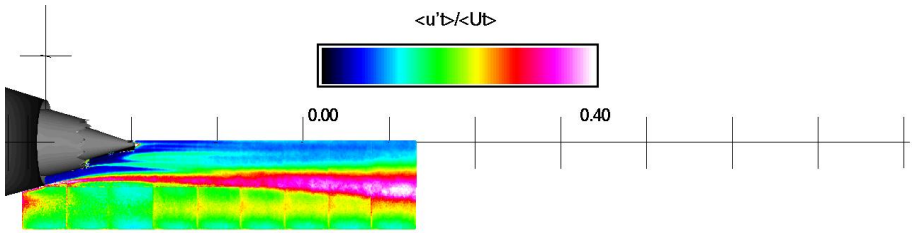

Figure 2.3.1.11 Model 3ab. Contour plots of turbulence intensity. Slice taken at circumferential angle = 10°.

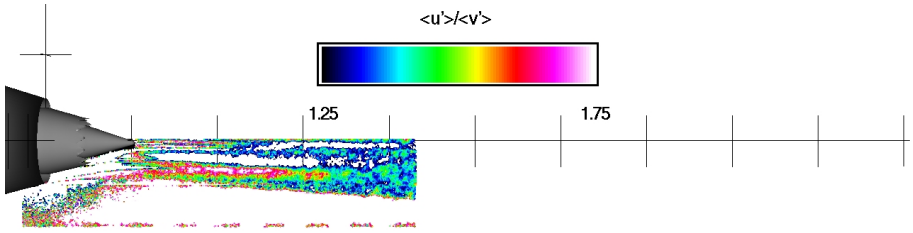

Figure 2.3.1.12 Model 3ab. Contour plots of ratio of axial to radial turbulence. Slice taken at circumferential angle = 10°.

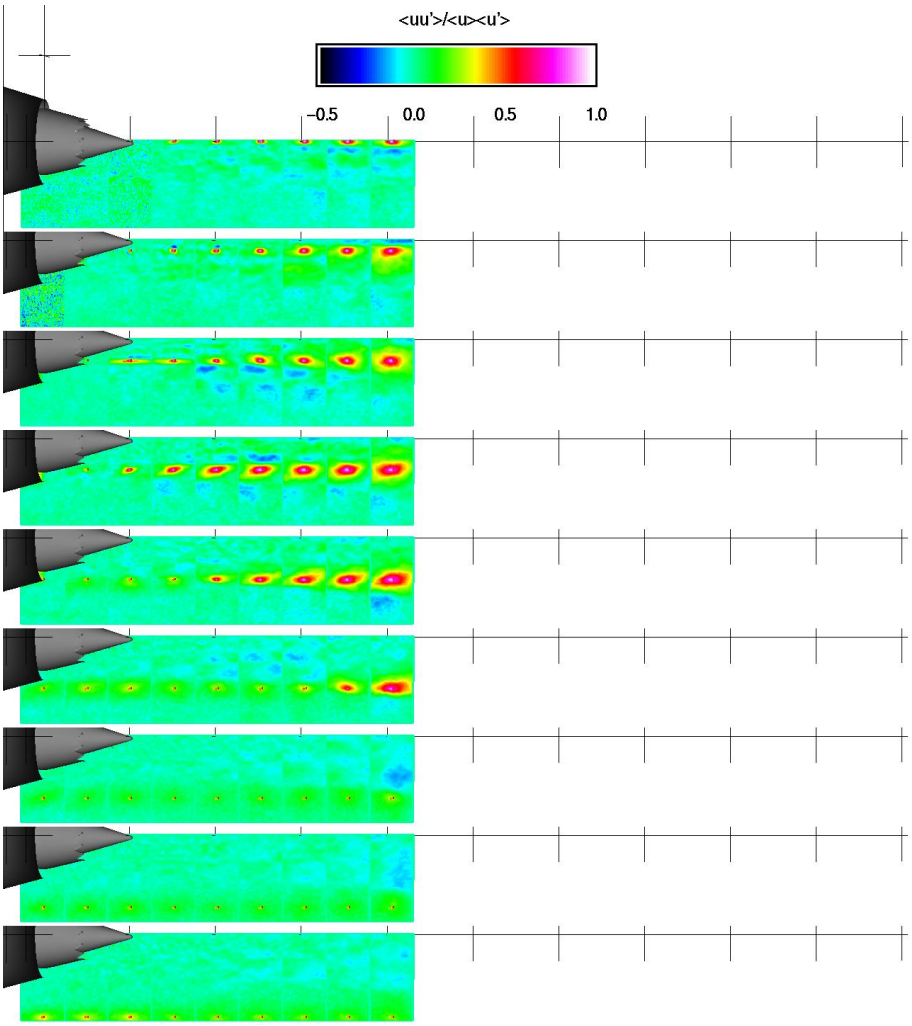

Figure 2.3.2.1 Model 3ab. Contour plots of u(xref)u(x). Slice taken at circumferential angle = 10°.

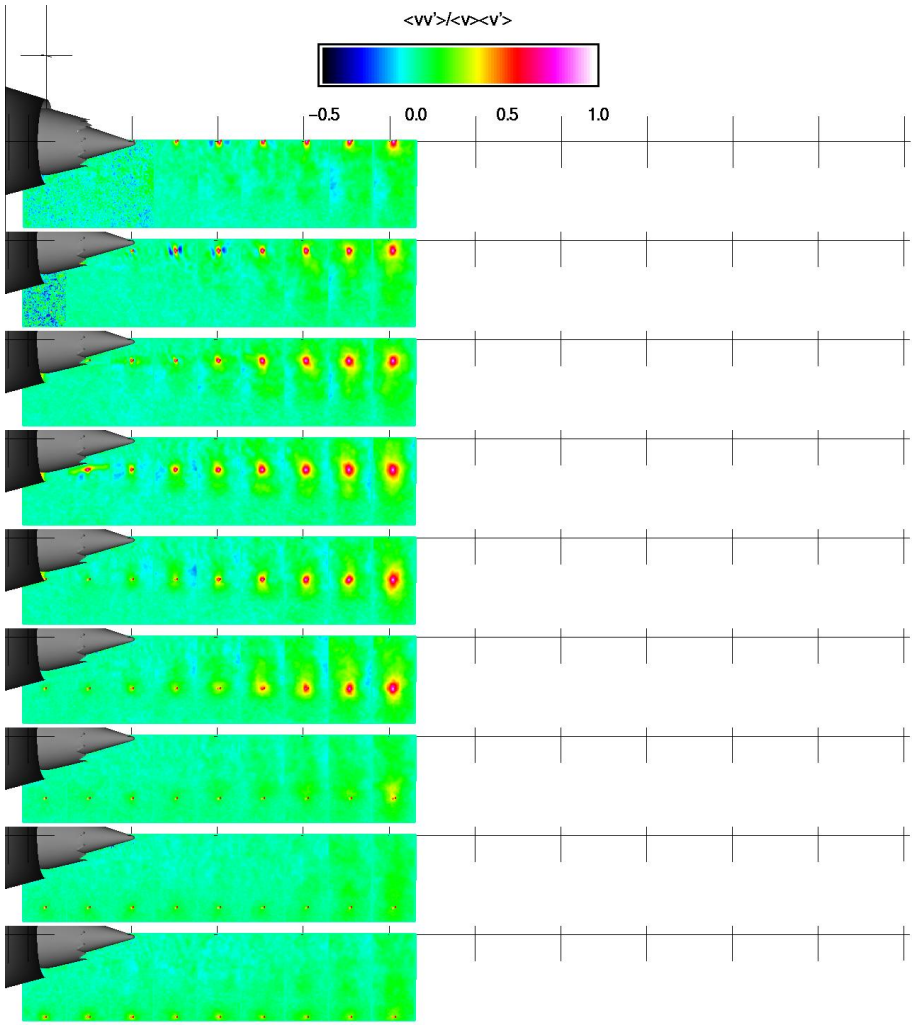

Figure 2.3.2.2 Model 3ab. Contour plots of v(xref)v(x). Slice taken at circumferential angle = 10°.

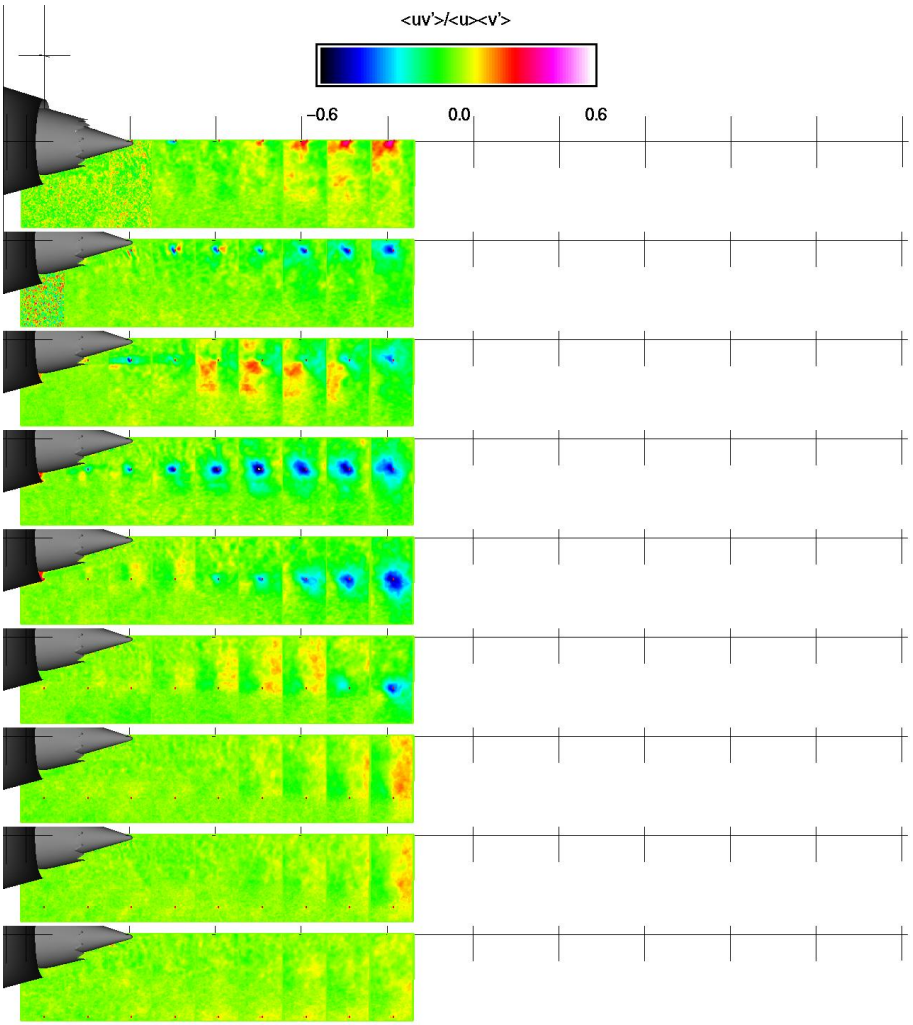

Figure 2.3.2.3 Model 3ab. Contour plots of u(xref)v(x). Slice taken at circumferential angle = 10°.

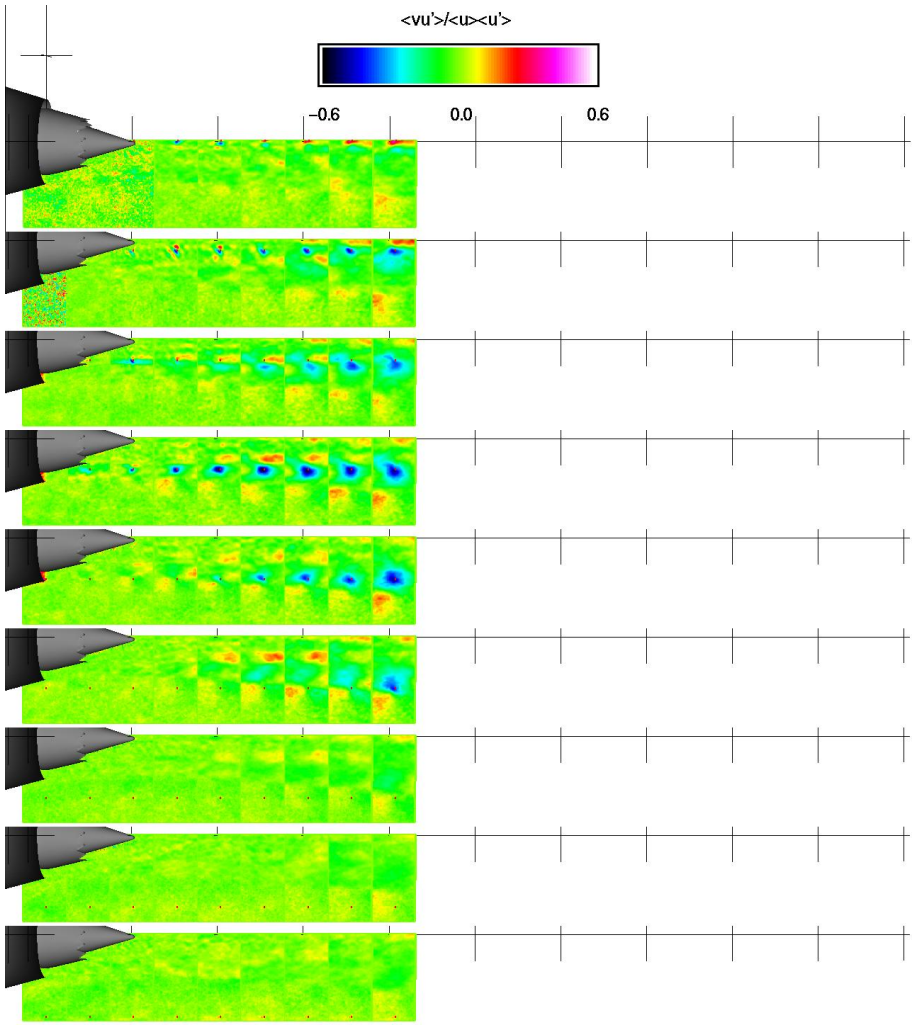

Figure 2.3.2.4 Model 3ab. Contour plots of v(xref)u(x). Slice taken at circumferential angle = 10°.

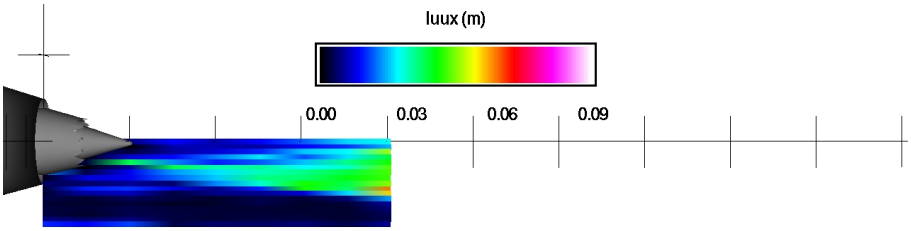

Figure 2.3.3.1 Model 3ab. Contour plots of Luu(x). Slice taken at circumferential angle = 10°.

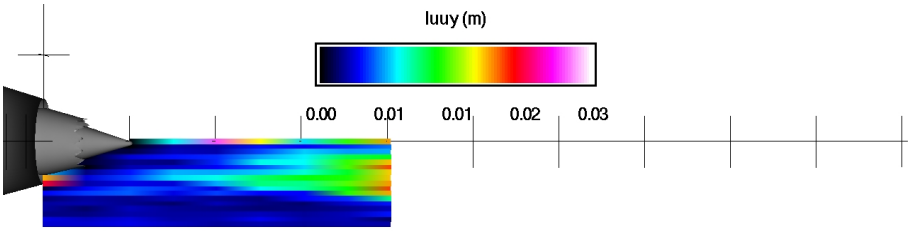

Figure 2.3.3.2 Model 3ab. Contour plots of Luu(y). Slice taken at circumferential angle = 10°.

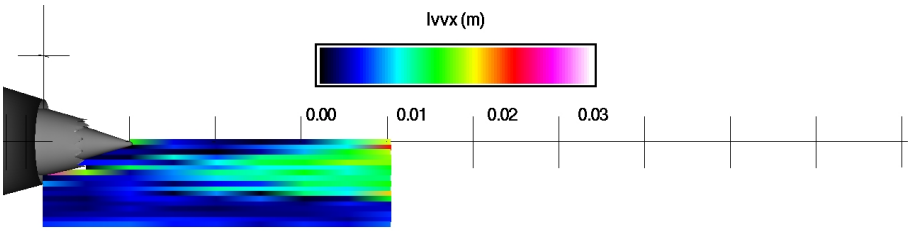

Figure 2.3.3.3 Model 3ab. Contour plots of Lvv(x). Slice taken at circumferential angle = 10°.

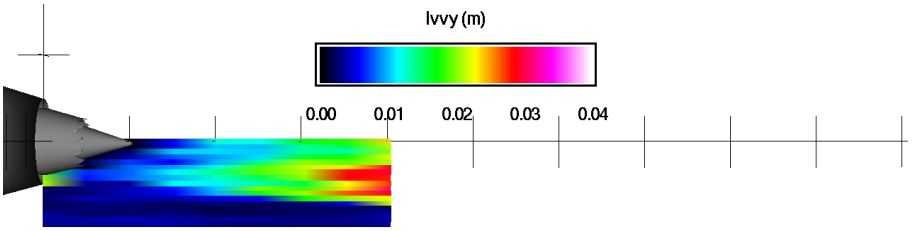

Figure 2.3.3.4 Model 3ab. Contour plots of Lvv(y). Slice taken at circumferential angle = 10°.

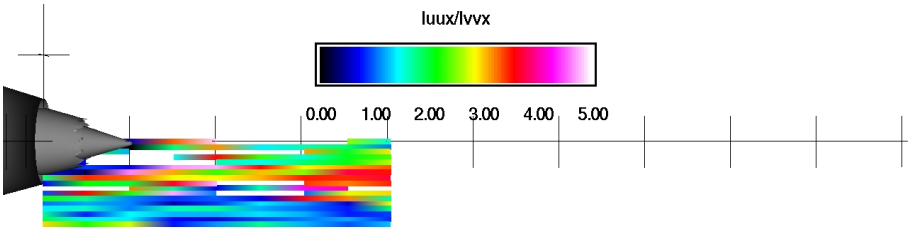

Figure 2.3.3.5 Model 3ab. Contour plots of Luu(x)/Lvv(x). Slice taken at circumferential angle = 10°.

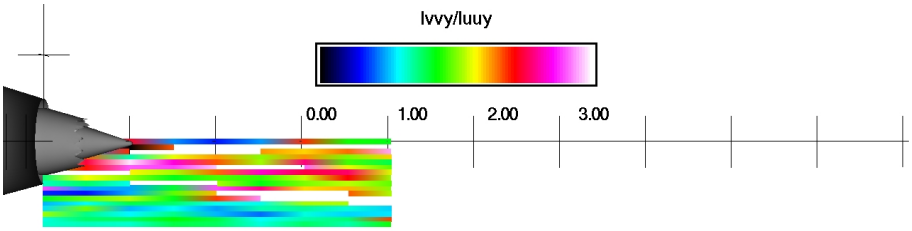

Figure 2.3.3.6 Model 3ab. Contour plots of Lvv(y)/Luu(y). Slice taken at circumferential angle = 10°.

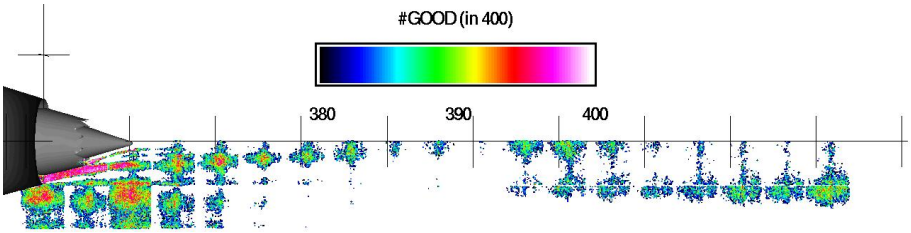

Figure 2.4.1.1 Model 3ab. Contour plots of data quality (#good out of 400). Slice taken at circumferential angle = 15°.

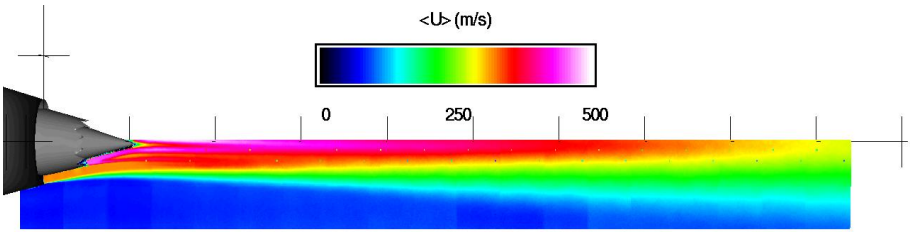

Figure 2.4.1.2 Model 3ab. Contour plots of time average axial velocity (m/s). Slice taken at circumferential angle = 15°.

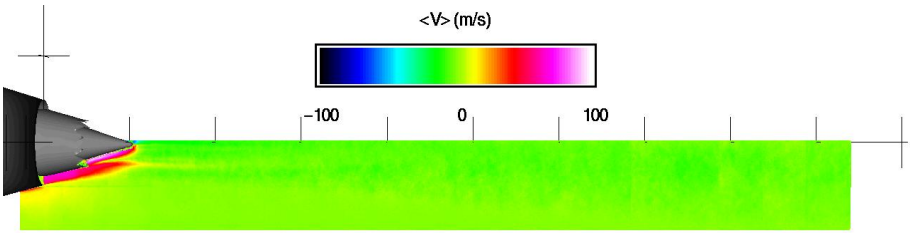

Figure 2.4.1.3 Model 3ab. Contour plots of time average radial velocity (m/s). Slice taken at circumferential angle = 15°.

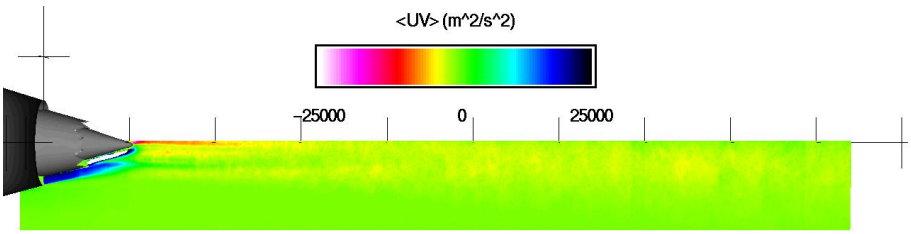

Figure 2.4.1.4 Model 3ab. Contour plots of time average Reynolds stress (m^2/s^2). Slice taken at circumferential angle = 15°.

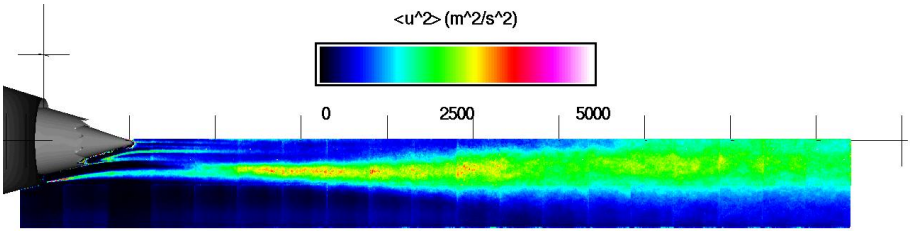

Figure 2.4.1.5 Model 3ab. Contour plots of variance of axial velocity (m^2/s^2). Slice taken at circumferential angle = 15°.

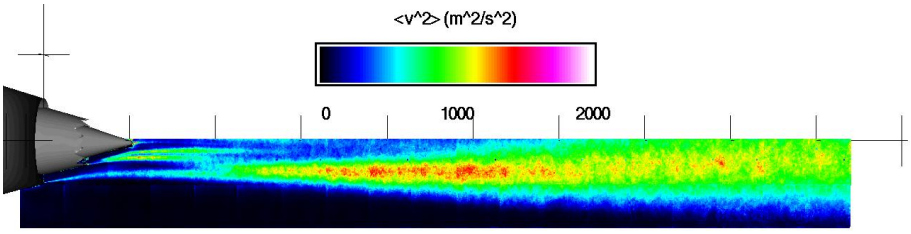

Figure 2.4.1.6 Model 3ab. Contour plots of variance in radial velocity (m^2/s^2). Slice taken at circumferential angle = 15°.

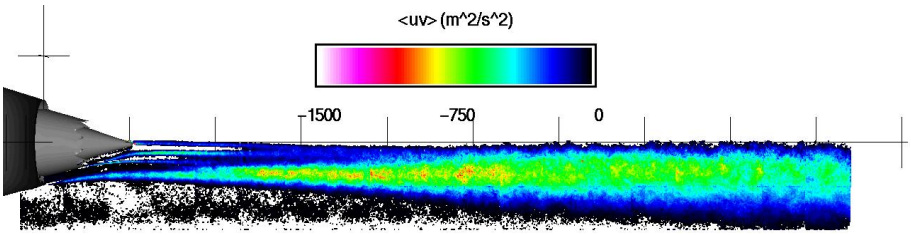

Figure 2.4.1.7 Model 3ab. Contour plots of unsteady Reynolds stress (m^2/s^2). Slice taken at circumferential angle = 15°.

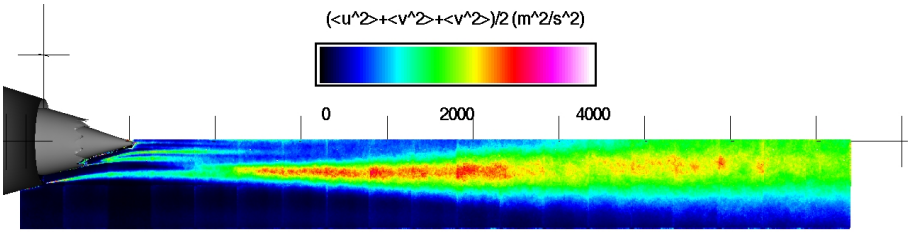

Figure 2.4.1.8 Model 3ab. Contour plots of turbulent kinetic energy (m^2/s^2). Slice taken at circumferential angle = 15°.

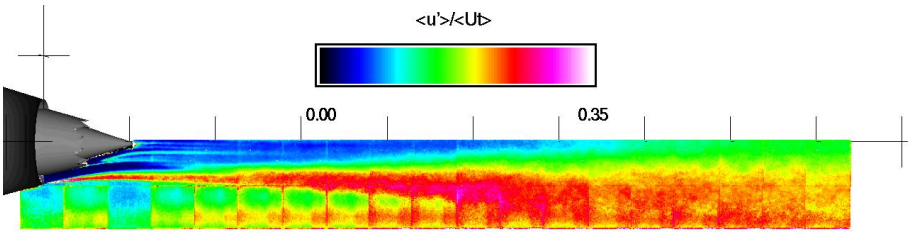

Figure 2.4.1.9 Model 3ab. Contour plots of axial turbulence intensity. Slice taken at circumferential angle = 15°.

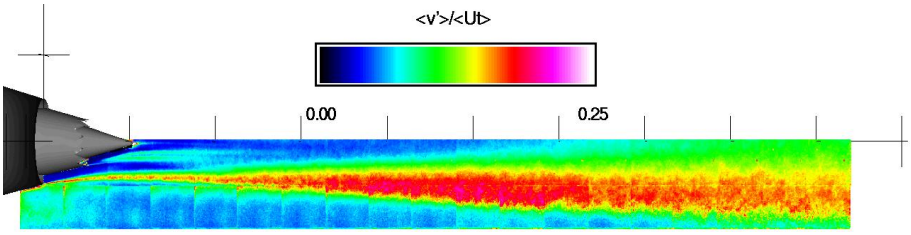

Figure 2.4.1.10 Model 3ab. Contour plots of radial turbulence intensity. Slice taken at circumferential angle = 15°.

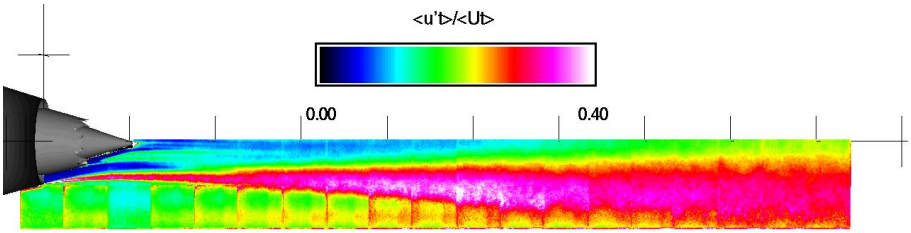

Figure 2.4.1.11 Model 3ab. Contour plots of turbulence intensity. Slice taken at circumferential angle = 15°.

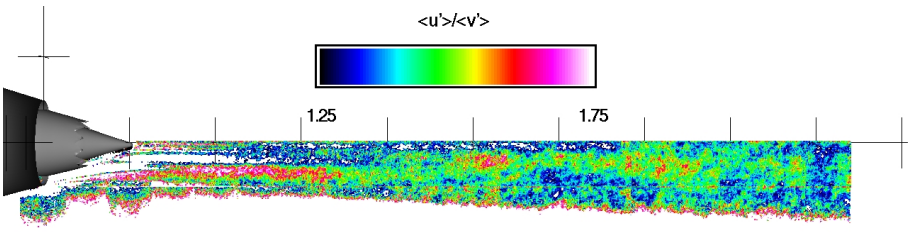

Figure 2.4.1.12 Model 3ab. Contour plots of ratio of axial to radial turbulence. Slice taken at circumferential angle = 15°.

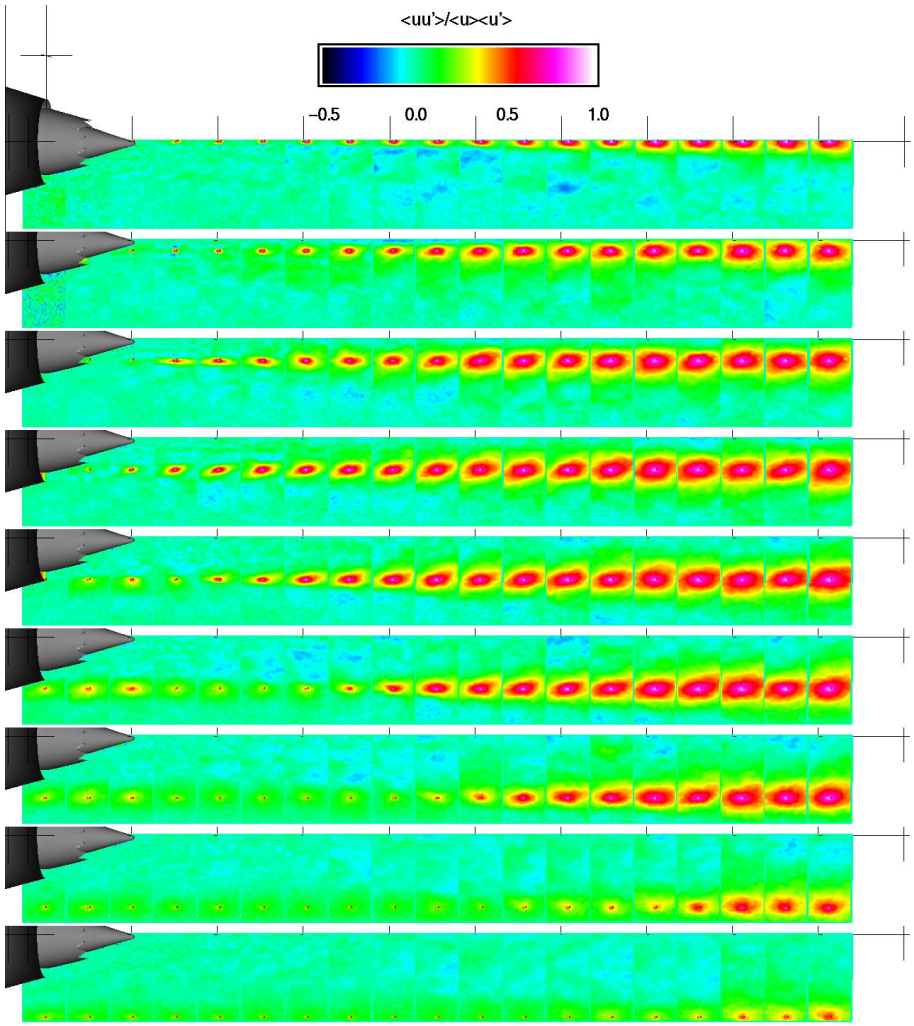

Figure 2.4.2.1 Model 3ab. Contour plots of u(xref)u(x). Slice taken at circumferential angle = 15°.

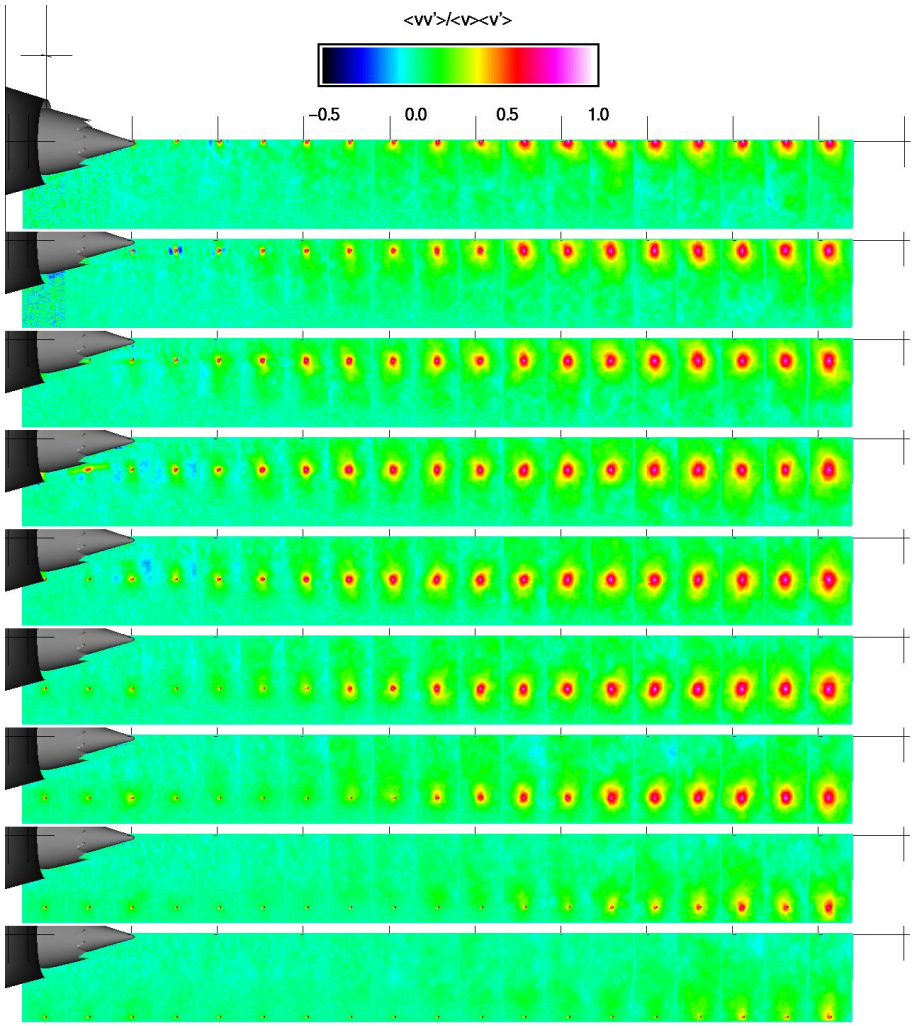

Figure 2.4.2.2 Model 3ab. Contour plots of v(xref)v(x). Slice taken at circumferential angle = 15°.

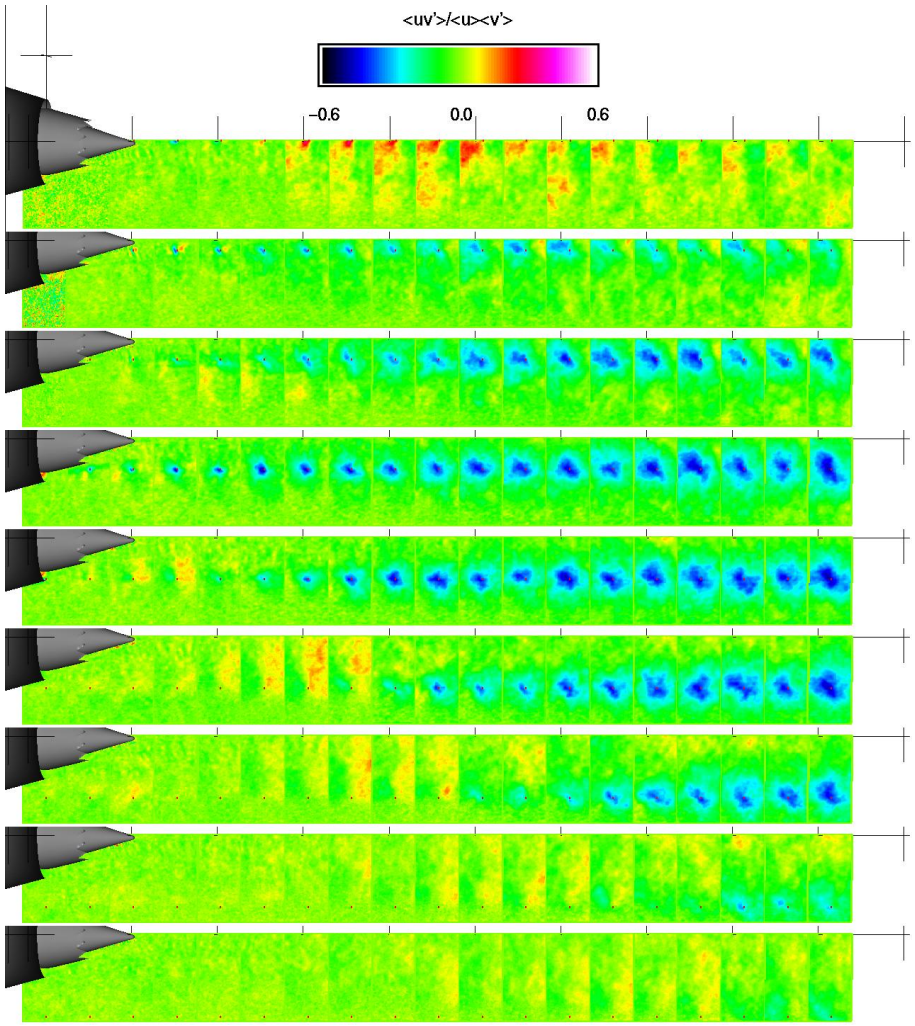

Figure 2.4.2.3 Model 3ab. Contour plots of u(xref)v(x). Slice taken at circumferential angle = 15°.

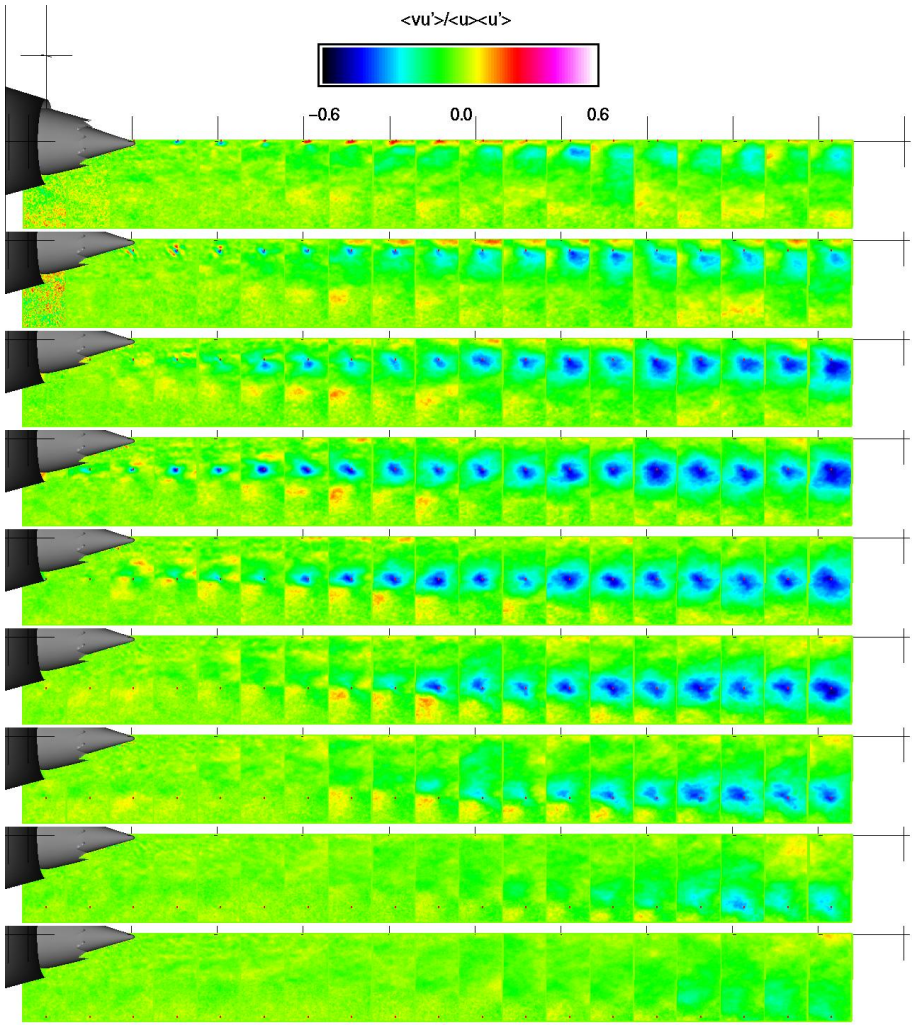

Figure 2.4.2.4 Model 3ab. Contour plots of v(xref)u(x). Slice taken at circumferential angle = 15°.

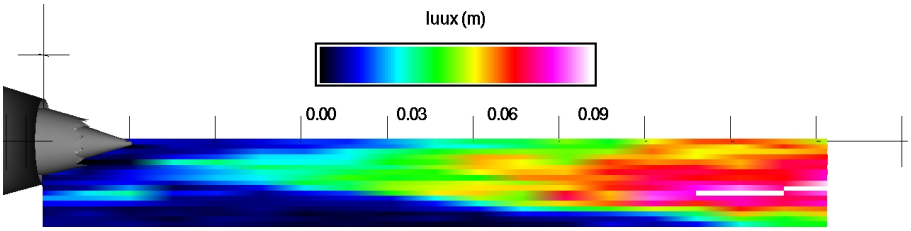

Figure 2.4.3.1 Model 3ab. Contour plots of Luu(x). Slice taken at circumferential angle = 15°.

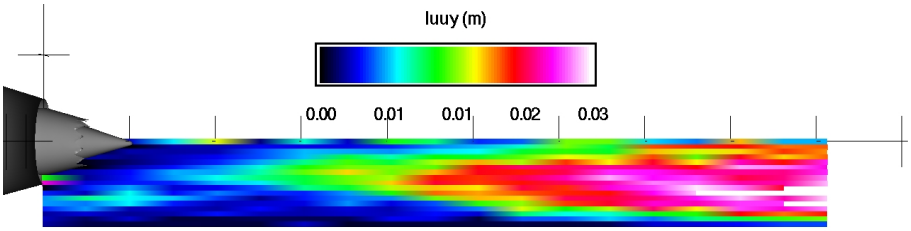

Figure 2.4.3.2 Model 3ab. Contour plots of Luu(y). Slice taken at circumferential angle = 15°.

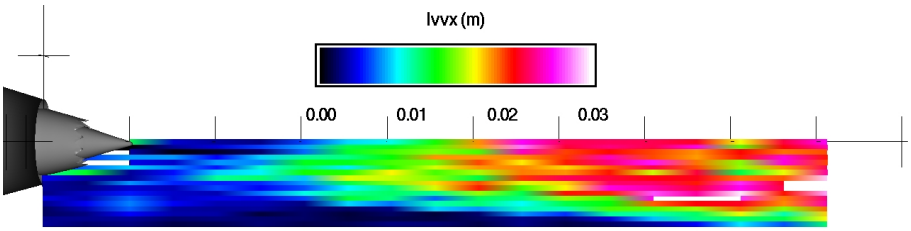

Figure 2.4.3.3 Model 3ab. Contour plots of Lvv(x). Slice taken at circumferential angle = 15°.

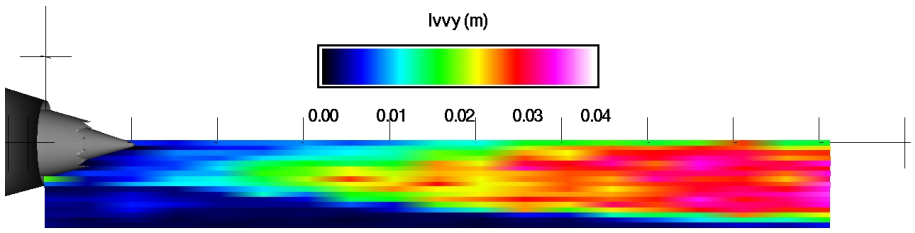

Figure 2.4.3.4 Model 3ab. Contour plots of Lvv(y). Slice taken at circumferential angle = 15°.

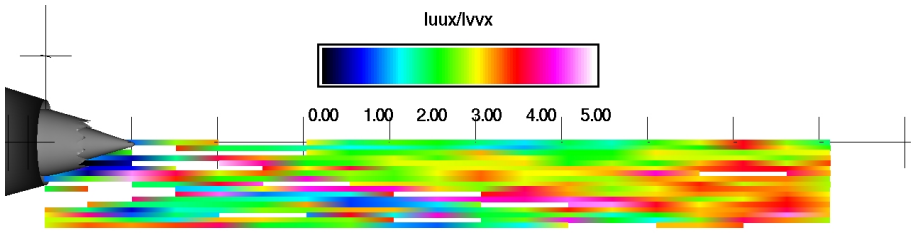

Figure 2.4.3.5 Model 3ab. Contour plots of Luu(x)/Lvv(x). Slice taken at circumferential angle = 15°.

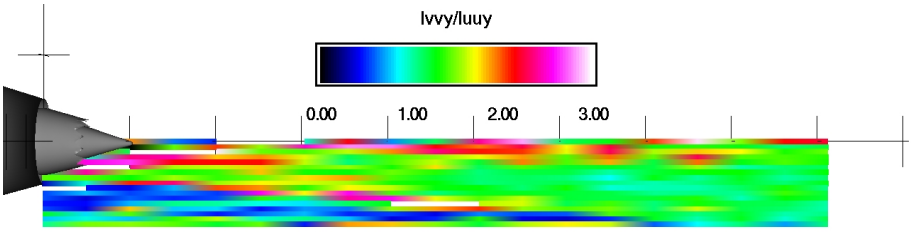

Figure 2.4.3.6 Model 3ab. Contour plots of Lvv(y)/Luu(y). Slice taken at circumferential angle = 15°.

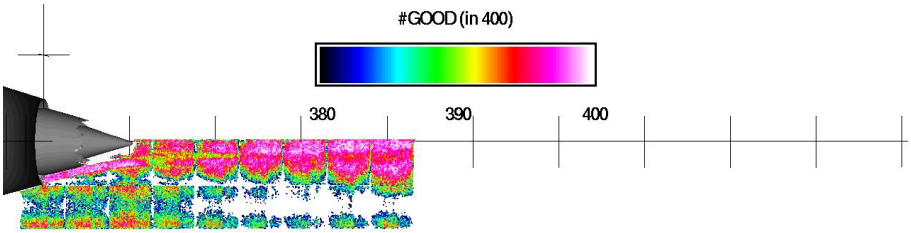

Figure 2.5.1.1 Model 3ab. Contour plots of data quality (#good out of 400). Slice taken at circumferential angle = 20°.

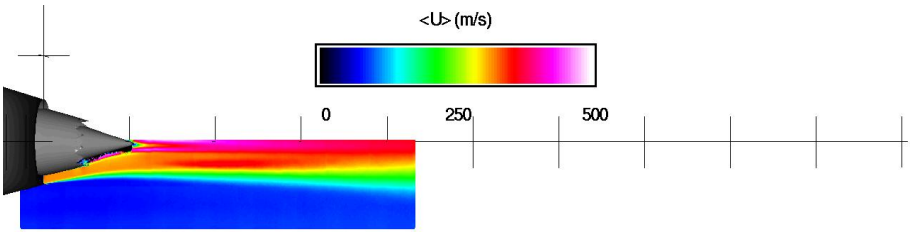

Figure 2.5.1.2 Model 3ab. Contour plots of time average axial velocity (m/s). Slice taken at circumferential angle = 20°.

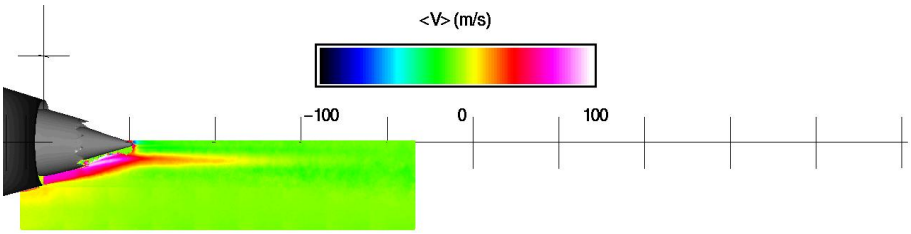

Figure 2.5.1.3 Model 3ab. Contour plots of time average radial velocity (m/s). Slice taken at circumferential angle = 20°.

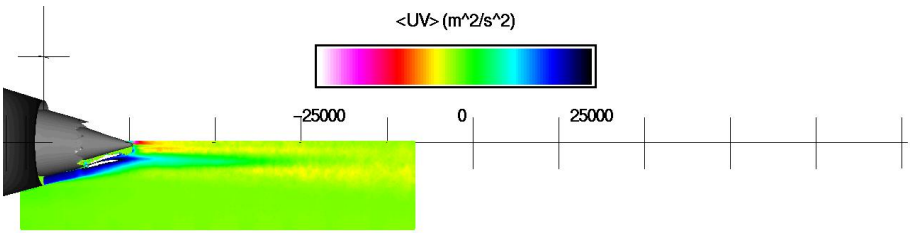

Figure 2.5.1.4 Model 3ab. Contour plots of time average Reynolds stress (m^2/s^2). Slice taken at circumferential angle = 20°.

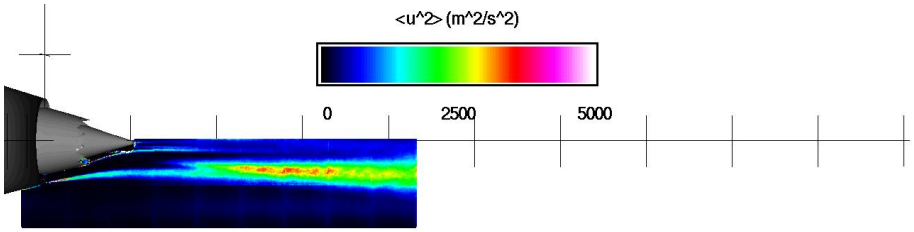

Figure 2.5.1.5 Model 3ab. Contour plots of variance of axial velocity (m^2/s^2). Slice taken at circumferential angle = 20°.

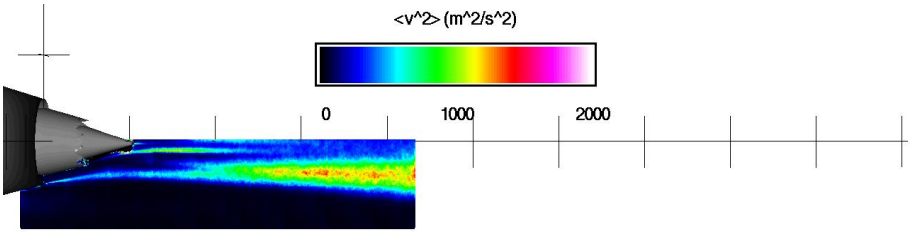

Figure 2.5.1.6 Model 3ab. Contour plots of variance in radial velocity (m^2/s^2). Slice taken at circumferential angle = 20°.

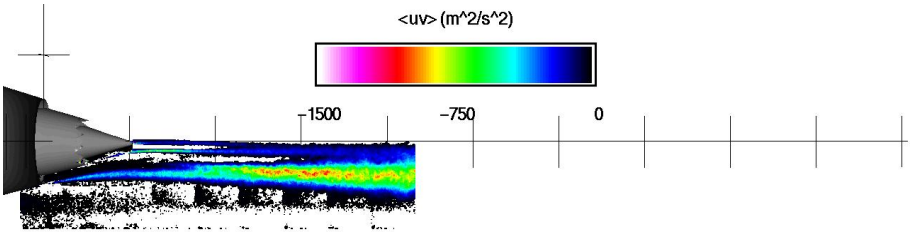

Figure 2.5.1.7 Model 3ab. Contour plots of unsteady Reynolds stress (m^2/s^2). Slice taken at circumferential angle = 20°.

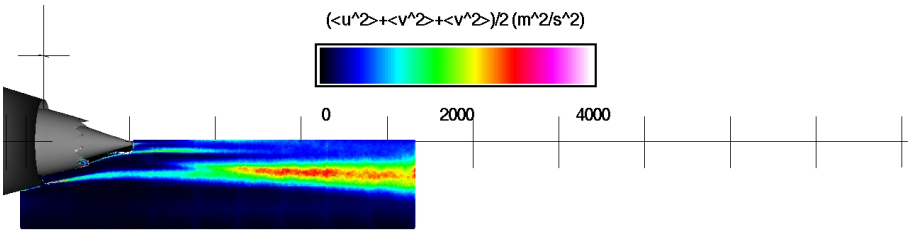

Figure 2.5.1.8 Model 3ab. Contour plots of turbulent kinetic energy (m^2/s^2). Slice taken at circumferential angle = 20°.

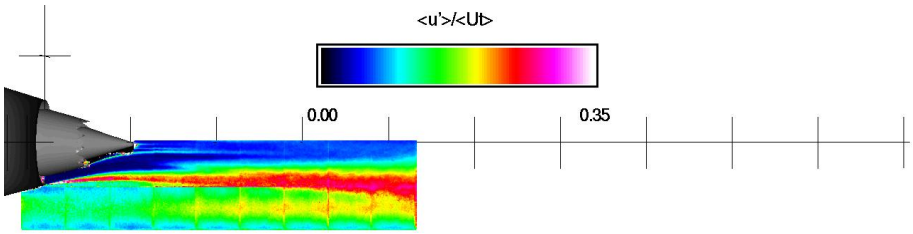

Figure 2.5.1.9 Model 3ab. Contour plots of axial turbulence intensity. Slice taken at circumferential angle = 20°.

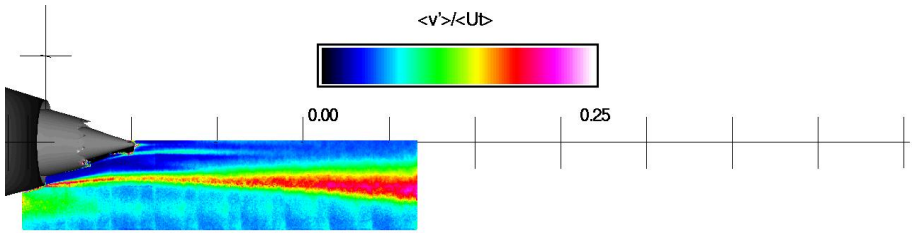

Figure 2.5.1.10 Model 3ab. Contour plots of radial turbulence intensity. Slice taken at circumferential angle = 20°.

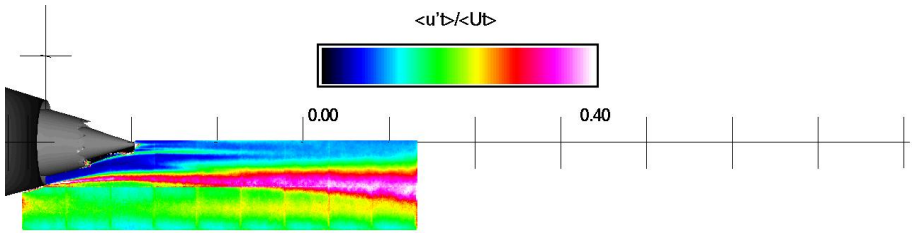

Figure 2.5.1.11 Model 3ab. Contour plots of turbulence intensity. Slice taken at circumferential angle = 20°.

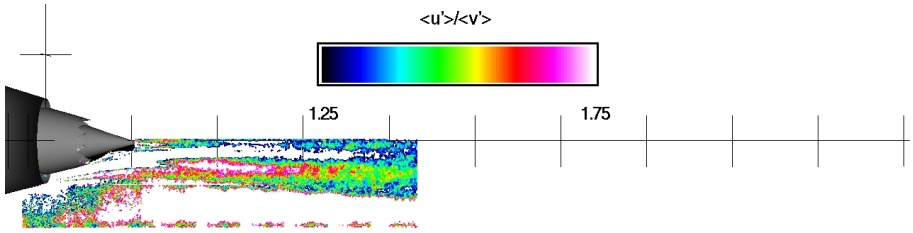

Figure 2.5.1.12 Model 3ab. Contour plots of ratio of axial to radial turbulence. Slice taken at circumferential angle = 20°.

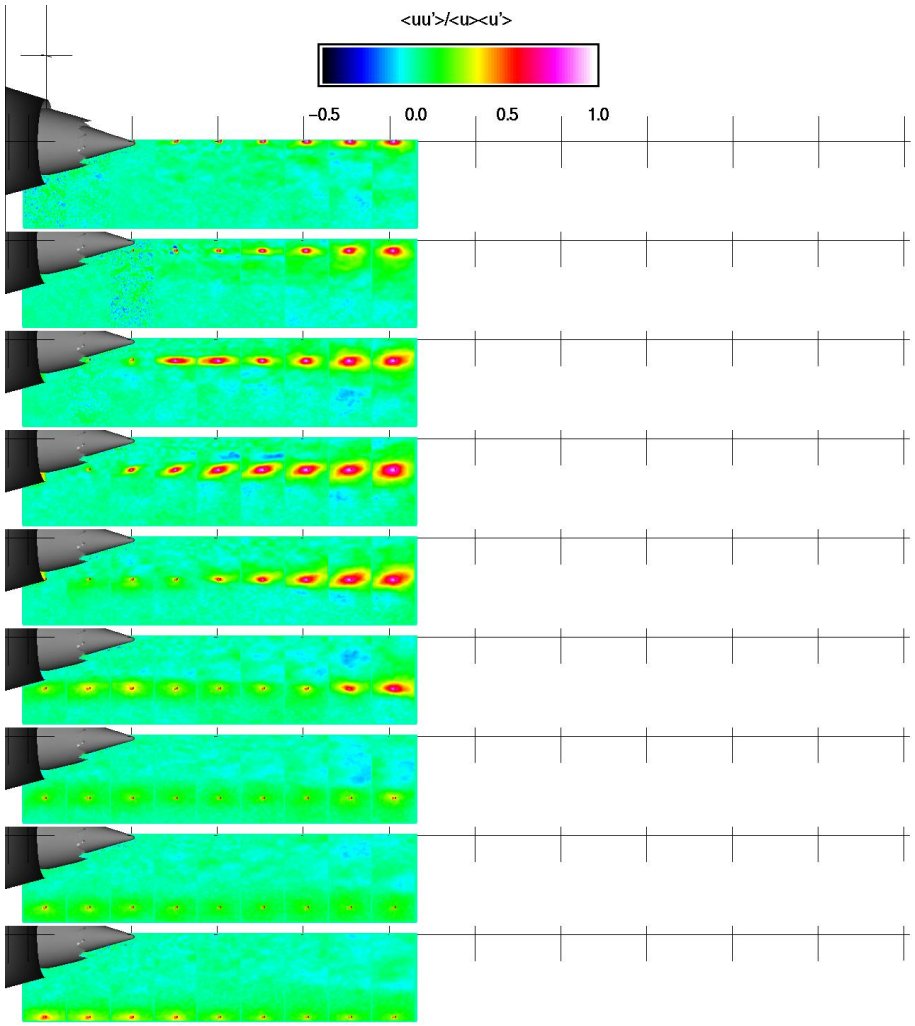

Figure 2.5.2.1 Model 3ab. Contour plots of u(xref)u(x). Slice taken at circumferential angle = 20°.

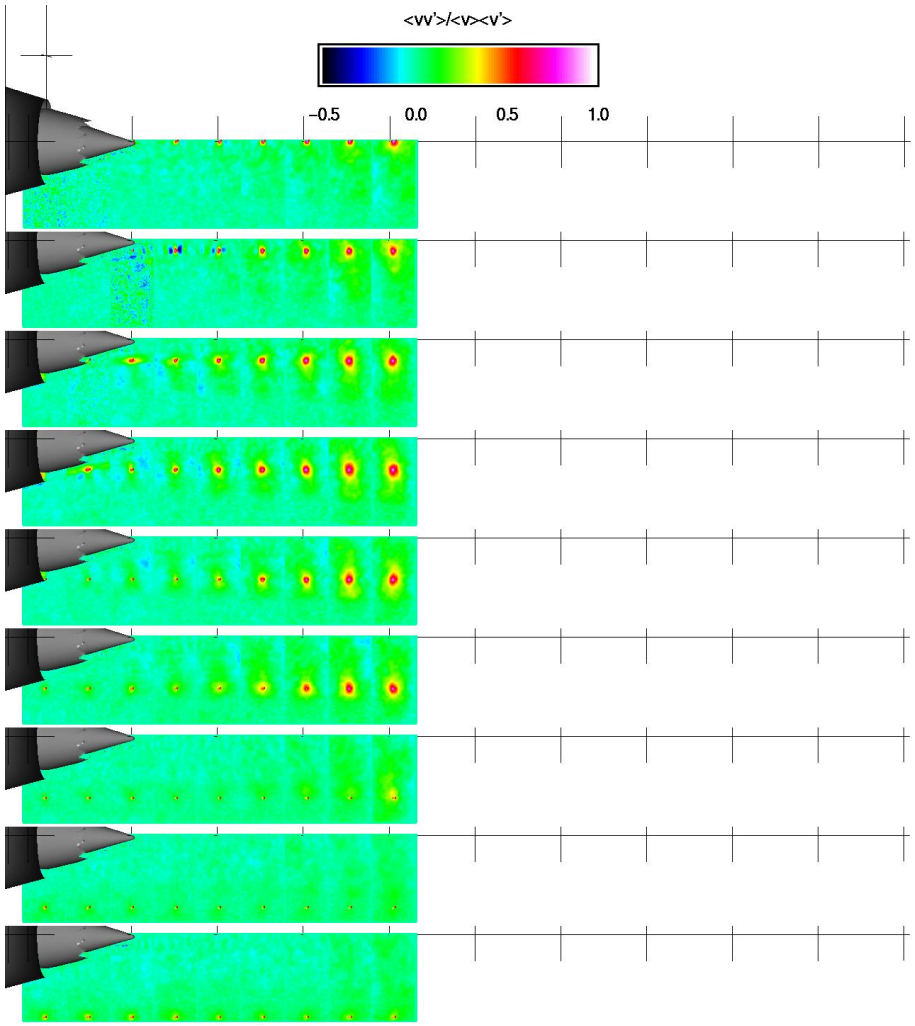

Figure 2.5.2.2 Model 3ab. Contour plots of v(xref)v(x). Slice taken at circumferential angle = 20°.

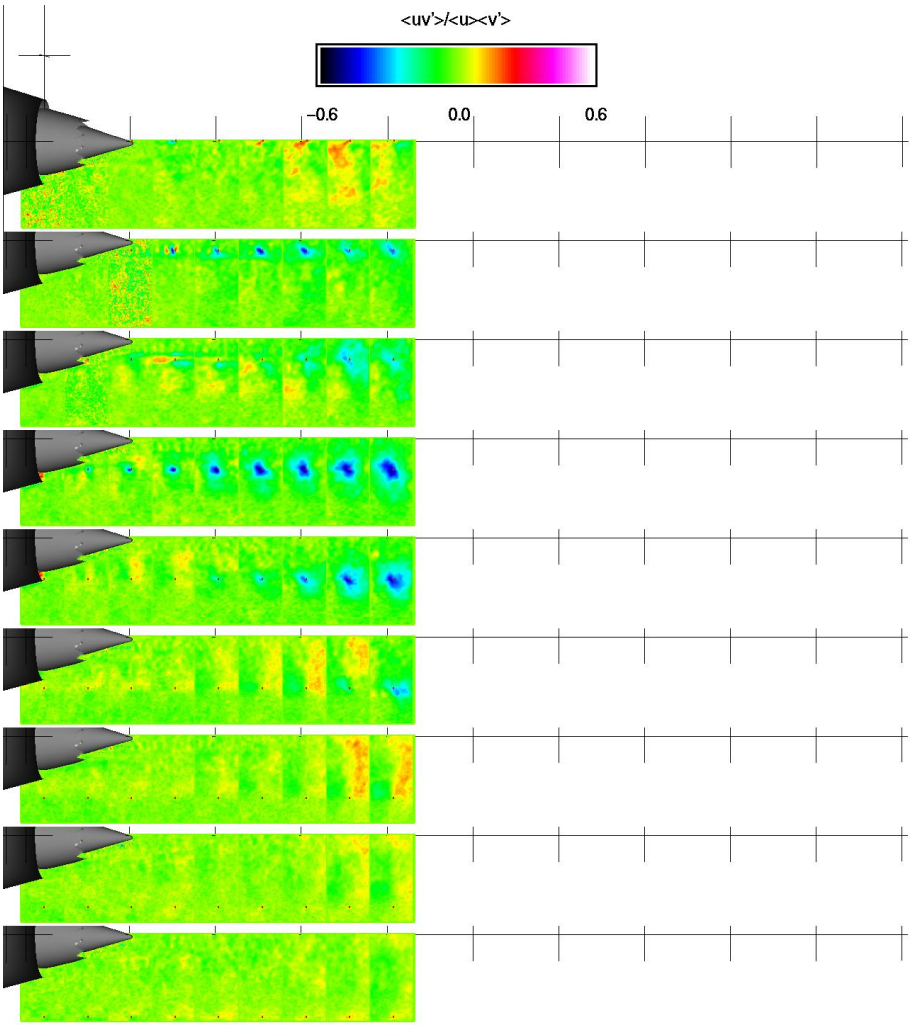

Figure 2.5.2.3 Model 3ab. Contour plots of u(xref)v(x). Slice taken at circumferential angle = 20°.

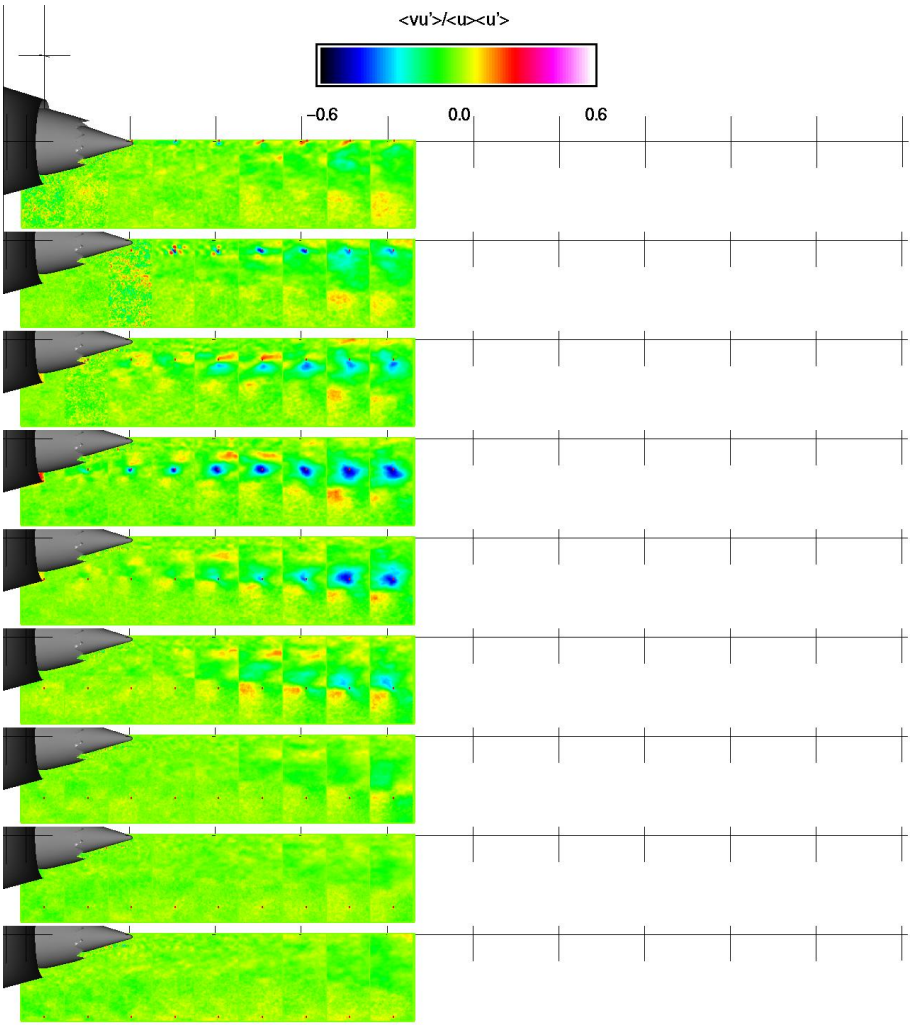

Figure 2.5.2.4 Model 3ab. Contour plots of v(xref)u(x). Slice taken at circumferential angle = 20°.

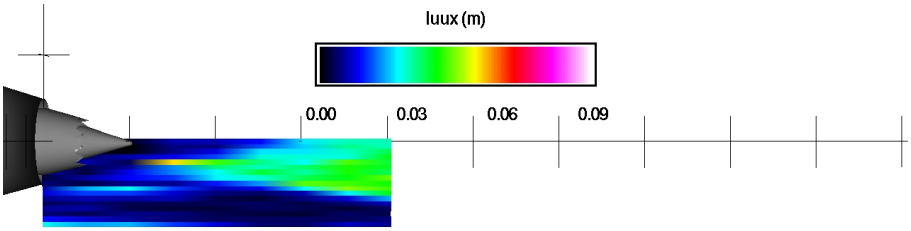

Figure 2.5.3.1 Model 3ab. Contour plots of Luu(x). Slice taken at circumferential angle = 20°.

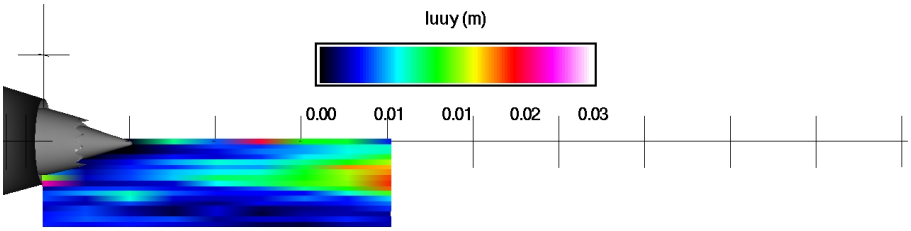

Figure 2.5.3.2 Model 3ab. Contour plots of Luu(y). Slice taken at circumferential angle = 20°.

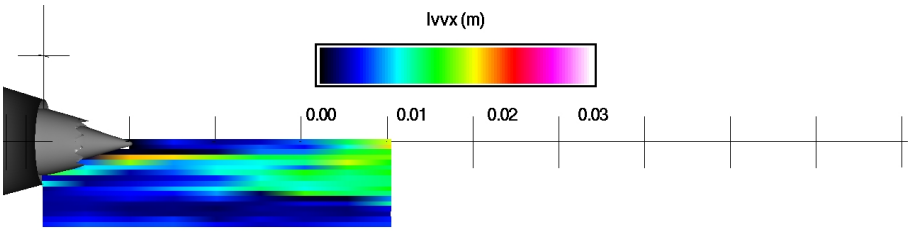

Figure 2.5.3.3 Model 3ab. Contour plots of Lvv(x). Slice taken at circumferential angle = 20°.

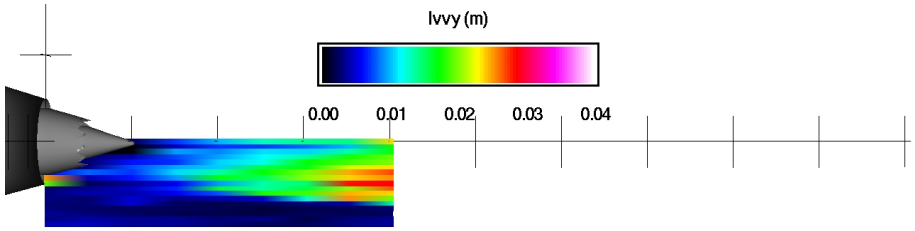

Figure 2.5.3.4 Model 3ab. Contour plots of Lvv(y). Slice taken at circumferential angle = 20°.

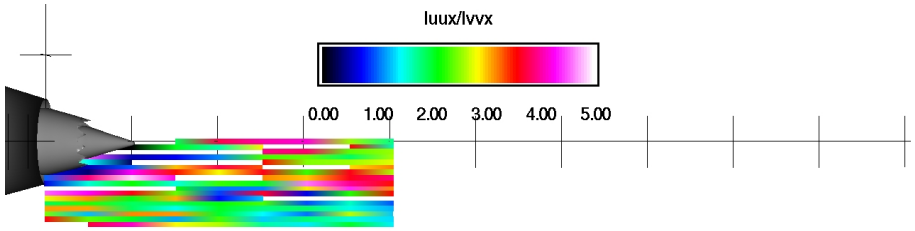

Figure 2.5.3.5 Model 3ab. Contour plots of Luu(x)/Lvv(x). Slice taken at circumferential angle = 20°.

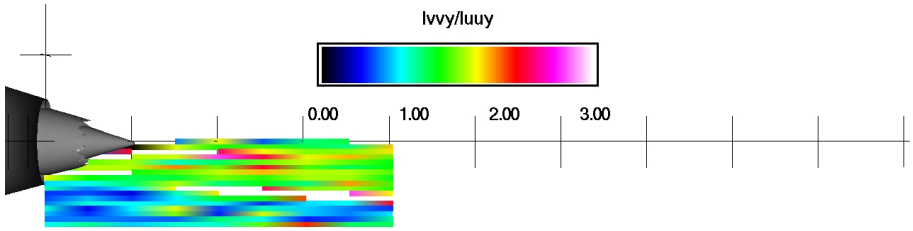

Figure 2.5.3.6 Model 3ab. Contour plots of Lvv(y)/Luu(y). Slice taken at circumferential angle = 20°.

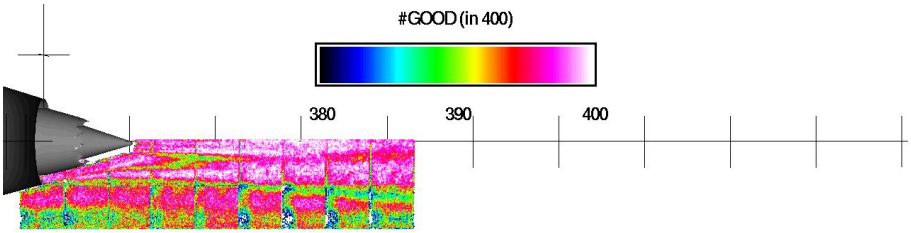

Figure 2.6.1.1 Model 3ab. Contour plots of data quality (#good out of 400). Slice taken at circumferential angle = 25°.

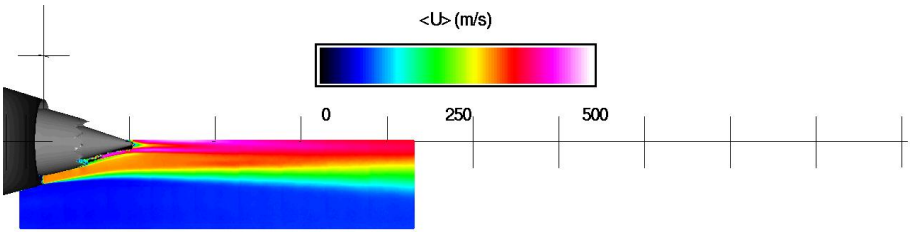

Figure 2.6.1.2 Model 3ab. Contour plots of time average axial velocity (m/s). Slice taken at circumferential angle = 25°.

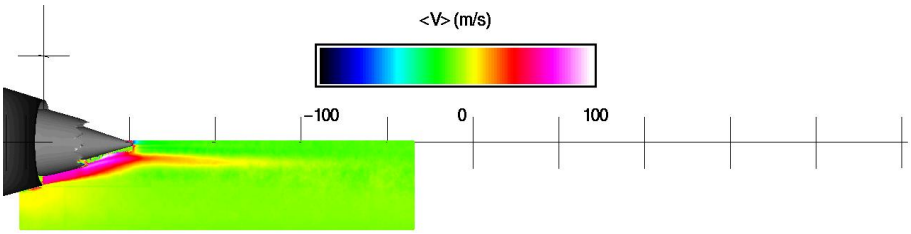

Figure 2.6.1.3 Model 3ab. Contour plots of time average radial velocity (m/s). Slice taken at circumferential angle = 25°.

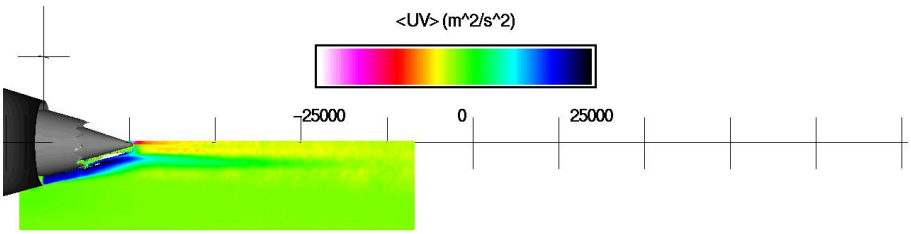

Figure 2.6.1.4 Model 3ab. Contour plots of time average Reynolds stress (m^2/s^2). Slice taken at circumferential angle = 25°.

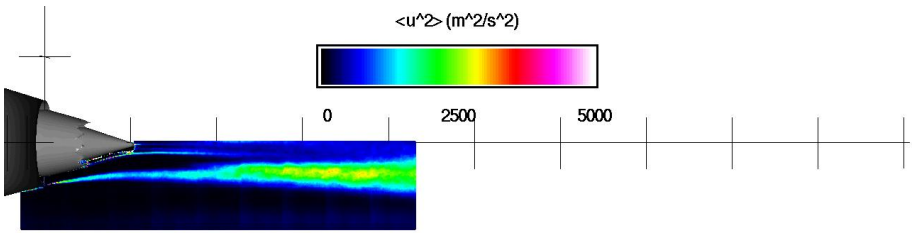

Figure 2.6.1.5 Model 3ab. Contour plots of variance of axial velocity (m^2/s^2). Slice taken at circumferential angle = 25°.

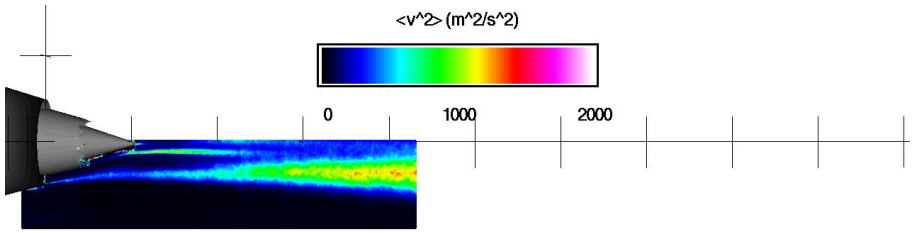

Figure 2.6.1.6 Model 3ab. Contour plots of variance in radial velocity (m^2/s^2). Slice taken at circumferential angle = 25°.

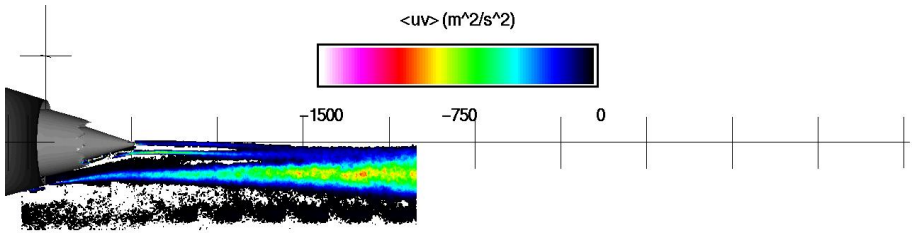

Figure 2.6.1.7 Model 3ab. Contour plots of unsteady Reynolds stress (m^2/s^2). Slice taken at circumferential angle = 25°.

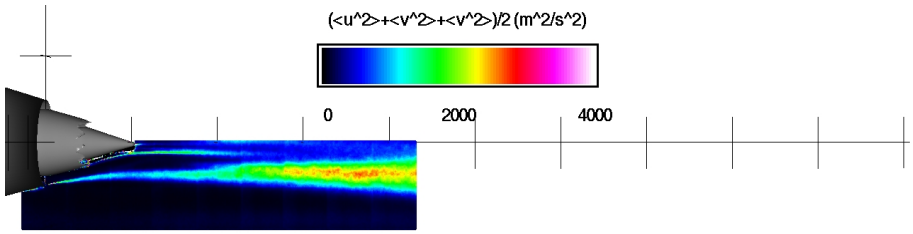

Figure 2.6.1.8 Model 3ab. Contour plots of turbulent kinetic energy (m^2/s^2). Slice taken at circumferential angle = 25°.

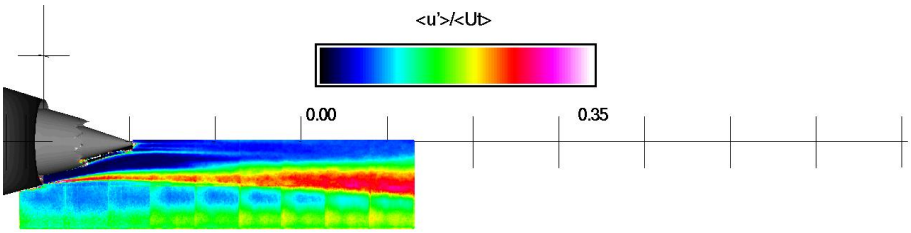

Figure 2.6.1.9 Model 3ab. Contour plots of axial turbulence intensity. Slice taken at circumferential angle = 25°.

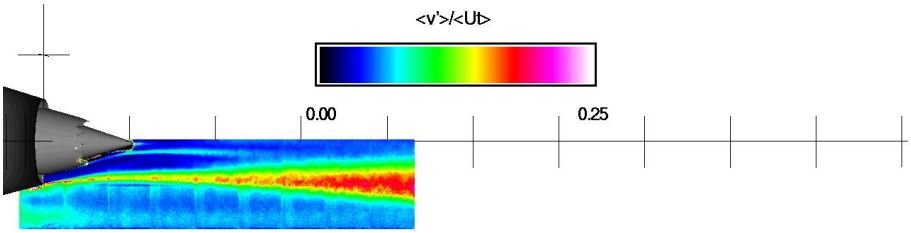

Figure 2.6.1.10 Model 3ab. Contour plots of radial turbulence intensity. Slice taken at circumferential angle = 25°.

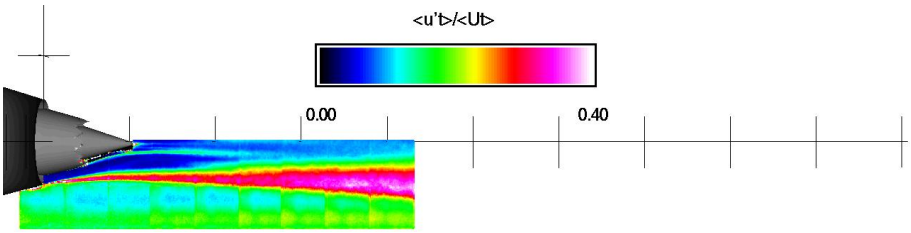

Figure 2.6.1.11 Model 3ab. Contour plots of turbulence intensity. Slice taken at circumferential angle = 25°.

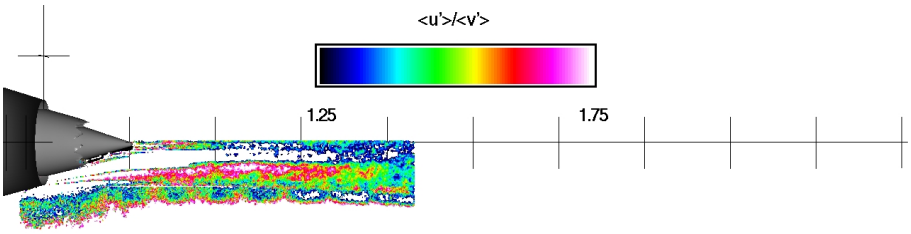

Figure 2.6.1.12 Model 3ab. Contour plots of ratio of axial to radial turbulence. Slice taken at circumferential angle = 25°.

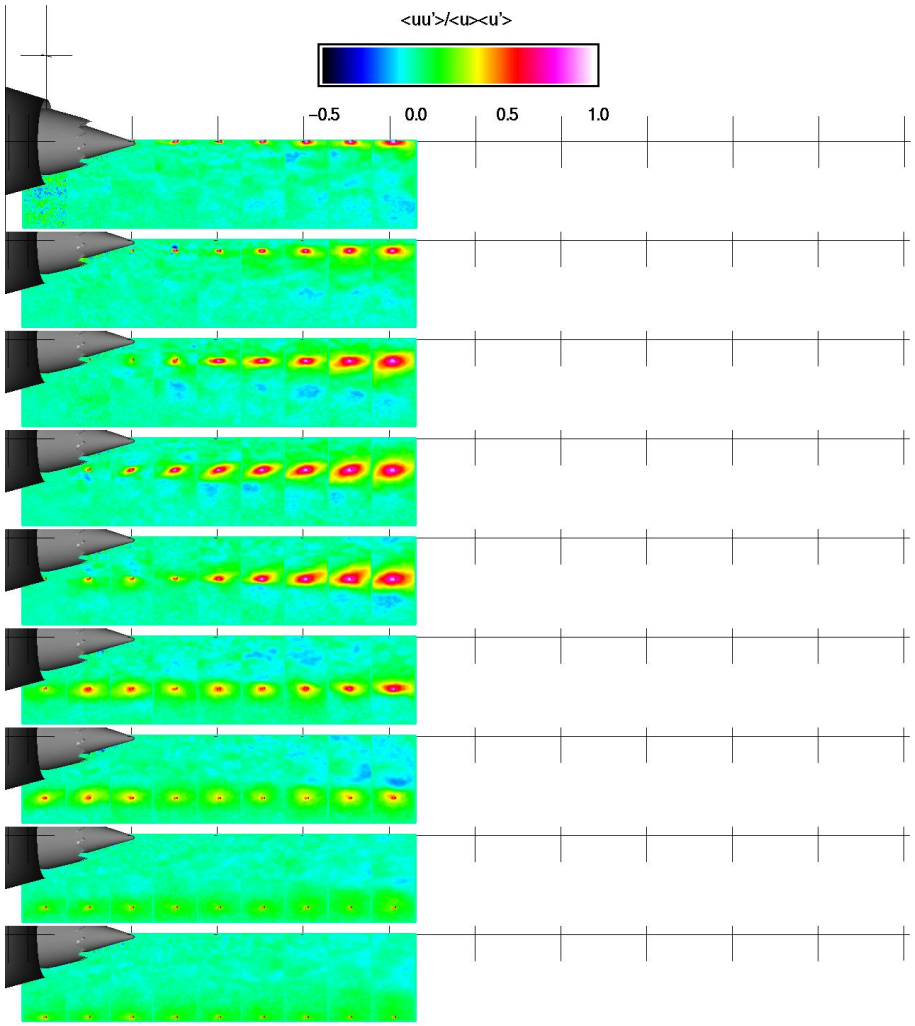

Figure 2.6.2.1 Model 3ab. Contour plots of u(xref)u(x). Slice taken at circumferential angle = 25°.

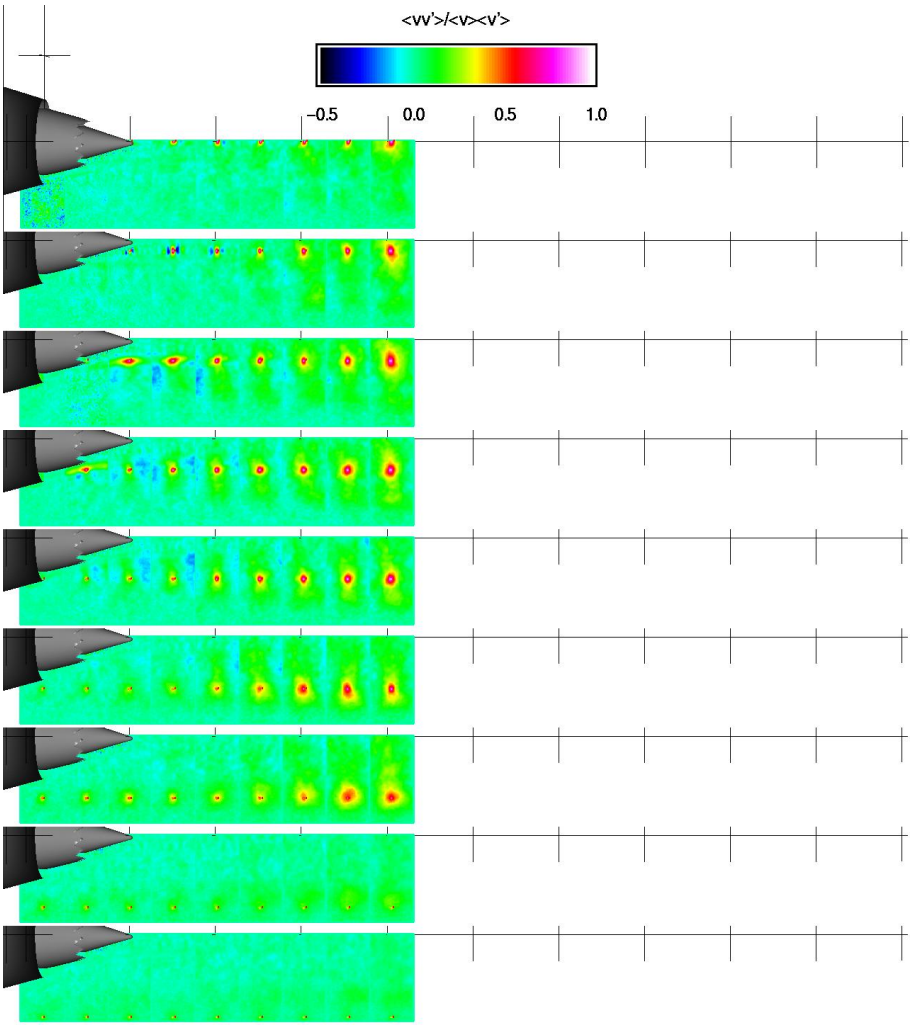

Figure 2.6.2.2 Model 3ab. Contour plots of v(xref)v(x). Slice taken at circumferential angle = 25°.

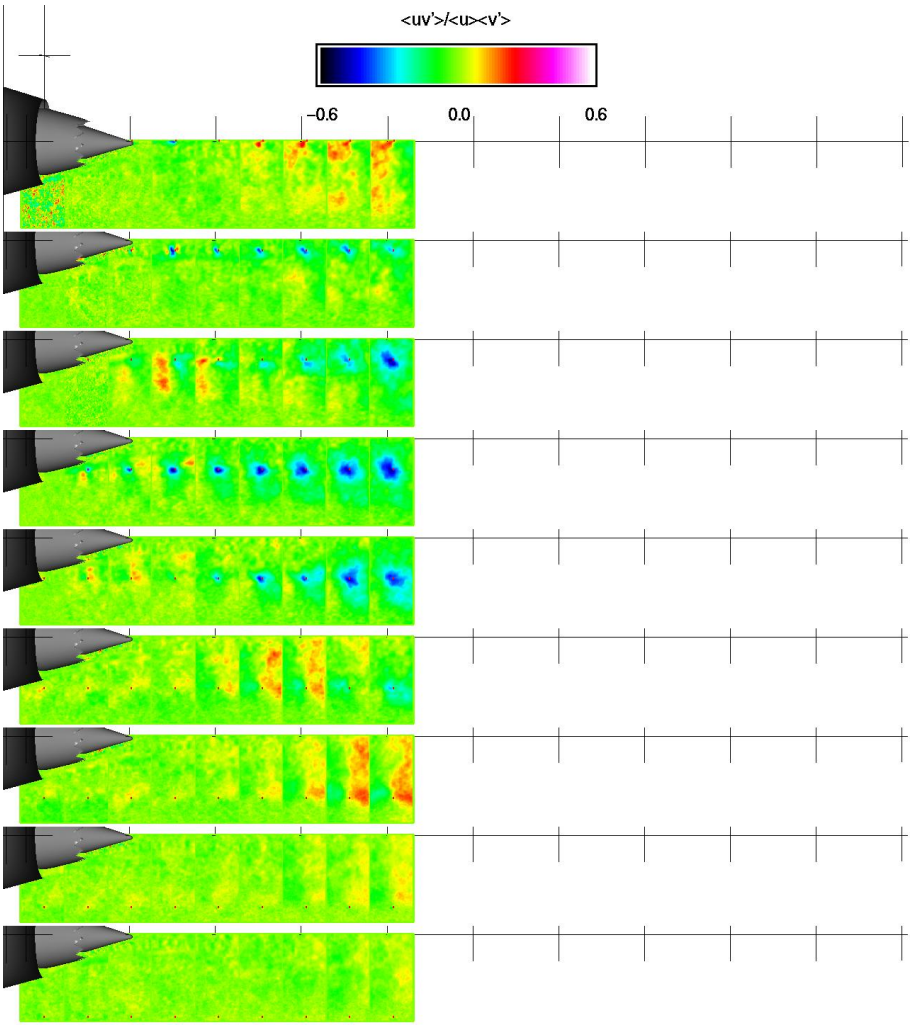

Figure 2.6.2.3 Model 3ab. Contour plots of u(xref)v(x). Slice taken at circumferential angle = 25°.

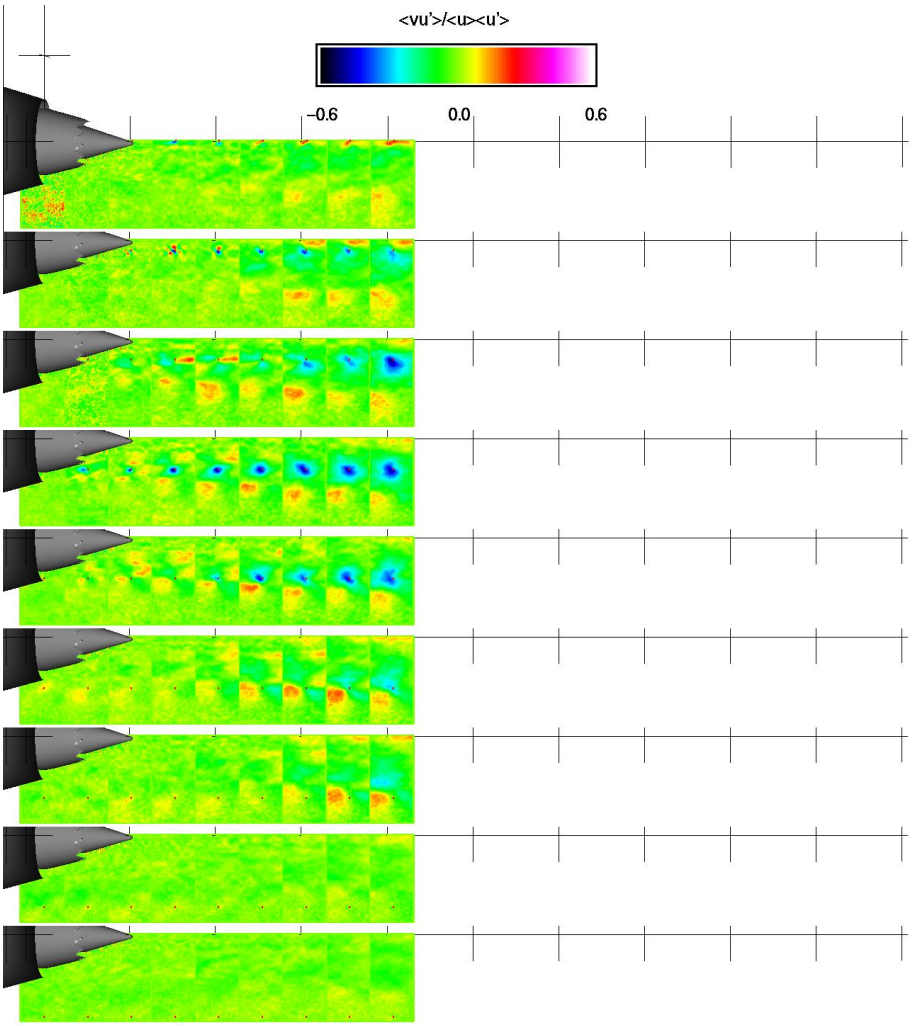

Figure 2.6.2.4 Model 3ab. Contour plots of v(xref)u(x). Slice taken at circumferential angle = 25°.

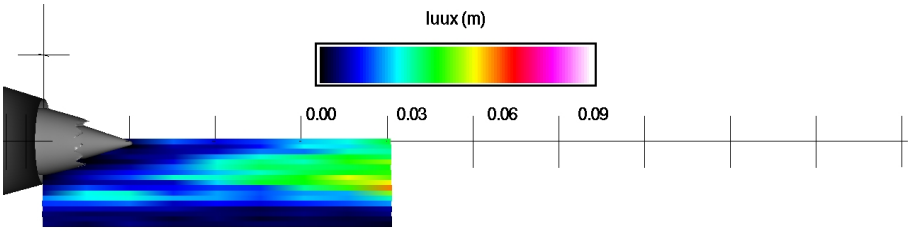

Figure 2.6.3.1 Model 3ab. Contour plots of Luu(x). Slice taken at circumferential angle = 25°.

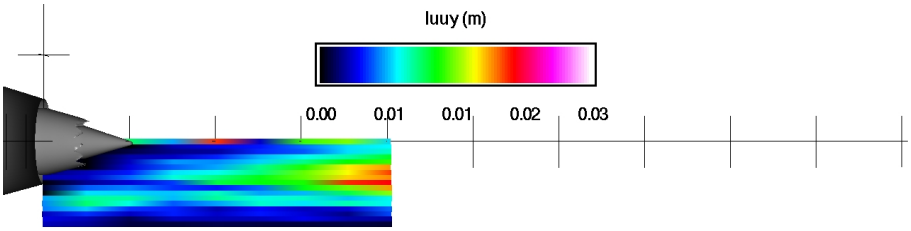

Figure 2.6.3.2 Model 3ab. Contour plots of Luu(y). Slice taken at circumferential angle = 25°.

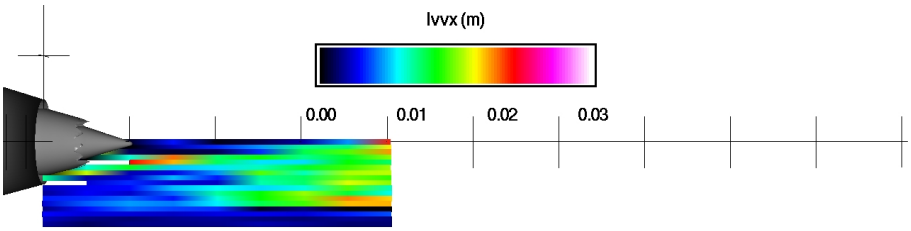

Figure 2.6.3.3 Model 3ab. Contour plots of Lvv(x). Slice taken at circumferential angle = 25°.

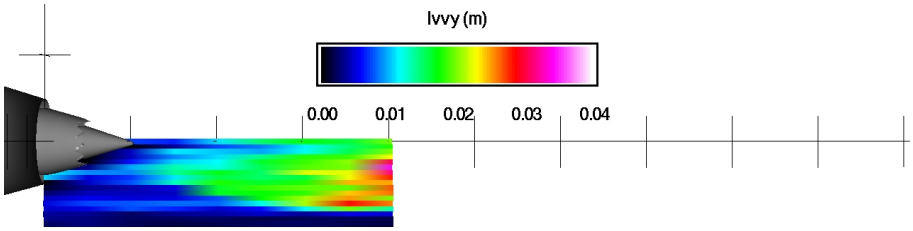

Figure 2.6.3.4 Model 3ab. Contour plots of Lvv(y). Slice taken at circumferential angle = 25°.

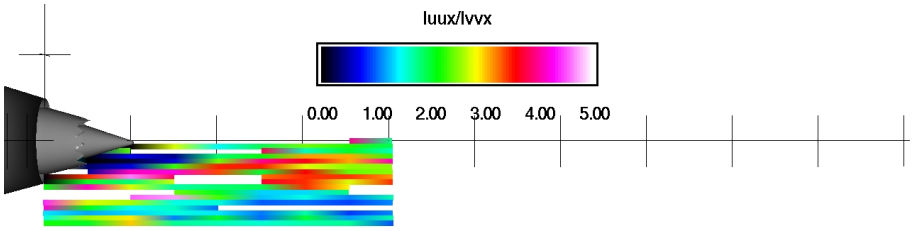

Figure 2.6.3.5 Model 3ab. Contour plots of Luu(x)/Lvv(x). Slice taken at circumferential angle = 25°.

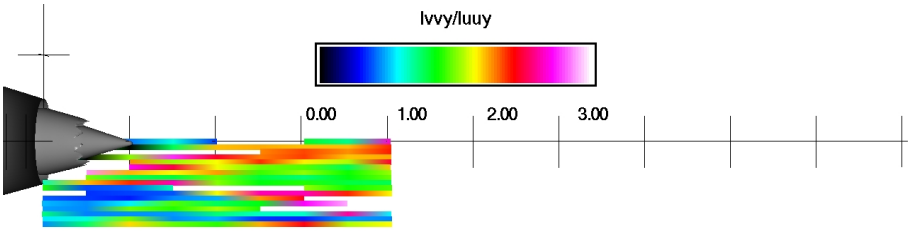

Figure 2.6.3.6 Model 3ab. Contour plots of Lvv(y)/Luu(y). Slice taken at circumferential angle = 25°.

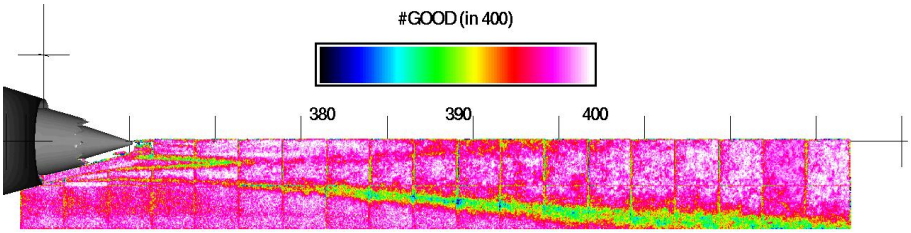

Figure 2.7.1.1 Model 3ab. Contour plots of data quality (#good out of 400). Slice taken at circumferential angle = 30°.

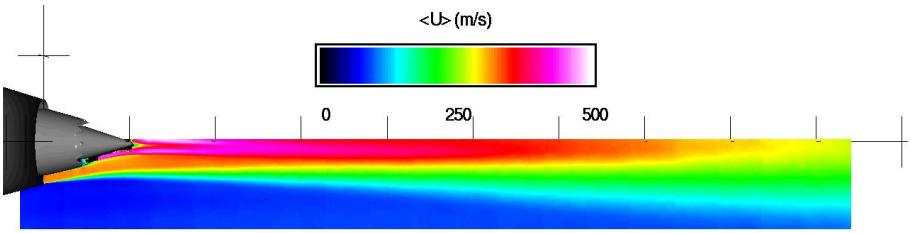

Figure 2.7.1.2 Model 3ab. Contour plots of time average axial velocity (m/s). Slice taken at circumferential angle = 30°.

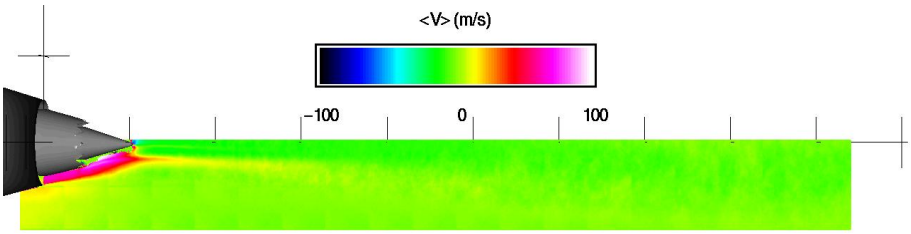

Figure 2.7.1.3 Model 3ab. Contour plots of time average radial velocity (m/s). Slice taken at circumferential angle = 30°.

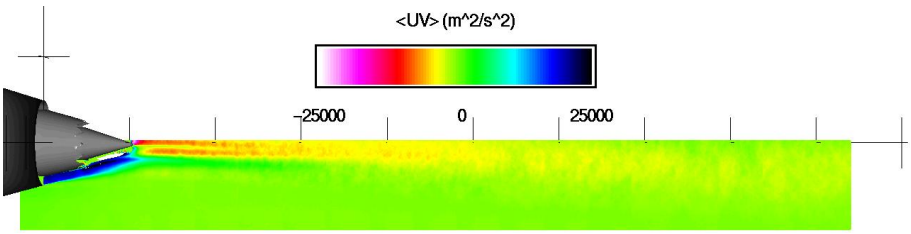

Figure 2.7.1.4 Model 3ab. Contour plots of time average Reynolds stress (m^2/s^2). Slice taken at circumferential angle = 30°.

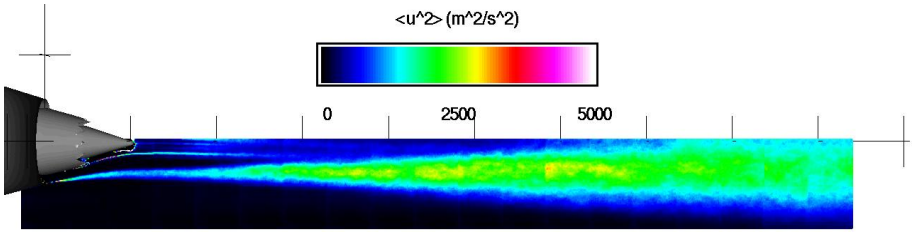

Figure 2.7.1.5 Model 3ab. Contour plots of variance of axial velocity (m^2/s^2). Slice taken at circumferential angle = 30°.

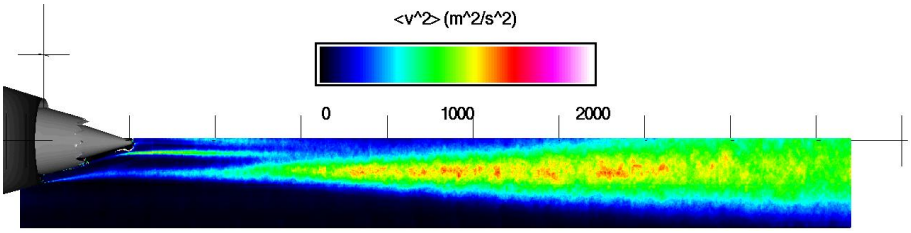

Figure 2.7.1.6 Model 3ab. Contour plots of variance in radial velocity (m^2/s^2). Slice taken at circumferential angle = 30°.

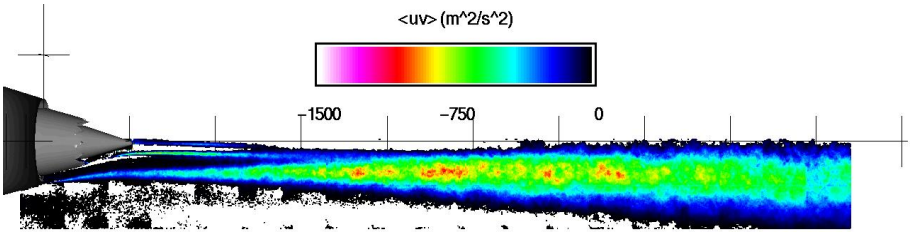

Figure 2.7.1.7 Model 3ab. Contour plots of unsteady Reynolds stress (m^2/s^2). Slice taken at circumferential angle = 30°.

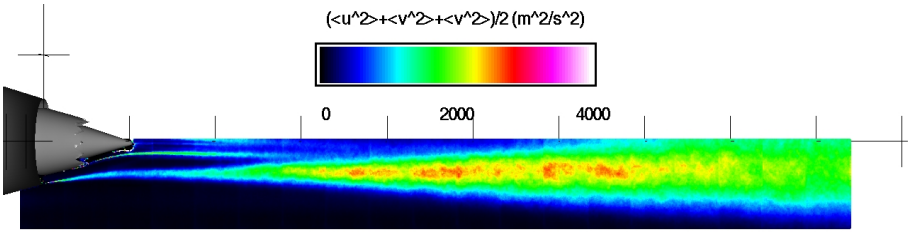

Figure 2.7.1.8 Model 3ab. Contour plots of turbulent kinetic energy (m^2/s^2). Slice taken at circumferential angle = 30°.

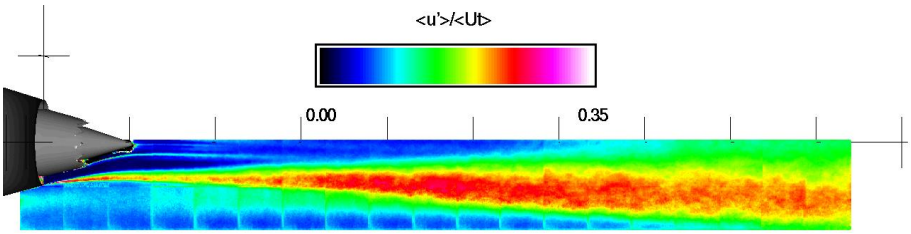

Figure 2.7.1.9 Model 3ab. Contour plots of axial turbulence intensity. Slice taken at circumferential angle = 30°.

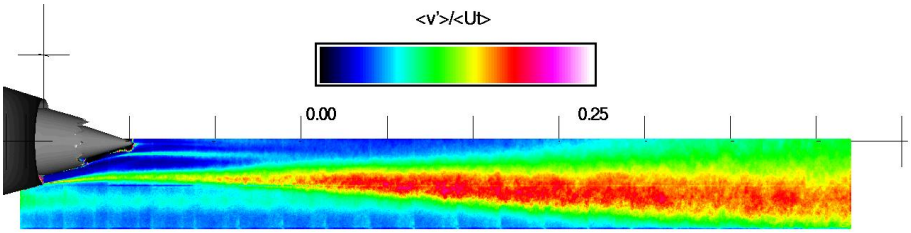

Figure 2.7.1.10 Model 3ab. Contour plots of radial turbulence intensity. Slice taken at circumferential angle = 30°.

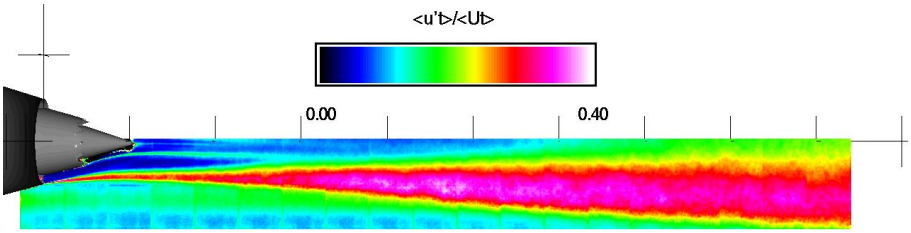

Figure 2.7.1.11 Model 3ab. Contour plots of turbulence intensity. Slice taken at circumferential angle = 30°.

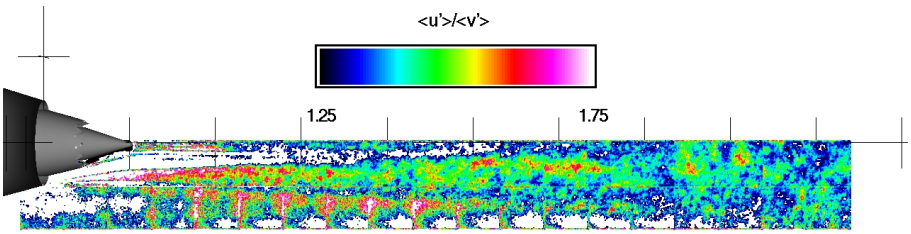

Figure 2.7.1.12 Model 3ab. Contour plots of ratio of axial to radial turbulence. Slice taken at circumferential angle = 30°.

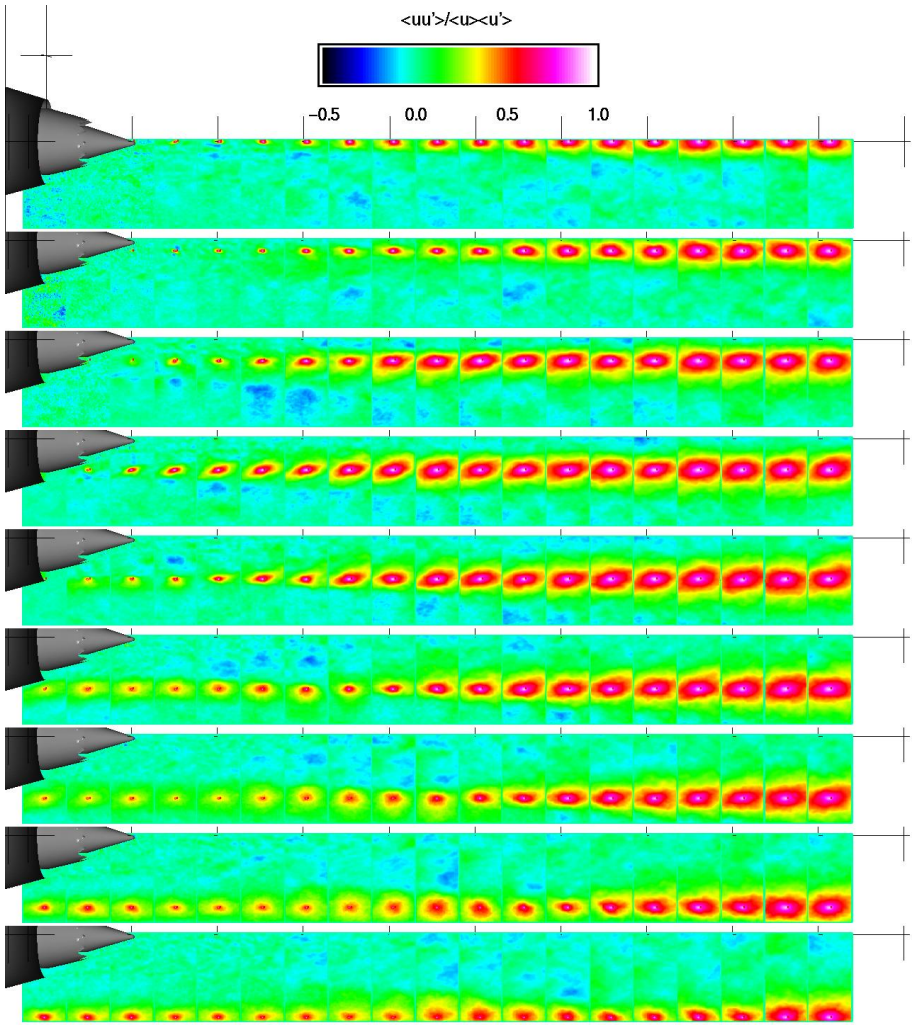

Figure 2.7.2.1 Model 3ab. Contour plots of u(xref)u(x). Slice taken at circumferential angle = 30°.

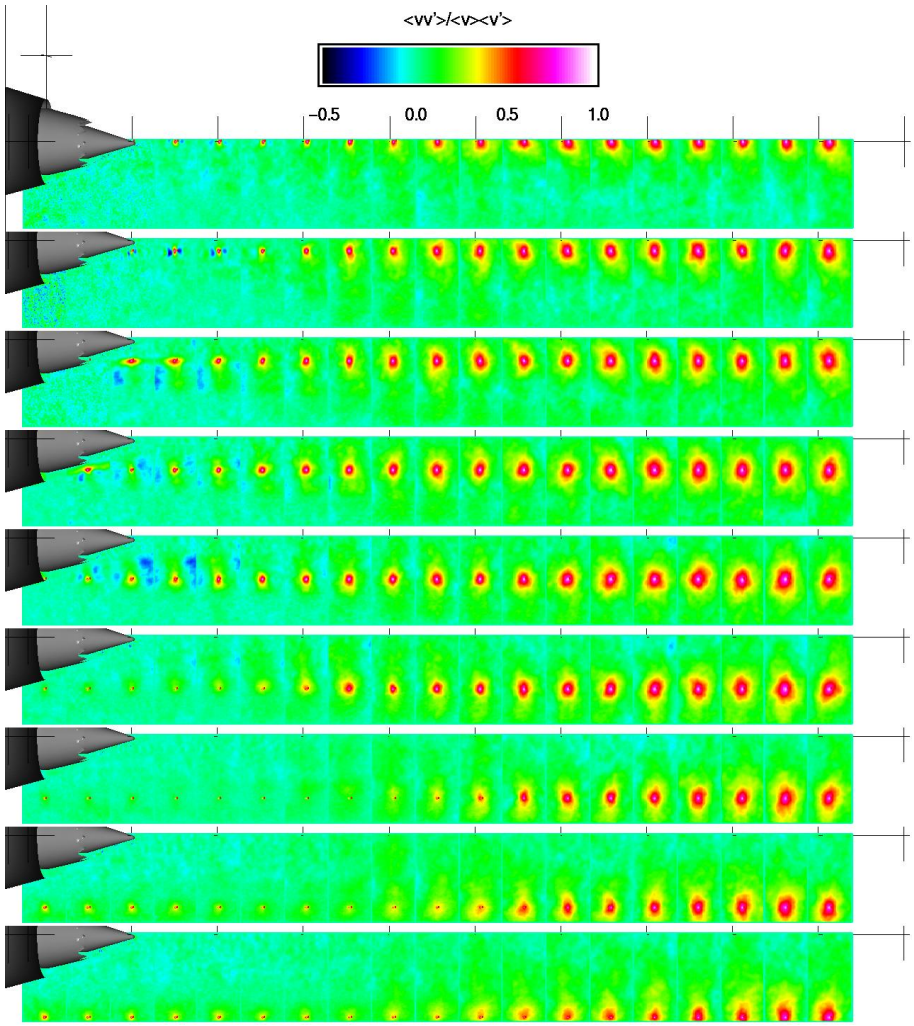

Figure 2.7.2.2 Model 3ab. Contour plots of v(xref)v(x). Slice taken at circumferential angle = 30°.

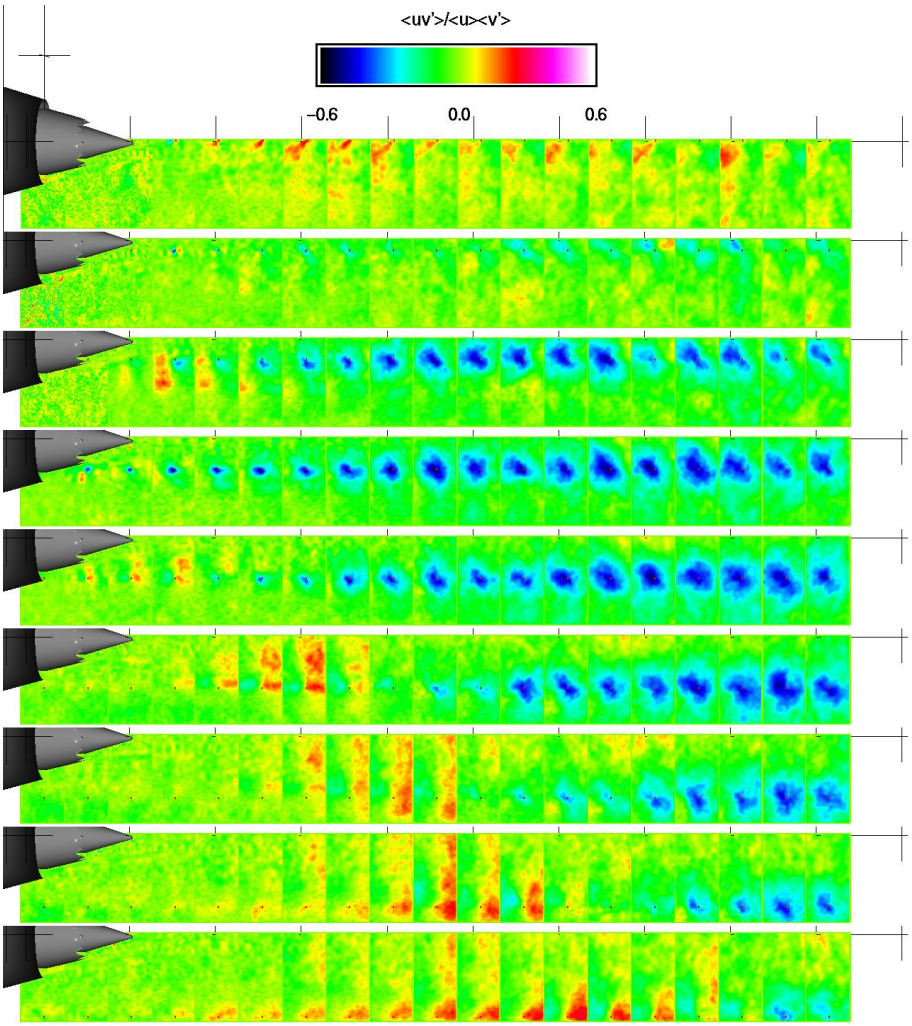

Figure 2.7.2.3 Model 3ab. Contour plots of u(xref)v(x). Slice taken at circumferential angle = 30°.

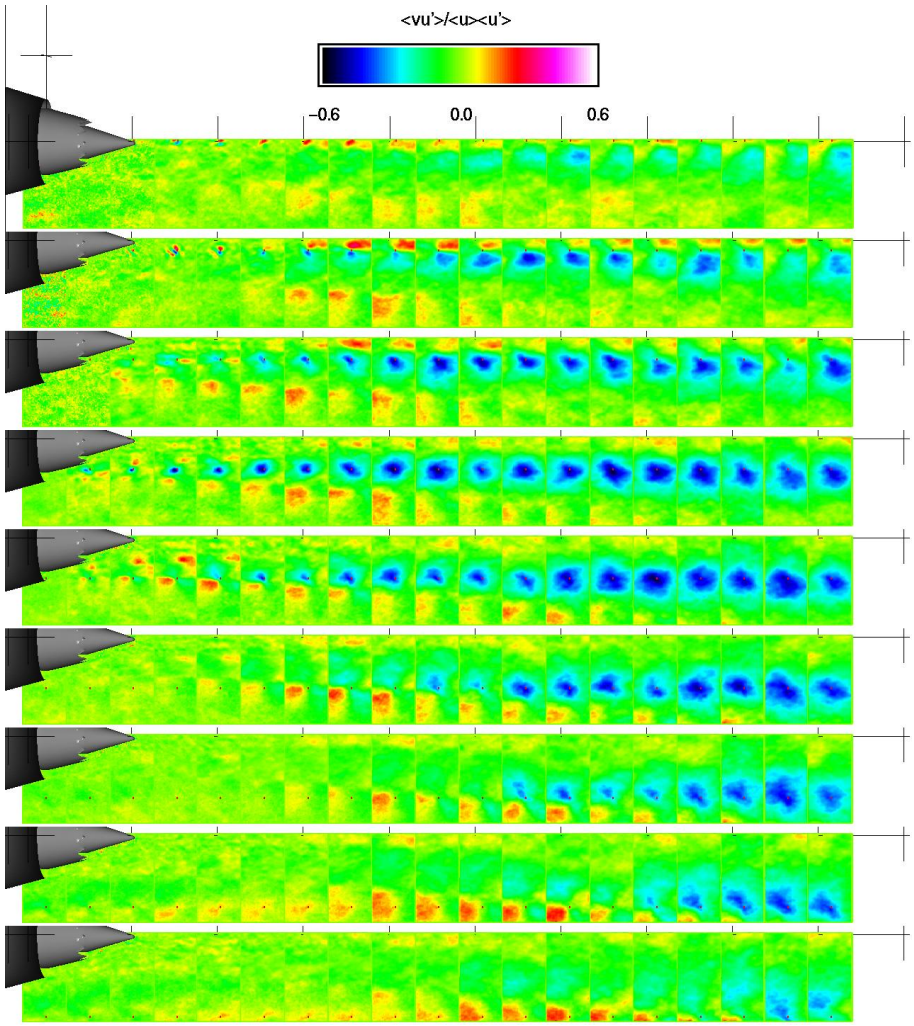

Figure 2.7.2.4 Model 3ab. Contour plots of v(xref)u(x). Slice taken at circumferential angle = 30°.

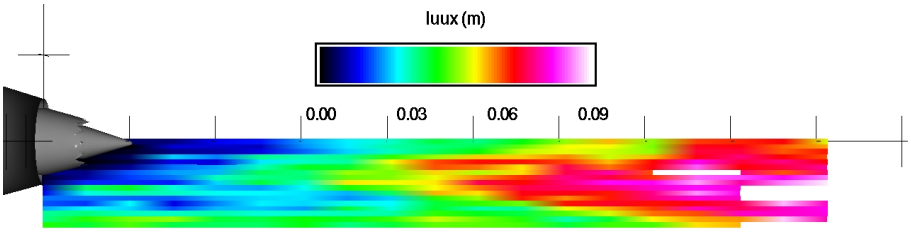

Figure 2.7.3.1 Model 3ab. Contour plots of Luu(x). Slice taken at circumferential angle = 30°.

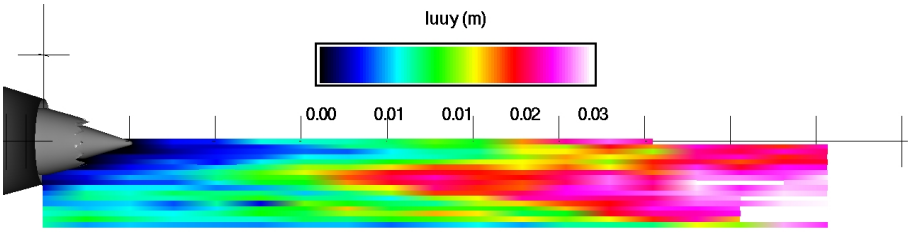

Figure 2.7.3.2 Model 3ab. Contour plots of Luu(y). Slice taken at circumferential angle = 30°.

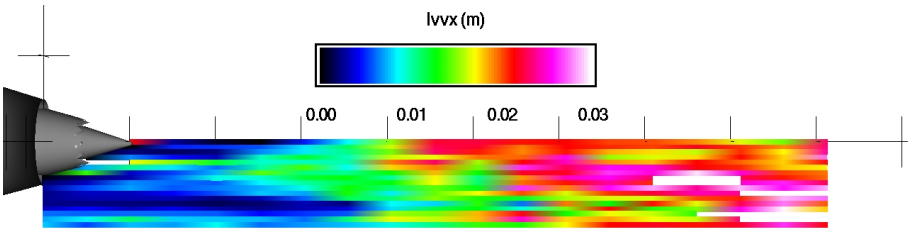

Figure 2.7.3.3 Model 3ab. Contour plots of Lvv(x). Slice taken at circumferential angle = 30°.

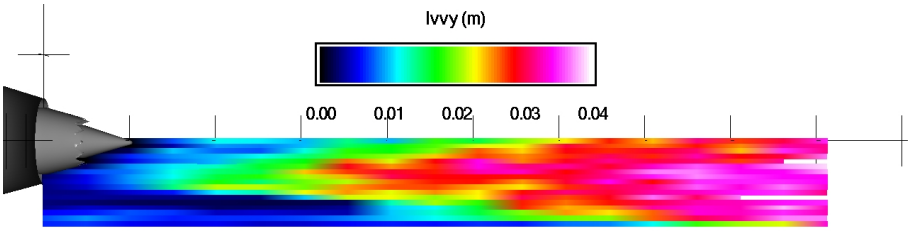

Figure 2.7.3.4 Model 3ab. Contour plots of Lvv(y). Slice taken at circumferential angle = 30°.

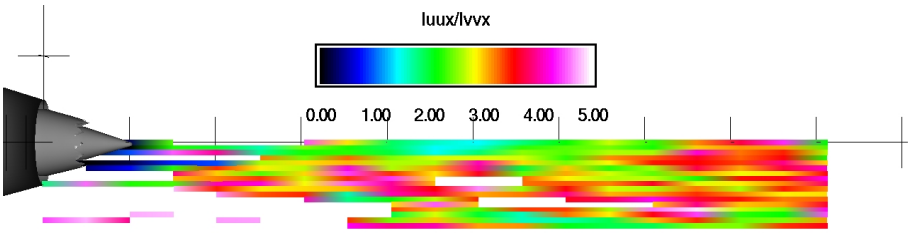

Figure 2.7.3.5 Model 3ab. Contour plots of Luu(x)/Lvv(x). Slice taken at circumferential angle = 30°.

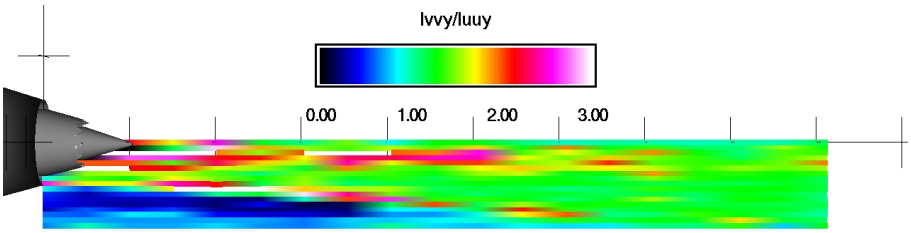

Figure 2.7.3.6 Model 3ab. Contour plots of Lvv(y)/Luu(y). Slice taken at circumferential angle = 30°.

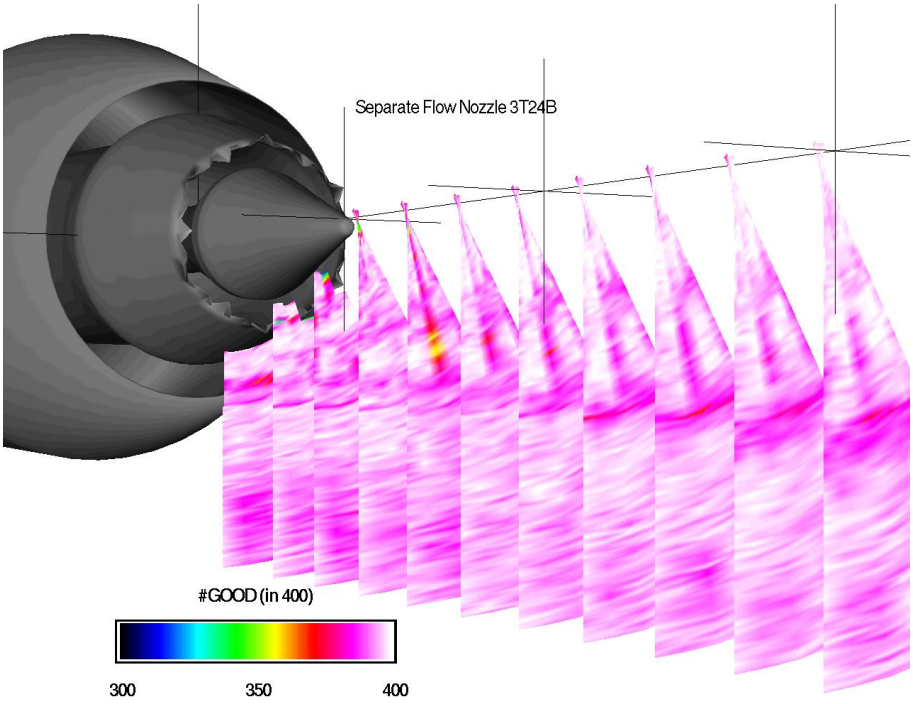

Figure 3.0.1.1 Model 3tb. Contour plots of data quality (#good out of 400). Slices taken at x = {0.047 0.132 0.199 0.267 0.334 0.401 0.468 0.535 0.603 0.670 0.737} meters.

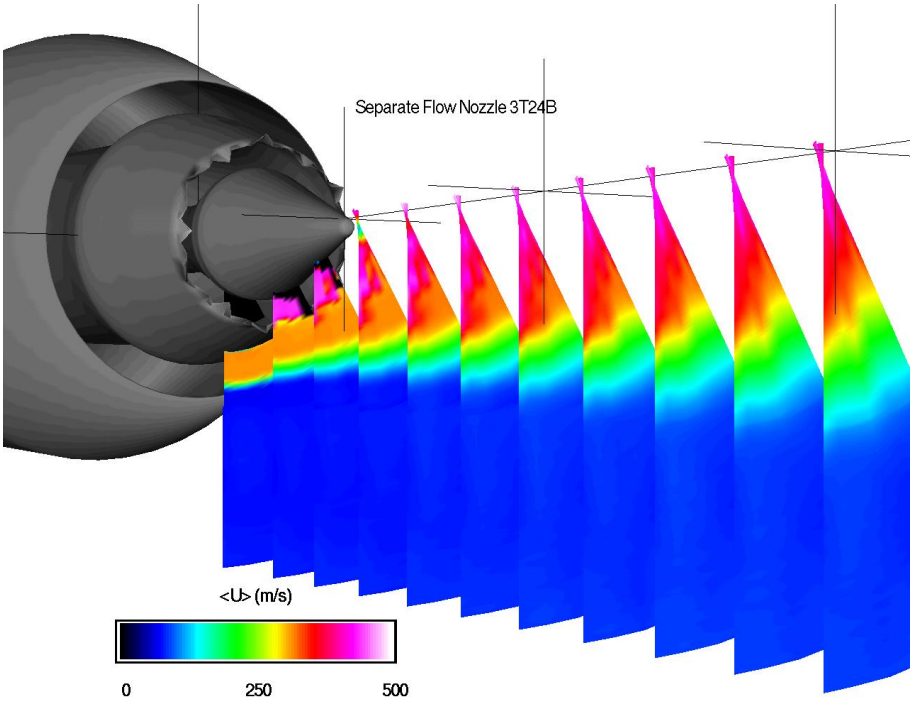

Figure 3.0.1.2 Model 3tb. Contour plots of time average axial velocity (m/s). Slices taken at x = {0.047 0.132 0.199 0.267 0.334 0.401 0.468 0.535 0.603 0.670 0.737} meters.

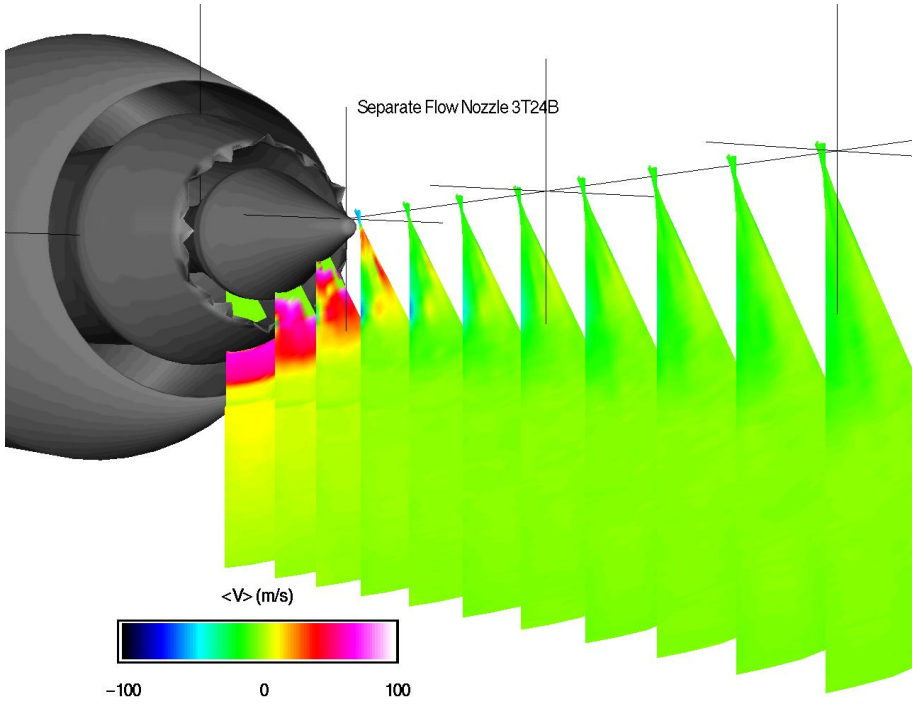

Figure 3.0.1.3 Model 3tb. Contour plots of time average radial velocity (m/s). Slices taken at x = {0.047 0.132 0.199 0.267 0.334 0.401 0.468 0.535 0.603 0.670 0.737} meters.

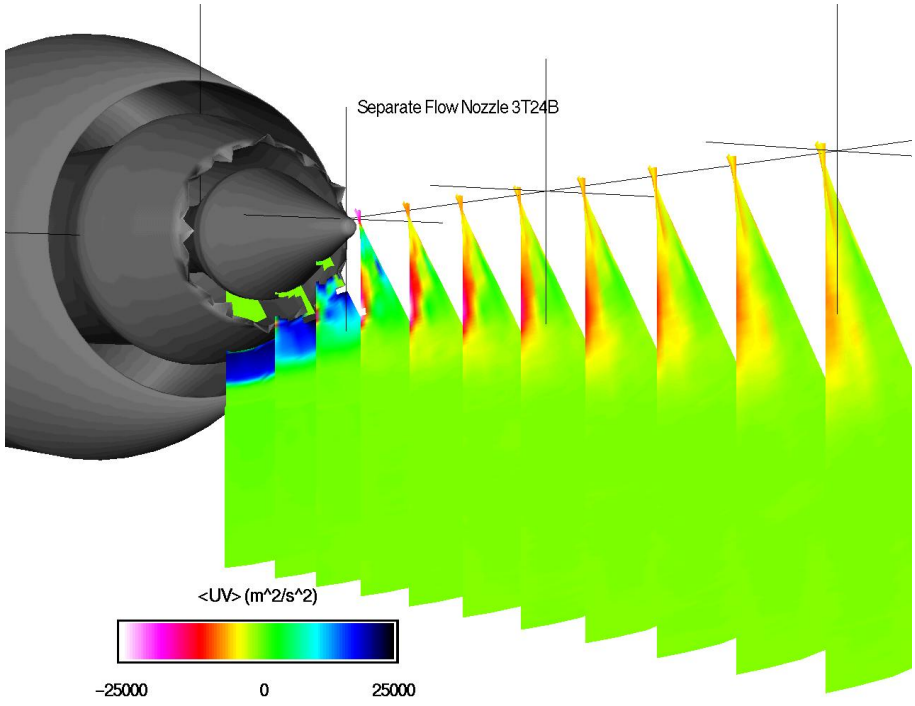

Figure 3.0.1.4 Model 3tb. Contour plots of time average Reynolds stress (m^2/s^2). Slices taken at x = {0.047 0.132 0.199 0.267 0.334 0.401 0.468 0.535 0.603 0.670 0.737} meters.

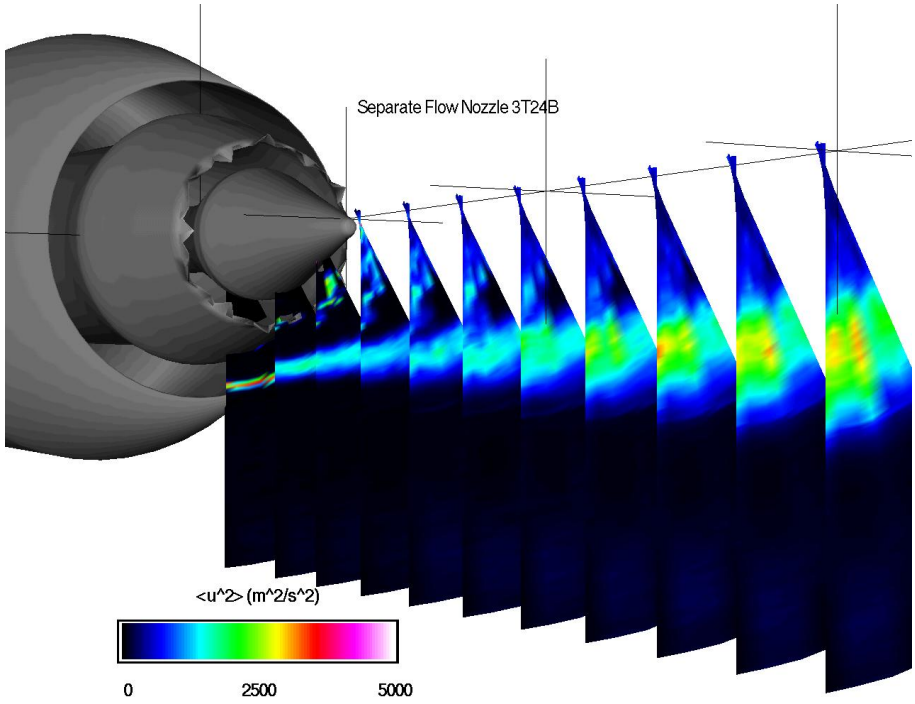

Figure 3.0.1.5 Model 3tb. Contour plots of variance of axial velocity (m^2/s^2). Slices taken at x = {0.047 0.132 0.199 0.267 0.334 0.401 0.468 0.535 0.603 0.670 0.737} meters.

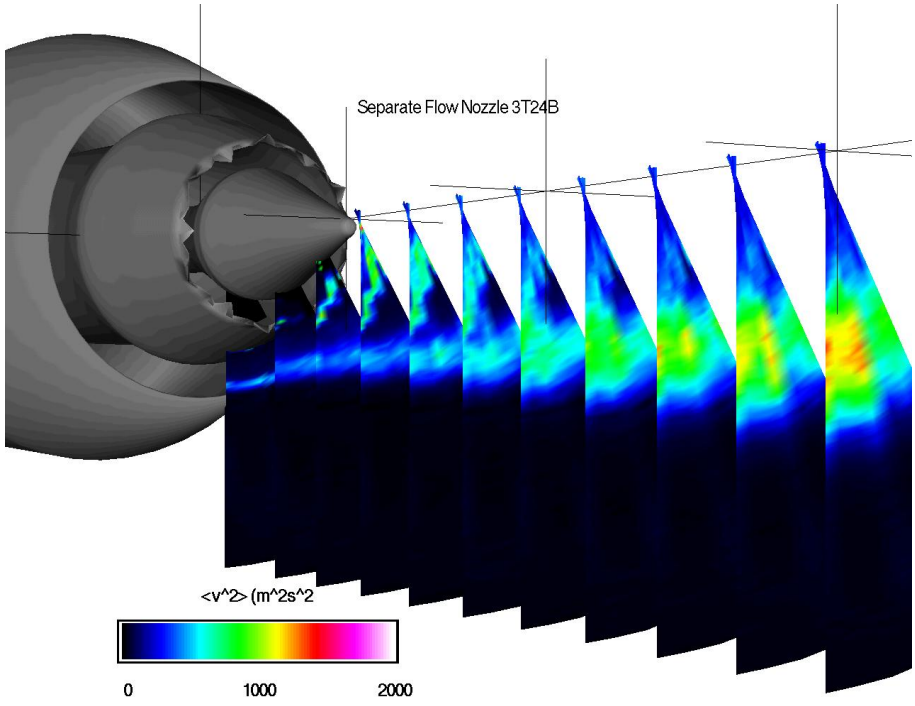

Figure 3.0.1.6 Model 3tb. Contour plots of variance in radial velocity (m^2/s^2). Slices taken at x = {0.047 0.132 0.199 0.267 0.334 0.401 0.468 0.535 0.603 0.670 0.737} meters.

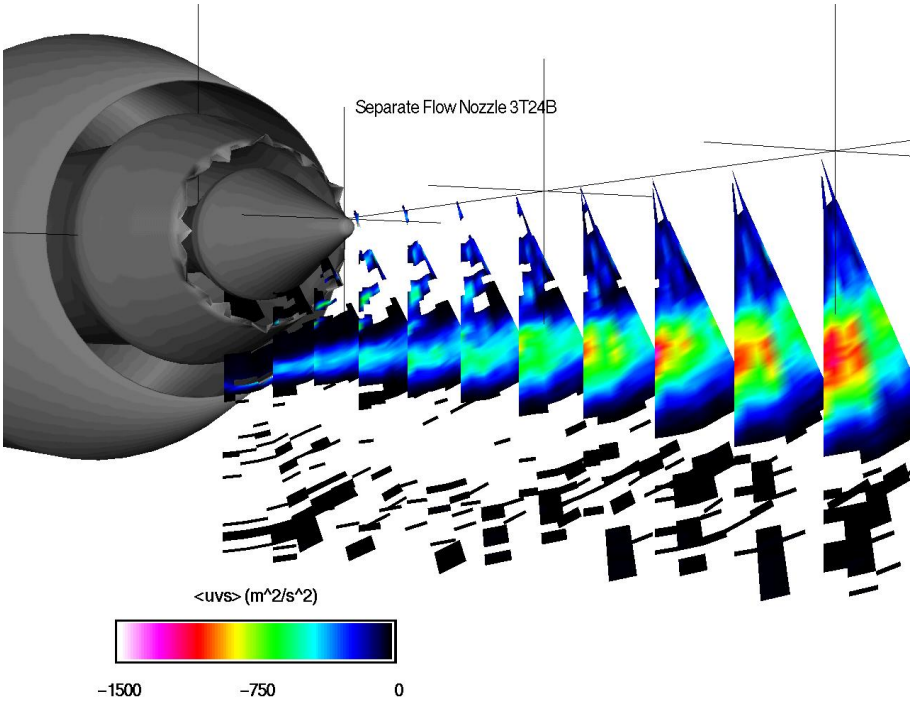

Figure 3.0.1.7 Model 3tb. Contour plots of unsteady Reynolds stress (m^2/s^2). Slices taken at x = {0.047 0.132 0.199 0.267 0.334 0.401 0.468 0.535 0.603 0.670 0.737} meters.

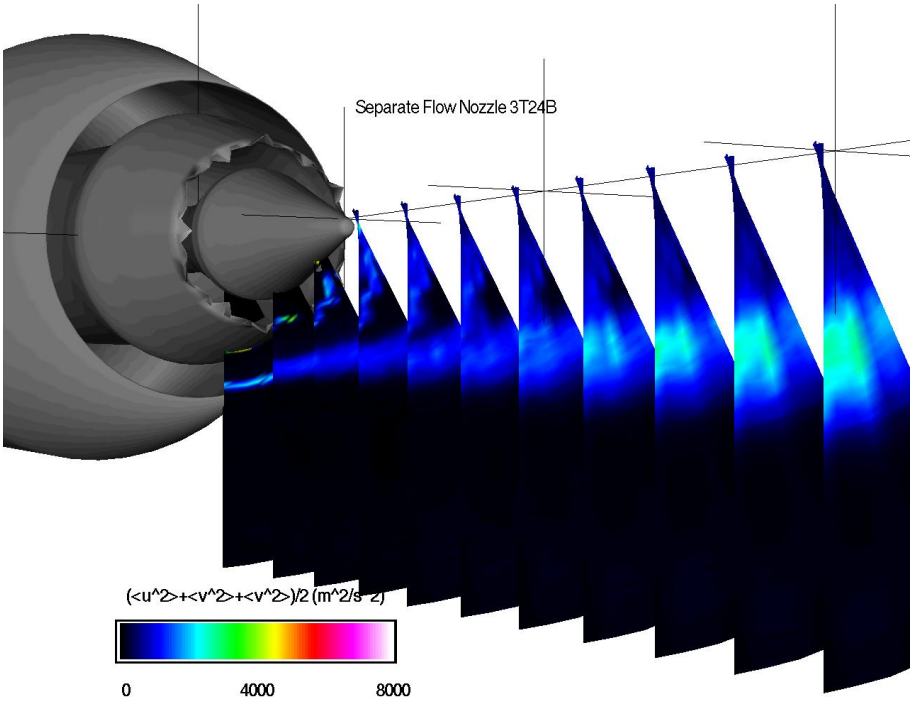

Figure 3.0.1.8 Model 3tb. Contour plots of turbulent kinetic energy (m^2/s^2). Slices taken at x = {0.047 0.132 0.199 0.267 0.334 0.401 0.468 0.535 0.603 0.670 0.737} meters.

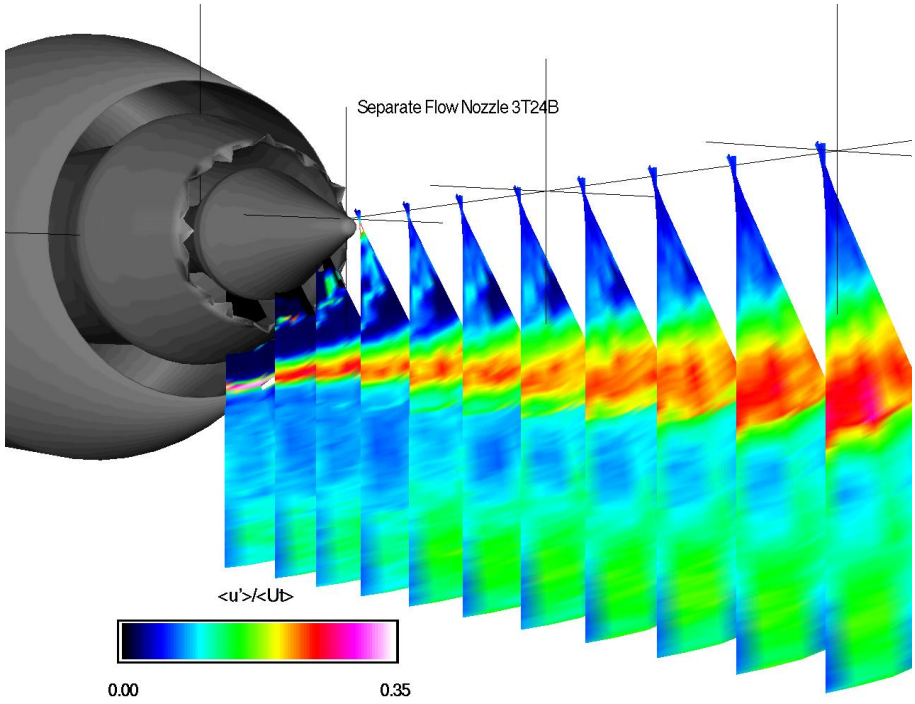

Figure 3.0.1.9 Model 3tb. Contour plots of axial turbulence intensity. Slices taken at x = {0.047 0.132 0.199 0.267 0.334 0.401 0.468 0.535 0.603 0.670 0.737} meters.

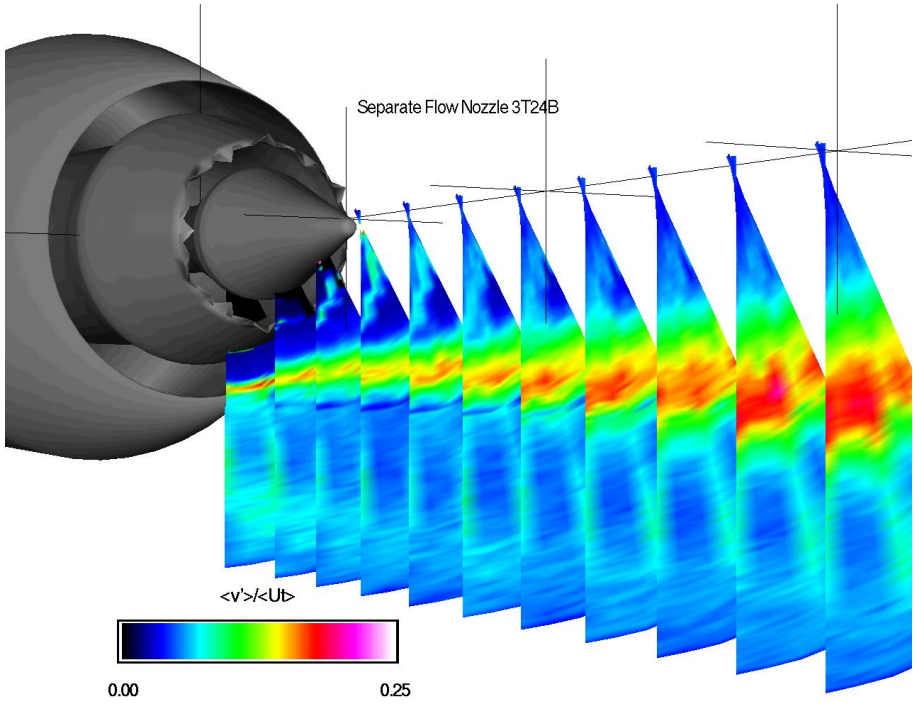

Figure 3.0.1.10 Model 3tb. Contour plots of radial turbulence intensity. Slices taken at x = {0.047 0.132 0.199 0.267 0.334 0.401 0.468 0.535 0.603 0.670 0.737} meters.

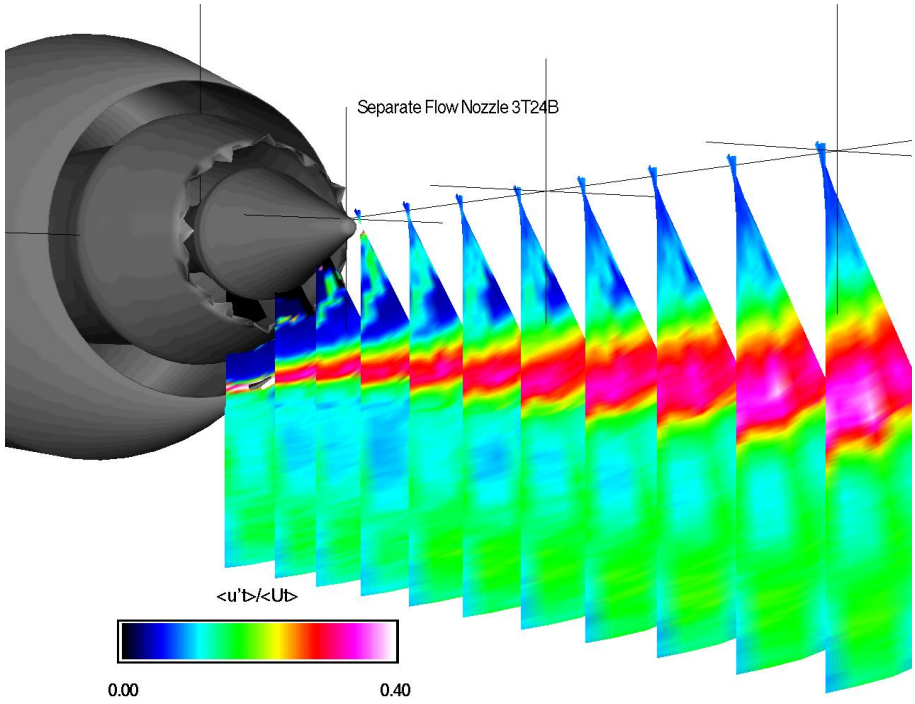

Figure 3.0.1.11 Model 3tb. Contour plots of turbulence intensity. Slices taken at x = {0.047 0.132 0.199 0.267 0.334 0.401 0.468 0.535 0.603 0.670 0.737} meters.

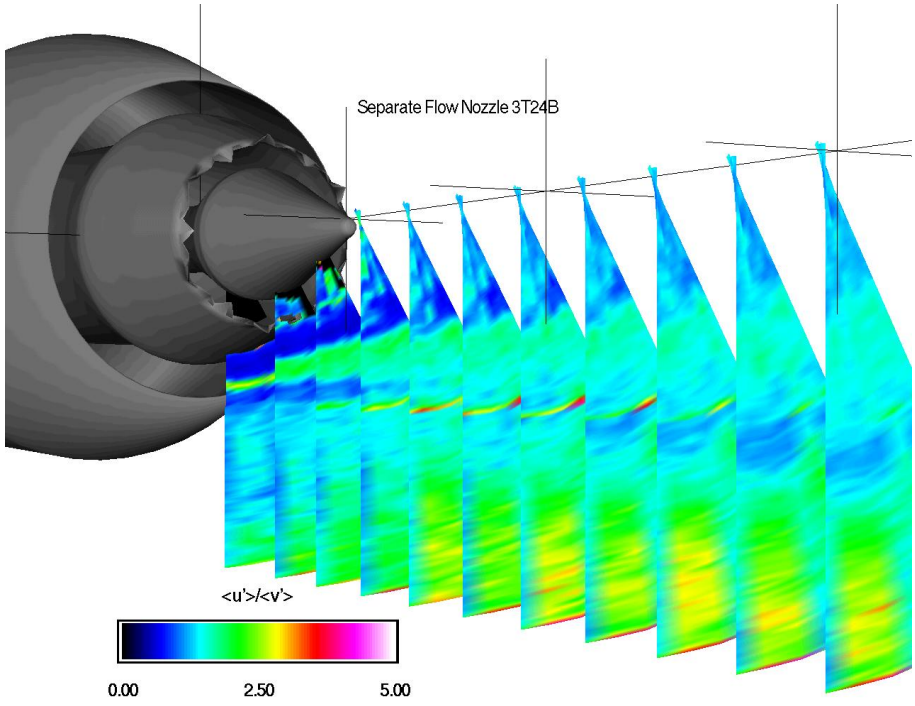

Figure 3.0.1.12 Model 3tb. Contour plots of ratio of axial to radial turbulence. Slices taken at x = {0.047 0.132 0.199 0.267 0.334 0.401 0.468 0.535 0.603 0.670 0.737} meters.

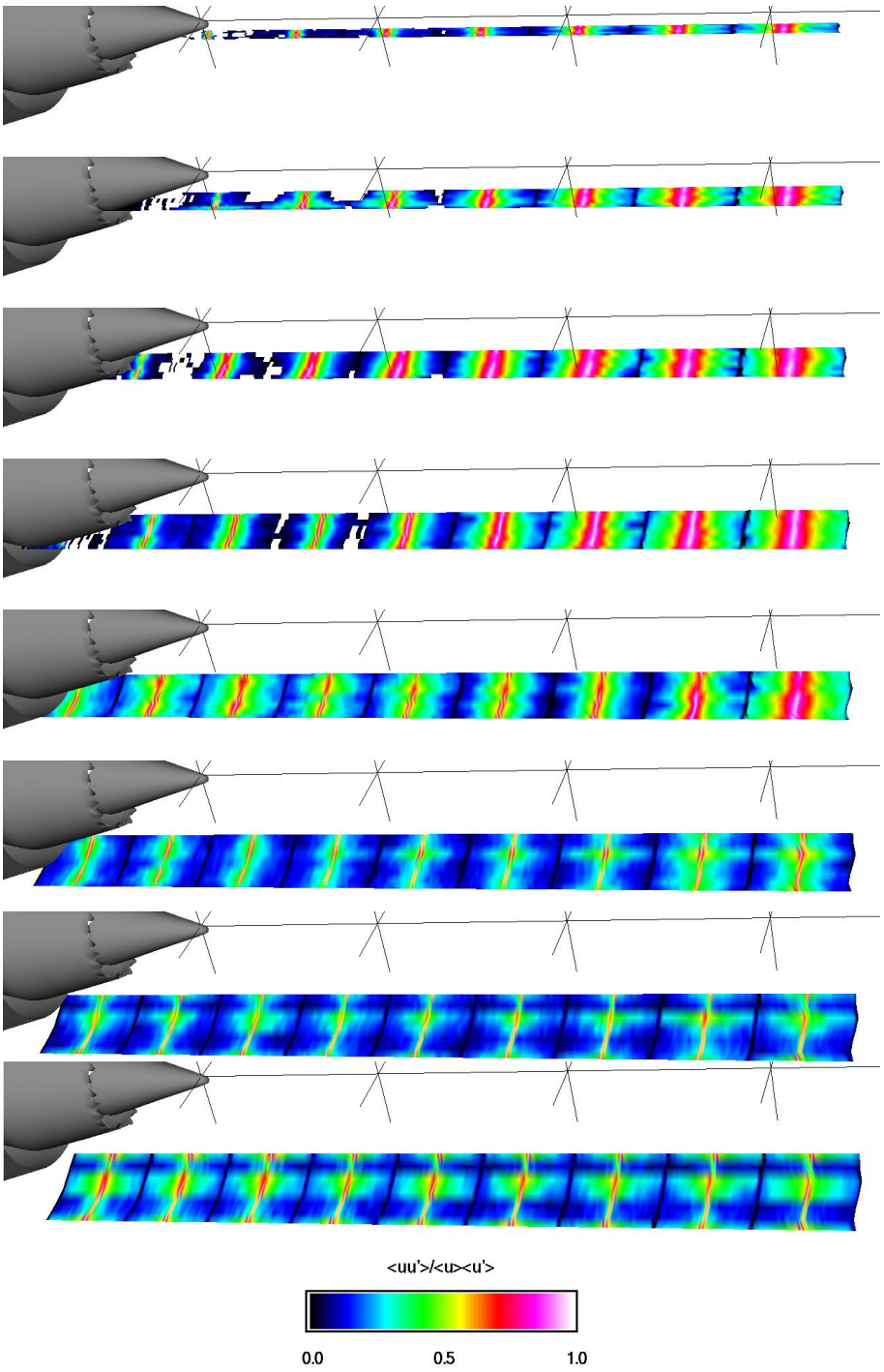

Figure 3.0.2.1 Model 3tb. Contour plots of u(xref)u(x). Slices taken at radius = {0.00 0.03 0.06 0.09 0.12 0.15 0.18 0.21 0.24} meters.

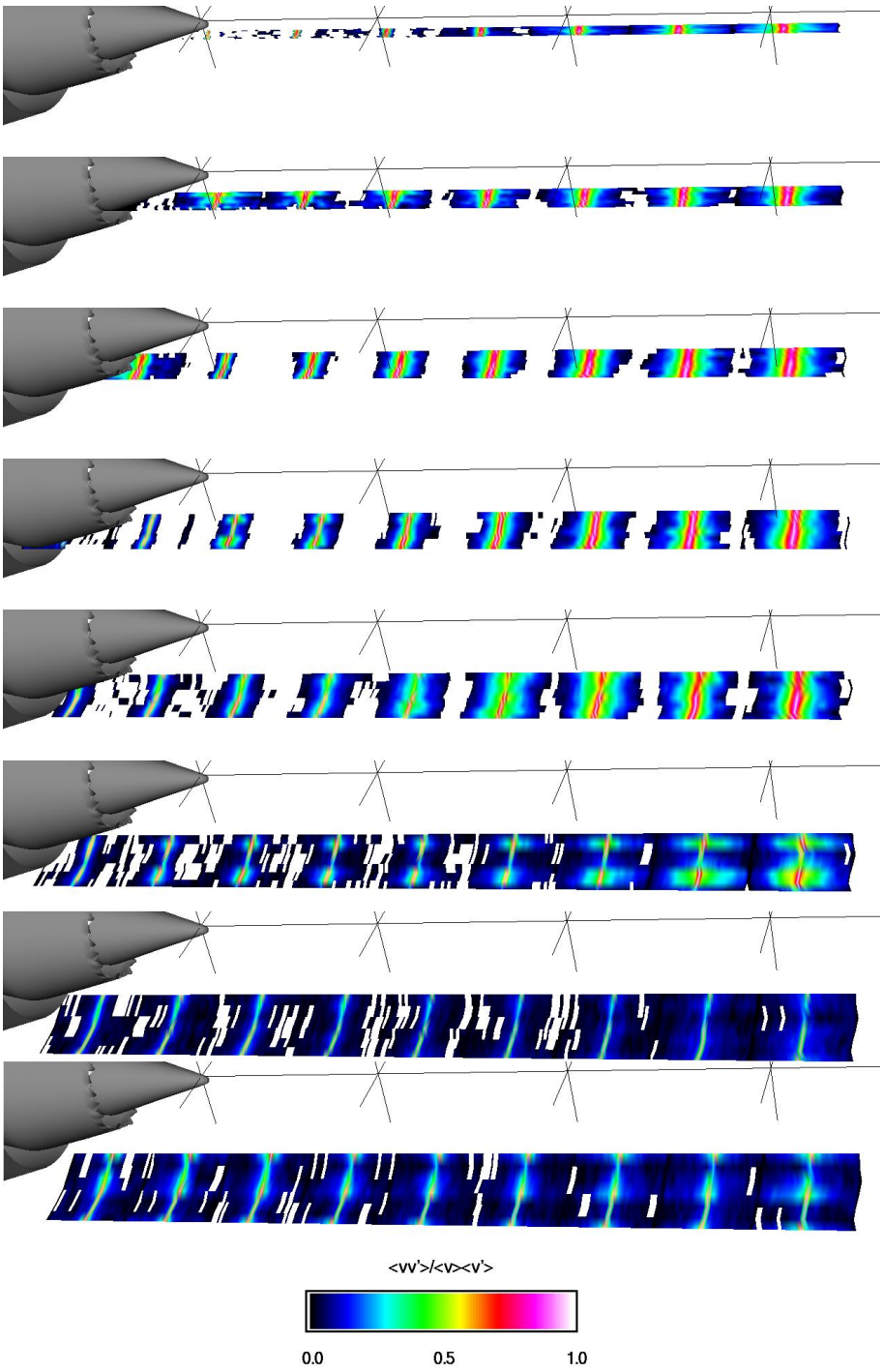

Figure 3.0.2.2 Model 3tb. Contour plots of v(xref)v(x). Slices taken at radius = {0.00 0.03 0.06 0.09 0.12 0.15 0.18 0.21 0.24} meters.

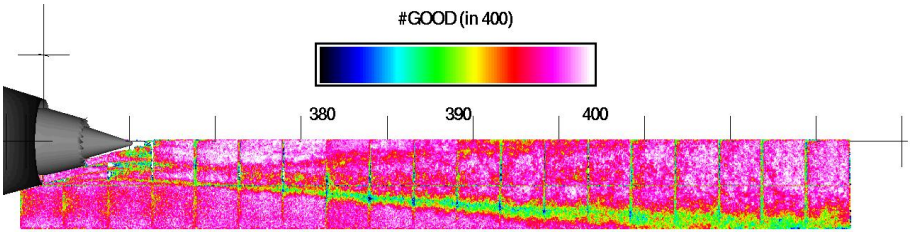

Figure 3.1.1.1 Model 3tb. Contour plots of data quality (#good out of 400). Slice taken at circumferential angle = 0°.

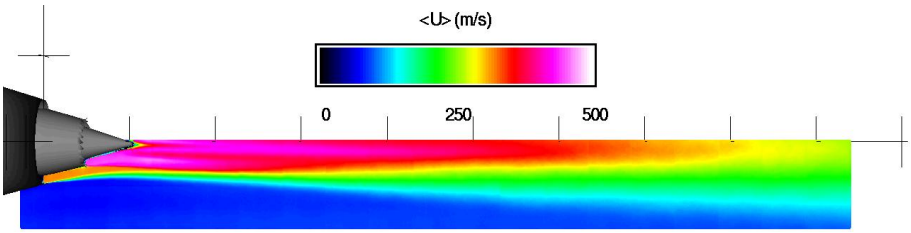

Figure 3.1.1.2 Model 3tb. Contour plots of time average axial velocity (m/s). Slice taken at circumferential angle = 0°.

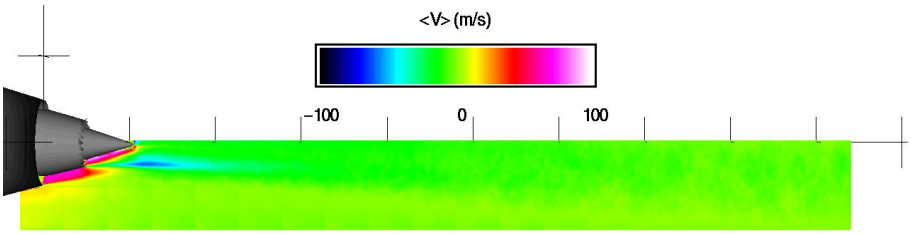

Figure 3.1.1.3 Model 3tb. Contour plots of time average radial velocity (m/s). Slice taken at circumferential angle = 0°.

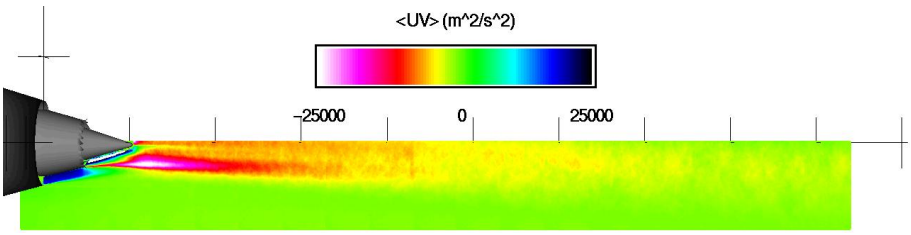

Figure 3.1.1.4 Model 3tb. Contour plots of time average Reynolds stress (m^2/s^2). Slice taken at circumferential angle = 0°.

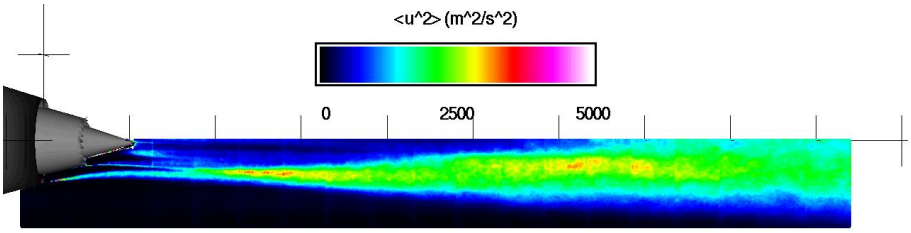

Figure 3.1.1.5 Model 3tb. Contour plots of variance of axial velocity (m^2/s^2). Slice taken at circumferential angle = 0°.

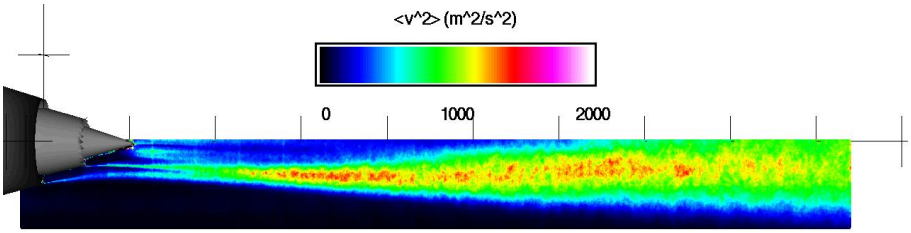

Figure 3.1.1.6 Model 3tb. Contour plots of variance in radial velocity (m^2/s^2). Slice taken at circumferential angle = 0°.

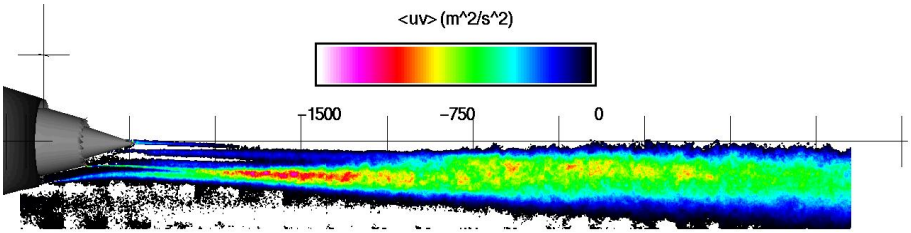

Figure 3.1.1.7 Model 3tb. Contour plots of unsteady Reynolds stress (m^2/s^2). Slice taken at circumferential angle = 0°.

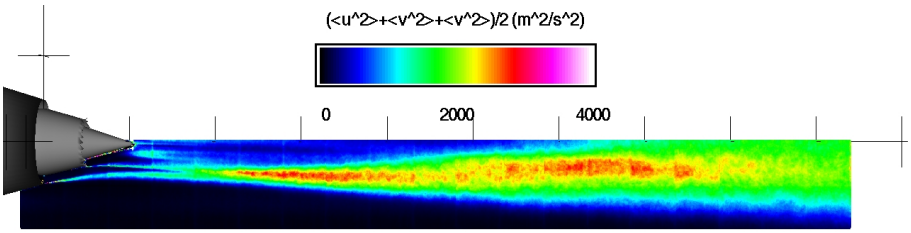

Figure 3.1.1.8 Model 3tb. Contour plots of turbulent kinetic energy (m^2/s^2). Slice taken at circumferential angle = 0°.

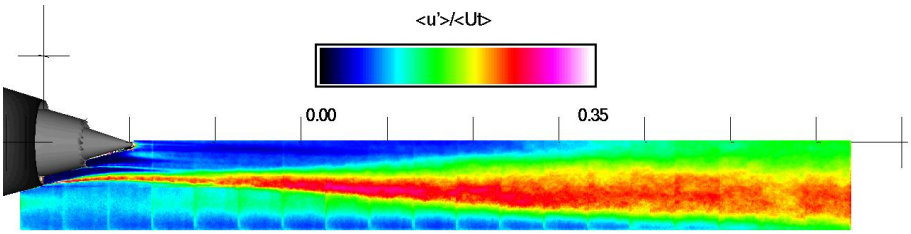

Figure 3.1.1.9 Model 3tb. Contour plots of axial turbulence intensity. Slice taken at circumferential angle = 0°.

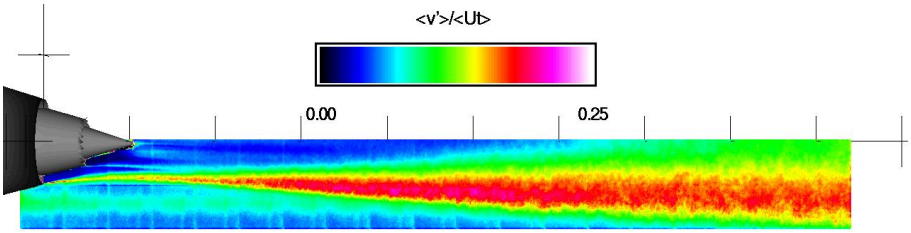

Figure 3.1.1.10 Model 3tb. Contour plots of radial turbulence intensity. Slice taken at circumferential angle = 0°.

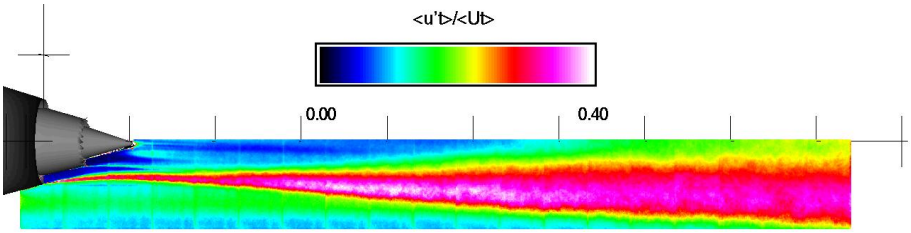

Figure 3.1.1.11 Model 3tb. Contour plots of turbulence intensity. Slice taken at circumferential angle = 0°.

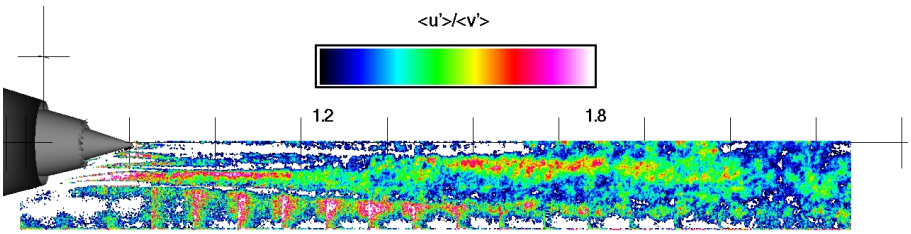

Figure 3.1.1.12 Model 3tb. Contour plots of ratio of axial to radial turbulence. Slice taken at circumferential angle = 0°.

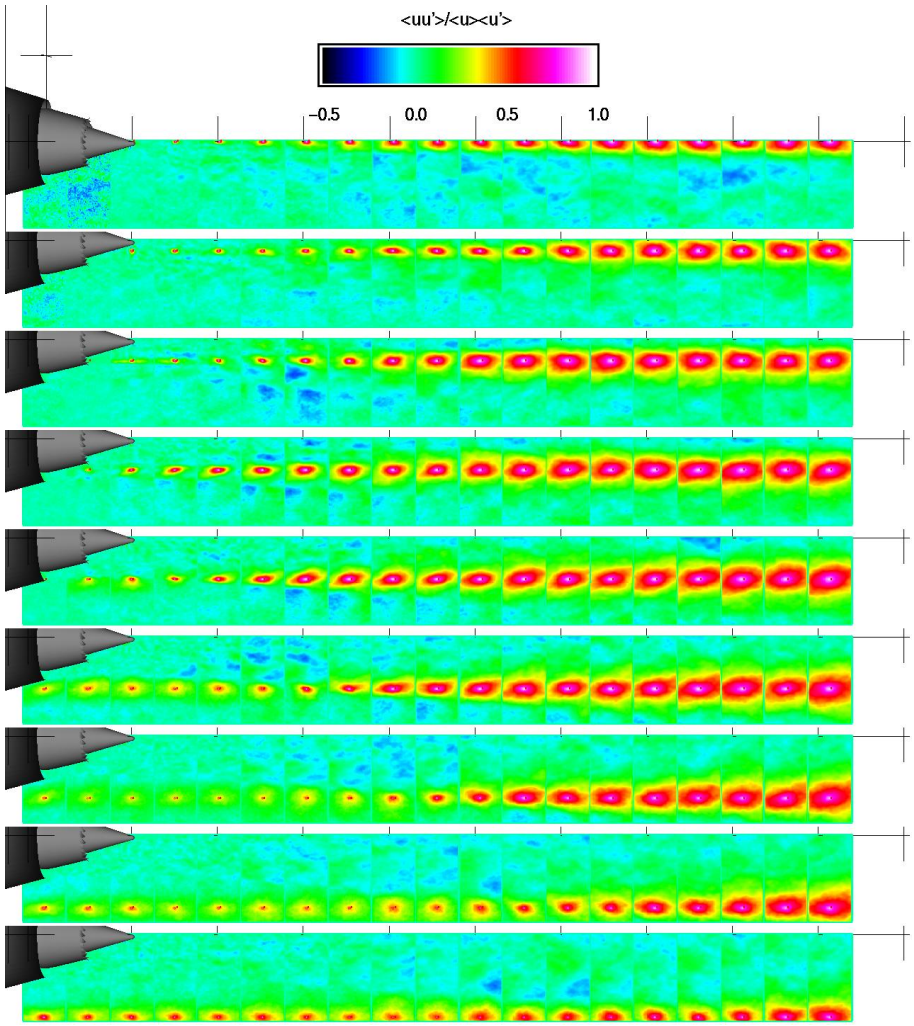

Figure 3.1.2.1 Model 3tb. Contour plots of u(xref)u(x). Slice taken at circumferential angle = 0°.

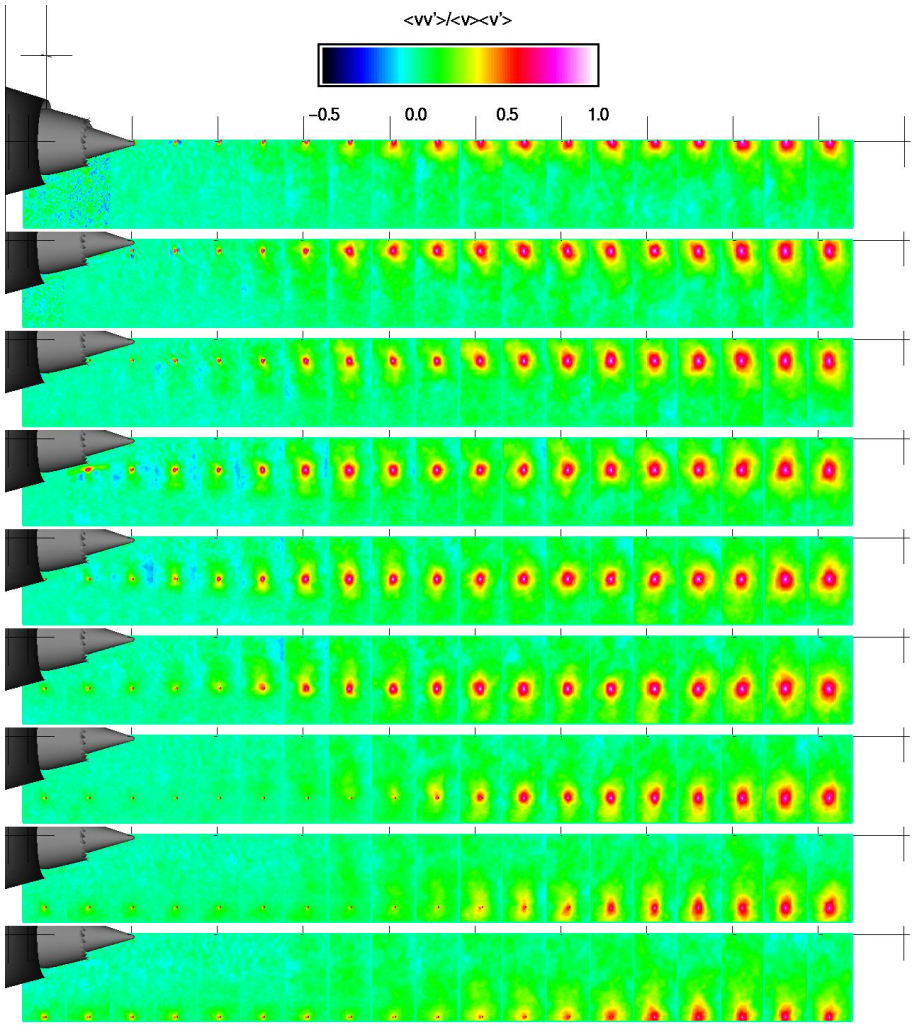

Figure 3.1.2.2 Model 3tb. Contour plots of v(xref)v(x). Slice taken at circumferential angle = 0°.

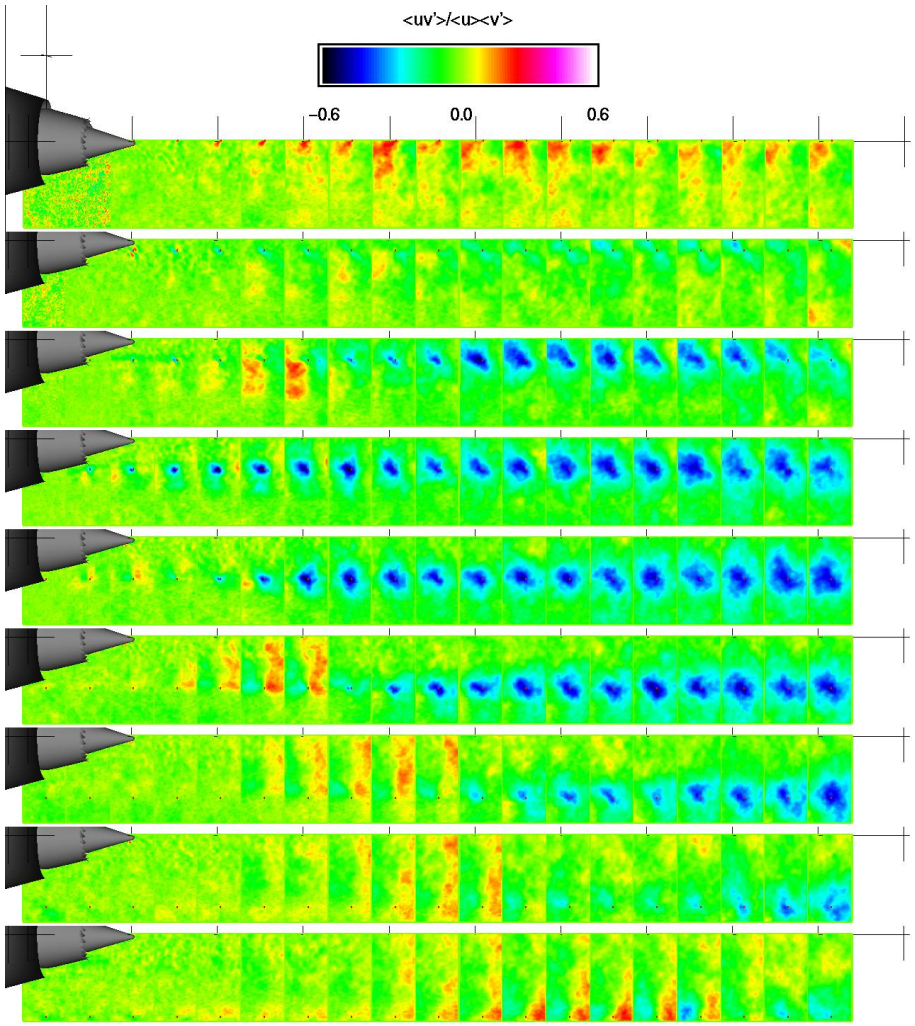

Figure 3.1.2.3 Model 3tb. Contour plots of u(xref)v(x). Slice taken at circumferential angle = 0°.

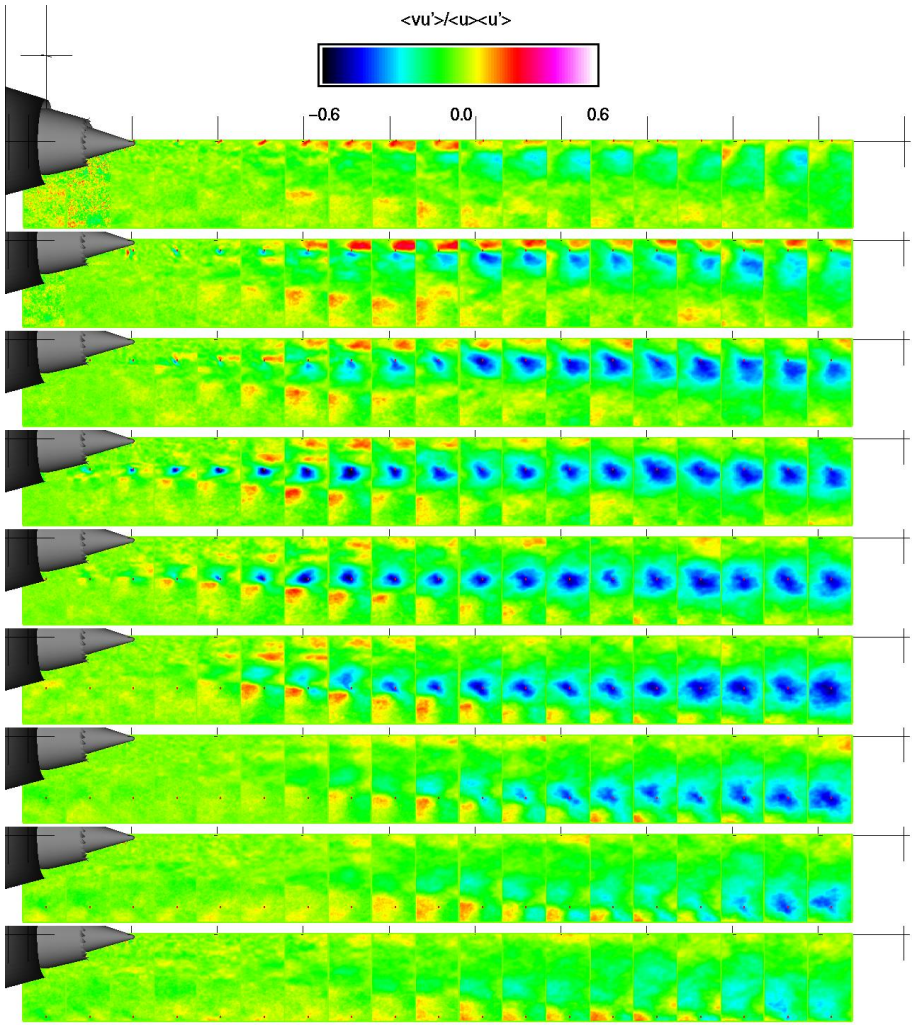

Figure 3.1.2.4 Model 3tb. Contour plots of v(xref)u(x). Slice taken at circumferential angle = 0°.

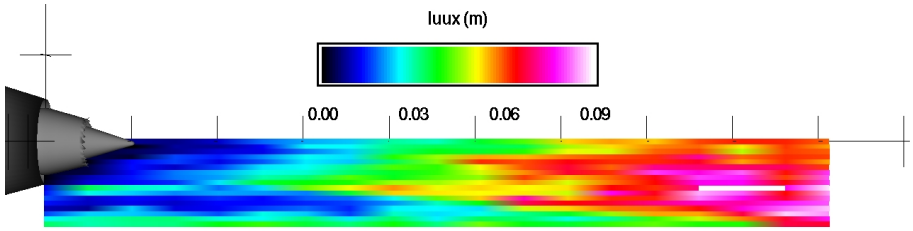

Figure 3.1.3.1 Model 3tb. Contour plots of Luu(x). Slice taken at circumferential angle = 0°.

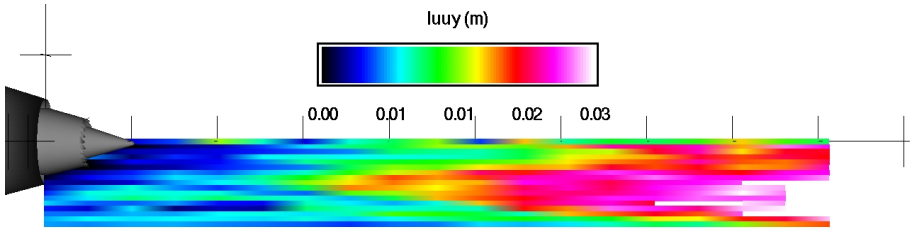

Figure 3.1.3.2 Model 3tb. Contour plots of Luu(y). Slice taken at circumferential angle = 0°.

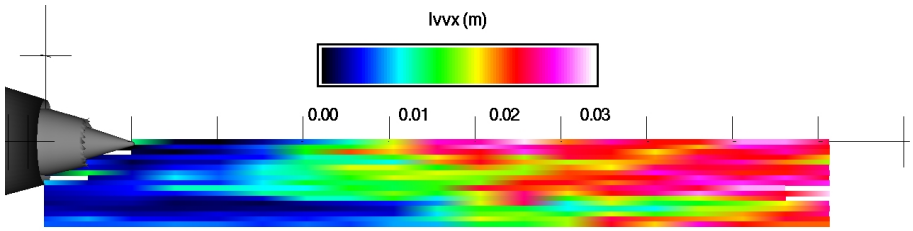

Figure 3.1.3.3 Model 3tb. Contour plots of Lvv(x). Slice taken at circumferential angle = 0°.

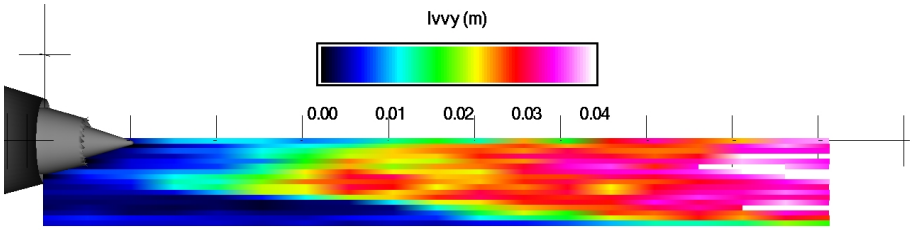

Figure 3.1.3.4 Model 3tb. Contour plots of Lvv(y). Slice taken at circumferential angle = 0°.

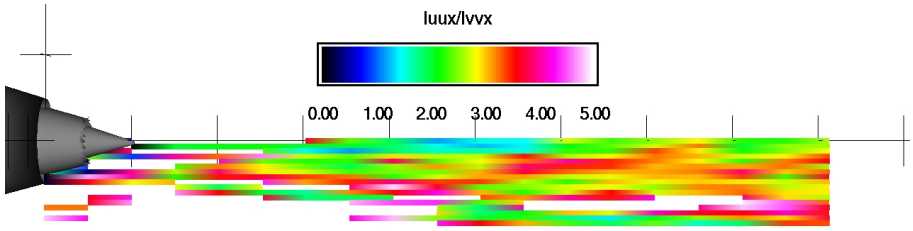

Figure 3.1.3.5 Model 3tb. Contour plots of Luu(x)/Lvv(x). Slice taken at circumferential angle = 0°.

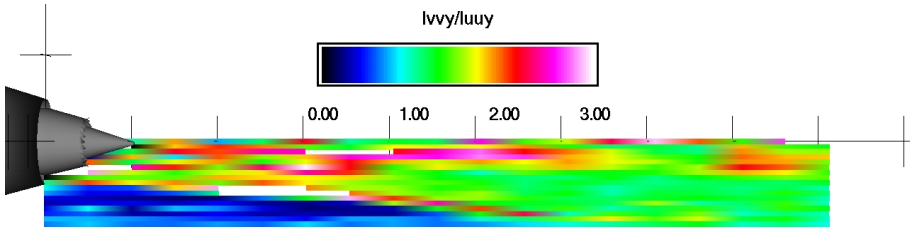

Figure 3.1.3.6 Model 3tb. Contour plots of Lvv(y)/Luu(y). Slice taken at circumferential angle = 0°.

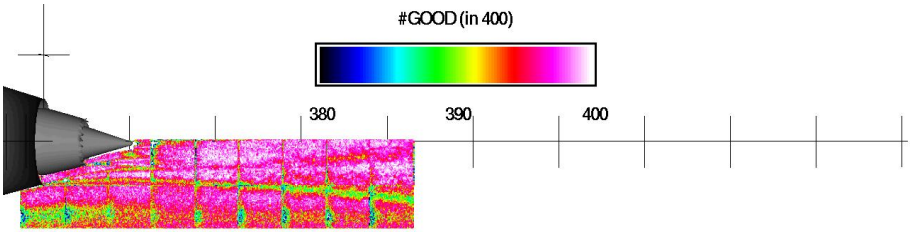

Figure 3.2.1.1 Model 3tb. Contour plots of data quality (#good out of 400). Slice taken at circumferential angle = 5°.

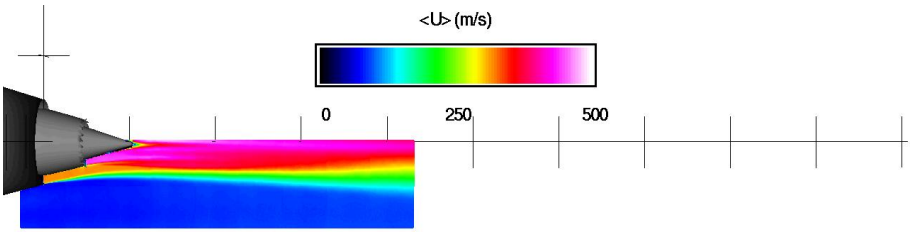

Figure 3.2.1.2 Model 3tb. Contour plots of time average axial velocity (m/s). Slice taken at circumferential angle = 5°.

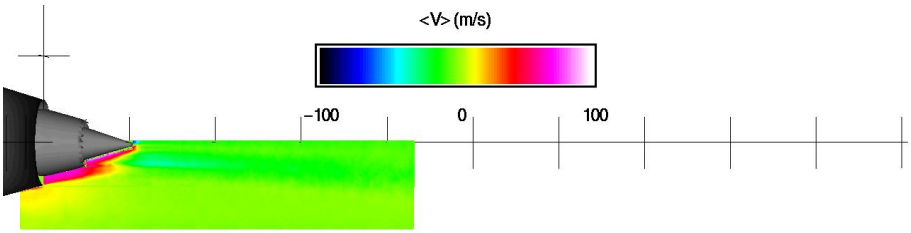

Figure 3.2.1.3 Model 3tb. Contour plots of time average radial velocity (m/s). Slice taken at circumferential angle = 5°.

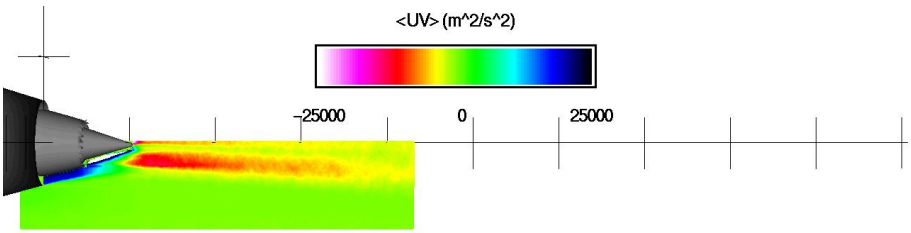

Figure 3.2.1.4 Model 3tb. Contour plots of time average Reynolds stress (m^2/s^2). Slice taken at circumferential angle = 5°.

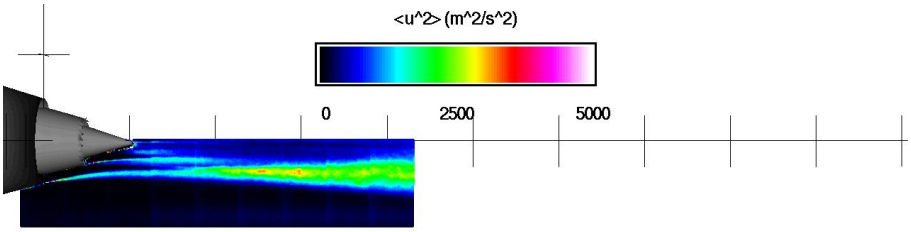

Figure 3.2.1.5 Model 3tb. Contour plots of variance of axial velocity (m^2/s^2). Slice taken at circumferential angle = 5°.

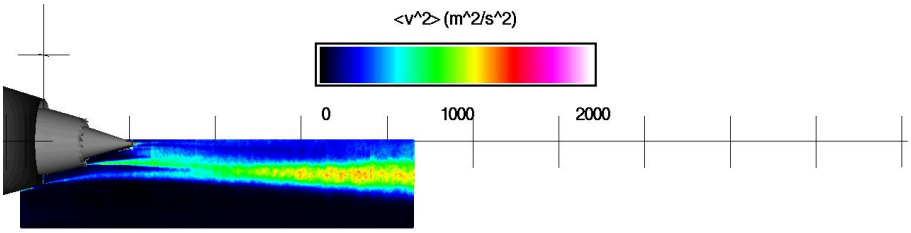

Figure 3.2.1.6 Model 3tb. Contour plots of variance in radial velocity (m^2/s^2). Slice taken at circumferential angle = 5°.

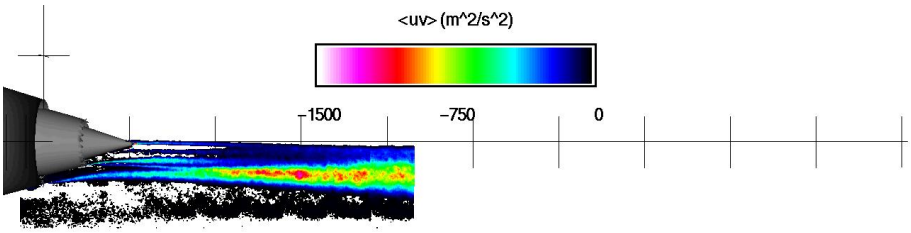

Figure 3.2.1.7 Model 3tb. Contour plots of unsteady Reynolds stress (m^2/s^2). Slice taken at circumferential angle = 5°.

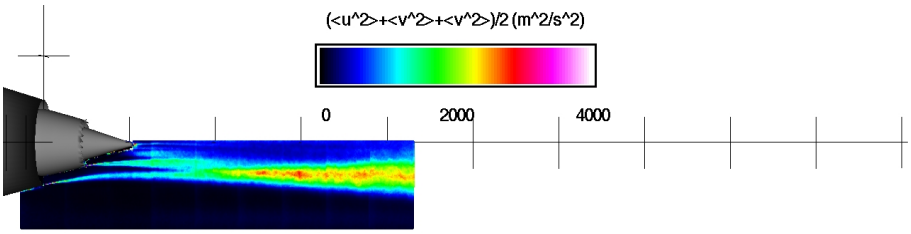

Figure 3.2.1.8 Model 3tb. Contour plots of turbulent kinetic energy (m^2/s^2). Slice taken at circumferential angle = 5°.

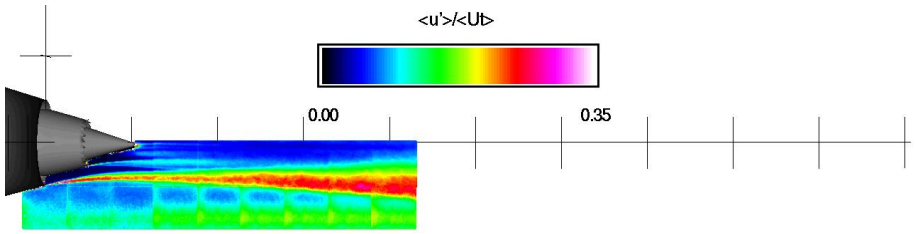

Figure 3.2.1.9 Model 3tb. Contour plots of axial turbulence intensity. Slice taken at circumferential angle = 5°.

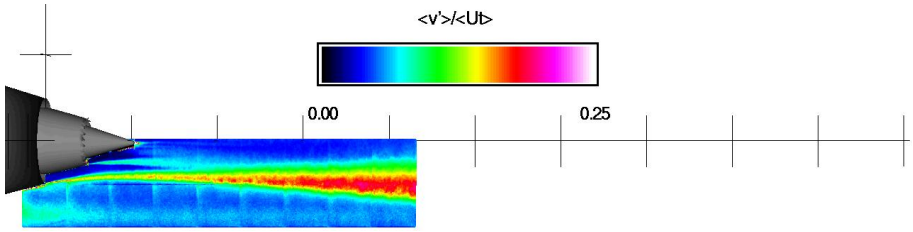

Figure 3.2.1.10 Model 3tb. Contour plots of radial turbulence intensity. Slice taken at circumferential angle = 5°.

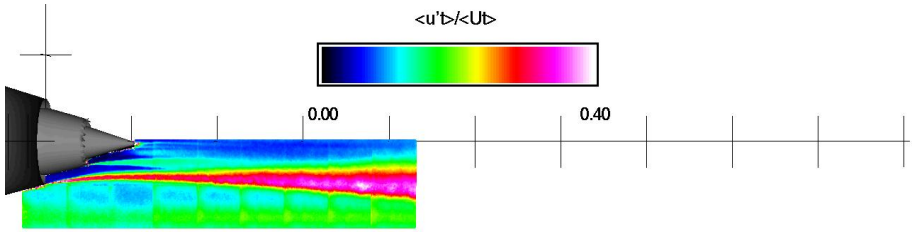

Figure 3.2.1.11 Model 3tb. Contour plots of turbulence intensity. Slice taken at circumferential angle = 5°.

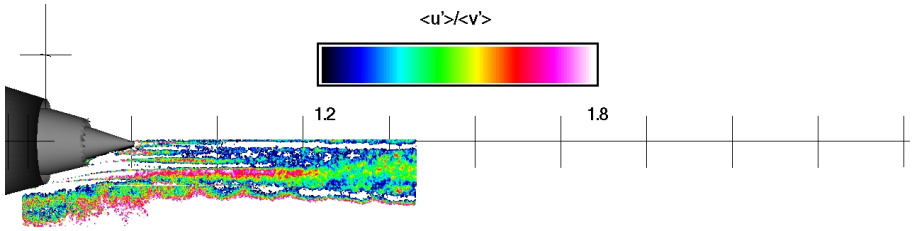

Figure 3.2.1.12 Model 3tb. Contour plots of ratio of axial to radial turbulence. Slice taken at circumferential angle = 5°.

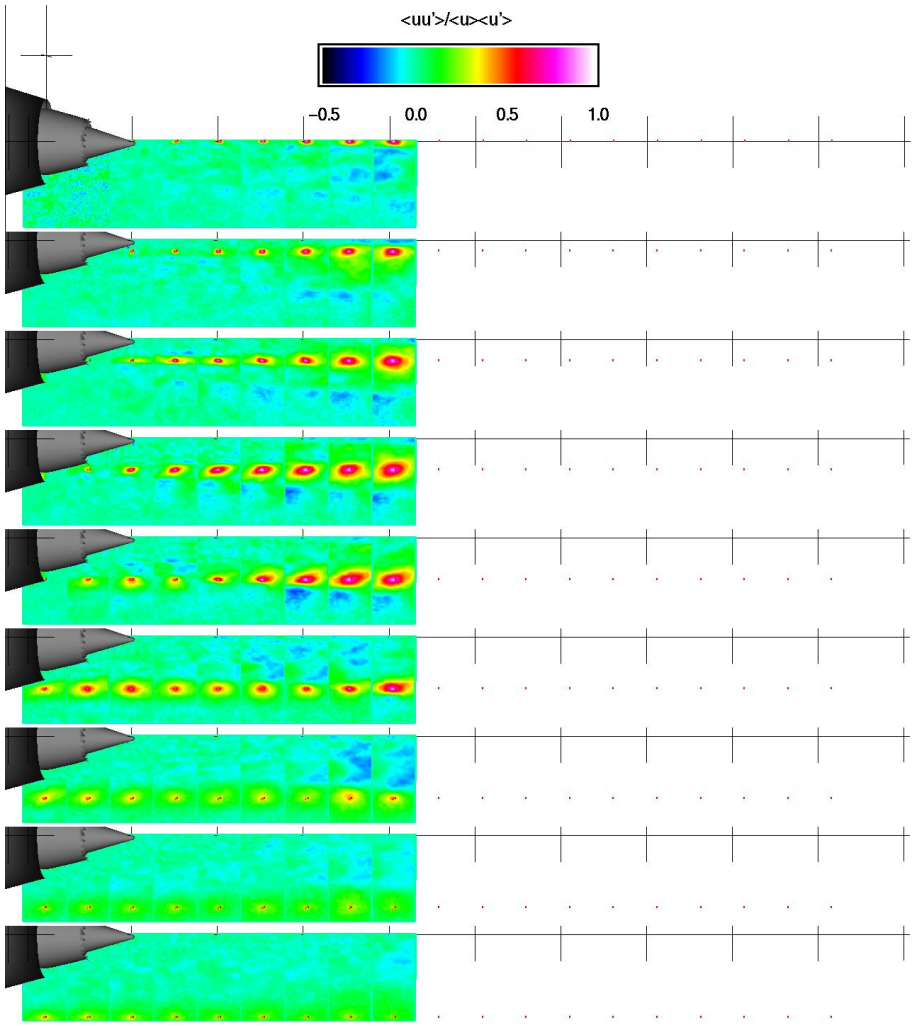

Figure 3.2.2.1 Model 3tb. Contour plots of u(xref)u(x). Slice taken at circumferential angle = 5°.

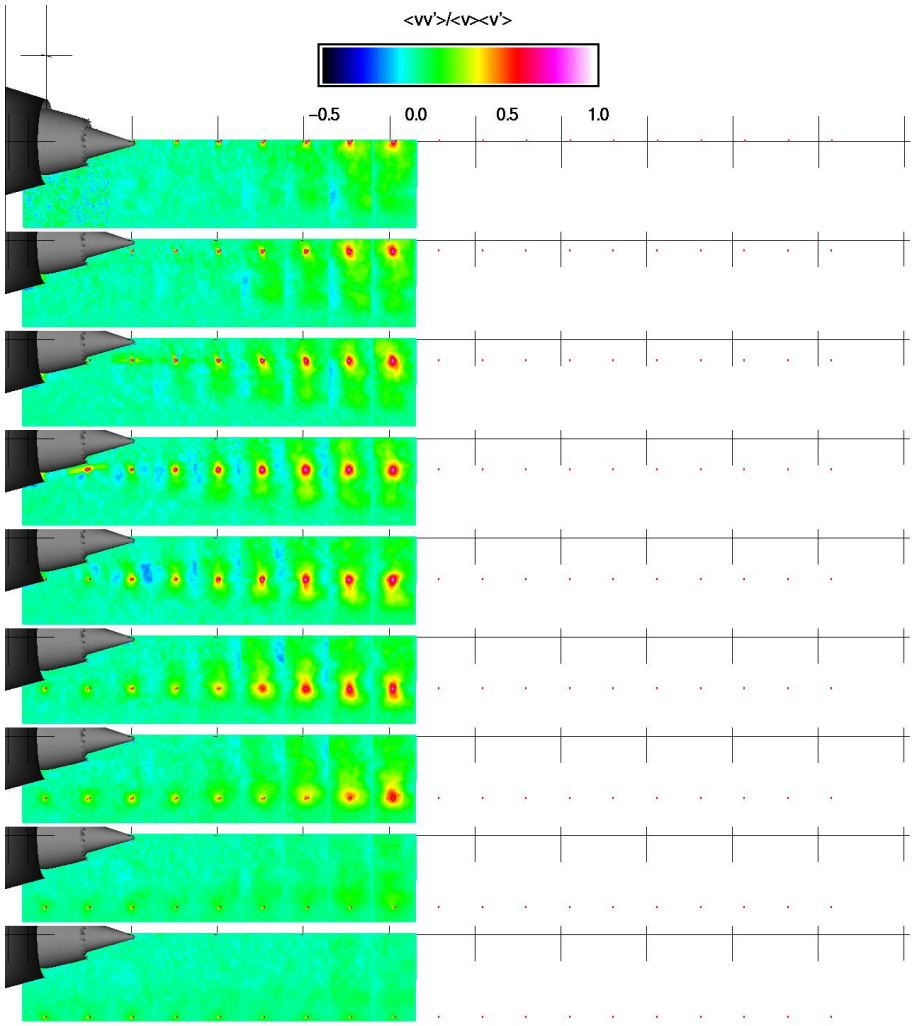

Figure 3.2.2.2 Model 3tb. Contour plots of v(xref)v(x). Slice taken at circumferential angle = 5°.

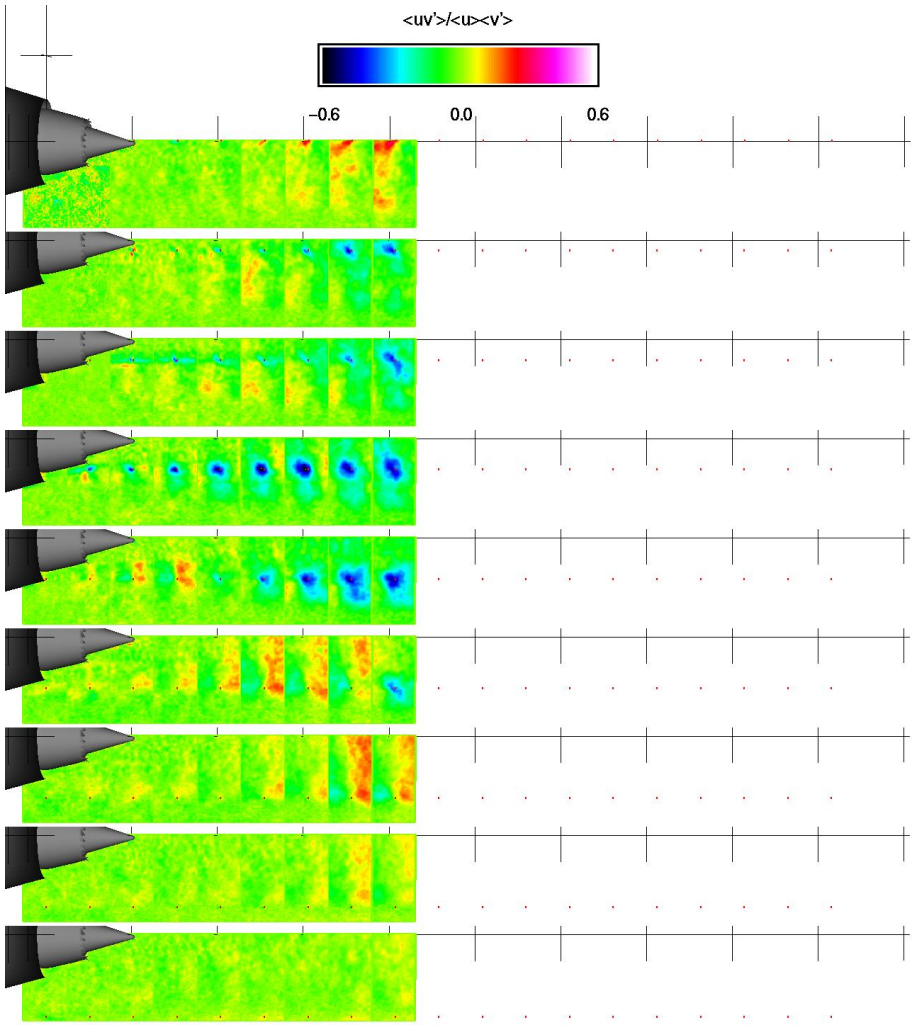

Figure 3.2.2.3 Model 3tb. Contour plots of u(xref)v(x). Slice taken at circumferential angle = 5°.

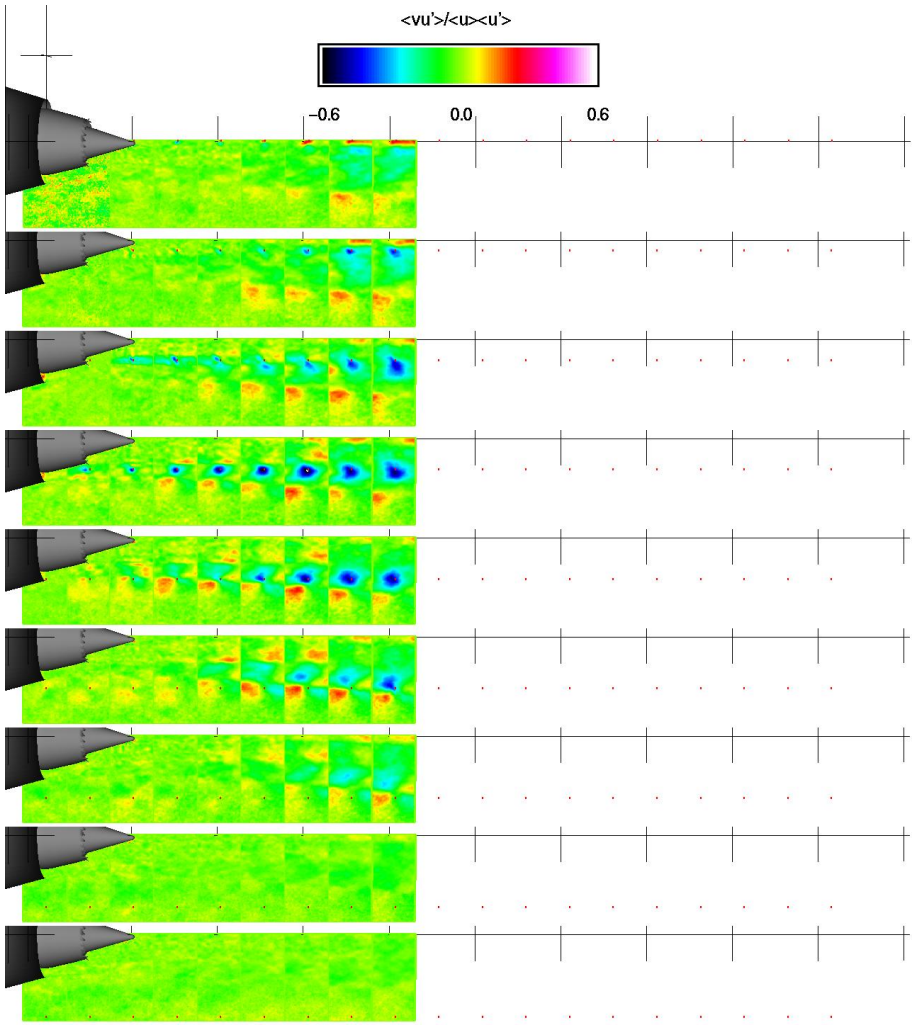

Figure 3.2.2.4 Model 3tb. Contour plots of v(xref)u(x). Slice taken at circumferential angle = 5°.

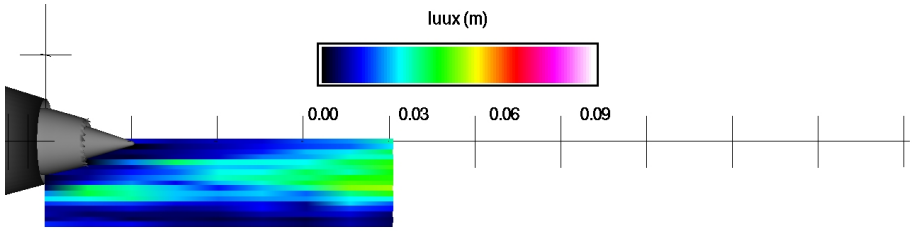

Figure 3.2.3.1 Model 3tb. Contour plots of Luu(x). Slice taken at circumferential angle = 5°.

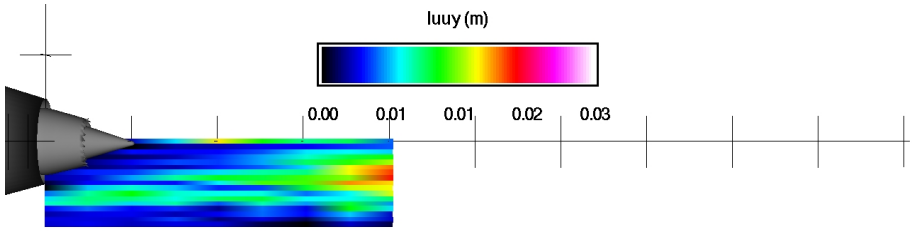

Figure 3.2.3.2 Model 3tb. Contour plots of Luu(y). Slice taken at circumferential angle = 5°.

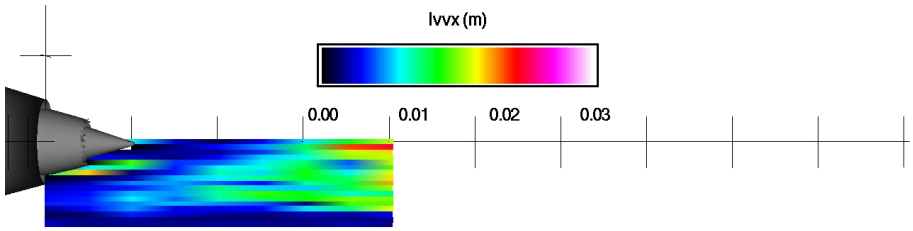

Figure 3.2.3.3 Model 3tb. Contour plots of Lvv(x). Slice taken at circumferential angle = 5°.

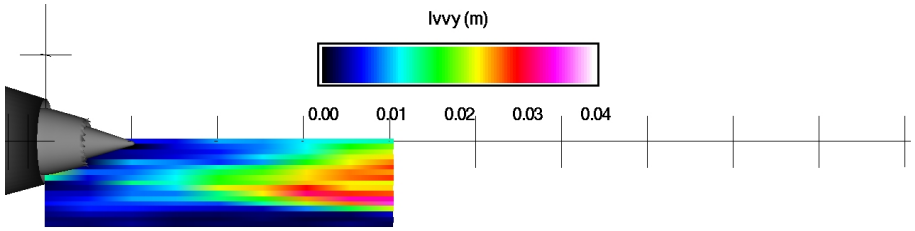

Figure 3.2.3.4 Model 3tb. Contour plots of Lvv(y). Slice taken at circumferential angle = 5°.

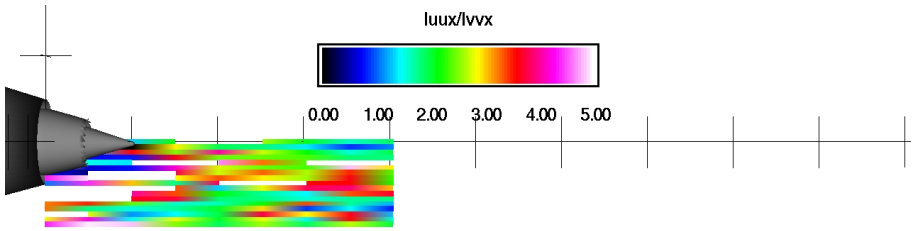

Figure 3.2.3.5 Model 3tb. Contour plots of Luu(x)/Lvv(x). Slice taken at circumferential angle = 5°.

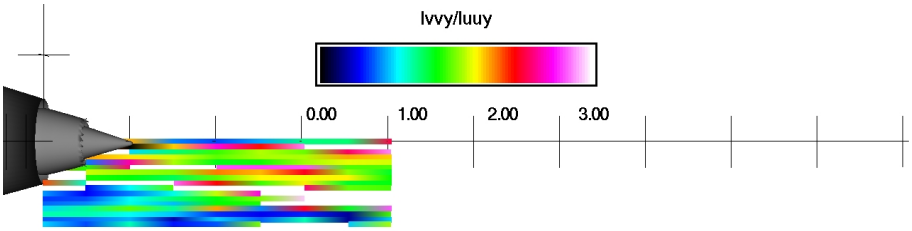

Figure 3.2.3.6 Model 3tb. Contour plots of Lvv(y)/Luu(y). Slice taken at circumferential angle = 5°.

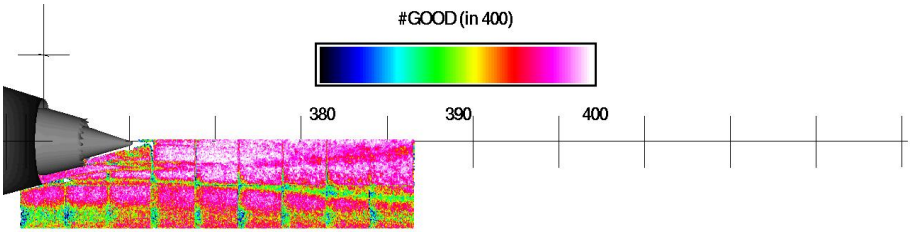

Figure 3.3.1.1 Model 3tb. Contour plots of data quality (#good out of 400). Slice taken at circumferential angle = 10°.

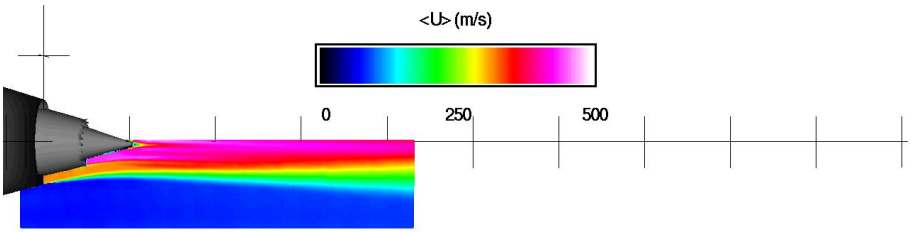

Figure 3.3.1.2 Model 3tb. Contour plots of time average axial velocity (m/s). Slice taken at circumferential angle = 10°.

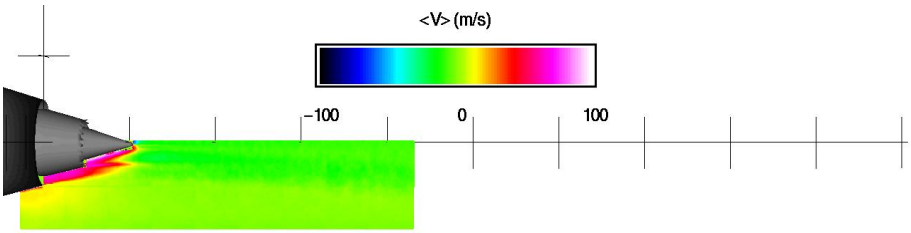

Figure 3.3.1.3 Model 3tb. Contour plots of time average radial velocity (m/s). Slice taken at circumferential angle = 10°.

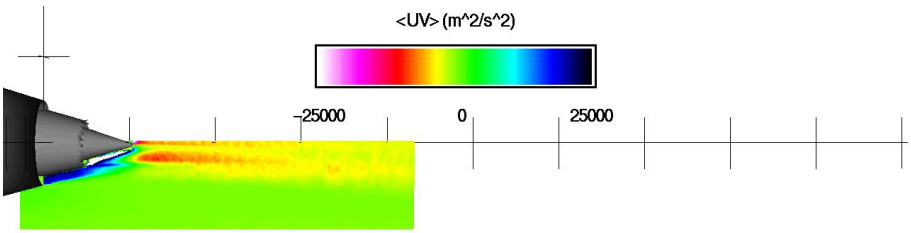

Figure 3.3.1.4 Model 3tb. Contour plots of time average Reynolds stress (m^2/s^2). Slice taken at circumferential angle = 10°.

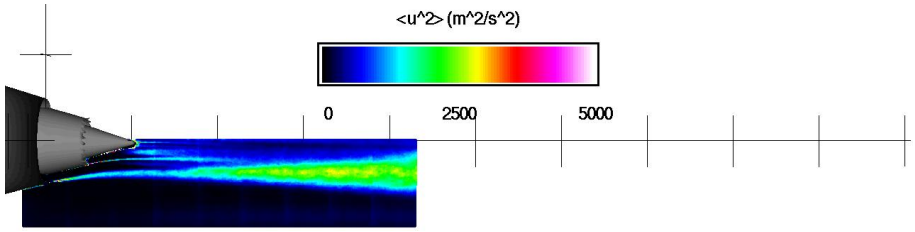

Figure 3.3.1.5 Model 3tb. Contour plots of variance of axial velocity (m^2/s^2). Slice taken at circumferential angle = 10°.

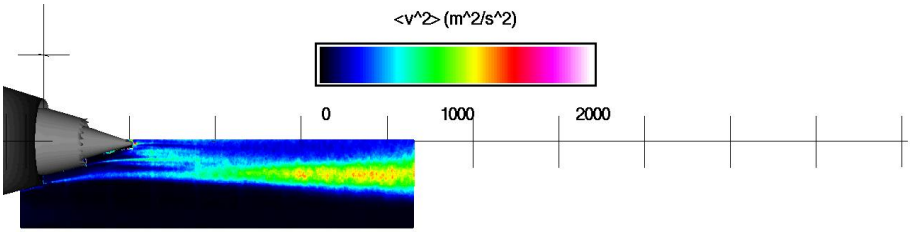

Figure 3.3.1.6 Model 3tb. Contour plots of variance in radial velocity (m^2/s^2). Slice taken at circumferential angle = 10°.

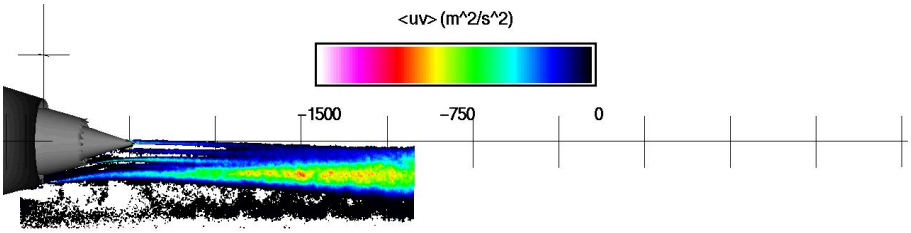

Figure 3.3.1.7 Model 3tb. Contour plots of unsteady Reynolds stress (m^2/s^2). Slice taken at circumferential angle = 10°.

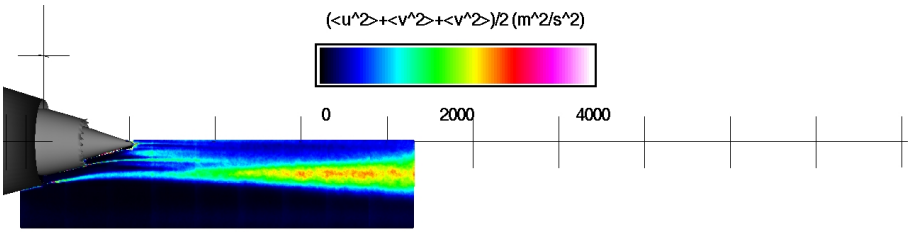

Figure 3.3.1.8 Model 3tb. Contour plots of turbulent kinetic energy (m^2/s^2). Slice taken at circumferential angle = 10°.

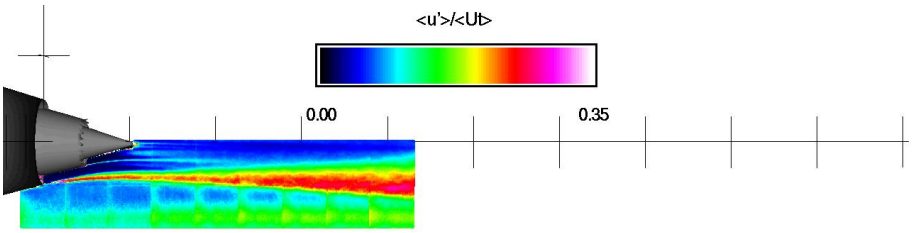

Figure 3.3.1.9 Model 3tb. Contour plots of axial turbulence intensity. Slice taken at circumferential angle = 10°.

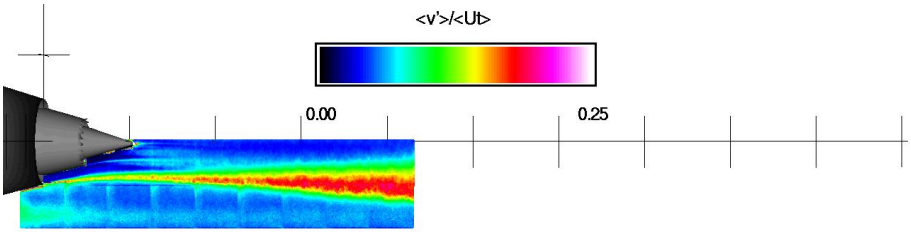

Figure 3.3.1.10 Model 3tb. Contour plots of radial turbulence intensity. Slice taken at circumferential angle = 10°.

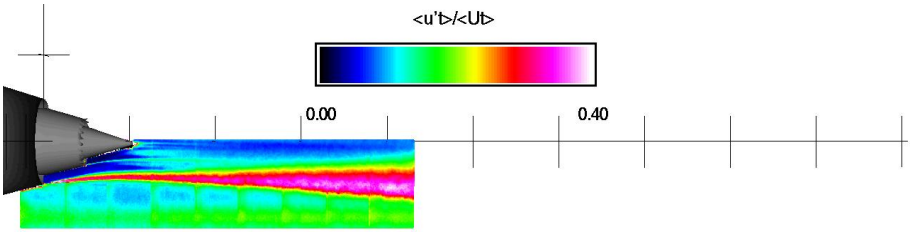

Figure 3.3.1.11 Model 3tb. Contour plots of turbulence intensity. Slice taken at circumferential angle = 10°.

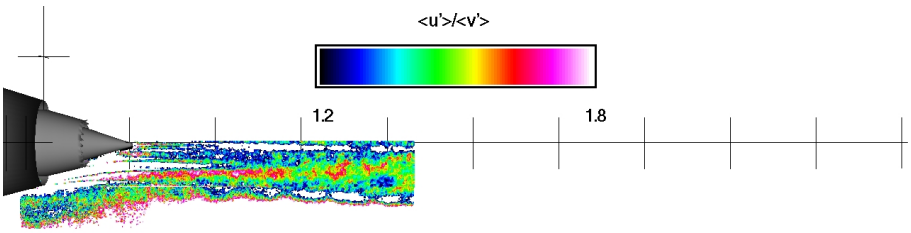

Figure 3.3.1.12 Model 3tb. Contour plots of ratio of axial to radial turbulence. Slice taken at circumferential angle = 10°.

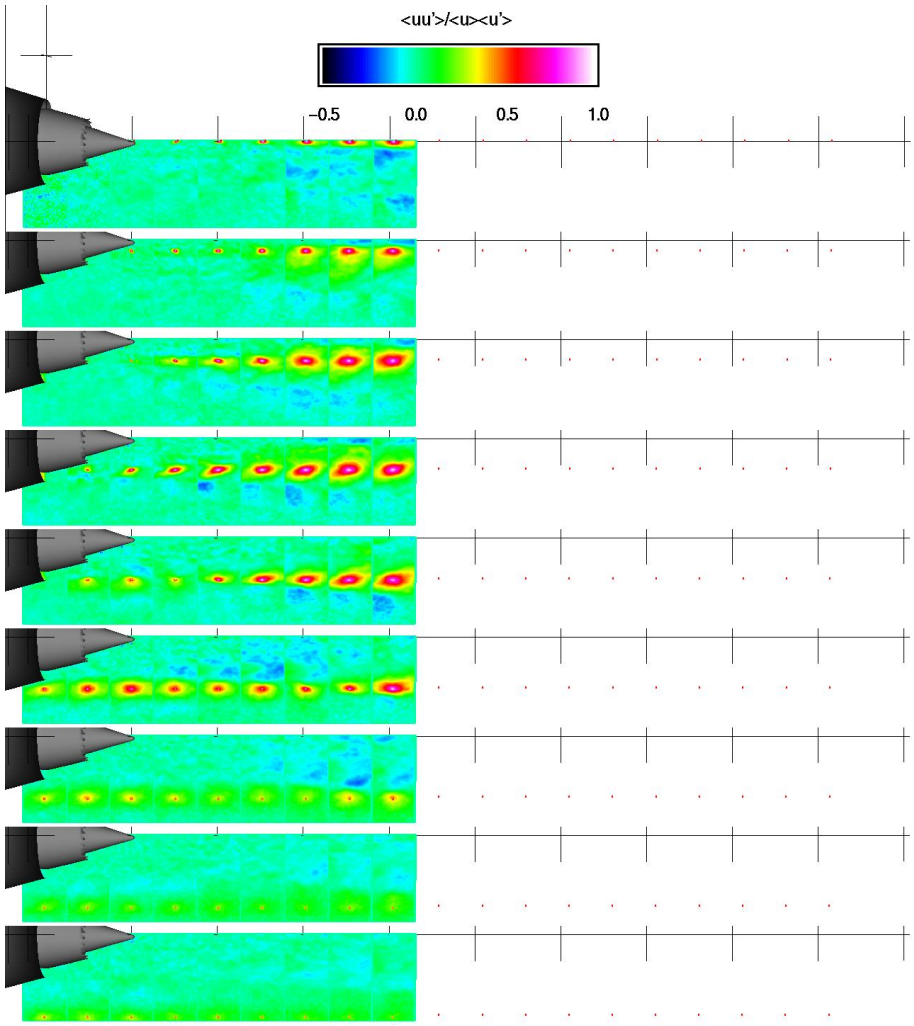

Figure 3.3.2.1 Model 3tb. Contour plots of u(xref)u(x). Slice taken at circumferential angle = 10°.

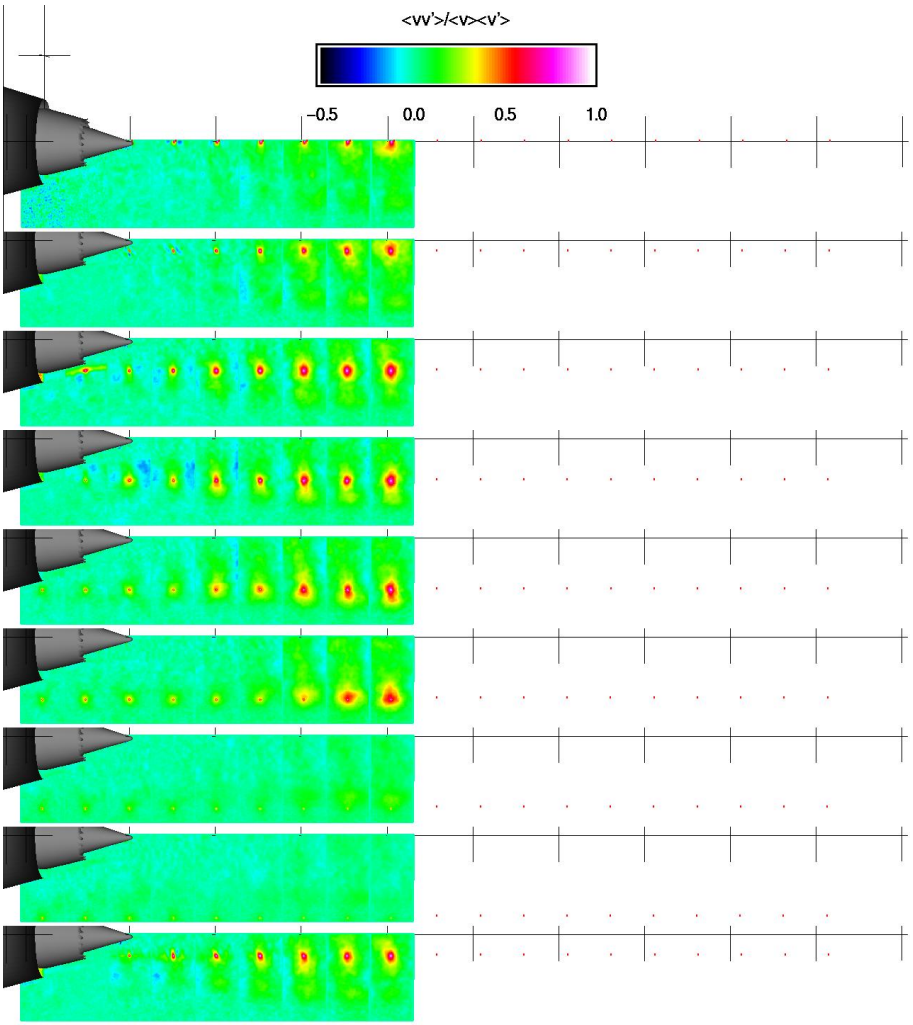

Figure 3.3.2.2 Model 3tb. Contour plots of v(xref)v(x). Slice taken at circumferential angle = 10°.

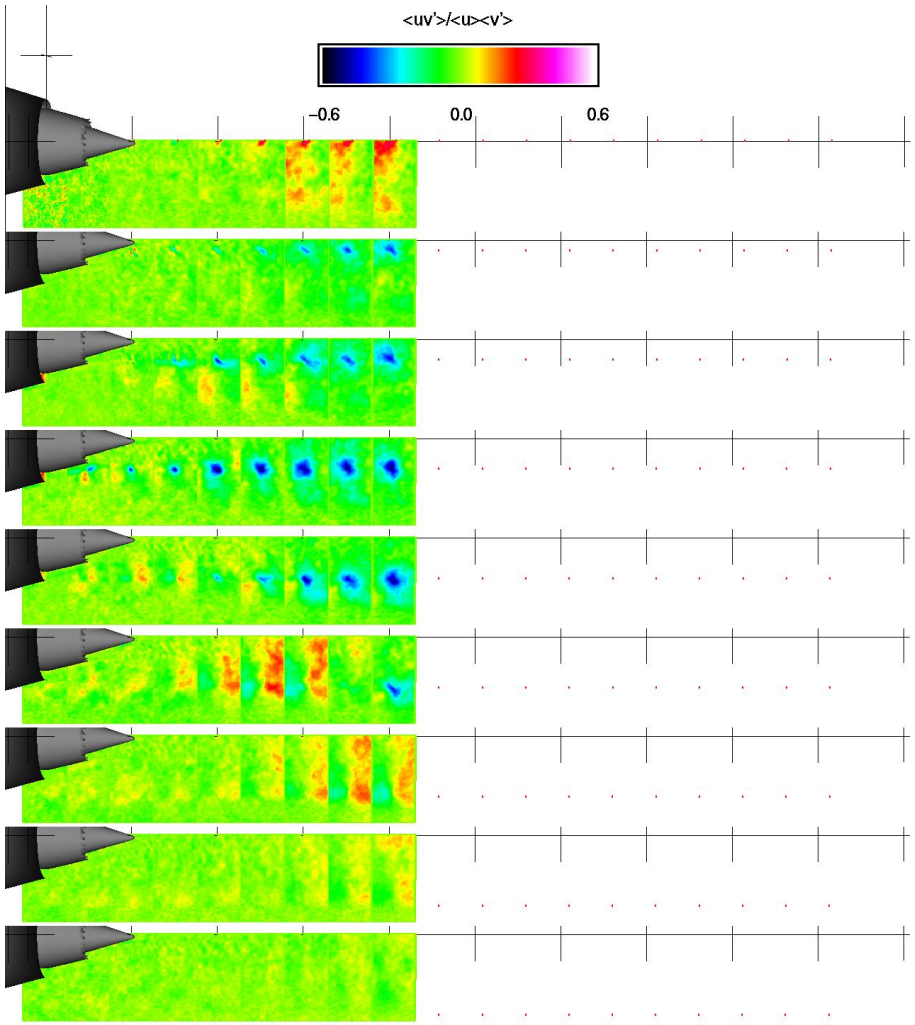

Figure 3.3.2.3 Model 3tb. Contour plots of u(xref)v(x). Slice taken at circumferential angle = 10°.

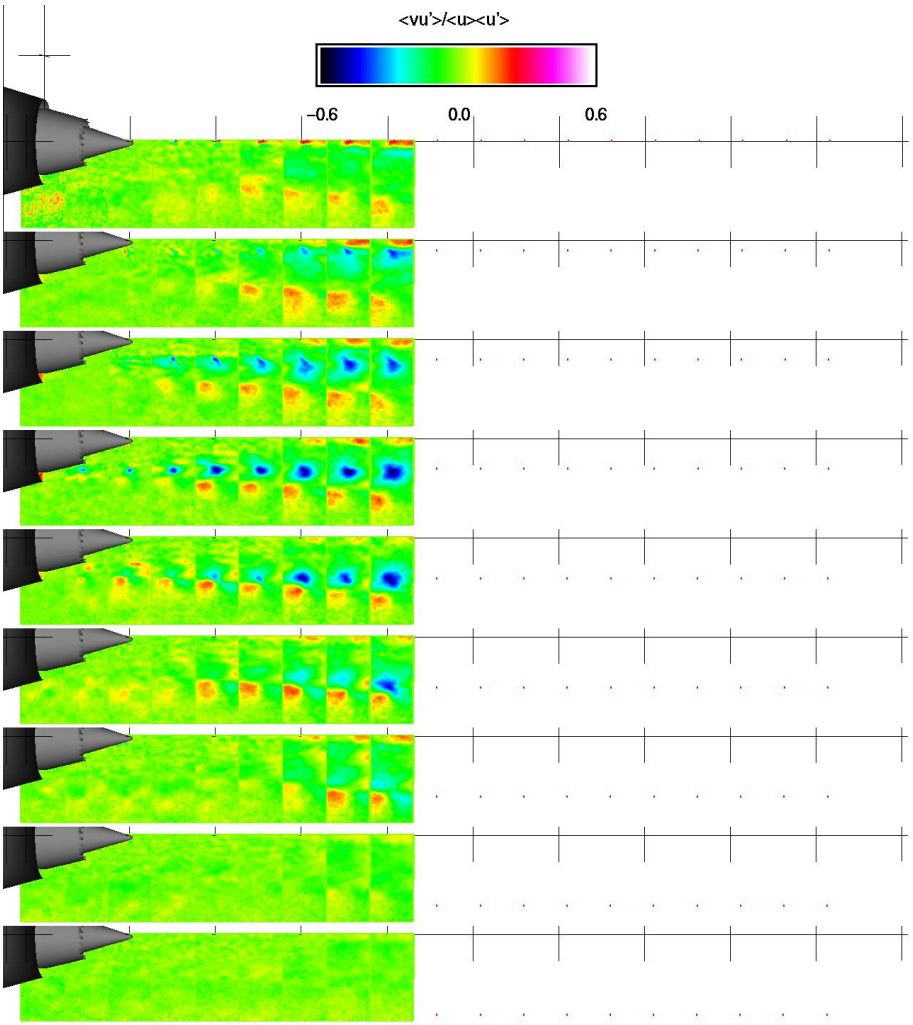

Figure 3.3.2.4 Model 3tb. Contour plots of v(xref)u(x). Slice taken at circumferential angle = 10°.

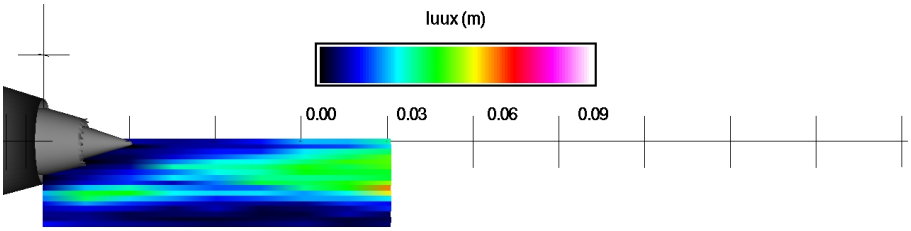

Figure 3.3.3.1 Model 3tb. Contour plots of Luu(x). Slice taken at circumferential angle = 10°.

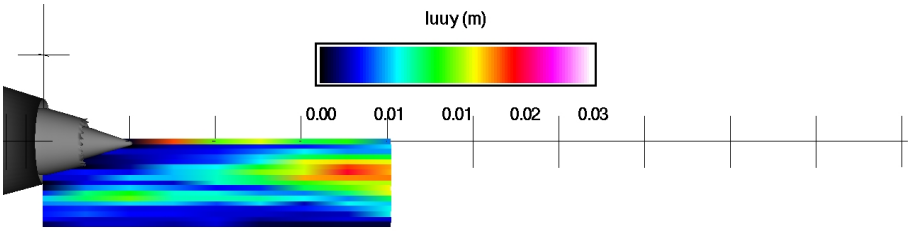

Figure 3.3.3.2 Model 3tb. Contour plots of Luu(y). Slice taken at circumferential angle = 10°.

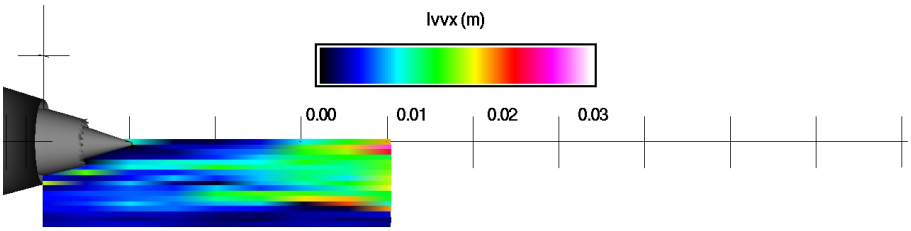

Figure 3.3.3.3 Model 3tb. Contour plots of Lvv(x). Slice taken at circumferential angle = 10°.

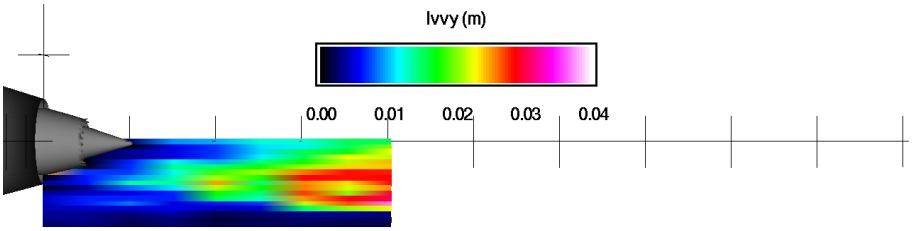

Figure 3.3.3.4 Model 3tb. Contour plots of Lvv(y). Slice taken at circumferential angle = 10°.

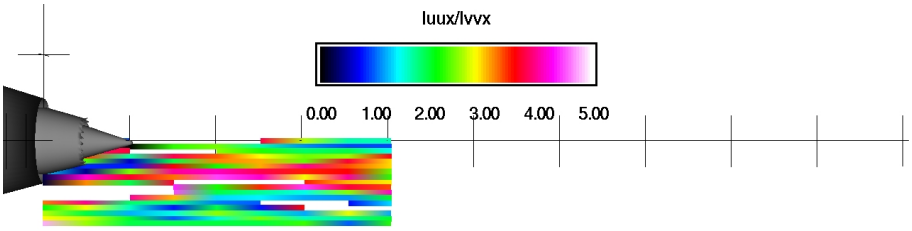

Figure 3.3.3.5 Model 3tb. Contour plots of Luu(x)/Lvv(x). Slice taken at circumferential angle = 10°.

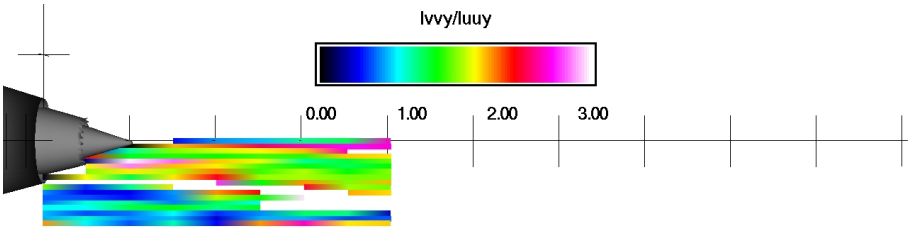

Figure 3.3.3.6 Model 3tb. Contour plots of Lvv(y)/Luu(y). Slice taken at circumferential angle = 10°.

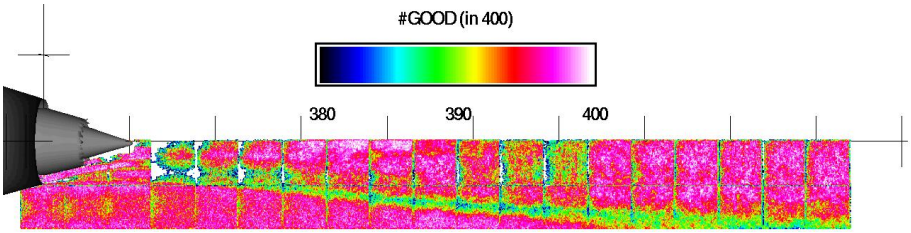

Figure 3.4.1.1 Model 3tb. Contour plots of data quality (#good out of 400). Slice taken at circumferential angle = 15°.

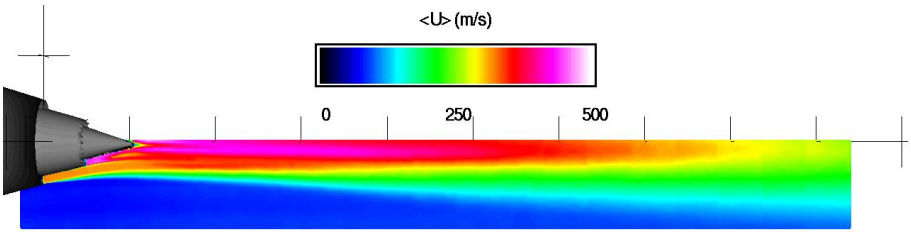

Figure 3.4.1.2 Model 3tb. Contour plots of time average axial velocity (m/s). Slice taken at circumferential angle = 15°.

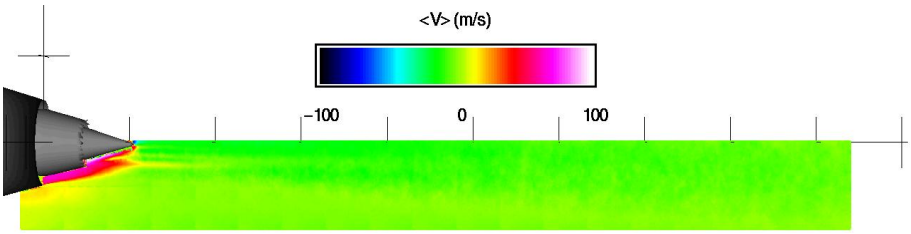

Figure 3.4.1.3 Model 3tb. Contour plots of time average radial velocity (m/s). Slice taken at circumferential angle = 15°.

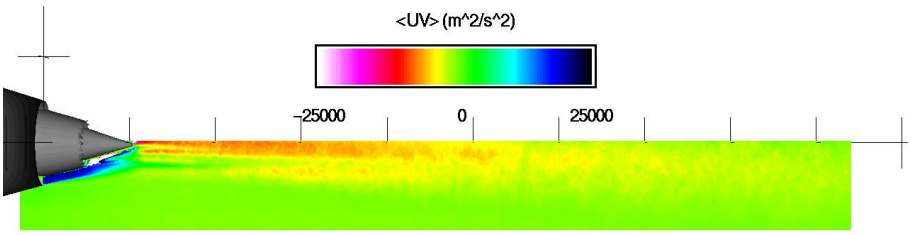

Figure 3.4.1.4 Model 3tb. Contour plots of time average Reynolds stress (m^2/s^2). Slice taken at circumferential angle = 15°.

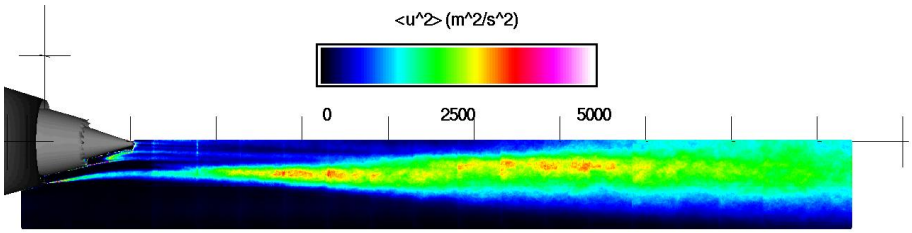

Figure 3.4.1.5 Model 3tb. Contour plots of variance of axial velocity (m^2/s^2). Slice taken at circumferential angle = 15°.

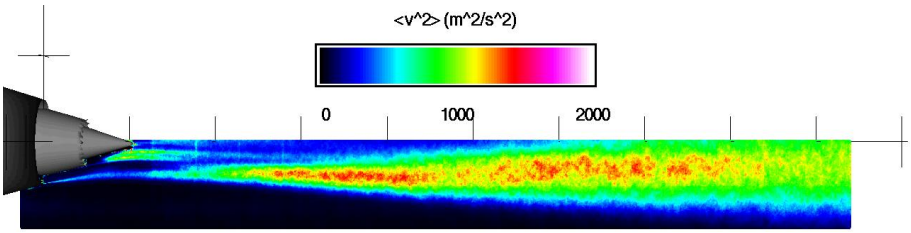

Figure 3.4.1.6 Model 3tb. Contour plots of variance in radial velocity (m^2/s^2). Slice taken at circumferential angle = 15°.

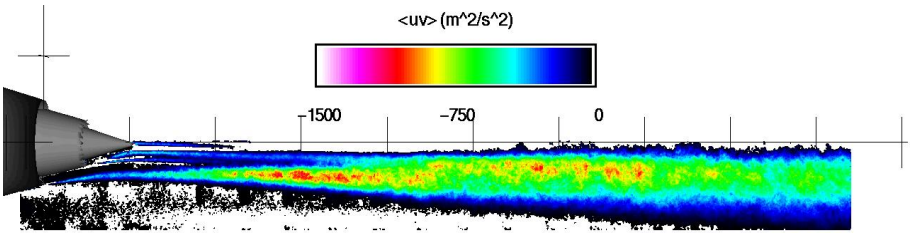

Figure 3.4.1.7 Model 3tb. Contour plots of unsteady Reynolds stress (m^2/s^2). Slice taken at circumferential angle = 15°.

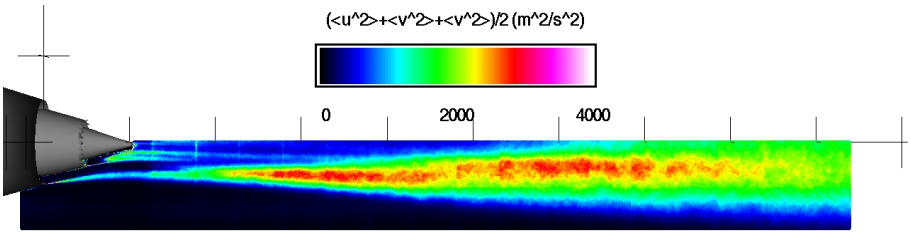

Figure 3.4.1.8 Model 3tb. Contour plots of turbulent kinetic energy (m^2/s^2). Slice taken at circumferential angle = 15°.

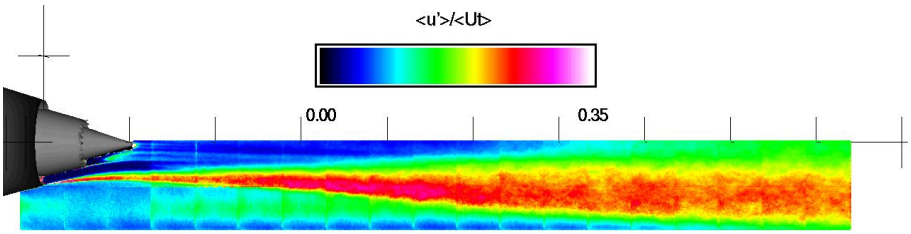

Figure 3.4.1.9 Model 3tb. Contour plots of axial turbulence intensity. Slice taken at circumferential angle = 15°.

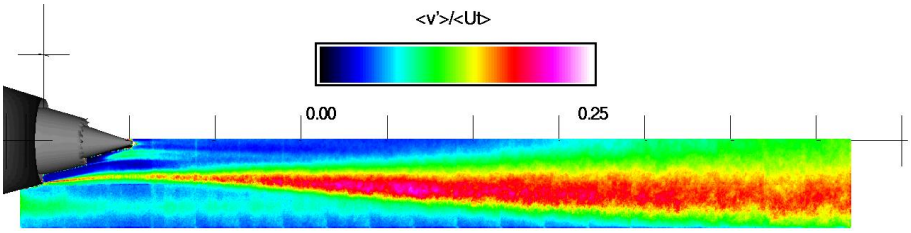

Figure 3.4.1.10 Model 3tb. Contour plots of radial turbulence intensity. Slice taken at circumferential angle = 15°.

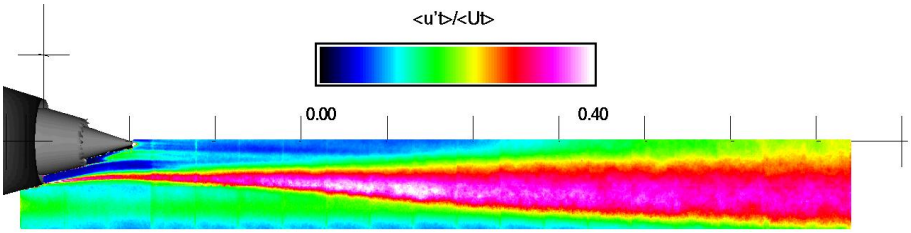

Figure 3.4.1.11 Model 3tb. Contour plots of turbulence intensity. Slice taken at circumferential angle = 15°.

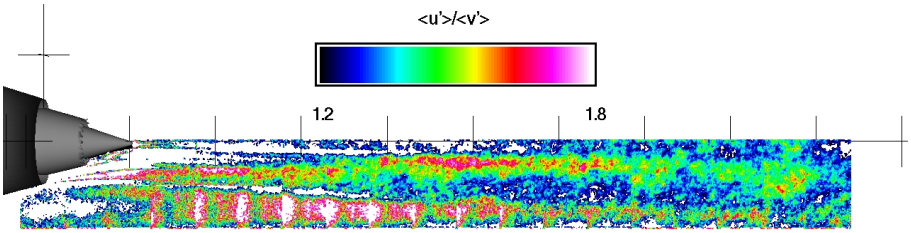

Figure 3.4.1.12 Model 3tb. Contour plots of ratio of axial to radial turbulence. Slice taken at circumferential angle = 15°.

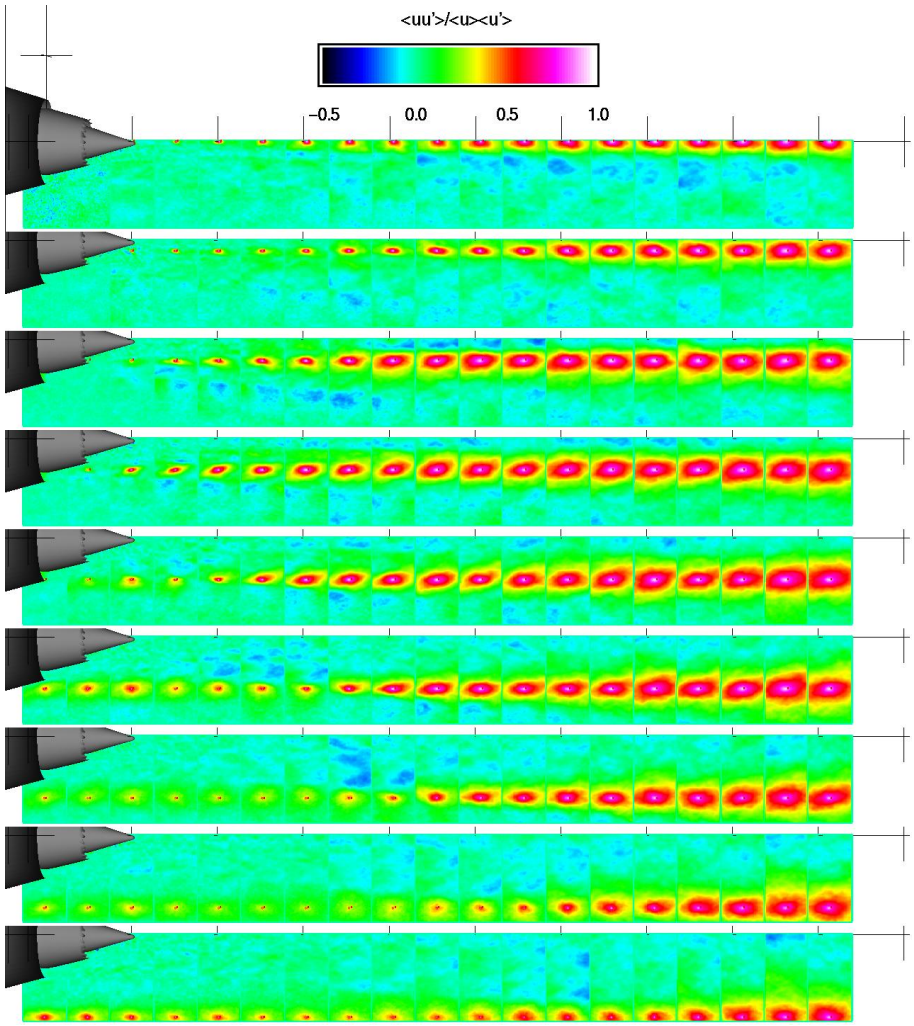

Figure 3.4.2.1 Model 3tb. Contour plots of u(xref)u(x). Slice taken at circumferential angle = 15°.

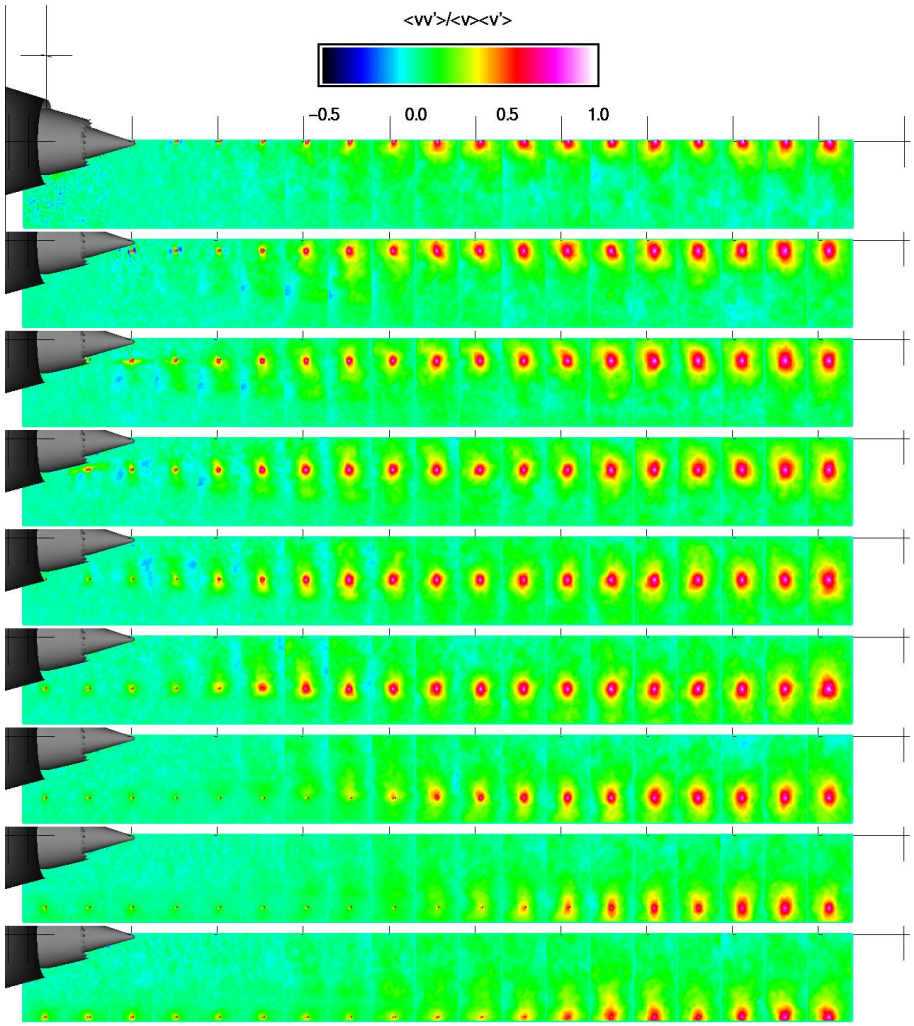

Figure 3.4.2.2 Model 3tb. Contour plots of v(xref)v(x). Slice taken at circumferential angle = 15°.

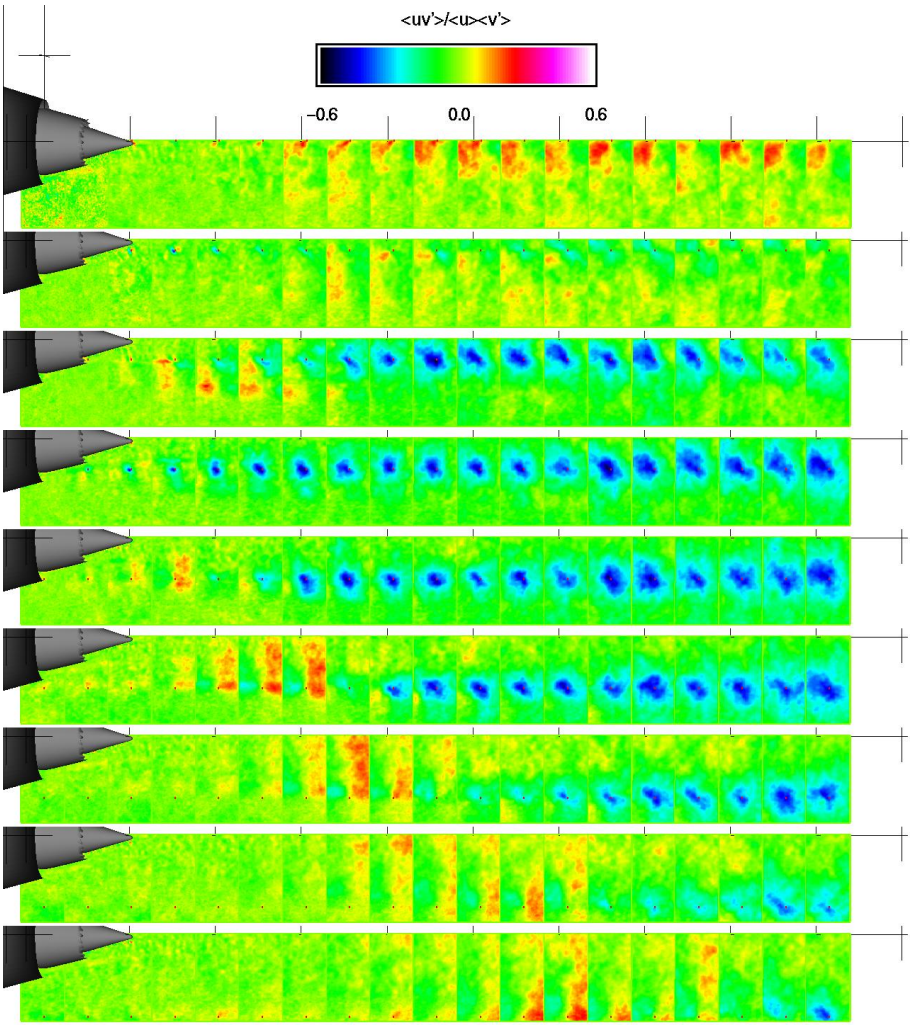

Figure 3.4.2.3 Model 3tb. Contour plots of u(xref)v(x). Slice taken at circumferential angle = 15°.

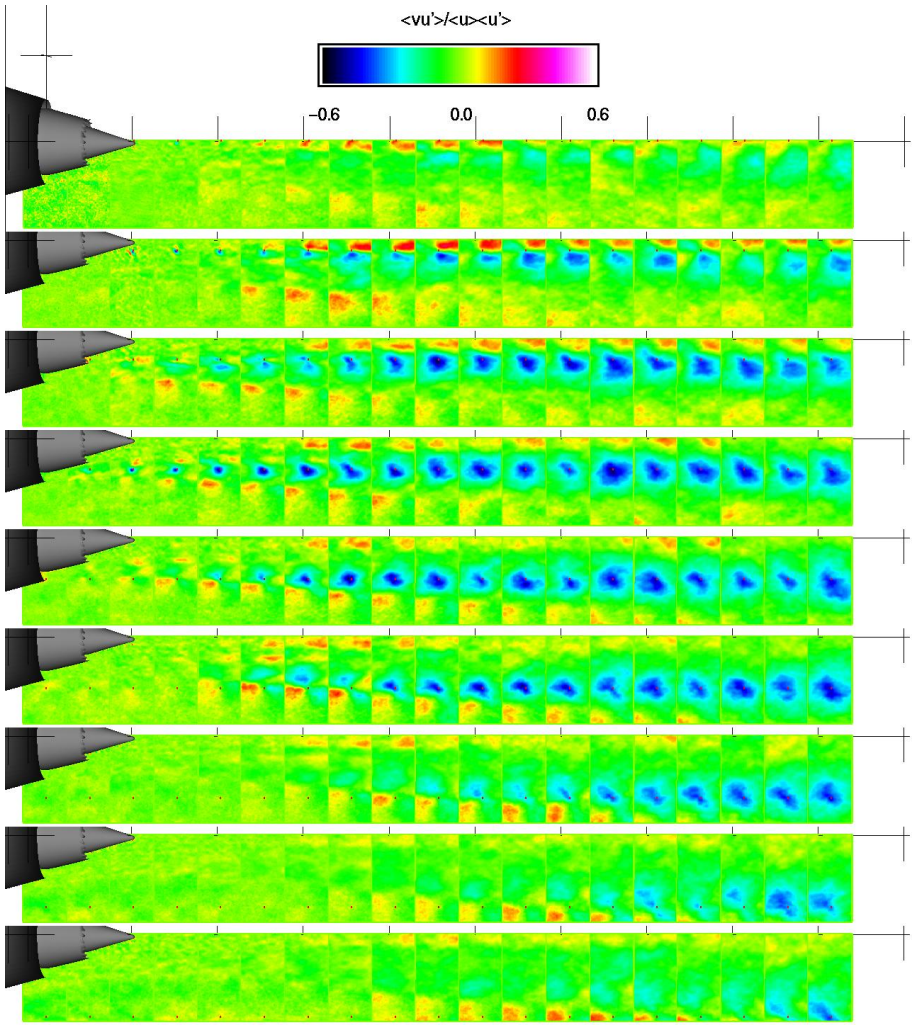

Figure 3.4.2.4 Model 3tb. Contour plots of v(xref)u(x). Slice taken at circumferential angle = 15°.

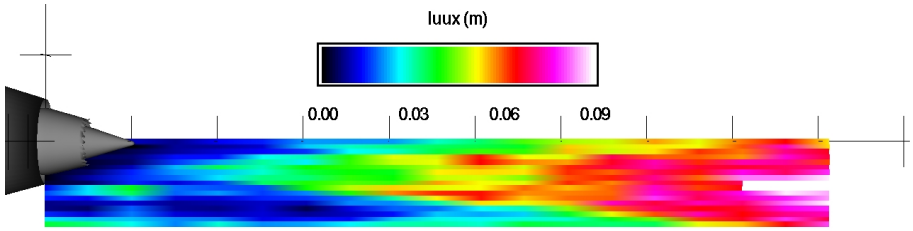

Figure 3.4.3.1 Model 3tb. Contour plots of Luu(x). Slice taken at circumferential angle = 15°.

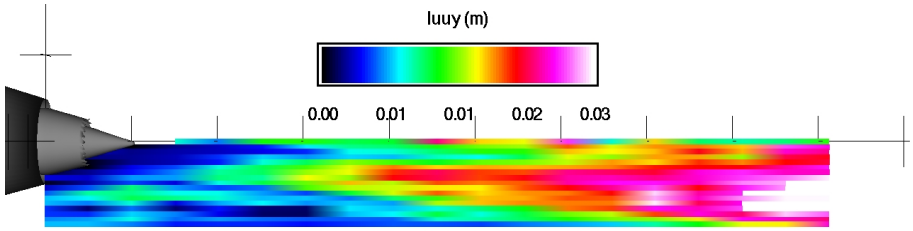

Figure 3.4.3.2 Model 3tb. Contour plots of Luu(y). Slice taken at circumferential angle = 15°.

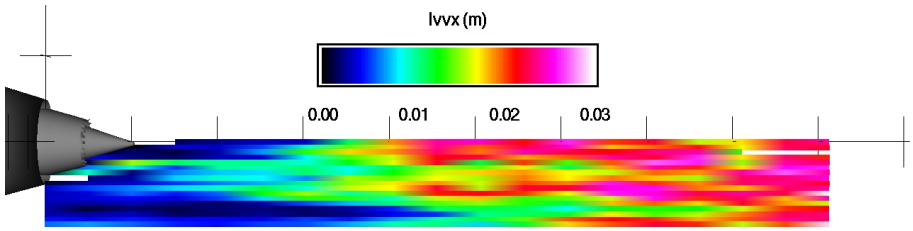

Figure 3.4.3.3 Model 3tb. Contour plots of Lvv(x). Slice taken at circumferential angle = 15°.

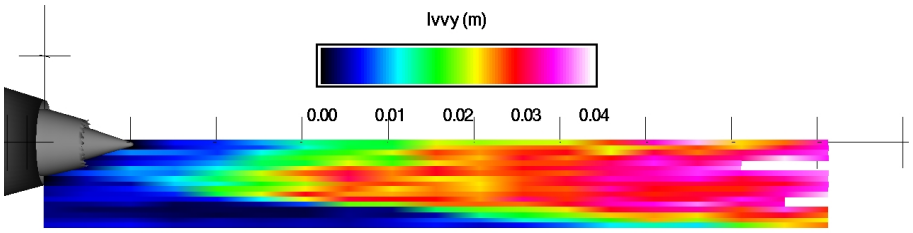

Figure 3.4.3.4 Model 3tb. Contour plots of Lvv(y). Slice taken at circumferential angle = 15°.

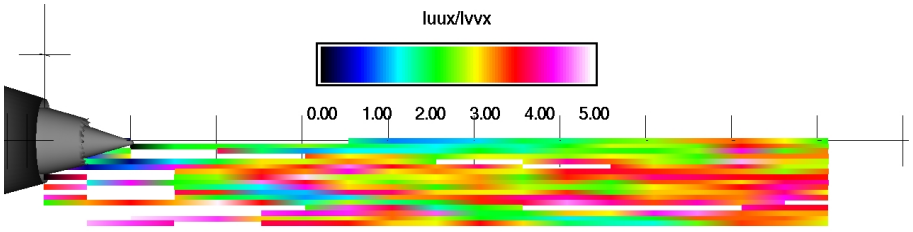

Figure 3.4.3.5 Model 3tb. Contour plots of Luu(x)/Lvv(x). Slice taken at circumferential angle = 15°.

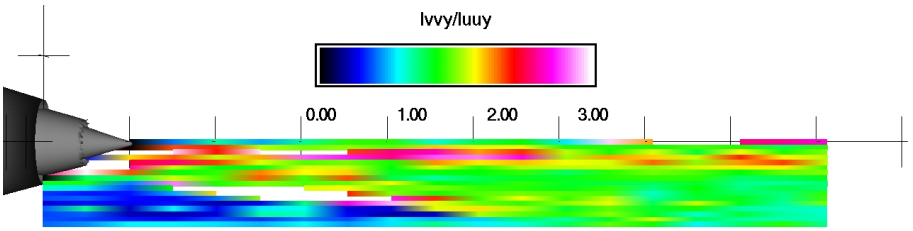

Figure 3.4.3.6 Model 3tb. Contour plots of Lvv(y)/Luu(y). Slice taken at circumferential angle = 15°.

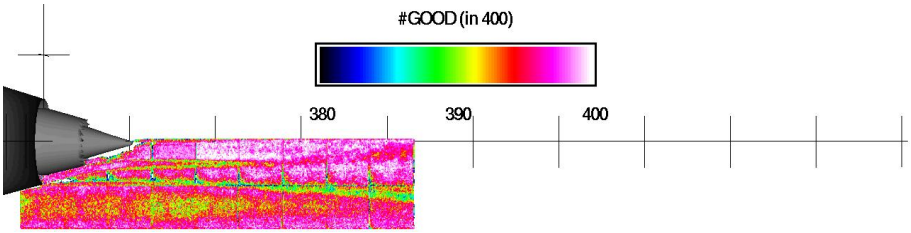

Figure 3.5.1.1 Model 3tb. Contour plots of data quality (#good out of 400). Slice taken at circumferential angle = 20°.

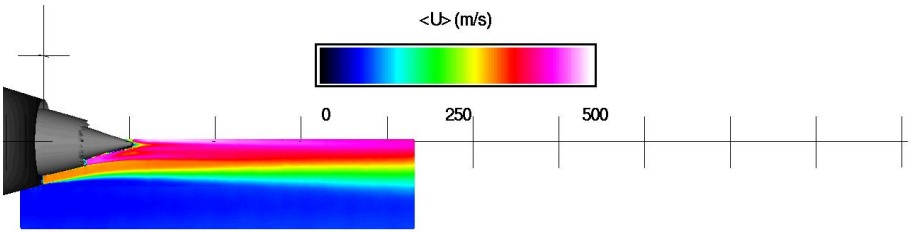

Figure 3.5.1.2 Model 3tb. Contour plots of time average axial velocity (m/s). Slice taken at circumferential angle = 20°.

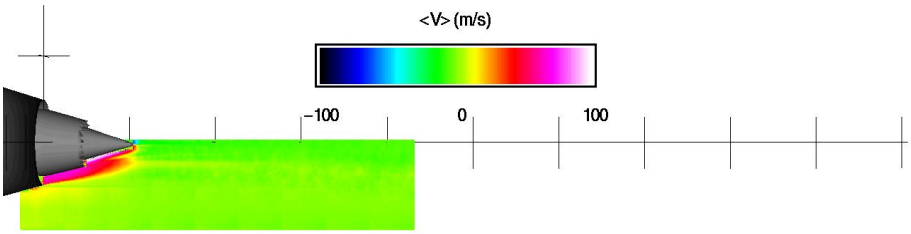

Figure 3.5.1.3 Model 3tb. Contour plots of time average radial velocity (m/s). Slice taken at circumferential angle = 20°.

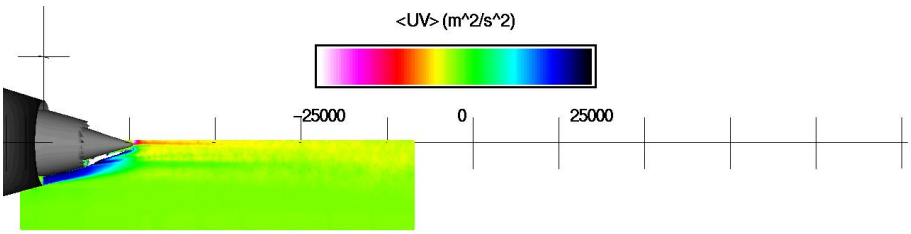

Figure 3.5.1.4 Model 3tb. Contour plots of time average Reynolds stress (m^2/s^2). Slice taken at circumferential angle = 20°.

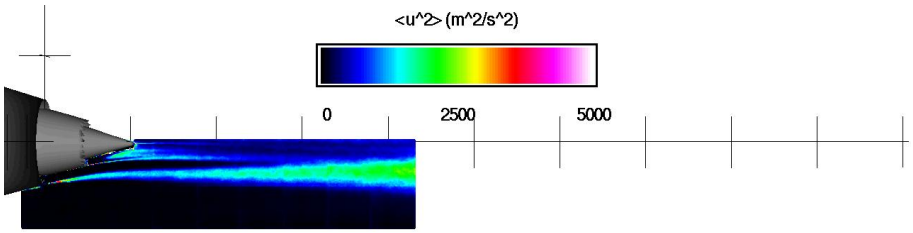

Figure 3.5.1.5 Model 3tb. Contour plots of variance of axial velocity (m^2/s^2). Slice taken at circumferential angle = 20°.

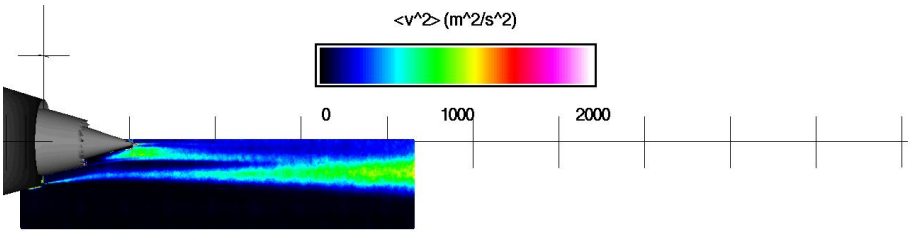

Figure 3.5.1.6 Model 3tb. Contour plots of variance in radial velocity (m^2/s^2). Slice taken at circumferential angle = 20°.

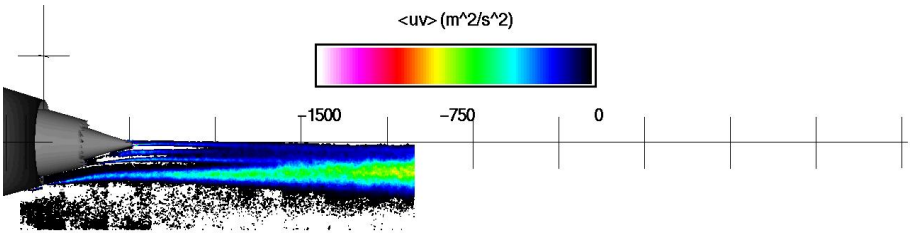

Figure 3.5.1.7 Model 3tb. Contour plots of unsteady Reynolds stress (m^2/s^2). Slice taken at circumferential angle = 20°.

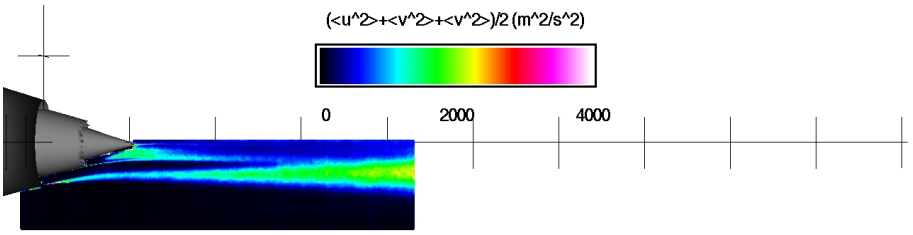

Figure 3.5.1.8 Model 3tb. Contour plots of turbulent kinetic energy (m^2/s^2). Slice taken at circumferential angle = 20°.

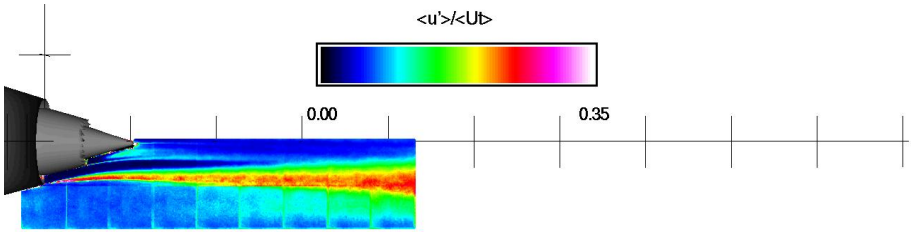

Figure 3.5.1.9 Model 3tb. Contour plots of axial turbulence intensity. Slice taken at circumferential angle = 20°.

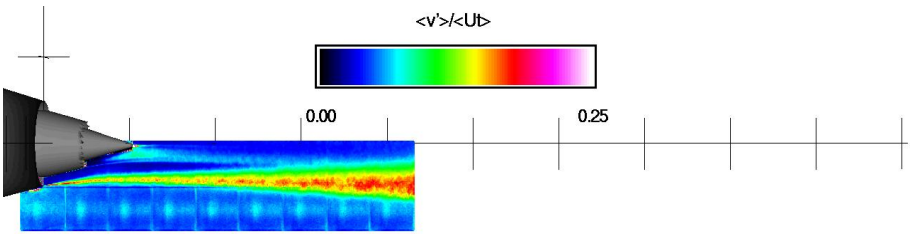

Figure 3.5.1.10 Model 3tb. Contour plots of radial turbulence intensity. Slice taken at circumferential angle = 20°.

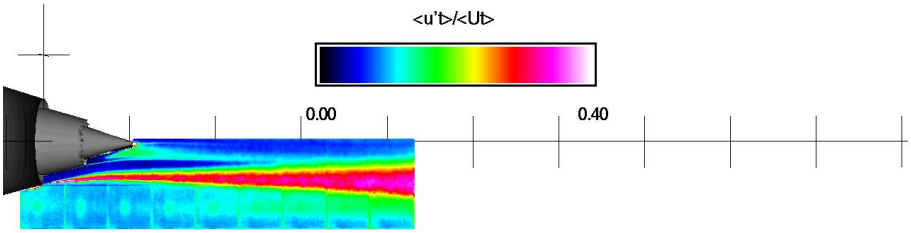

Figure 3.5.1.11 Model 3tb. Contour plots of turbulence intensity. Slice taken at circumferential angle = 20°.

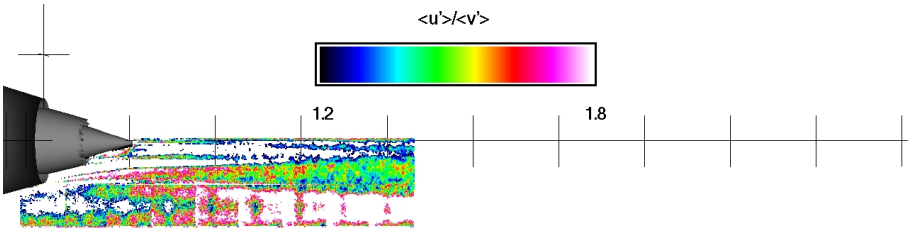

Figure 3.5.1.12 Model 3tb. Contour plots of ratio of axial to radial turbulence. Slice taken at circumferential angle = 20°.

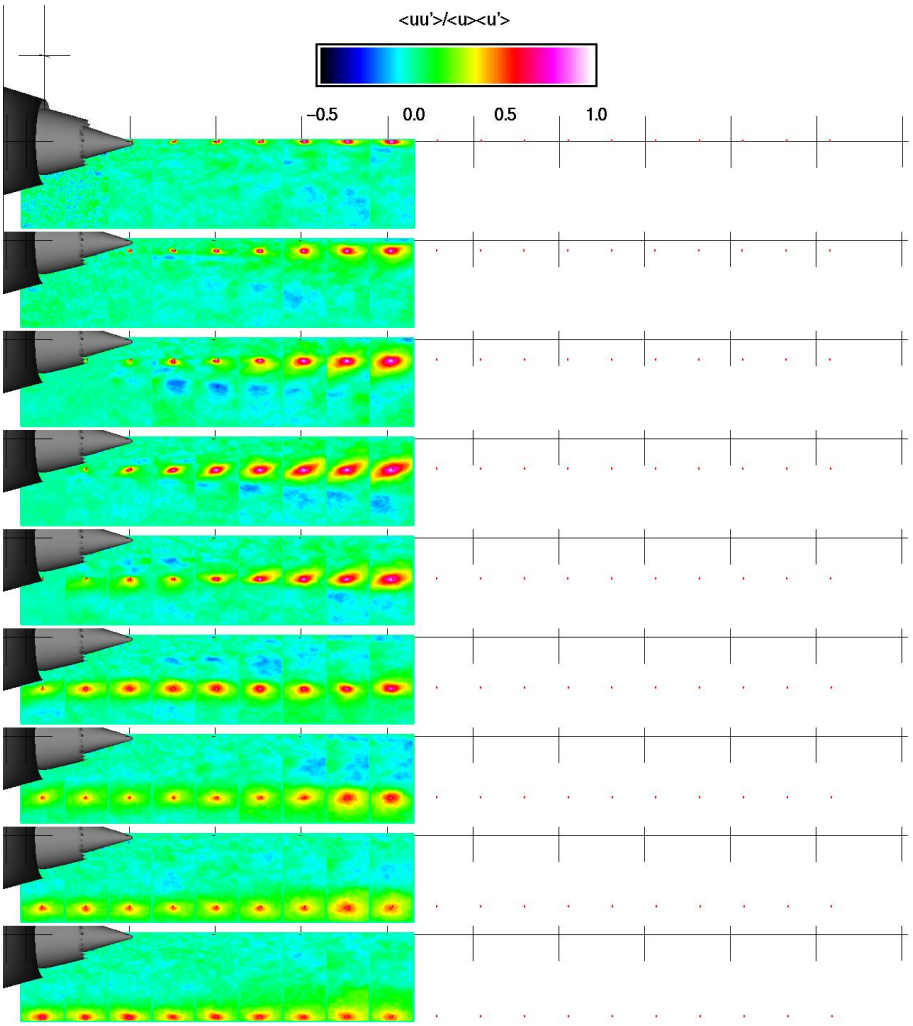

Figure 3.5.2.1 Model 3tb. Contour plots of u(xref)u(x). Slice taken at circumferential angle = 20°.

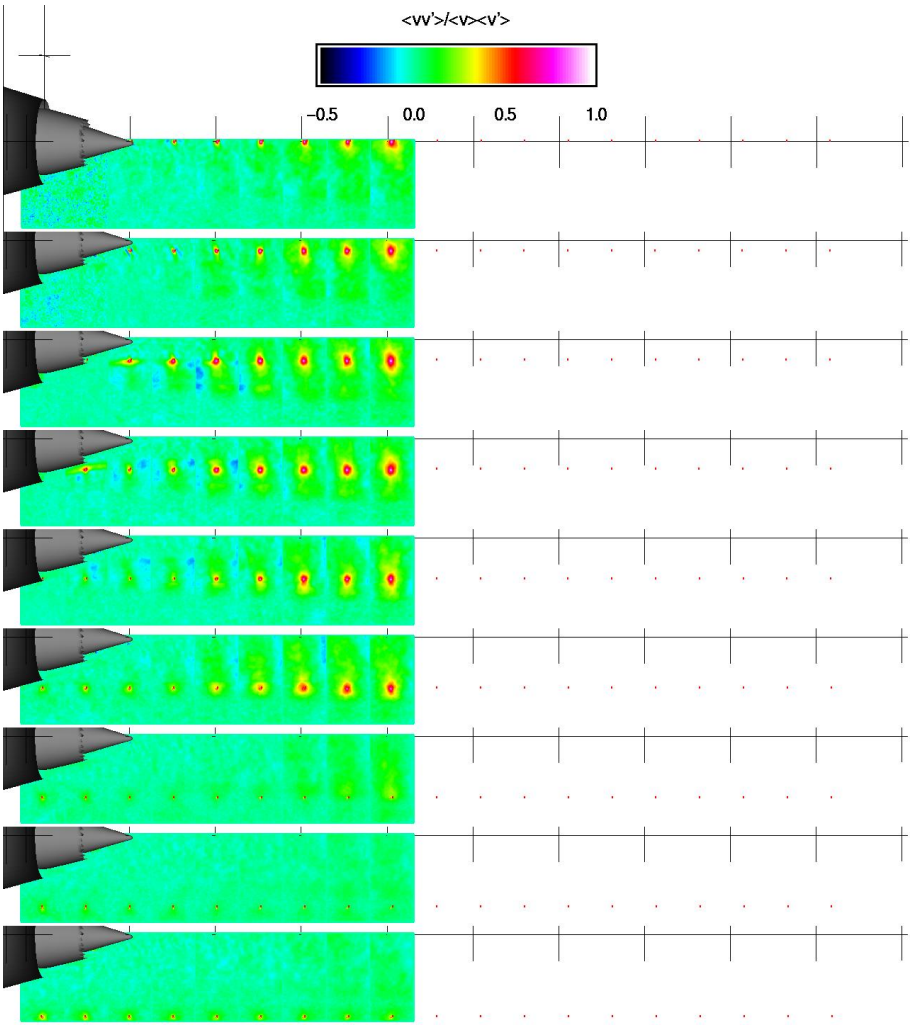

Figure 3.5.2.2 Model 3tb. Contour plots of v(xref)v(x). Slice taken at circumferential angle = 20°.

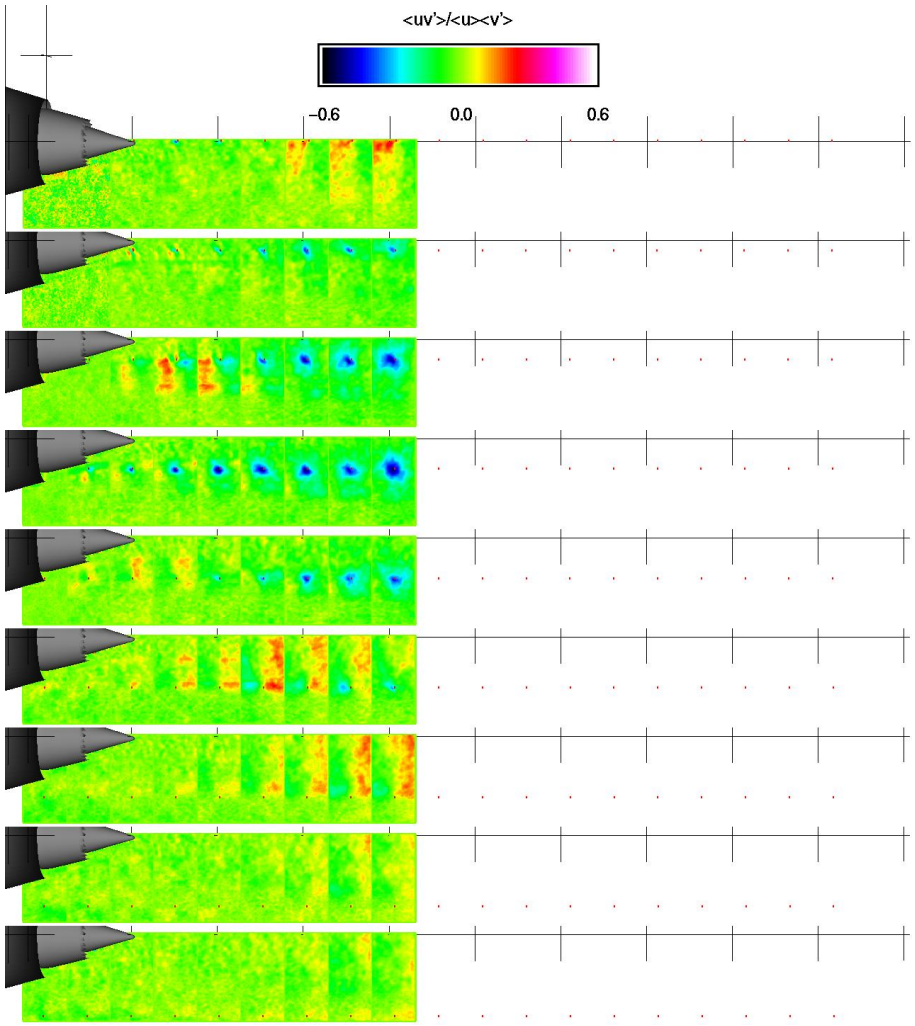

Figure 3.5.2.3 Model 3tb. Contour plots of u(xref)v(x). Slice taken at circumferential angle = 20°.

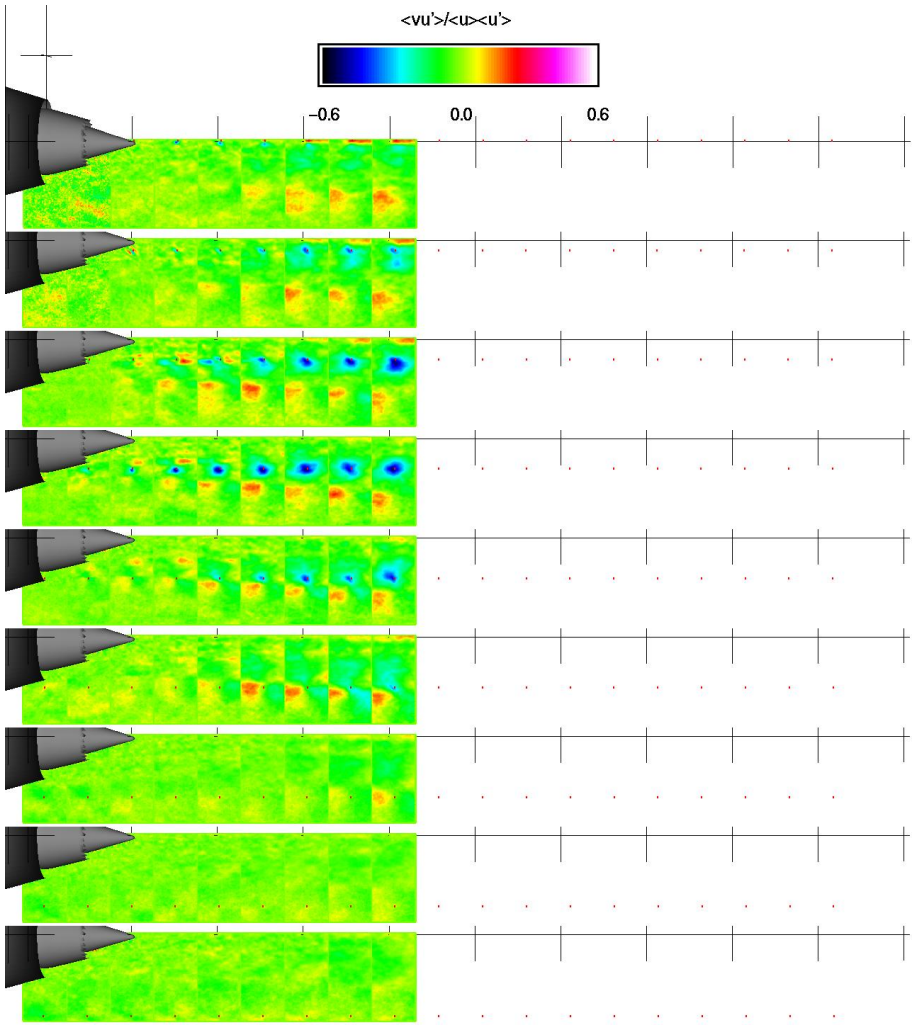

Figure 3.5.2.4 Model 3tb. Contour plots of v(xref)u(x). Slice taken at circumferential angle = 20°.

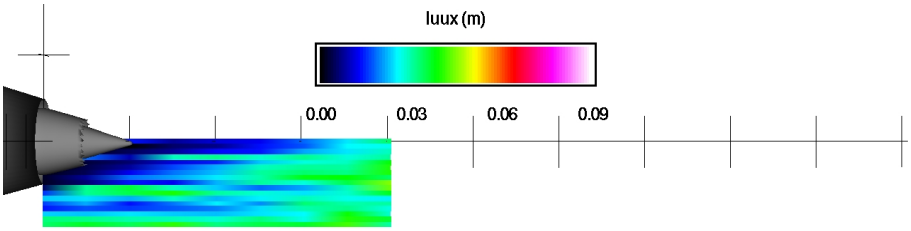

Figure 3.5.3.1 Model 3tb. Contour plots of Luu(x). Slice taken at circumferential angle = 20°.

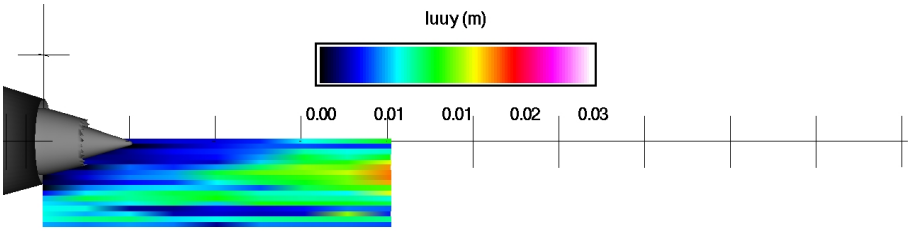

Figure 3.5.3.2 Model 3tb. Contour plots of Luu(y). Slice taken at circumferential angle = 20°.

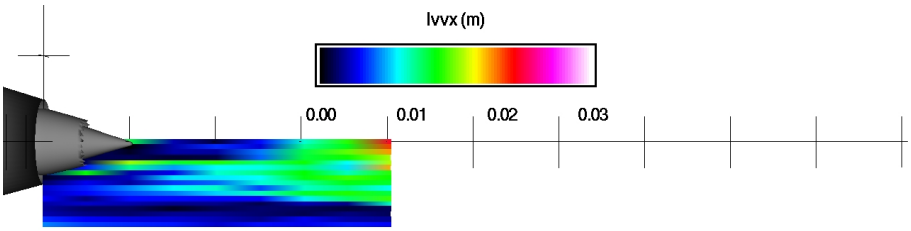

Figure 3.5.3.3 Model 3tb. Contour plots of Lvv(x). Slice taken at circumferential angle = 20°.

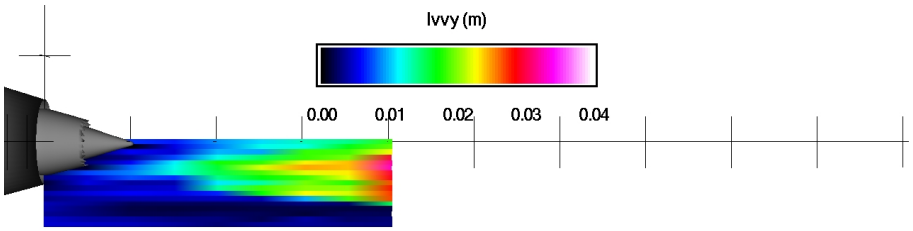

Figure 3.5.3.4 Model 3tb. Contour plots of Lvv(y). Slice taken at circumferential angle = 20°.

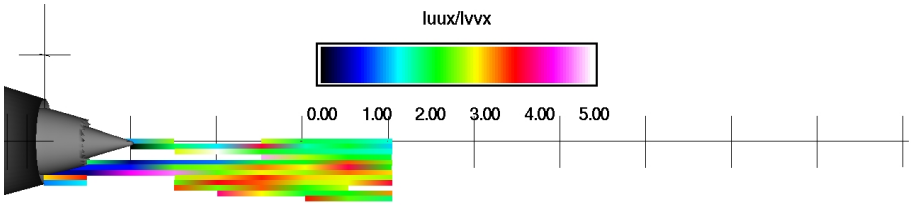

Figure 3.5.3.5 Model 3tb. Contour plots of Luu(x)/Lvv(x). Slice taken at circumferential angle = 20°.

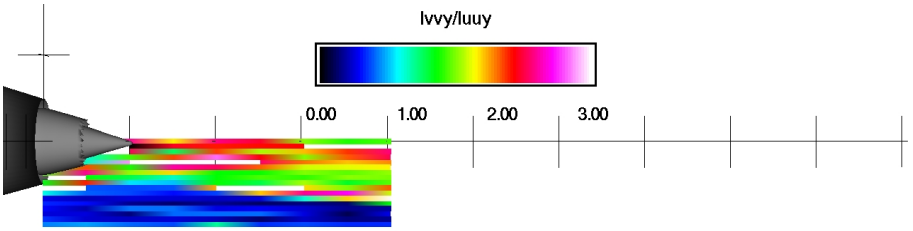

Figure 3.5.3.6 Model 3tb. Contour plots of Lvv(y)/Luu(y). Slice taken at circumferential angle = 20°.

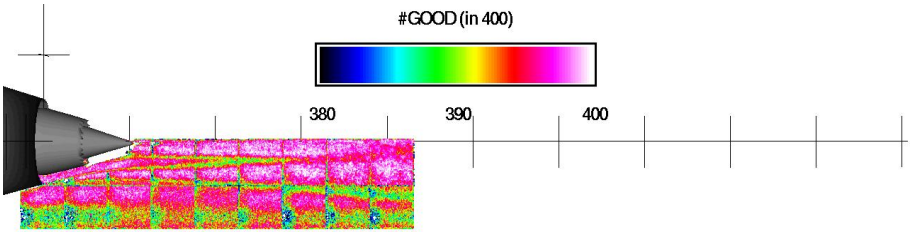

Figure 3.6.1.1 Model 3tb. Contour plots of data quality (#good out of 400). Slice taken at circumferential angle = 25°.

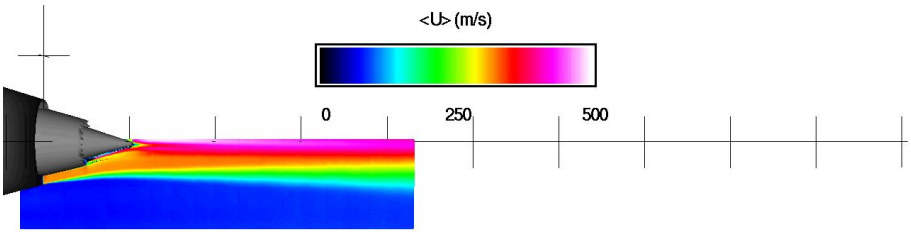

Figure 3.6.1.2 Model 3tb. Contour plots of time average axial velocity (m/s). Slice taken at circumferential angle = 25°.

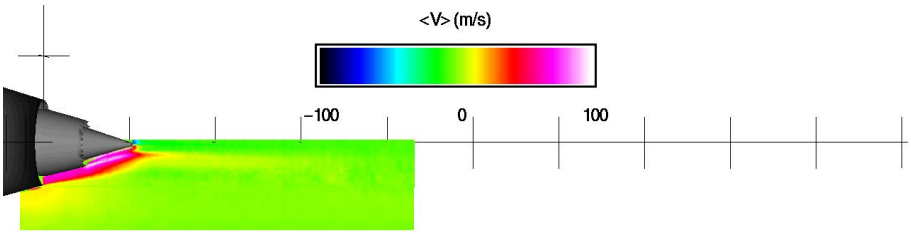

Figure 3.6.1.3 Model 3tb. Contour plots of time average radial velocity (m/s). Slice taken at circumferential angle = 25°.

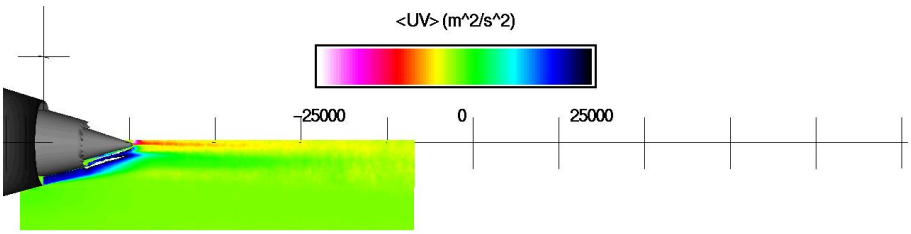

Figure 3.6.1.4 Model 3tb. Contour plots of time average Reynolds stress (m^2/s^2). Slice taken at circumferential angle = 25°.

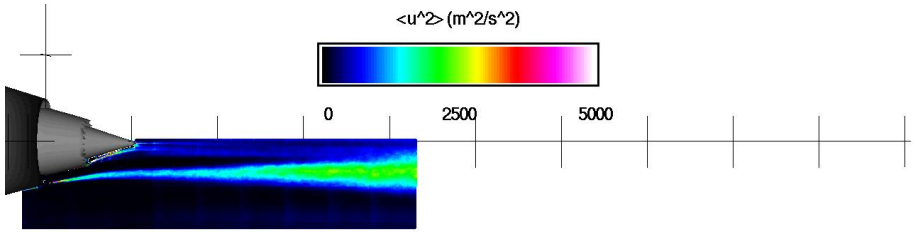

Figure 3.6.1.5 Model 3tb. Contour plots of variance of axial velocity (m^2/s^2). Slice taken at circumferential angle = 25°.

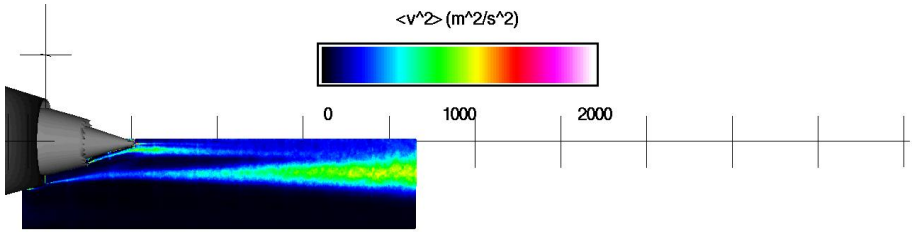

Figure 3.6.1.6 Model 3tb. Contour plots of variance in radial velocity (m^2/s^2). Slice taken at circumferential angle = 25°.

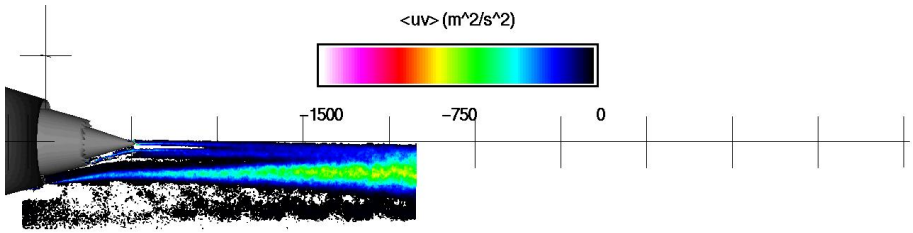

Figure 3.6.1.7 Model 3tb. Contour plots of unsteady Reynolds stress (m^2/s^2). Slice taken at circumferential angle = 25°.

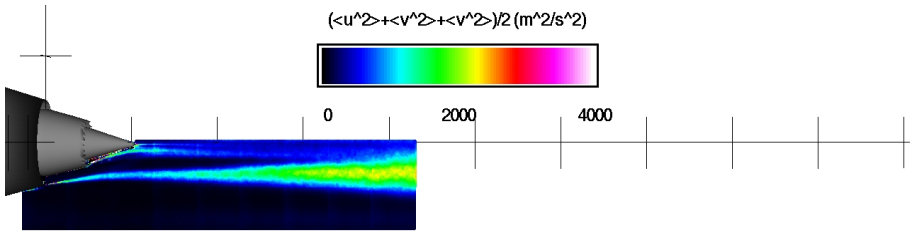

Figure 3.6.1.8 Model 3tb. Contour plots of turbulent kinetic energy (m^2/s^2). Slice taken at circumferential angle = 25°.

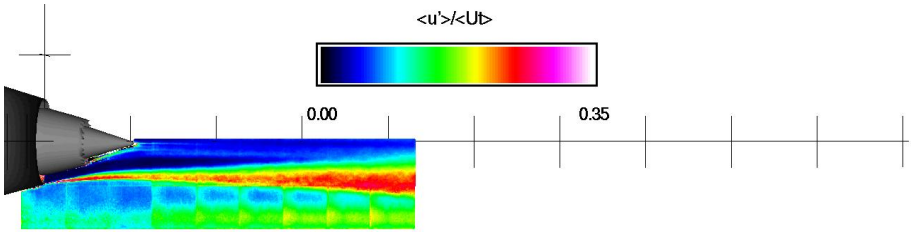

Figure 3.6.1.9 Model 3tb. Contour plots of axial turbulence intensity. Slice taken at circumferential angle = 25°.

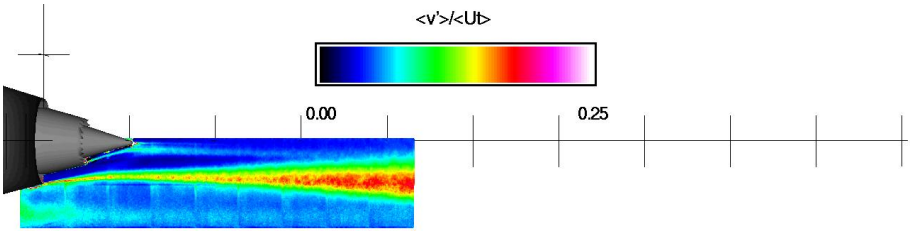

Figure 3.6.1.10 Model 3tb. Contour plots of radial turbulence intensity. Slice taken at circumferential angle = 25°.

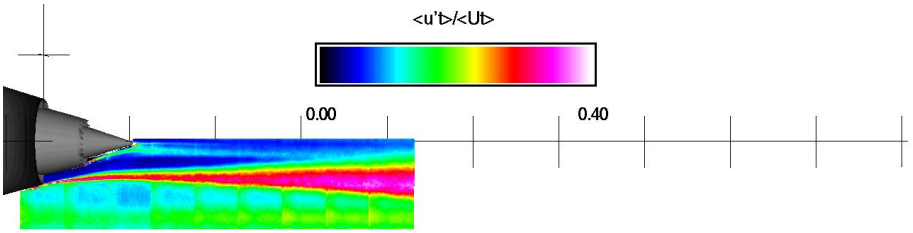

Figure 3.6.1.11 Model 3tb. Contour plots of turbulence intensity. Slice taken at circumferential angle = 25°.

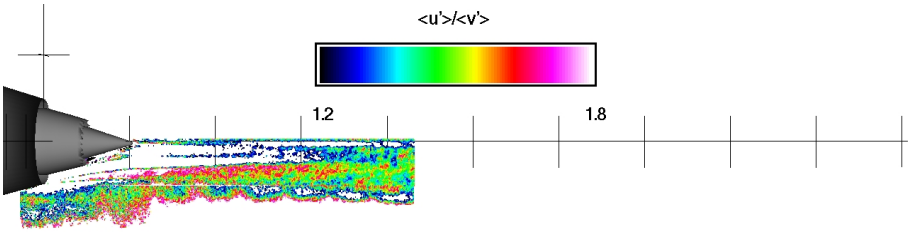

Figure 3.6.1.12 Model 3tb. Contour plots of ratio of axial to radial turbulence. Slice taken at circumferential angle = 25°.

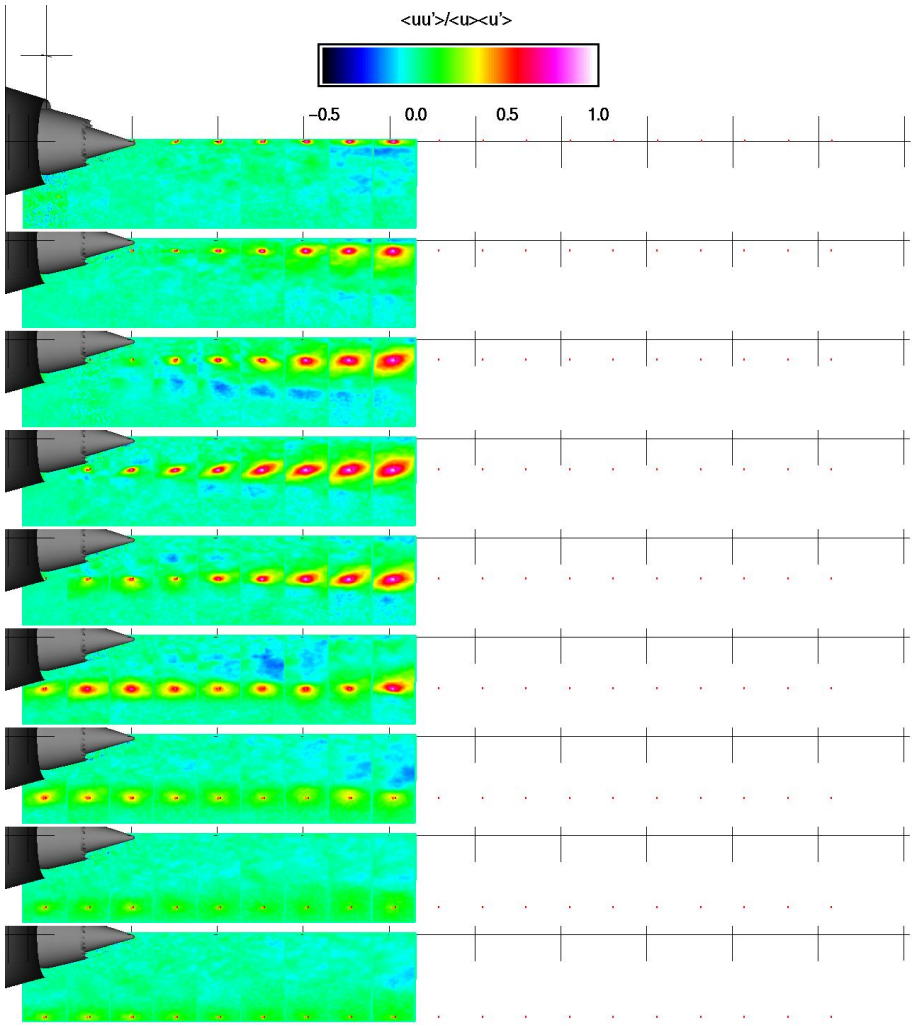

Figure 3.6.2.1 Model 3tb. Contour plots of u(xref)u(x). Slice taken at circumferential angle = 25°.

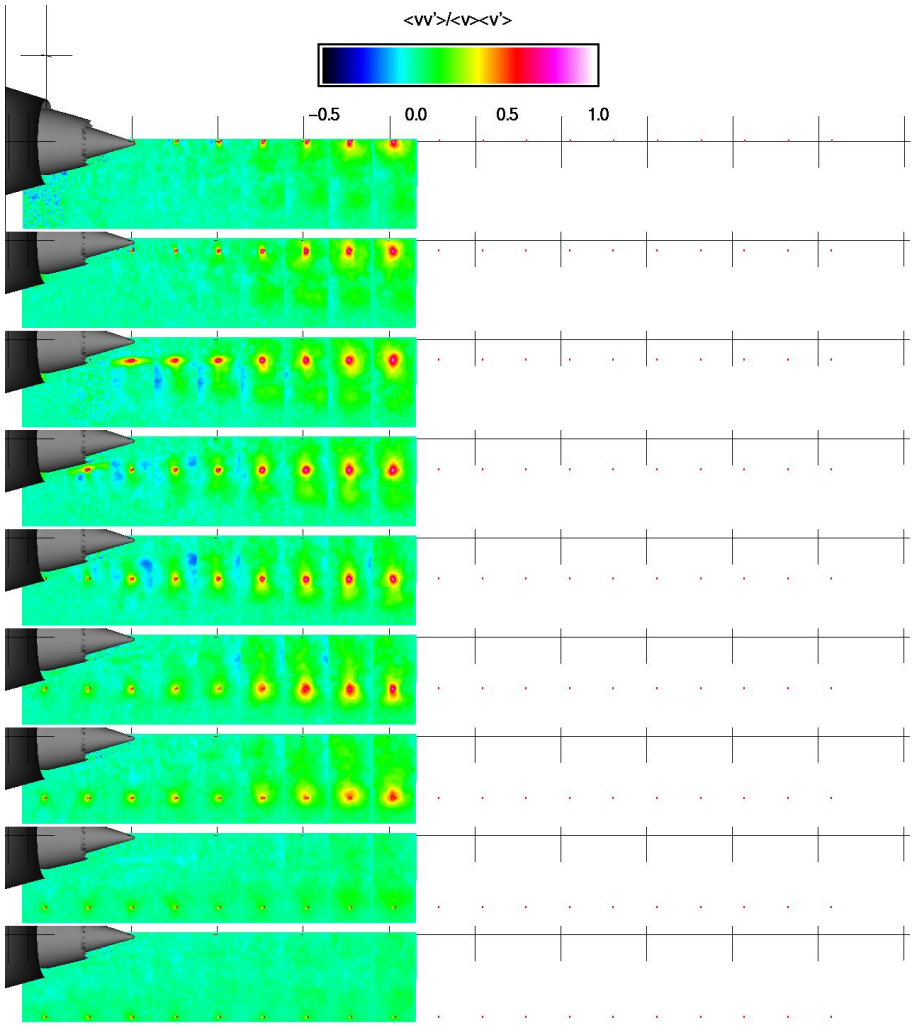

Figure 3.6.2.2 Model 3tb. Contour plots of v(xref)v(x). Slice taken at circumferential angle = 25°.

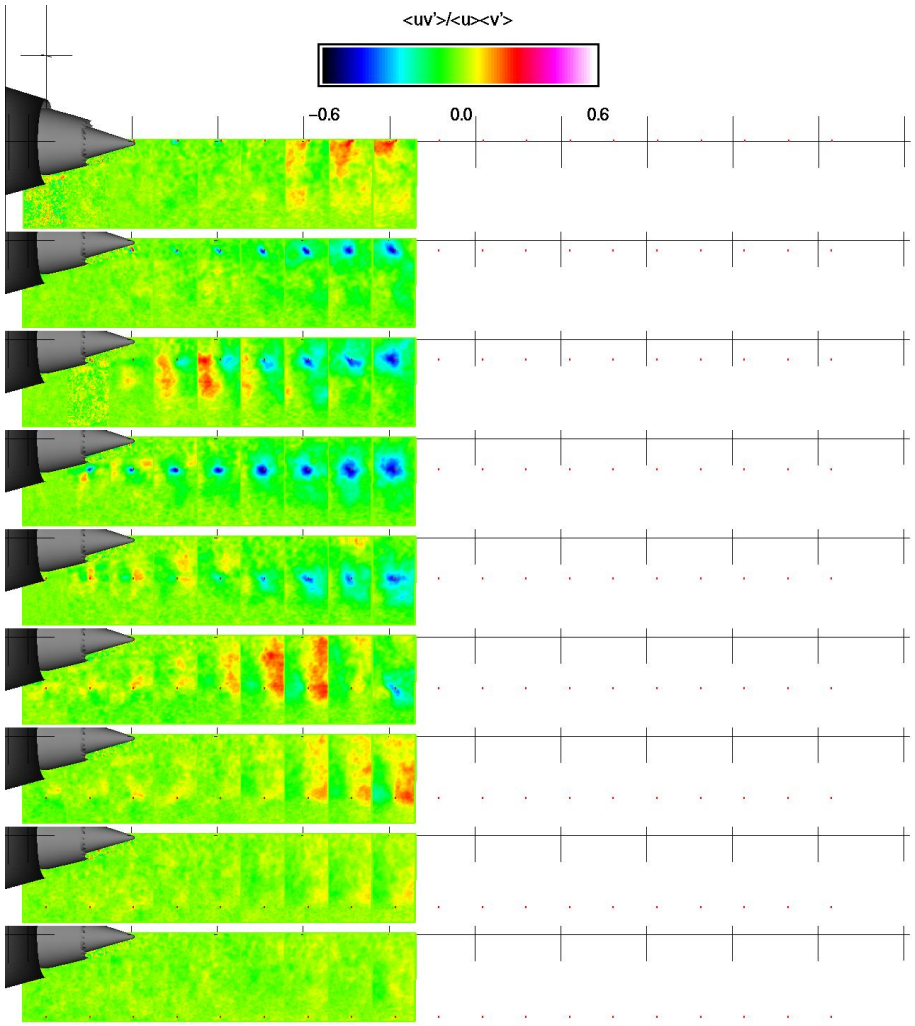

Figure 3.6.2.3 Model 3tb. Contour plots of u(xref)v(x). Slice taken at circumferential angle = 25°.

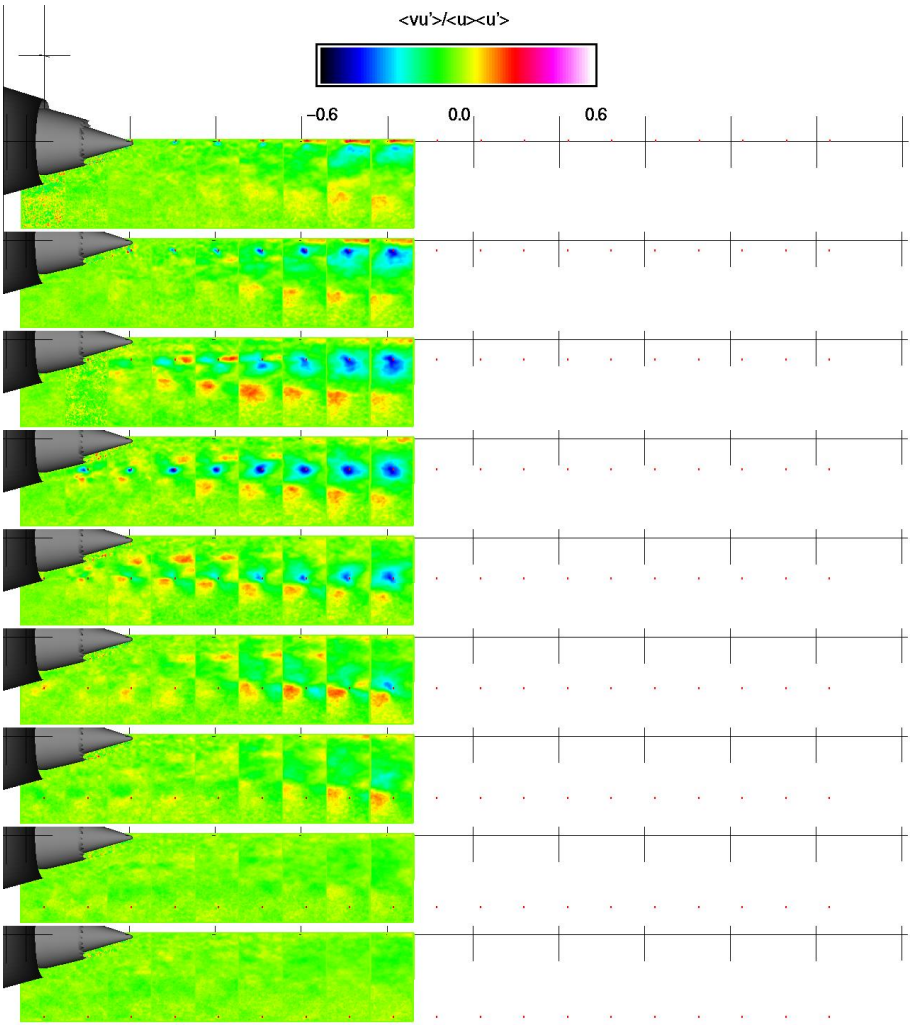

Figure 3.6.2.4 Model 3tb. Contour plots of v(xref)u(x). Slice taken at circumferential angle = 25°.

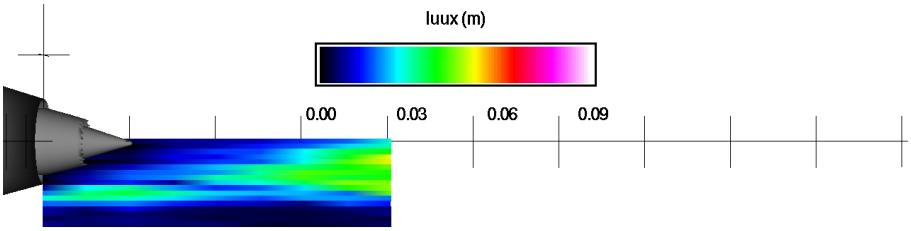

Figure 3.6.3.1 Model 3tb. Contour plots of Luu(x). Slice taken at circumferential angle = 25°.

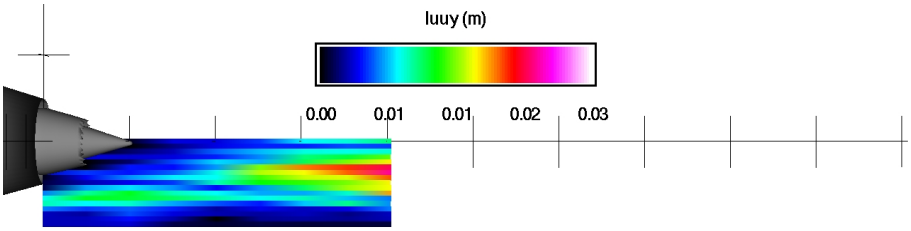

Figure 3.6.3.2 Model 3tb. Contour plots of Luu(y). Slice taken at circumferential angle = 25°.

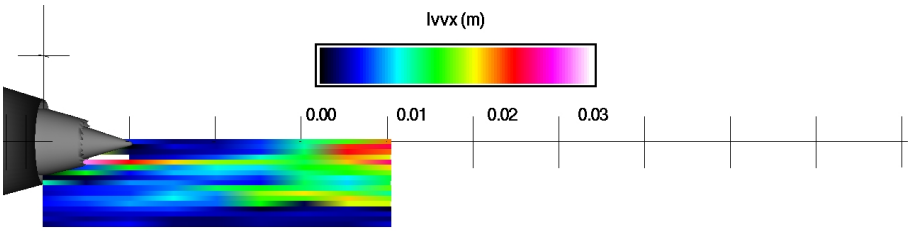

Figure 3.6.3.3 Model 3tb. Contour plots of Lvv(x). Slice taken at circumferential angle = 25°.

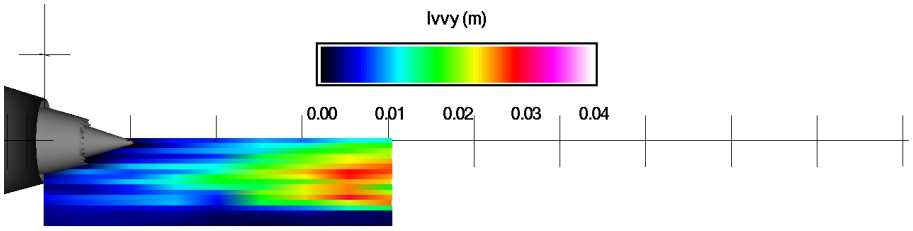

Figure 3.6.3.4 Model 3tb. Contour plots of Lvv(y). Slice taken at circumferential angle = 25°.

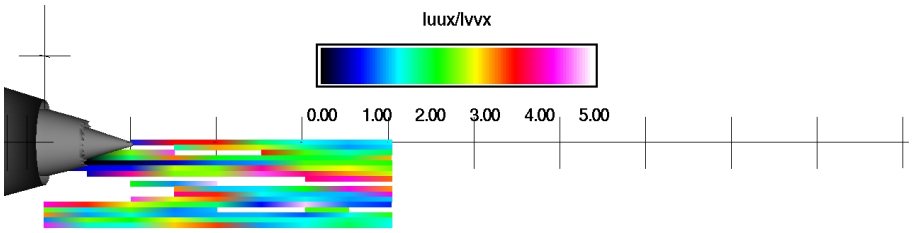

Figure 3.6.3.5 Model 3tb. Contour plots of Luu(x)/Lvv(x). Slice taken at circumferential angle = 25°.

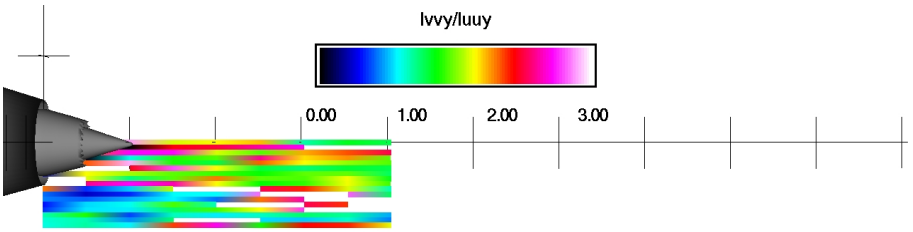

Figure 3.6.3.6 Model 3tb. Contour plots of Lvv(y)/Luu(y). Slice taken at circumferential angle = 25°.

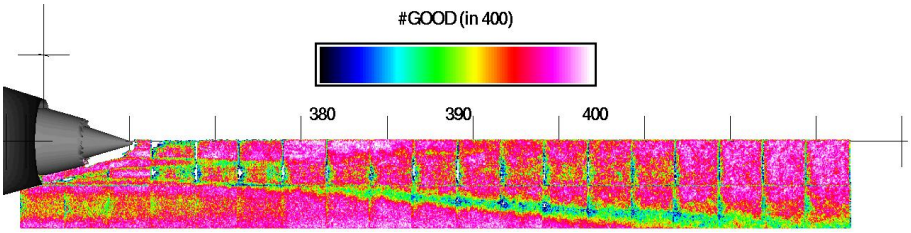

Figure 3.7.1.1 Model 3tb. Contour plots of data quality (#good out of 400). Slice taken at circumferential angle = 30°.

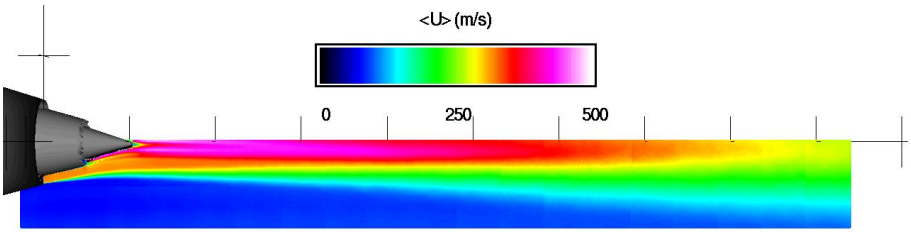

Figure 3.7.1.2 Model 3tb. Contour plots of time average axial velocity (m/s). Slice taken at circumferential angle = 30°.

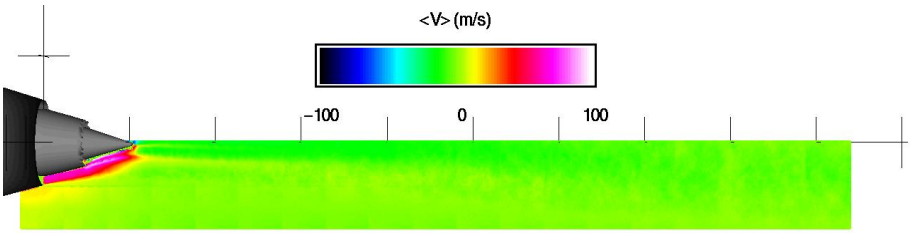

Figure 3.7.1.3 Model 3tb. Contour plots of time average radial velocity (m/s). Slice taken at circumferential angle = 30°.

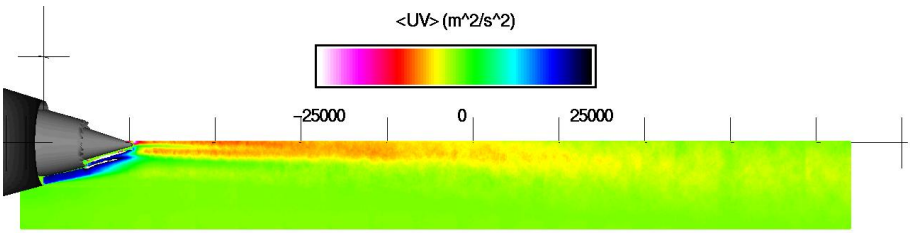

Figure 3.7.1.4 Model 3tb. Contour plots of time average Reynolds stress (m^2/s^2). Slice taken at circumferential angle = 30°.

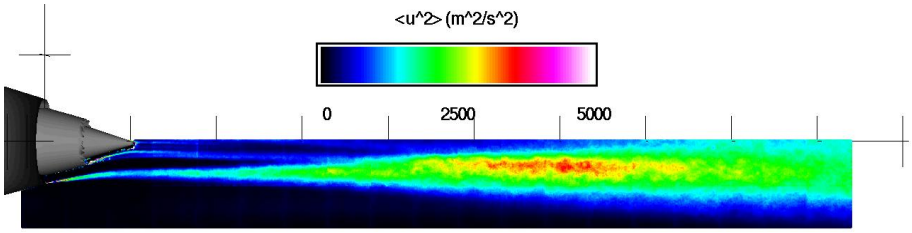

Figure 3.7.1.5 Model 3tb. Contour plots of variance of axial velocity (m^2/s^2). Slice taken at circumferential angle = 30°.

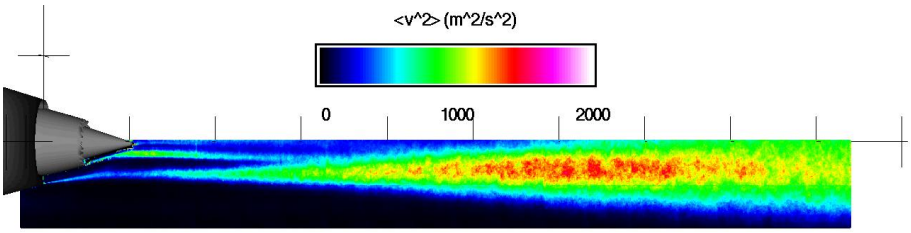

Figure 3.7.1.6 Model 3tb. Contour plots of variance in radial velocity (m^2/s^2). Slice taken at circumferential angle = 30°.

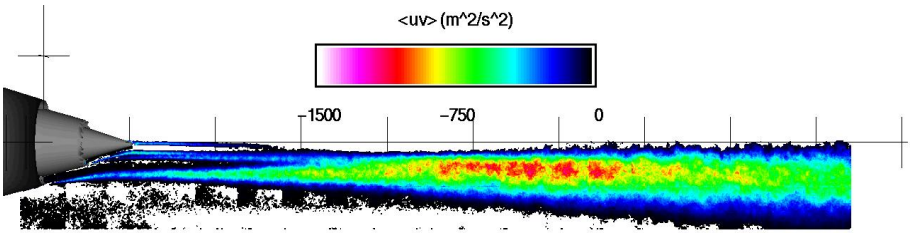

Figure 3.7.1.7 Model 3tb. Contour plots of unsteady Reynolds stress (m^2/s^2). Slice taken at circumferential angle = 30°.

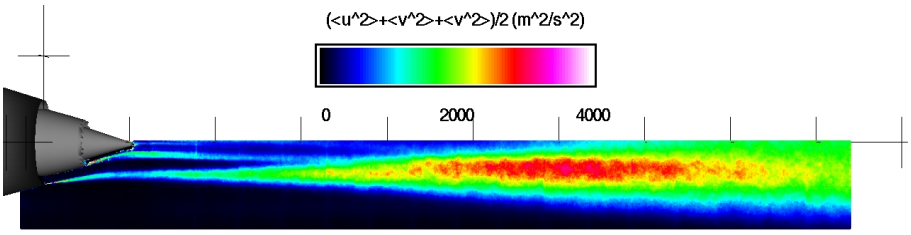

Figure 3.7.1.8 Model 3tb. Contour plots of turbulent kinetic energy (m^2/s^2). Slice taken at circumferential angle = 30°.

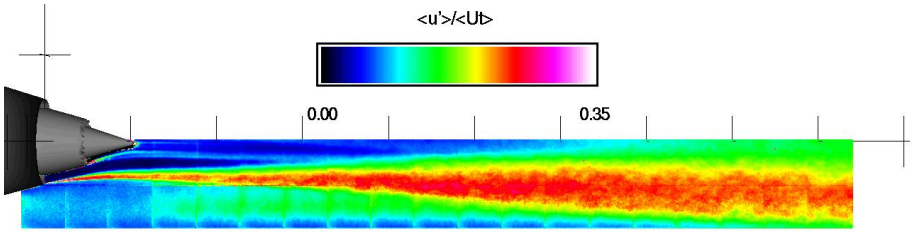

Figure 3.7.1.9 Model 3tb. Contour plots of axial turbulence intensity. Slice taken at circumferential angle = 30°.

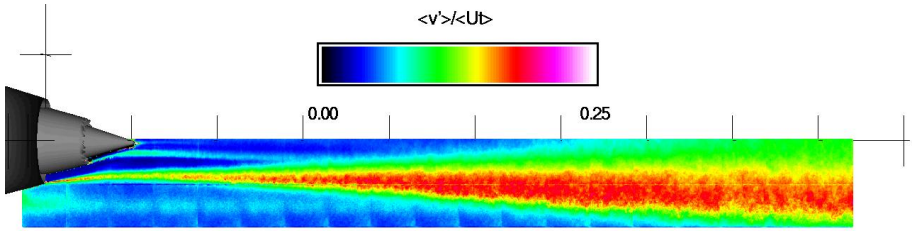

Figure 3.7.1.10 Model 3tb. Contour plots of radial turbulence intensity. Slice taken at circumferential angle = 30°.

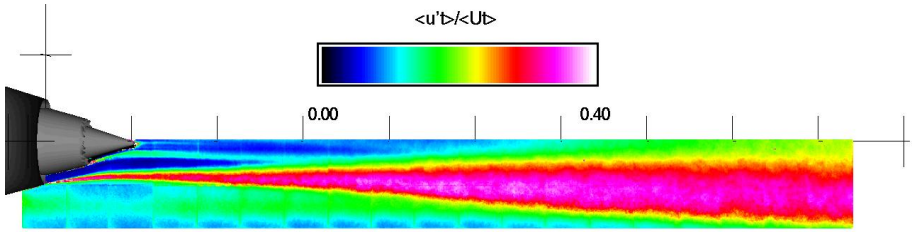

Figure 3.7.1.11 Model 3tb. Contour plots of turbulence intensity. Slice taken at circumferential angle = 30°.

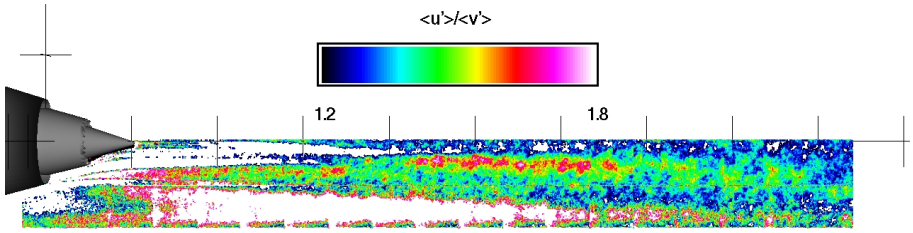

Figure 3.7.1.12 Model 3tb. Contour plots of ratio of axial to radial turbulence. Slice taken at circumferential angle = 30°.

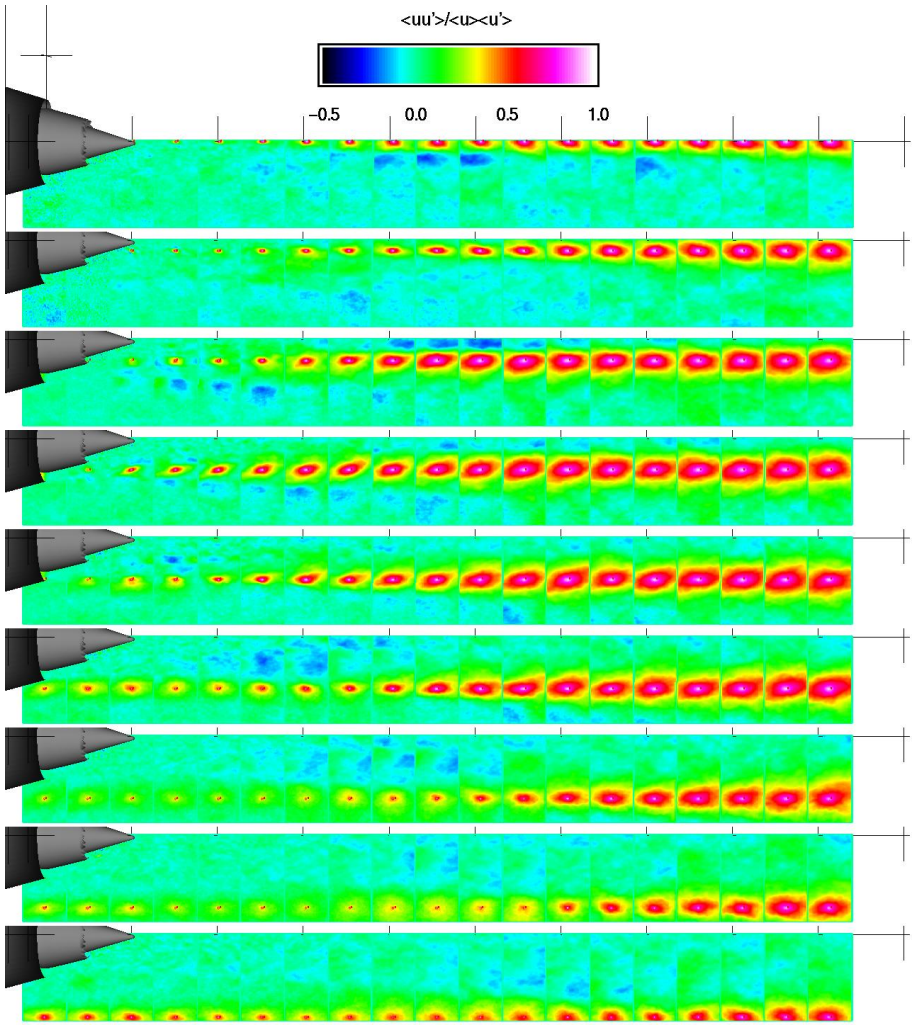

Figure 3.7.2.1 Model 3tb. Contour plots of u(xref)u(x). Slice taken at circumferential angle = 30°.

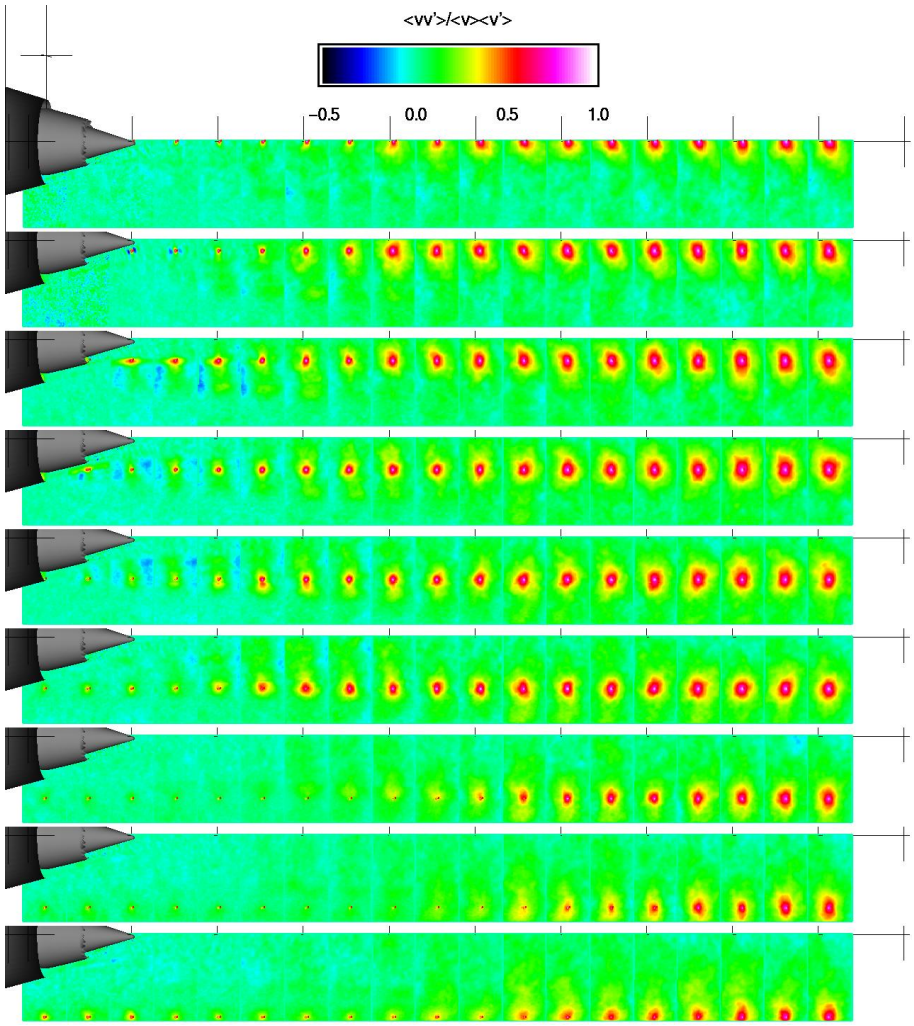

Figure 3.7.2.2 Model 3tb. Contour plots of v(xref)v(x). Slice taken at circumferential angle = 30°.

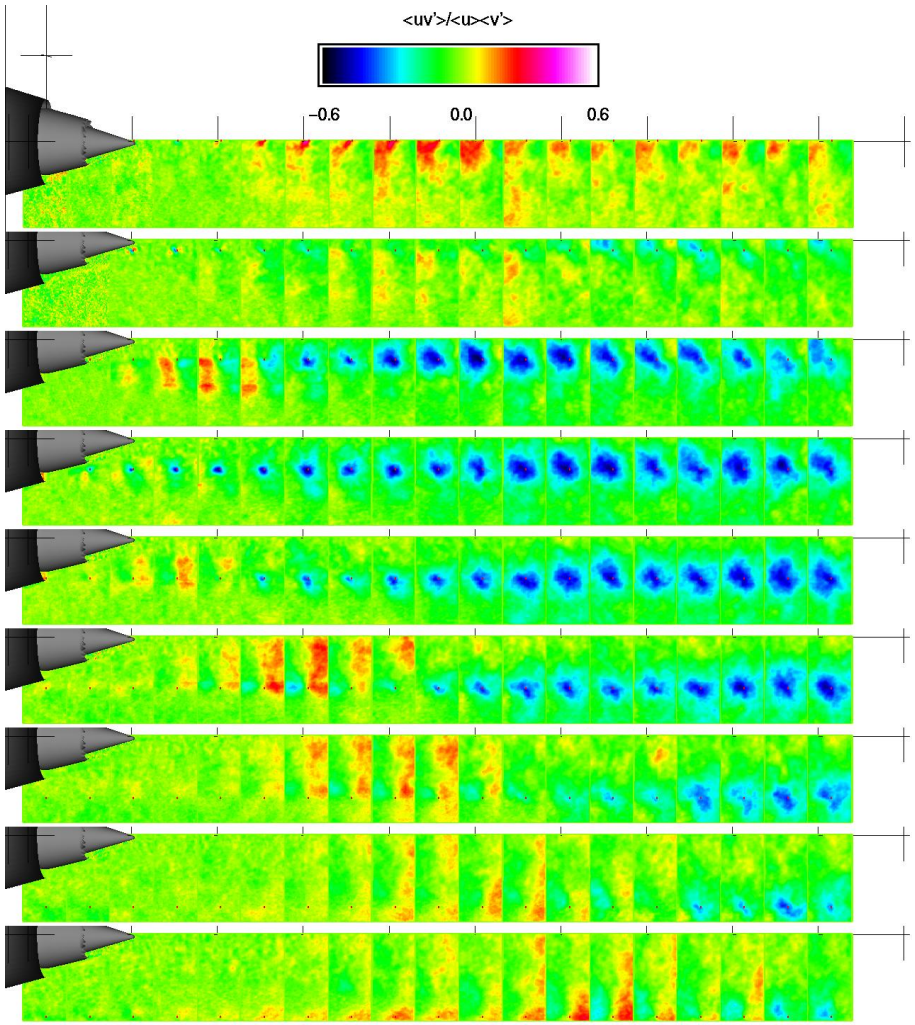

Figure 3.7.2.3 Model 3tb. Contour plots of u(xref)v(x). Slice taken at circumferential angle = 30°.

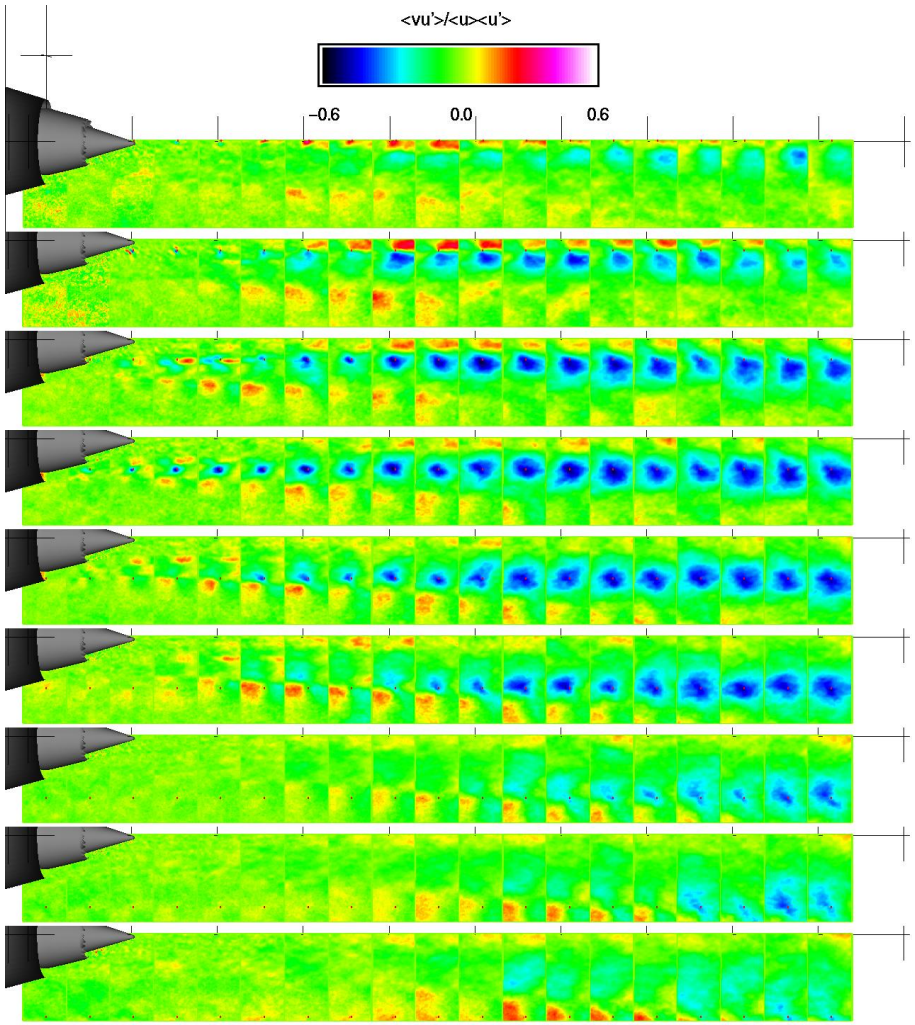

Figure 3.7.2.4 Model 3tb. Contour plots of v(xref)u(x). Slice taken at circumferential angle = 30°.

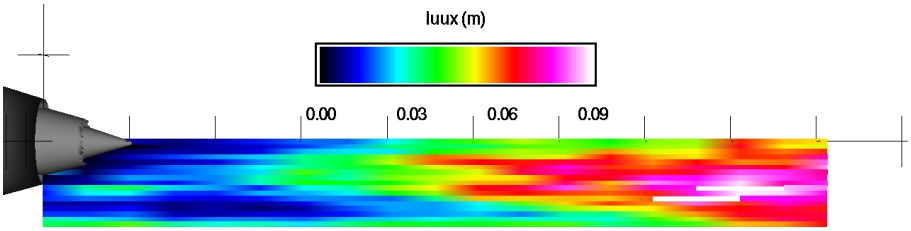

Figure 3.7.3.1 Model 3tb. Contour plots of Luu(x). Slice taken at circumferential angle = 30°.

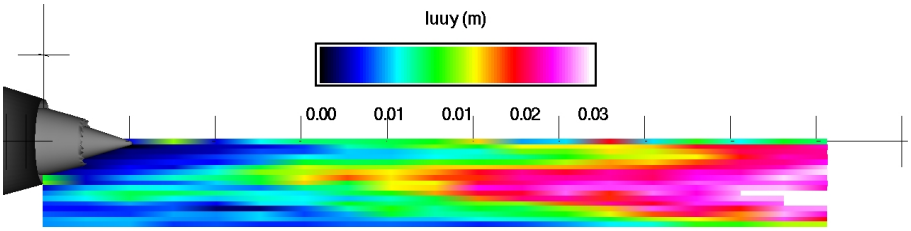

Figure 3.7.3.2 Model 3tb. Contour plots of Luu(y). Slice taken at circumferential angle = 30°.

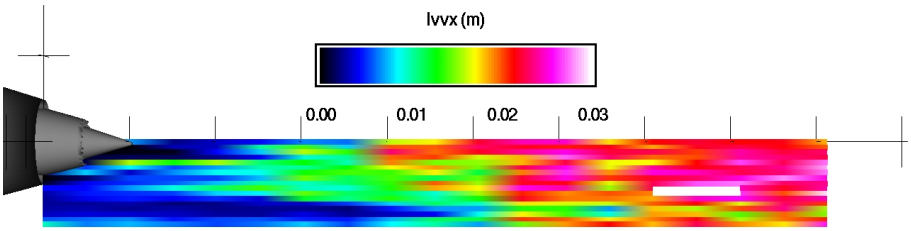

Figure 3.7.3.3 Model 3tb. Contour plots of Lvv(x). Slice taken at circumferential angle = 30°.

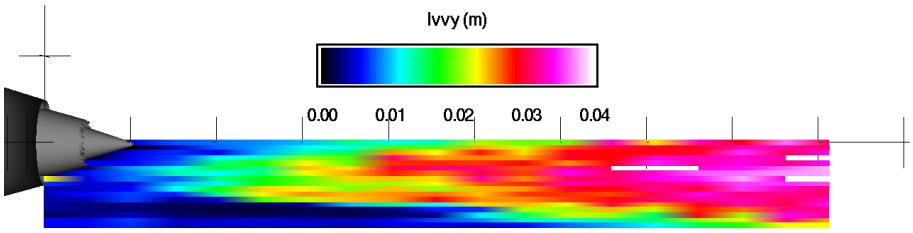

Figure 3.7.3.4 Model 3tb. Contour plots of Lvv(y). Slice taken at circumferential angle = 30°.

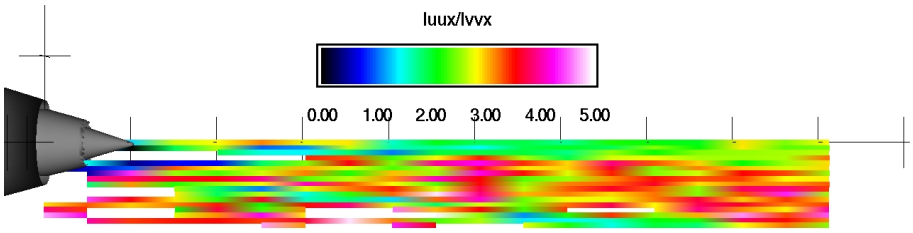

Figure 3.7.3.5 Model 3tb. Contour plots of Luu(x)/Lvv(x). Slice taken at circumferential angle = 30°.

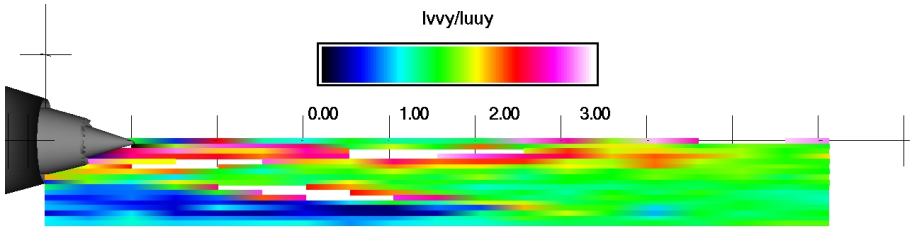

Figure 3.7.3.6 Model 3tb. Contour plots of Lvv(y)/Luu(y). Slice taken at circumferential angle = 30°.

14 Appendix C: Data files

Data files are provided in electronic versions of this document. They are files of the turbulence statistics calculated and plotted in Appendix B. The data files are in ASCII formatted ‘plot3D’ function format and located in the folder entitled 'p3d_data'.

REPORT DOCUMENTATION PAGE

Form Approved
OMB No. 0704-0188

1. AGENCY USE ONLY (*Leave blank*)	2. REPORT DATE	3. REPORT TYPE AND DATES COVERED
	February 2002	Technical Memorandum

4. TITLE AND SUBTITLE

Measurements of Turbulent Flow Field in Separate Flow Nozzles With Enhanced Mixing Devices—Test Report

5. FUNDING NUMBERS

WU–781–30–12–00

6. AUTHOR(S)

James Bridges

7. PERFORMING ORGANIZATION NAME(S) AND ADDRESS(ES)

National Aeronautics and Space Administration
John H. Glenn Research Center at Lewis Field
Cleveland, Ohio 44135–3191

8. PERFORMING ORGANIZATION REPORT NUMBER

E–13188

9. SPONSORING/MONITORING AGENCY NAME(S) AND ADDRESS(ES)

National Aeronautics and Space Administration
Washington, DC 20546–0001

10. SPONSORING/MONITORING AGENCY REPORT NUMBER

NASA TM—2002-211366

11. SUPPLEMENTARY NOTES

Responsible person, James Bridges, organization code 5940, 216–433–2693.

12a. DISTRIBUTION/AVAILABILITY STATEMENT

Unclassified - Unlimited
Subject Categories: 07, 09, and 34 Distribution: Nonstandard

Available electronically at http://gltrs.grc.nasa.gov/GLTRS

This publication is available from the NASA Center for AeroSpace Information, 301–621–0390.

12b. DISTRIBUTION CODE

13. ABSTRACT ***(Maximum 200 words)***

As part of the Advanced Subsonic Technology Program, a series of experiments was conducted at NASA Glenn Research Center on the effect of mixing enhancement devices on the aeroacoustic performance of separate flow nozzles. Initial acoustic evaluations of the devices showed that they reduced jet noise significantly, while creating very little thrust loss. The explanation for the improvement required that turbulence measurements, namely single point mean and RMS statistics and two-point spatial correlations, be made to determine the change in the turbulence caused by the mixing enhancement devices that lead to the noise reduction, These measurements were made in the summer of 2000 in a test program called Separate Nozzle Flow Test 2000 (SFNT2K) supported by the Aeropropulsion Research Program at NASA Glenn Research Center. Given the hot high-speed flows representative of a contemporary bypass ratio 5 turbofan engine, unsteady flow field measurements required the use of an optical measurement method. To achieve the spatial correlations, the Particle Image Velocimetry technique was employed, acquiring high-density velocity maps of the flows from which the required statistics could be derived. This was the first successful use of this technique for such flows, and shows the utility of this technique for future experimental programs. The extensive statistics obtained were likewise unique and give great insight into the turbulence which produces noise and how the turbulence can he modified to reduce jet noise. This report documents the test facilities and procedures used to obtain the turbulence data. It also contains an indexed overview of the results, both in graphical and numerical formats.

14. SUBJECT TERMS

Particle image velocimetry; Unsteady flow; Turbofan engines; Turbulent flow; Nozzle flow; Flow measurement; Noise reduction; Jet aircraft noise; Turbulence

15. NUMBER OF PAGES

205

16. PRICE CODE

17. SECURITY CLASSIFICATION OF REPORT	18. SECURITY CLASSIFICATION OF THIS PAGE	19. SECURITY CLASSIFICATION OF ABSTRACT	20. LIMITATION OF ABSTRACT
Unclassified	Unclassified	Unclassified	